Proteomic Studies on Intracellular Nanocarrier Trafficking and Regenerative Bone Substitute Materials

Dissertation

zur Erlangung des Grades
Doktor der Naturwissenschaften
im Promotionsfach Chemie

am Fachbereich Chemie, Pharmazie,
Geographie und Geowissenschaften
der Johannes Gutenberg-Universität Mainz

vorgelegt von
Richard da Costa Marques
geboren in Wiesbaden

Mainz, 2022

Dekanin: ___

Prodekane: ___

___

1. Gutachterin: ___

2. Gutachter: ___

Tag der mündlichen Prüfung: 13.03.2023

Declaration

The research presented herein was conducted from April 2019 until October 2022 at the Max Planck Institute for Polymer Research in Mainz in the department of ___. The experiments and thesis writing were supervised by ___ and ___.

I, Richard da Costa Marques, declare that this dissertation was prepared by myself without any unauthorized use of external assistance. I indicated or cited all utilized resources, such as materials, equipment, or literature. I did not submit this work or parts of it to a different faculty or department as a dissertation.

Mainz, December 8th, 2022 _____

Richard da Costa Marques

Table of Contents

Abstract

The design and medical performance of nano- and biomaterials remain impacted by the adsorption of biomolecules, specifically the adsorption of proteins. Protein adsorption is inevitably initiated upon contact with biological fluids or tissues, leading to a change in the surface properties of the materials. These changed surface properties evoke undesired biological effects, posing a major drawback for indented medical purposes. To overcome this drawback, or even exploit protein adsorption, it is necessary to analyze the composition of adsorbed proteins and study the interactions with cells, tissues, and organisms. This thesis addresses the challenges of protein adsorption on nanoparticles (NPs) in intracellular environments and on calcium phosphate (CaP) biomaterial surfaces for bone substitution.

The layers of adsorbed proteins on NPs are termed protein corona. The formation of the protein corona is influenced by the protein milieu and the physicochemical properties of the NPs. The protein corona has been studied with various biological fluids and NP systems, but the comparability of these studies remains challenging. To address the lacking comparability, the study presented in chapter A of this thesis analyzed the protein corona formation under different plasma protein concentrations, temperatures, and NP surface modifications. Here, we observed different outcomes in protein adsorption and cell uptake when varying surface charge and surfactant on polystyrene NPs at consistent concentration and temperature. Notably, decreasing protein concentration and temperature during the protein corona formation resulted in increased cellular uptake for all studied NP types. The results highlight the necessity to thoughtfully select experimental conditions for protein corona studies.

Despite numerous studies of the protein corona in extracellular environments, the cellular processing of NPs and the formation of the intracellular protein corona continue to be poorly studied. Considering that the protein corona influences the cellular uptake and intracellular NP cargo release, it is crucial to characterize the intracellular protein corona. The first study of chapter B investigated the intracellular separation and fate of a preabsorbed protein corona on polystyrene NPs. By utilizing correlative light and electron microscopy and flow cytometry, the endosomal separation of corona proteins and NPs into morphologically distinct endosomal compartments was demonstrated. Eventually, the NPs were exocytosed, and the protein corona was processed for lysosomal degradation. The second study of chapter B revealed the intracellular trafficking of two biocompatible NP types by implementing proteomic analysis. We demonstrated a gradual evolution of the protein corona for hydroxyethyl starch NPs with a slower uptake while demonstrating a stable protein corona for human serum albumin nanocapsules with an accelerated uptake. Additionally, by unraveling the intracellular protein corona, we reconstructed molecular details during the intracellular trafficking and

complemented the results by flow cytometry and microscopy. For the third study of chapter B, the analysis of the intracellular protein corona was applied to investigate the endocytosis of gold NPs for imaging applications in stromal cells. The exocytosis of gold NPs was dependent on the performed loading protocol. Especially higher loading with gold NPs resulted in lower exocytosis when compared to a lower loading. Here, the analysis of the intracellular protein corona revealed that a higher loading led to an enrichment of intracellular proteins, decreasing exocytosis. Overall, the studies in this chapter demonstrated that detailed characterizations of the intracellular protein corona will improve NP application in drug delivery and imaging.

Chapter C focuses on protein adsorption on bulk biomaterial with nanostructured surfaces. To provide regenerative properties to synthetic biomaterials for bone substitution, the biomaterials are combined with growth factor-rich hemoderivatives. However, the composition of the adsorbed proteins is rarely investigated. The study in chapter C investigated the protein adsorption from hemoderivative protein sources on CaP bone substitutes regarding their regenerative potential for angiogenesis. Using proteomic studies, we identified abundantly adsorbed non-angiogenic and anti-angiogenic proteins. Furthermore, we measured the depletion of pro-angiogenic growth factors. The pro-angiogenic effects were analyzed by tube-formation assays with endothelial cells. Here, we observed pro-angiogenic effects when the CaPs were kept in the hemoderivative protein source but not after washing with PBS. These results emphasize the importance of analyzing protein adsorption to improve the regenerative, e. g. pro-angiogenic capabilities of biomaterials.

In conclusion, the presented studies emphasize the benefits of protein adsorption analysis for the development of nano- and biomaterials with medical applications. The future design of these materials will tremendously profit from studying surface-adsorbed proteins and exploiting this knowledge to modulate desired biological effects.

Zusammenfassung

Das Design und die medizinische Wirkung von Nano- und Biomaterialien werden durch die Adsorption von Biomolekülen, insbesondere von Proteinen, beeinflusst. Die Adsorption von Proteinen wird unweigerlich durch den Kontakt mit biologischen Flüssigkeiten oder Geweben ausgelöst, was zur Veränderung der Oberflächeneigenschaften der Materialien führt. Diese veränderten Oberflächeneigenschaften führen wiederum zu unerwünschten biologischen Effekten, die einen großen Nachteil für die medizinische Anwendung darstellen. Um diesen Nachteil zu überwinden oder die Proteinadsorption sogar gezielt auszunutzen, ist es notwendig, die Zusammensetzung der adsorbierten Proteine zu analysieren und deren Wechselwirkungen mit Zellen, Geweben und Organismen zu untersuchen. Die vorliegende Dissertation befasst sich mit den Untersuchungen der Proteinadsorption an Nanopartikeln (NPs) in intrazellulären Umgebungen und an Kalziumphosphat-basierten (CaP) Biomaterialoberflächen für den Knochenersatz.

Proteine adsorbieren schichtenartig an NPs, was als Proteinkorona bezeichnet wird. Die Bildung der Proteinkorona wird durch das Proteinmilieu und die physikochemischen Eigenschaften der NPs beeinflusst. Bisher wurde die Proteinkorona in verschiedenen biologischen Flüssigkeiten und mit unterschiedlichen NP-Systemen untersucht, jedoch lassen sich die Studien nur schwer vergleichen. Um diese mangelnde Vergleichbarkeit zu adressieren, wurde in der Studie des Kapitels A dieser Arbeit die Bildung der Proteinkorona bei unterschiedlichen Proteinkonzentrationen, Temperaturen und NP-Oberflächenmodifikationen untersucht. Durch Variation von Oberflächenladungen und Tensiden bei Polystyrol-NPs wurden unterschiedliche Ergebnisse in Proteinadsorption und Zellaufnahme bei gleichbleibender Konzentration und Temperatur beobachtet. Insbesondere führte eine Verringerung der Proteinkonzentration und Temperatur während der Bildung der Proteinkorona bei allen untersuchten NP-Typen zu einer erhöhten zellulären Aufnahme. Die Ergebnisse unterstreichen die Notwendigkeit, die experimentellen Bedingungen für Proteinkorona-Studien sorgfältig auszuwählen.

Trotz zahlreicher Studien zur Proteinkorona in extrazellulären Umgebungen bleiben die zelluläre Verarbeitung von NPs und die Bildung der intrazellulären Proteinkorona nur unzureichend untersucht. Da die Proteinkorona jedoch die zelluläre Aufnahme von NPs und die intrazelluläre Wirkstofffreisetzung beeinflusst, ist es von entscheidender Bedeutung, die intrazelluläre Proteinkorona zu charakterisieren. Die erste Studie in Kapitel B untersuchte die intrazelluläre Trennung und den Verbleib einer voradsorbierten Proteinkorona auf Polystyrol-NPs. Mittels korrelativer Licht- und Elektronenmikroskopie und Durchflusszytometrie wurde die endosomale Trennung von Korona-Proteinen und NPs in morphologisch unterschiedliche endosomale Kompartimente nachgewiesen. Schließlich wurden die NP exozytiert und die

Proteinkorona für in den lysosomalen Abbauweg geschleust. In der zweiten Studie des Kapitels B wurde der intrazelluläre Transport von zwei biokompatiblen NP-Systemen durch die Implementierung von Proteomanalysen untersucht. Die vergleichbar langsame zelluläre Aufnahme von Hydroxyethylstärke-NPs korrelierte mit einer zeitlichen Veränderung der intrazellulären Proteinkorona, während eine beschleunigte Aufnahme der Humanalbumin-Nanokapseln mit einer stabilen Proteinkorona korrelierten. Durch die Analyse der intrazellulären Proteinkorona wurden zusätzlich molekulare Details der intrazellulären Verarbeitung rekonstruieren, was die Ergebnisse durch Durchflusszytometrie und Mikroskopie ergänzte. In der dritten Studie des Kapitels B wurde die intrazelluläre Proteinkorona analysiert, um die Endozytose von Gold-NPs für bildgebende Anwendungen in Stromazellen zu untersuchen. Die untersuchte Exozytose der Gold-NPs war abhängig vom durchgeführten Beladungsprotokoll. Insbesondere eine höhere Beladung mit Gold-NPs führte zu einer geringeren Exozytose, im Vergleich zu einer geringeren Beladung. Hier zeigte die Analyse der intrazellulären Proteinkorona, dass eine höhere Beladung zu einer Anreicherung von intrazellulären Proteinen führte und dies vermutlich die Exozytose verringerte. Insgesamt haben die Studien in diesem Kapitel gezeigt, dass eine detaillierte Charakterisierung der intrazellulären Proteinkorona die Anwendung von NP in der Wirkstofffreisetzung und in bildgebenden Verfahren verbessern.

Kapitel C befasst sich mit der Proteinadsorption an Oberflächen von Biomaterialien mit nanostrukturierten Oberflächen. Um synthetische Biomaterialien für den Knochenersatz regenerative Eigenschaften zu verleihen, werden die Biomaterialien mit Wachstumsfaktor-reichen Blutprodukten kombiniert. Die Zusammensetzung der adsorbierten Proteine wird jedoch nur selten untersucht. Die Studie in Kapitel C untersuchte die Proteinadsorption aus Blutprodukten an CaP-Knochenersatzmaterialien im Hinblick auf ihr regeneratives Potenzial für die Angiogenese. Durch proteomische Studien wurde eine Anreicherung von nicht-angiogenen und anti-angiogenen Proteinen nachgewiesen. Darüber hinaus wurde die Abreicherung von pro-angiogenen Wachstumsfaktoren gemessen. Die pro-angiogenen Wirkungen wurden mittels Tube-Formation Assays mit Endothelzellen analysiert. Hier wurden pro-angiogene Effekte beobachtet, solange die CaPs in den Blutprodukten verblieben, jedoch nicht nach dem Waschen mit PBS. Diese Ergebnisse unterstreichen die Bedeutung von Untersuchungen der Proteinadsorption zur Verbesserung der regenerativen oder pro-angiogenen Wirkung von Biomaterialien.

Zusammengefasst unterstreichen die dargestellten Studien den Nutzen der Analyse von Proteinadsorption auf Nano- und Biomaterialien für die medizinische Anwendung. Das Design dieser Materialien wird von Proteinadsorptionsanalysen zukünftig profitieren. Die hierbei gesammelte Expertise kann zudem zur Modulation von gewünschten biologischen Wirkungen genutzt werden.

Publication list

This thesis covers publications **[1-5]**. Publications **[6-8]** are not covered but are listed for the reason of completeness.

[1] ___, ___, **da Costa Marques, R.**, ___, ___. Temperature, concentration, and surface modification influence the cellular uptake and the protein corona of polystyrene nanoparticles. *Acta Biomaterialia*, **2022**, *148*, 271–278.

[2] ___, **da Costa Marques, R.***, ___, ___, ___, ___, ___, ___. Endosomal sorting results in a selective separation of the protein corona from nanoparticles. *Nature Communication.* (*shared first, accepted by reviewers, under editorial revision)

[3] **da Costa Marques, R.**, ___, ___, ___, ___, ___. Proteomics-guided intracellular trafficking analysis reveals time-dependent protein corona changes and the intracellular pathway. *Nanoscale Horizons*. (submitted)

[4] ___, ___, ___, **da Costa Marques, R.**, ___, ___, ___, ___, ___, ___. Higher Loading of Gold Nanoparticles in PAD Mesenchymal-like Stromal Cells Leads to a Decreased Exocytosis. *Cells*, **2022**, *11*(15), 2323.

[5] **da Costa Marques, R.***, ___, ___, ___, ___, ___. Proteomics reveals differential adsorption of angiogenic platelet lysate proteins on calcium phosphate bone substitute materials. *Regenerative Biomaterials*, **2022**, *9*, rbac044. (* shared first)

[6] ___, **da Costa Marques, R.**, ___, ___, ___. Polysaccharide-Based pH-Responsive Nanocapsules Prepared with Bio-Orthogonal Chemistry and Their Use as Responsive Delivery Systems. *Biomacromolecules*, **2020**, *21*(7), 2764–2771.

[7] ___, ___, **da Costa Marques, R.**, ___, ___. PEG Spacer Length Substantially Affects Antibody-Based Nanocarrier Targeting of Dendritic Cell Subsets. *Pharmaceutics*, **2022**, *14*, 1614.

[8] ___, ___, ___, **da Costa Marques, R.**, ___, ___, ___, ___, ___. Systematic modulation of the lipid composition enables the tuning of liposome cellular uptake. *Acta Biomaterialia*. (under revision)

Introduction

Protein adsorption on nano- and biomaterials is a mostly inevitable process that impacts the performance of these materials for their desired purpose, such as in nanomedical applications and biomaterial bone substitution [1-4].

Nanomedicine is a field of medicine that utilizes precisely engineered nanoscale materials - nanoparticles (NPs), to address medical challenges in the field of imaging, diagnosis, tissue engineering, and drug delivery [5-6]. The first clinically approved nanomedical systems, such as liposomal Doxil® (Janssen) for different cancer types, have showcased the potential of nanoscale drug delivery solutions [6-7]. Several types of NP were established, and more approved NPs for nanomedical applications followed by one of the most recent being the Corona Virus Disease 2019 (COVID-19) vaccine BNT162b1 (Pfizer/BioNTech). This example of a smart nanocarrier design transports messenger ribonucleic acid (mRNA) in order to achieve efficient vaccination [6, 8-9]. Here, nanomedicine has proven to create effective solutions for complex medical problems, such as the COVID-19 pandemic.

However, to fabricate a smart nanoparticular system to reach its desired application numerous challenges must be overcome. A significant challenge that NPs face when being introduced to biological systems is the spontaneous adsorption of biomolecules [1-2, 10]. Biomolecules, such as proteins, lipids, and metabolites are abundant in biological fluids, often as a complex mixture. The biomolecules adsorb on the surface of NPs in a short amount of time and form a coat which is referred to as the biomolecular corona [1, 11-12]. When studying the proteins that are part of this coat, the term protein corona is commonly applied. Upon formation, the protein corona changes the identity of the nanocarrier and therefore parameters such as targeting, toxicity, and blood circulation [2, 13-14].

Nanomedical research has dedicated numerous studies to investigate the underlying principles of the protein corona and the impact on nanomedical applications to further enhance smart NP design [2, 10]. However, the formation of the protein corona is influenced by different conditions that are not always systematically studied. Thus, conditions like nanocarrier surface functionalization, protein source concentration, and incubation temperature remain essential to study.

While protein corona research has specifically progressed in the extracellular environment [1, 14-16], only little is known about the protein corona in intracellular environments. Questions, such as how the protein corona is processed by cells and how the protein corona evolves during intracellular trafficking remain only sparsely investigated. Yet, the solution to these questions

about the interactions of the NPs with the subcellular environment will improve NP engineering with intracellular applications.

Besides nanoparticular materials, bulk biomaterials with nanostructured surfaces are also subjected to protein adsorption [3-4]. Generally, bulk biomaterials comprise a variety of materials outside of the nano-range that share a specialized application in medicine, such as in medical devices or implants [17-18]. Synthetic bone substitute materials, such as calcium phosphates (CaPs), are biomaterials that provide a biocompatible solution for patients with bone defects [19-20]. However, biomaterials as CaPs miss inherent growth factors to induce regenerative effects [19, 21]. Commonly, growth factors can be provided by adding hemoderivatives, which are protein sources derived from blood products, such as plasma or platelet lysates [22-23]. Hemoderivatives are combined with CaPs to induce regenerative capacities such as increased bone growth and blood vessel sprouting, termed angiogenesis [21-23]. Yet, the regenerative potential of this method is still limited [22-23], and the underlying protein adsorption remains only poorly investigated.

In order to address the challenges of protein adoption on nanocarriers and bone substitute biomaterials, various studies were carried out and are presented in this thesis. The thesis is divided into three chapters (Fig. 1).

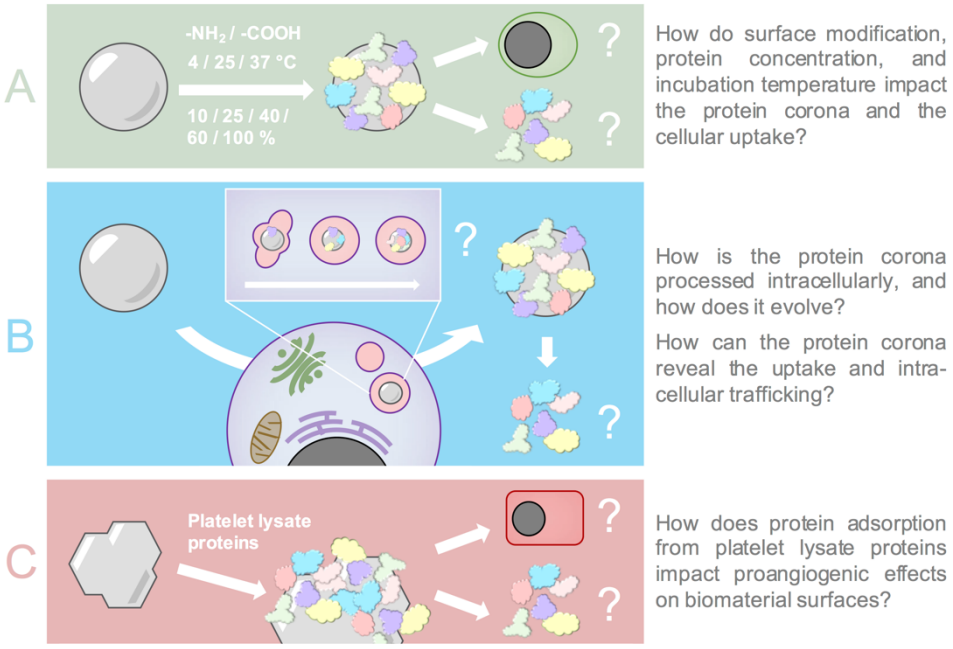

Figure 1: Schematic overview of the thesis chapters and the addressed scientific questions. **(A)** Chapter A presents the impact of different preparation conditions on the protein corona. **(B)** Chapter B demonstrates studies of the protein corona in the intracellular environment. **(C)** Chapter C analyzes the potential of protein adsorption for proangiogenic effects of biomaterial surfaces for bone substitution.

Chapter A introduces the field of nanomedicine, established nanomaterials, and the protein corona. Furthermore, this chapter includes a study that investigated the influence of surface modification, protein concentration, and temperature on the formation of the protein corona and the consequences for cellular uptake.

Chapter B focuses on the protein corona in intracellular environments. Briefly, a theoretical background is given to cellular uptake mechanisms of NPs, intracellular trafficking, and exocytosis. This chapter presents three studies. The first study in this chapter analyzed the intracellular processing and separation of a pre-formed protein corona on NPs. The second study investigated the intracellular trafficking on two different nanocarriers and elucidated the composition of the intracellularly-formed protein corona. This intracellular protein composition was then studied to reconstruct molecular details of the intracellular trafficking of the nanocarriers. The third study investigated the composition of the intracellular protein corona to detail processes of exocytosis for a cell-labeling NP system.

Chapter C addresses protein adsorption for bulk biomaterials, specifically CaPs for bone substitution. First, an introduction is given to biomaterials, bone regeneration, and protein adsorption on biomaterials. Next, a study is presented that analyzes the adsorption of platelet proteins on CaP surfaces with a focus on proangiogenic proteins. The proangiogenic effect is studied on endothelial cells.

Chapter A – Conditional impact on the formation of the protein corona

Chapter A consists of two subchapters. Subchapter 1 introduces the reader to the field of nanomedicine and nanomaterials for medical applications. Furthermore, the concept of the protein corona is explained, and methods to analyze the protein corona are discussed. Subchapter 2 is based on publication **[1]** that analyzed the formation of the protein corona under different conditions and its effect on cellular uptake. Publication **[1]** was previously published in a peer-reviewed journal and was shortened and edited to highlight my contributions to the work.

[1] ___, ___, **da Costa Marques, R.**, ___, ___. Temperature, concentration, and surface modification influence the cellular uptake and the protein corona of polystyrene nanoparticles. *Acta Biomaterialia*, **2022**, *148*, 271–278.

1. Theoretical background

1.1 Nanomedicine

Nanomedicine is a young science that was even termed a “key science of the 21st century” [24]. Several definitions of nanomedicine exist [25]. One way of defining nanomedicine is similar to defining medicine itself: “the science and art dealing with the maintenance of health and the prevention, alleviation, or cure of disease” [26]. However, what makes nanomedicine distinct from the general definition of medicine is the additional use of precisely engineered nanoscale materials – mostly nanoparticles (NPs) – that typically lie in the nanoscale range of 1-1000 nm [6]. The term nanomedicine was originally mentioned in 1991 by Drexler, Peterson, and Pergamit [24, 27], and was later fully established by Freitas in the book *Nanomedicine* in 1999 [24, 28]. Previously, the field of nanotechnology had emerged in the early 20th century as the science of nanosized matter or materials and led to the progressive creation of nanomedicine [24]. Thus, nanomedicine can also be seen as a specialized progression of nanotechnology and is likewise an interdisciplinary science that relies on medicine, biology, chemistry, physics, electronics, and information technology [24].

Since 1989, around 80 nanomedical formulations have been approved by the Food and Drug Administration (FDA) and the European Medicines Agency (EMA) [29]. A timeline of selected highlights of approved nanomedicines is depicted in Figure 1.1. Today, nanomedical research has improved several medical areas, such as therapy, diagnosis, imaging, and implants [5-6]. In therapy, NPs function as efficient drug delivery systems that can outperform conventional drugs without a delivery system [5]. Particularly the research of anti-cancer drugs has profited from the emergence of NPs [5, 29]. Here, nanoscale drug delivery systems bypass biological barriers, target the tumor cells passively or actively, and even protect fragile anti-cancer drugs as their cargos [5, 29]. One of the earliest approved nanomedical formulation, Doxil® (Janssen, approved 1995) delivers the cancer chemotherapeutic agent Doxorubicin in a liposomal formulation to treat ovarian cancer and Kaposi’s sarcoma [6-7]. This platform increased the delivery to the tumor site while decreasing systemic toxicity [6-7]. In diagnosis, NPs are utilized to detect molecules, cells, and tissues outside the human body. For instance, gold nanoparticles were modified with ligands to bind respective proteins. The protein binding then causes NP agglomeration, leading to a colorimetric readout [5, 30]. NPs are also utilized to function as contrast agents in imaging procedures, such as computed tomography (CT), magnetic resonance imaging (MRI), positron emission tomography (PET), and more [5]. In the field of implants, durable and biocompatible or bioabsorbable NPs can improve implant materials by providing a molecular-modifiable platform. Here, implant-incorporated NPs can,

for example, provide additional drug or growth factor release or serve as an antimicrobial coating [5, 31-32].

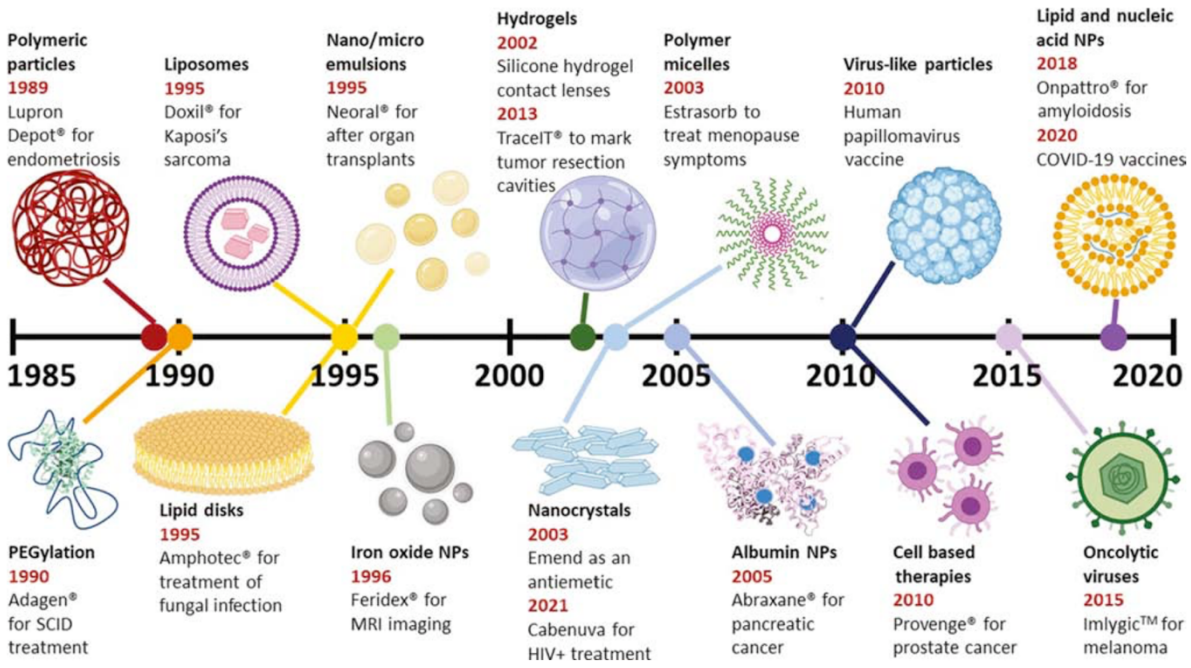

Figure 1.1: Timeline of selected FDA-approved nanomedicines. The timeline presents selected nanoparticles for therapeutic use. The date of the FDA approval, nanoparticle type, commercial name, and indication are described. Abbreviations: polyethylene glycol (PEG), severe combined immunodeficiency (SCID), magnetic resonance imaging (MRI), human immunodeficiency virus (HIV). The figure was adapted from "Historical Perspective of Clinical Nano and Microparticle Formulations for Delivery of Therapeutics" [33] and reprinted with permission from Trends in Molecular Medicine, Elsevier. Copyright @ 2021 Elsevier.

Overall, nanomedicine provides answers to existing challenges of conventional medicine, such as low drug stability, low drug solubility, adverse effects, poor pharmacokinetics, and poor pharmacodynamics [6]. However, for nanomedicines to effectively master the transition from "bench to bedside", several concerns at different stages need to be addressed. Major concerns are the safety of the carrier systems, the therapeutic efficacy, and the scale-up ability [34]. To address these concerns, researchers need to fully characterize the nanomaterials' physicochemical properties and precisely investigate the nanotechnology-biology (nano-bio) interactions [5]. Only if these conditions are given, nanomedical research will be able to create safe and biocompatible nanomaterials with an optimized bioavailability, efficient cellular targeting, and precise drug release.

1.2 Nanomaterials in nanomedicine

The key components of nanomedicine are the name-giving nanomaterials. In a traditional and narrow definition, these materials have at least one dimension of 1-100 nm size [25]. In broader definitions, particularly for nanomedical applications, materials with at least one dimension of 1-1000 nm can be defined as nanomaterials [6, 25]. While larger materials and surfaces with a nanostructure can be classified as nanomaterials, the following two chapters of this thesis will revolve around NPs, which attribute to nanomedicine to a significant extent.

Nanotechnological and nanomedical research have generated different NP systems that come with various ranges of physicochemical properties and fulfill different applications. These NPs can be grouped in different ways, such as by the components or the synthesis approach. One way of classifying and presenting different NP types is depicted in Figure 1.2.

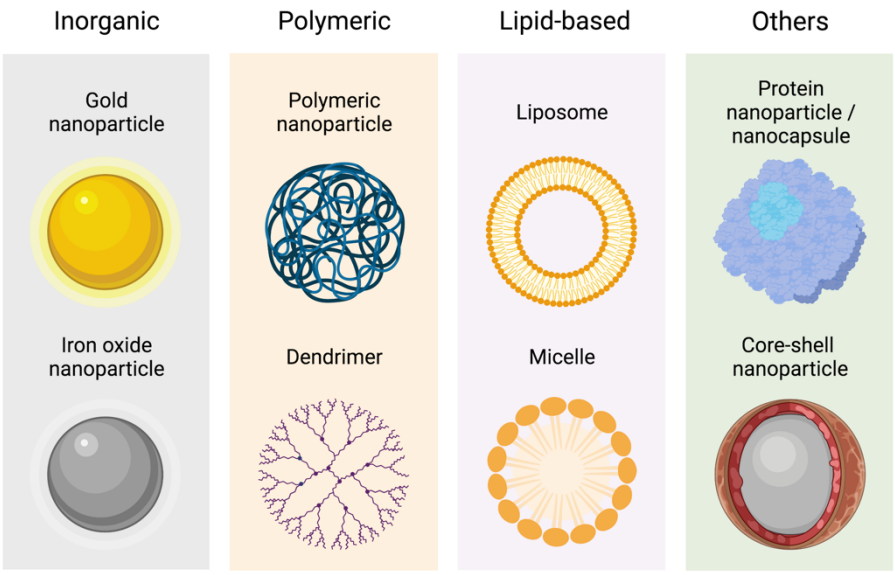

Figure 1.2: Common types of nanoparticles in nanomedicine. Different categories of NPs with selected NP types. The figure was created with BioRender.com.

Inorganic NPs, such as gold or iron oxide NPs offer unique electrical, magnetic, and optical properties [35-36]. Furthermore, gold particles are among the earliest established types of NPs and can be produced in various sizes and shapes [37-38]. The versatility of these NPs types has been generously exploited, particularly for drug delivery, imaging, and diagnostic applications [6, 35, 38]. However, inorganic NPs usually face low solubility and higher toxicity compared to their organic counterparts [36-39].

Polymeric NPs offer precise control over many physicochemical properties due to the variety of different monomers and polymerization techniques [40]. Additionally, a wide range of surface modifications exists to further customize the NPs for the application [41]. Polymeric NPs are ideal candidates for drug delivery due to different strategies to incorporate or encapsulate delivery cargoes with different physicochemical properties [42-43]. While polymeric NPs recently gained a more popular position in nanomedicine, they are still prone to aggregation and toxicity [35], which initially limited the success of clinical translation of these systems [6]. Nevertheless, promising candidates are currently undergoing clinical trials [6].

Lipid-based NPs usually consist of a unilamellar self-assembled layer (e. g. micelles) or bilayer (e. g. liposomes) of lipids. Particularly in the early stages of nanomedicine, lipid-based NPs were an advantageous system for drug delivery applications due to their self-assembly and excellent biocompatibility [6, 44]. Additionally, the physicochemical properties are tunable (based on the lipid composition and modifications), and hydrophilic or hydrophobic cargos can be encapsulated [35]. However, liposomes face a low encapsulation efficiency, low in-vivo stability, and are easily taken up by the reticuloendothelial system [35, 44-45]. Therefore, modifications are required to prevent unspecific uptake [46].

Despite the described classes, NPs can be synthesized with other biomolecules, such as proteins or carbohydrates [47-49]. These biocompatible materials offer interesting modification perspectives and a high payload encapsulation [50]. Furthermore, different materials can be combined, such as in core-shell approaches in which inorganic materials are covered with modifiable polymers or biomolecules [48]. These combinations allow for a variety of new options and application perspectives.

Due to the diverse nature of NPs and their various purposes in nanomedicine, it is essential to characterize and control their physicochemical properties. The most important physicochemical properties to investigate are size, dispersity, surface charge, morphology surface modifications, and hydrophobicity [5-6]. However, every NP system administered into a biological system will interact with the surrounding biomolecules. Unless NPs are not specifically designed to repel proteins, protein adsorption will most likely occur and will alter the previously defined properties of the NP.

1.3 The biomolecular corona – principles and biological effects

Nanomaterials for nanomedical applications interact with the biological system that they are addressing. These interactions are referred to as nano-bio interactions, and the understanding and control of these are crucial for the success of NPs in nanomedicine [1, 51]. Once exposed to a biological fluid, the present biomolecules adsorb to the surface of NPs [11, 51]. Well-studied adsorbing biomolecules include proteins [16, 52], lipids [53-54], and sugars [55], but less-studied adsorbed biomolecules, such as nucleic acids and metabolites, might play a role in future studies [1]. The adsorption process happens due to the high surface free energy of the NPs and upon biomolecule adsorption, the energetic value is lowered, which results in a stable NP-biomolecule complex [1, 10]. The NP with previously tailored and characterized physicochemical properties termed the “chemical identity” becomes surrounded by a coat of biomolecules that presents itself with new physicochemical properties [1, 12]. This state is termed the “biological identity” and impacts the fate of NPs drastically [1, 12].

Adsorption of proteins on nanostructures with a biochemical effect was described early in the 60s by Vroman [56]. However, it was several years later that the term “protein corona” was introduced by Dawson’s group in 2007 [11]. This term developed further to the “biomolecular corona” as research began to focus on the presence and effects of other adsorbed biomolecules. However, the term “protein corona” remains in use, especially when analyzing the adsorbed proteins on NP surfaces and their effect on biological systems. The formation of the protein corona happens spontaneously upon introduction to a biological fluid [12, 57]. Studies proved a stable protein corona formation within a few minutes to one hour [12, 57], but longer time spans until reaching a stable protein corona were also demonstrated [58]. The driving forces of the protein corona formation are predominantly intermolecular forces, such as Van-der-Waal forces, dipole-dipole forces, hydrogen bonds, or electrostatic forces [51]. Additionally, the displacement of the hydration layer contributes to an increased entropy [10], favoring the stable NP-protein complex. Initially, highly abundant or highly mobile proteins adsorb to NPs but get then gradually replaced by proteins with a lower abundance or lower mobility but a higher affinity towards the NPs surface. This effect is known as the Vroman effect [59]. A stable protein corona undergoes potential changes if challenged with a new protein source, but also retains pre-adsorbed proteins [1]. Several studies investigated this behavior with single proteins or with complex protein mixtures [60-61]. The protein corona does not consist of one simple layer of proteins. Instead, the morphology of the protein corona was described as a loose network of proteins around the associated NP [62]. This is due to the existence of a hard and a soft corona. The hard corona is defined as the closest layer of adsorbed proteins on the NP surface [63]. These proteins show a high affinity towards the NP’s surface and have low exchange rates [63].

The soft corona is described as the proteins in the vicinity of the NP, close to the protein hard corona [63]. The proteins of the soft corona have a lower affinity towards the NP's surface and higher exchange rates when compared to the hard corona [63]. The formation of the protein corona remains a process that is bound to multiple factors [51]. Indeed, the properties of NPs and the environment contribute to the final identity of the protein corona [51, 64]. The formation of the protein corona, the influencing properties of NP and protein/environment, and the consequences for the biological systems are depicted in Figure 1.3.

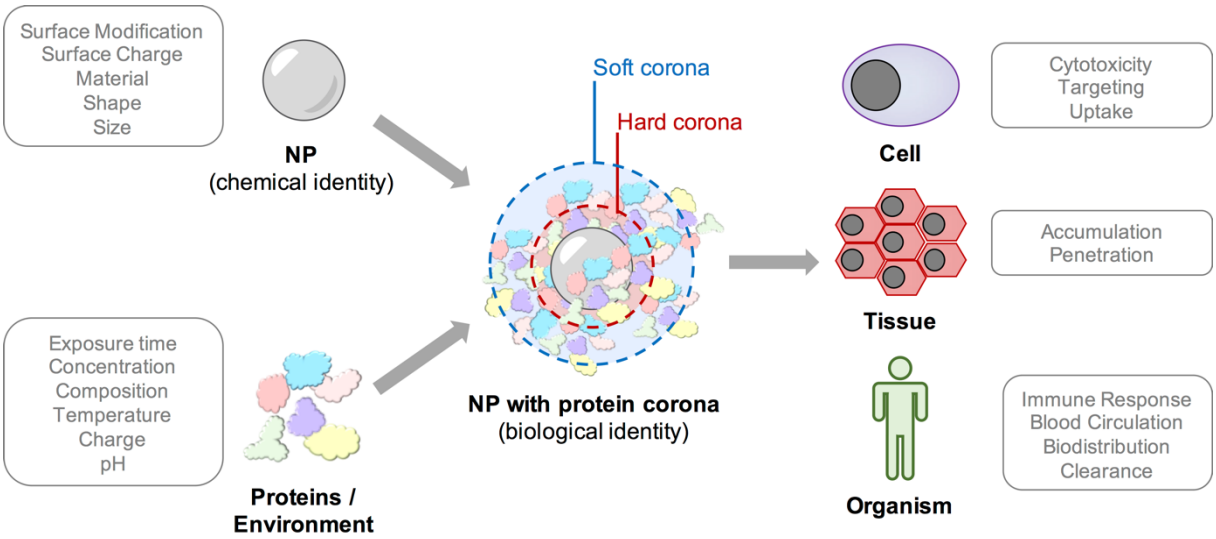

Figure 1.3: Formation of the protein corona on NPs and consequences for nanomedical applications. The scheme visualizes the process of the protein corona formation. Properties of NPs and the proteins/environment that influence the outcome of the protein corona are listed. Parameters for cells, tissues, and organisms that are impacted by the protein corona are described.

First, the physicochemical properties of the NPs (as described in 1.2) influence the type and quantity of adsorbed proteins. Surface modification [65], surface charge [66], material, shape [67], and size [52, 65] were all described to play a role in the protein corona formation [64]. The characterization of the physicochemical properties of the NP remains therefore, still of high importance even if the surface of the NP will be masked by proteins. Second, the properties of the environment contribute to the formation of the protein corona. Exposure time [58, 68], protein concentration [69], protein composition [15, 68], protein charge [52, 70], environment temperature [71-72], and pH value [73] influence the identity of the protein corona [64].

Upon the formation of the protein corona, the NPs' fate and the success of the nanomedical application can be tremendously altered. On the cellular level, the presence of the protein corona proved to induce or lower cytotoxic effect [13]. On the one hand, cytotoxic effects by the protein corona were mainly assigned to denatured proteins, which unfolded or re-folded

through the adsorption process [74-75]. On the other hand, the protein corona masks the potential reactive or highly charged surface of NPs, which decreases cytotoxicity [76-77]. The protein corona also affects the cellular uptake of NPs [13, 64]. Proteins adsorbed on the NP surface can either function as opsonins, leading to increased cellular uptake, or as dysopsonins, which reduce uptake [64]. Common opsonins include immunoglobulins, fibrinogen, or complement factors [64]. Common dysopsonins include apolipoproteins [64, 78]. This concept was further exploited by modifying NPs with so-called “stealth” moieties, such as poly(ethylene glycol) (PEG) or poly(phosphoester) (PEEP) [78]. Specifically, PEG was originally associated with reduced protein adsorption, which was commonly interpreted to lead to a reduced uptake in macrophages [78]. This effect was named the “stealth effect” [79]. However, a later study investigated the role of the specific proteins adsorbed on PEG and PEEP. These proteins, such as apolipoproteins, were found to mediate the actual decreased uptake [78]. Eventually, these proteins were pre-adsorbed on NPs as an artificial protein corona to purposely induce a stealth effect [80]. Logically, the protein corona also impacts the cell-specific targeting of NPs [81].

Generally, the described alterations on NP-cell interaction by the protein corona influence the performance of NP on tissue and organism-level. NP accumulation in and penetration through tissues can be mediated by the presence of the protein corona [82-83]. Furthermore, systematic NP clearance, blood circulation, biodistribution, and immune responses were described to be impacted by the protein corona [13, 64].

Ultimately, nanomedicine will improve by achieving a progressive understanding of nano-bio interactions. Precisely describing the protein corona of an established and characterized NP system will lead to higher success in biological systems. Additionally, exploiting the protein corona to achieve controlled effects opens new possibilities for modifications.

1.4 Characterization of the protein corona

To improve the understanding of nano-bio interactions and create refined NPs for nanomedical applications, the composition of the protein corona must be carefully studied [51]. Since the discovery of the protein corona on nanomaterials, research has aimed to investigate and improve methods to uncover the identity, gather structural information, and determine the physicochemical characteristics of the adsorbed proteins. As stated above, the protein corona presents itself with a soft corona and a hard corona [63]. In order to analyze these layers of the protein corona, soft or hard, different workflows must be performed to prepare the sample of interest [84]. Additionally, different analytical methods must be applied, based on the desired

characterizing parameter. Typical characterizing parameters include visualization, protein identification, quantification, thermodynamic information, conformation, and altered NP properties [85-86]. To access these parameters for the soft or the hard corona, the analytical methods can be further classified by indirect or direct methods [85, 87]. On the one hand, indirect analytical methods allow a mostly undisturbed analysis of the protein-NP complex with an intact soft corona [85, 87]. On the other hand, direct methods involve the separation and purification of the adsorbed proteins, which allows for more precise identification of the proteins but usually includes the depletion of the soft protein corona due to the “invasive” nature of the involved workflows [85, 87].

Generally, indirect characterization methods for the soft protein corona derive from conventional NP characterization methods. Here, the comparison before and after the protein corona formation on the NP reveals information about the protein corona [85]. These methods require little or no media exchanges, wash steps, or separation methods, ensuring the integrity of the adsorbed low-affinity proteins of the soft protein corona [85]. For example, the increase in size can be determined by dynamic light scattering (DLS) [58, 84] or fluorescence correlation spectroscopy (FCS) [88]. However, these methods can fail to reveal the exact size difference if aggregates form after protein corona formation [85]. The change of the protein corona surface can be measured by ζ-potential measurements [58, 84]. Furthermore, size and visualization can both be obtained by microscopic methods, such as transmission electron microscopy (TEM) [62, 89] and scanning electron microscopy (SEM) [90]. Circular dichroism (CD) spectroscopy can reveal protein structural changes in the secondary structure upon adsorbing on NPs [91]. Last, isothermal titration calorimetry (ITC) can be performed to obtain thermodynamic parameters, such as protein binding affinities and enthalpy change [84].

The direct methods rely on more complex preparations after protein corona formation to ensure the separation and isolation of the proteins (Fig. 1.4). This comes with possible alterations of the original protein corona [85]. While mild separation methods of soft corona separation were established, such as by asymmetric flow field–flow fractionation (AF4), most separation and washing procedures retain only the hard corona for downstream analysis [92]. Such conventional separation techniques are centrifugation, magnetism, and size exclusion chromatography (SEC) [92-93]. Upon separation of the NPs with a hard corona, the adsorbed proteins are desorbed by detergents [93]. Next, the protein amount can be quantified by protein assays, such as Bradford assay, bicinchoninic acid (BCA) assay, or pierce assay [84-85, 87]. Another method to quantify the protein mass is quartz crystal microbalance (QCM) [94]. The protein composition can be studied by sodium dodecyl sulfate-polyacrylamide gel electrophoresis (SDS-PAGE) [11, 84]. However, depending on the gel staining, protein quantification is not possible [95]. However, to combine the identification and quantification of complex adsorbed protein compositions, as

found in protein coronas on NPs from biological fluids, proteomic liquid chromatography-mass spectrometry (LC-MS) workflows can be employed [52, 96].

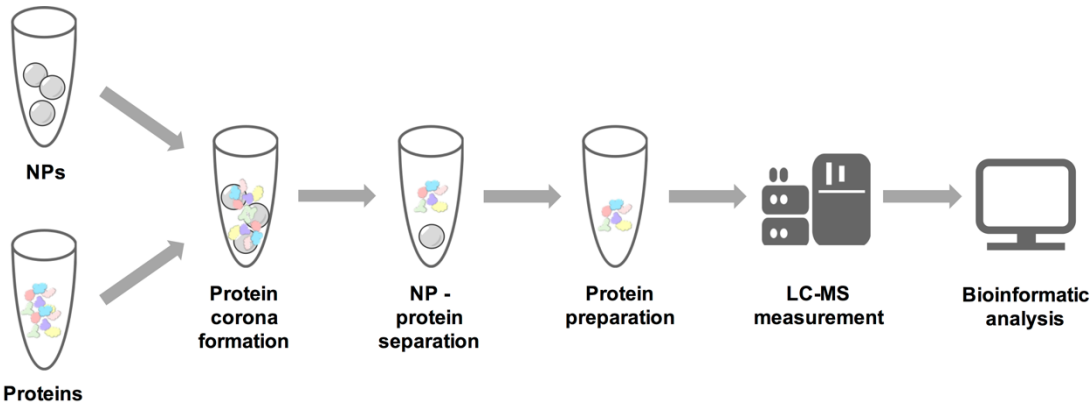

Figure 1.4: Typical workflow to analyze the hard corona by LC-MS proteomics. NPs and protein fluids are incubated together to form a protein corona on the NPs. Next, separation, such as by centrifugation or magnetism, is performed to isolate NPs with adsorbed protein corona from unbound protein. Wash steps can be implemented to ensure an efficient separation. The adsorbed proteins are then desorbed with detergents. The protein samples are then prepared, such as by in-solution digestion to obtain peptides which are measured by LC-MS. Through proteomic database comparison, the peptides are matched to proteins. This method allows for efficient identification and absolute quantification of proteins in the protein hard corona of NPs.

Early proteomic workflows isolated and desorbed protein corona samples and separated these by SDS-PAGE. The bands were excised and prepared for subsequent characterization by LC-MS [11, 96]. However, this approach excluded low abundant or low staining proteins from the analysis [97]. Today, bottom-up proteomic approaches, specifically shotgun proteomics, are favored for the analysis of the protein corona [93]. Compared to the analysis of complete proteins in top-down proteomics, bottom-up proteomics analyze peptides from proteolytically digested proteins [93]. Indeed, peptides are easier to ionize and fragment in comparison to complete proteins, facilitating the downstream MS analysis [93]. Consequently, analyzing a mixture of proteins by a bottom-up approach is termed shotgun proteomics [93]. The preparation of the proteins is usually performed according to a proteolytic digestion protocol, such as in-solution digestion or on-particle digestion [93].

After digestion, the complex peptide mixture is separated and ionized for MS analysis. While off-line gel-separation techniques (1D or 2D gels) are preferably utilized with matrix-assisted laser desorption ionization (MALDI), on-line LC separation is used with electrospray ionization (ESI) [98]. Subsequently, MS measurements are performed, which can vary in the method depending on the mass spectrometer and the scientific question. Various MS methods for

biomedical questions - protein corona analysis being one– were established in the past [99]. The method shown within this thesis is MS^E, a tandem-MS (also MS/MS) method with data-independent acquisition (DIA) [100]. Due to the sample complexity of protein corona samples, tandem-MS facilitates the discrimination of similar peptides due to additional ion fragmentation [98]. The DIA-nature of the MS^E method allows for a more unbiased product ion – precursor ion match without relying on the preselection of precursor data [99-101]. Instead, MS^E relies on alternating scans at low and high collision energy, providing accurate mass spectra data for precursor and product ions [99-100]. The MS^E method allows label-free absolute quantification of the analyzed peptides which makes it suitable for protein corona analysis [99]. Additionally, by implementing ion mobility separation (IMS), the proteomic coverage can be increased [99, 102]. IMS is a separation technique that separates ions in the gas phase and can be used complementary in LC-MS setups [102]. The resulting method, LC-IMS-MS, also called $HDMS^E$ in combination with MS^E, offers an additional degree of separation to increase protein identification coverage, making it suitable for high-complex protein corona samples [57 99]. Nevertheless, MS^E still delivers a more precise quantification, especially for highly abundant proteins [99 103]. LC-MS proteomic datasets require tailored deconvolution software to identify the peptides and subsequently proteins through proteomic database searches [99]. Once the proteins are assigned, absolute quantification can be performed. One method of absolute quantification is the TOP3 approach, established by Silva et al [104]. Here, the average MS signal of the three most intense tryptic peptides of a spike protein of known concentration is used to calculate a universal factor [104]. The absolute quantity of each respective protein is then calculated by dividing the average MS signal of the three most intense peptides of the protein by the universal factor of the spike protein [104]. The identified and quantified proteins of a protein corona can then be further classified through bioinformatic tools. Information, such as biochemical functions, cellular locations, or participation in a biological pathway can be assigned to individual proteins, leading to the powerful characterization of the protein corona [98].

Overall, the efficient and precise use of characterization methods for the protein corona will bring a refined understanding of the nano-bio interactions and thus improve the performance of nanomaterials in nanomedicine.

2. Temperature, concentration, and surface modification influence the cellular uptake and the protein corona of polystyrene nanoparticles

Aim:

The protein corona determines the performance of nanomaterials for medical applications. Previous studies have aimed to understand the principle of the protein corona formation and its direct effect on the application. However, the comparability of these studies is challenging due to different preparation conditions during the protein corona formation. This study presents a comparative overview of the protein corona formation by varying temperature, protein concentration, and surface modification. In this regard, the protein corona composition is revealed, and the effect on cellular uptake is demonstrated.

Copyright:

[1] ___, ___, **da Costa Marques, R.**, ___, ___. Temperature, concentration, and surface modification influence the cellular uptake and the protein corona of polystyrene nanoparticles. *Acta Biomaterialia*, **2022**, *148*, 271–278.

Contributions:

I performed the HUVEC cell culture, viability assays, protein corona preparation, and cellular uptake experiments. ___ and ___ conducted the protein corona preparation, nanoparticle characterization, protein quantification, SDS-PAGE, LC-MS sample preparation, LC-MS measurements, and LC-MS data evaluation. ___ and ___ wrote the manuscript. ___ created Figures 2.1, 2.2, S2.1, S2.2, and S2.3 in the following version. ___ created all other figures and tables in the following version. ___ edited the figures for the original manuscript. I edited all the figures in the following version. The project was supervised by ___. and ___.

2.1 Abstract

The composition of the protein corona varies depending on several parameters and influences the cellular fate of the nanocarriers. Here, we investigated the influence of three key parameters (surface charge, temperature, and plasma concentration) on the formation and composition of the protein corona of polystyrene nanoparticles and ultimately on the cellular uptake of pre-coated nanoparticles. At a fixed temperature and concentration, the surface charge, and surfactant influence its composition. We observed that the composition of the corona formed at low temperatures (4 °C) is different from that formed at physiological temperatures (37 °C). At low plasma concentrations (up to 25%), the corona consists of more diverse proteins than at higher concentrations. Finally, we concluded that regardless of the nanoparticle formulation, the degree of uptake by endothelial cells of the nanoparticles decreased when pre-coated at increasing temperature or plasma concentration.

2.2 Introduction

Research groups around the world have developed their own polymer, silica, or gold nanoparticles and more recently liposomal formulations, to improve drug delivery to cells [105-106]. Pre-coating nanoparticles with a defined protein corona has been investigated and successfully applied [107-108]. However, consistency regarding coating conditions (type of plasma, plasma concentration, temperature...) is not always achieved, making it difficult to cross-reference results [109-111]. The formulation of a nanoparticle has been at the core of studies carried out over the last decade regarding the protein corona composition [10]. Key parameters such as size, charge, surface hydrophobicity, or the addition of polyethylene glycol (PEG) to the surface have been changed to provide important insights into protein corona and cellular uptake [78, 96, 112].

In addition to formulation considerations, the pre-coating conditions are also critical during pre-clinical testing of new nanoparticles. The protein source (human vs mouse, serum vs plasma) is known to influence the cellular uptake [16]. The temperature used during the coating has been investigated for temperature-responsive nanomaterials [113-114], yet it is not clear if it is relevant for other, non-temperature-responsive materials. Temperature-responsive nanoparticles have been used for the catch and release of proteins [115]. Moreover, small changes in incubation temperature, close to the physiological temperature, have been shown to influence the adsorption of individual proteins [71]. Furthermore, heat inactivation of serum resulted in a different protein corona composition and therefore in a different cellular uptake [116-117]. However, an analysis of the temperature-dependent protein corona in human plasma is still missing.

Similarly, the concentration of plasma used for pre-coating has been varied; and changes in the protein corona have been studied in the past [64, 69, 90, 96, 109, 118], however such studies were limited to one type of nanoparticles and no cellular uptake test were performed. Dawson's group did several studies on this topic using silica and polystyrene nanoparticles concluding that the plasma concentration influences the protein content in the corona [96, 109]. However, they did not relate these results to the effect on cellular uptake. Gräfe et al. demonstrated that the protein concentration used for the pre-coating of positively charge magnetic nanoparticles altered their uptake into brain endothelial cells [69]. Yet, different groups still use different concentrations during their pre-clinical assays without always clearly explaining the reasons for their choices.

To address some concerns about pre-coating conditions, we test here five nanoparticles formulations stabilized with three different surfactants: CTMA-Cl, Lutensol, and SDS, and having surface charge ranging from +40 mV to -40 mV. Each nanoparticle from this panel is incubated either at 4 °C, 25 °C, or 37 °C in presence of undiluted human citrate plasma, or at

37 °C with 10%, 25%, 40%, 60%, or 100% plasma. Through these extensive and systematic tests, we are able to evaluate and conclude on the effect of temperature and concentration on the pre-coating step in regard to the protein corona composition and more importantly their impact on the cellular uptake. We demonstrate that increasing the human plasma concentration or increasing the coating temperature leads to a decrease of the uptake of nanoparticles into human umbilical vein endothelial cells (HUVEC). This can be attributed to an increase in the ratio of clusterin in the protein corona for most formulations.

2.3 Materials and methods

Synthesis of PS nanoparticles. Polystyrene nanoparticles (PS NPs) were synthesized by free-radical miniemulsion polymerization as mentioned in a previous work for the CMTA_NH2 and SDS_COOH [80]. **PS CTMA_NH2.** The macro emulsion was composed of an aqueous continuous phase containing 2-aminoethyl methacrylate hydrochloride (3 %wt. to styrene) and cetyl trimethyl ammonium chloride (25 %wt. in water) in sterile Milli-Pore water. The organic dispersed phase contained distilled styrene, BODIPY 523/535 as fluorescent dye, and 2,2-Azobis(2-methylpropionamidine) dihydrochloride in hexadecane. The continuous phase was added slowly to the dispersed phase under constant stirring. The macro emulsion was stirred for 1 h at high speed. The emulsion was then passed through a microfluidizer (Microfluidics USA, LM10). The miniemulsion obtained was directly transferred into a flask and let to polymerize under stirring condition for 18 h at 72 °C. The dispersion was purified by filtration followed by successive centrifugations at 13 200*g*. The supernatant was removed and the pellet was dispersed in sterile Milli-Pore water. The purification step was repeated twice. **PS Lut_NH2.** The same procedure as for PS CTMA_NH2 was followed, yet Lutensol AT50 replaced cetyl trimethyl ammonium chloride in the continuous phase. The dispersion was purified by successive centrifugations at 20 000*g*. Half of the supernatant was removed and replaced by sterile Milli-Pore water. The purification step was repeated four times. **PS SDS_COOH.** For these particles, acrylic acid was used as a co-monomer along with styrene in the disperse phase. In addition, sodium dodecyl sulphate was added to the continuous phase as surfactant. The emulsion and polymerization was carried as for the PS CTMA_NH2. The purification was done by dialysis for 3 days against Milli-Pore water using 14 000 kDa MWCO dialysis bags. **PS Lut_COOH.** The same procedure as for PS SDS_COOH was followed, yet Lutensol AT50 replaced sodium dodecyl sulfate in the continuous phase. The dispersion was purified by successive centrifugations at 20 000*g*. Half of the supernatant was removed and replaced by sterile Milli-Pore water. The purification step was repeated four times. **PS Lut.** The same procedure as for PS Lut_COOH was followed, except no acrylic acid was used as co-monomer.

Characterization of PS nanoparticles. The nanoparticles were characterized in terms of surface charge using a Zetasizer Nano Z instrument (Malvern, Germany), size using a Zetasizer S90 instrument (Malvern, Germany), and fluorescence intensity using an Infinity M1000 plate reader (Tecan, USA). The characterization of the nanoparticles with protein corona was performed after preparation, centrifugation, and washing of the nanoparticles as described for the cellular experiments.

Protein corona preparation. Human blood plasma was taken from healthy donors at the Department of Transfusion Medicine Mainz after physical examination and after obtaining written informed consent in accordance with the Declaration of Helsinki. Plasma of 10 donors was pooled and stored at -20 °C. The study was approved by the local ethics committee "Landesärztekammer Rheinland-Pfalz" (Bearbeitungsnummer: 837.439.12 (8540-F)). The protein corona experiments were performed as previously described by our group [62, 80]. To ensure comparability between the different types of PS nanoparticles, a constant ratio between the particle surface and plasma concentration was chosen. Therefore, 0.0625 m^2 of nanoparticles were incubated in 1 ml of human plasma for 1 h to allow the formation of a stable protein corona. In order to study the concentration-dependency of the protein corona, the incubation was performed at 37 °C in human plasma diluted with Dulbecco's Modified Eagle Medium to a final concentration of 10%, 25%, 40%, 60%, and 100%. The temperature-dependent protein corona formation was performed with undiluted plasma at the incubation temperatures of 4 °C, 25 °C, and 37 °C. Following the incubation, nanoparticles were isolated by centrifugation (20 000*g*, 1 h, 4 °C) and washed three times with 1 ml PBS. Proteins from the hard protein corona were desorbed from the NP surface by adding 100 µl of 2% SDS in 62.5 mM Tris-HCl solution followed by incubation at 95 °C for 5 min. Proteins and nanoparticles were separated by centrifugation and the supernatant containing the protein was labeled as "hard protein corona" and used for protein quantification, SDS-PAGE, and LC-MS analysis.

Protein quantification and SDS-PAGE. The protein quantification was performed using the Pierce 660 nm Protein Assay (Thermo Fisher, Germany) according to the manufacturer's manual. Adsorption was measured with a Tecan Infinite M1000 plate reader using bovine serum albumin (Merck, Germany) for a calibration curve. Following quantification, the proteins were separated on a NuPAGE™ 10% Bis-Tris Bolt™ polyacrylamide gel. A fix amount of hard corona proteins (2.5 µg for silver staining and 7.5 µg for Coomassie staining) was mixed with 26 µl water, 4 µl Nu NuPAGE ™ Reducing Agent, and 10 µl Nu NuPAGE ™ LDS Sample Buffer. SeeBlue™ Plus2 Pre Stained Standard (Invitrogen, Germany) was used as a marker. After protein denaturation for 10 min at 70 °C, the samples were loaded the gel and run in 1x NuPAGE™ MES SDS for 1.25 h at 100 V. The gel was either stained using Pierce SilverQuest™ Silver Staining Kit or SimplyBlue™ SafeStain according to the manufacturer's protocol. If not otherwise mentioned, materials were obtained from Thermo Fisher Scientific.

In solution digestion, sample preparation and liquid chromatography mass spectrometry (LC-MS). The in-solution digestion and liquid chromatography-mass spectrometry was performed according to former protocols from our group [119-120]. SDS was removed before digesting the proteins using Pierce Detergent Removal Spin Columns (Thermo Fisher Scientific, Germany). The proteins were precipitated using ProteoExtract protein precipitation kit (CalBioChem, USA). Afterwards, the proteins were isolated by centrifugation (14 000*g*; 10 min) and re-solubilized with 50 mM RapiGest SF (Waters, Germany) in ammonium bicarbonate buffer. The proteins were reduced in 5 mM dithiothreitol (Sigma-Aldrich, USA) for 45 min at 56 °C and alkylated with 15 mM iodacetamide (Sigma-Aldrich, USA) for 1 h at room temperature in the dark. The tryptic digestion was carried out at a protein:trypsin ratio of 50:1 at 37 °C. After 18 h, digestion was stopped by lowering the pH with hydrochloric acid (Sigma-Aldrich, USA) and the samples were centrifuged (14 000*g*; 15 min; 4 °C) in order to remove degradation products. For the measurement, 0.1% formic acid was added to the sample and to allow absolute protein quantification, samples were spiked with 50 fmol μl^{-1} Hi3 E.coli. (Waters, Germany). LC-MS measurements were performed using a nanoACQUITY UPLC system coupled to a Synapt G2-Si mass spectrometer based on a previous protocol [104]. Shortly, the system was operated in a positive resolution mode performing data-independent acquisition for the electrospray ionization source. The samples were injected with a flow rate of 0.3 µl min^{-1} and Glu-Fibrinopeptide (150 fmol μl^{-1}) and Leu-Enkephalin (200 pg μl^{-1}) were used as reference. The data was acquired using MassLynx 4.1. Proteins were analyzed using Progenesis GI 2.0 (thresholds for noise reduction were set at 120, 25, and 750 counts for low energy, high energy, and peptide intensity) and identified based on a reviewed database downloaded from Uniprot. For protein identification, at least two assigned peptides and five assigned fragments are required. The peptide identification needs three assigned fragments.

Cell culture. Human umbilical vein endothelial cells (HUVECs) were cultured with Medium 200, supplemented with 1X large vessel endothelial supplement (LVES). Both media were supplemented with 100 U ml^{-1} penicillin and 100 mg ml^{-1} streptomycin. The cells were grown at 37 °C and 5% CO_2 in a humidified incubator and 0.25% Trypsin-EDTA was used for cell passaging and harvesting (all reagents from Gibco, Germany). The cell count and viability were determined using a 1:1 dilution with trypan blue. To ensure cell stability, the passage number was kept below 8.

Flow cytometry. HUVEC cells were seeded at a density of 80 000 cells per well in 24 well plates (Greiner, Germany) and incubated over night at 37 °C and 5% CO_2. One hour before

the uptake experiment, M200 with LVES was removed, the cells washed with PBS, and M200 without LVES was added. The plasma-coated nanoparticles were prepared as described above with two centrifugation steps to remove the excess proteins before dispersing them in M200 without LVES. One ml nanoparticles solution (40 µg ml^{-1}) was incubated with the cells for 24 h at 37 °C in a cell incubator. Afterwards, cells were washed with PBS and collected using 0.25% Trypsin-EDTA. The cells were centrifuged (300*g*, 5 min) and the pellet was suspended in PBS for measurements. The BODIPY signal of the nanoparticles was recorded using the BL1 channel of the Attune™ Nxt (Thermo Fisher Scientific, Germany) Flow Cytometer with an excitation laser of 488 nm and a band-pass filter of 530/30 nm. Cell debris was excluded by selecting a cell population in an FSC/SSC scatter plot processing the data with Attune™ NxT Software. The uptake experiments were carried out twice as independent experiments and within an experiment, for each condition, the cells were seeded as a triplicate.

Cell viability. Briefly, cells were seeded at a density of 5 000 cells per well in white bottom 96 well plates and incubated over-night at 37 °C and 5% CO_2. On the next day, the cells were treated in the same way as for the flow cytometry experiments. Additionally, cells were treated with a solution of 20% DMSO as a positive control. After 24 h of incubation, a volume of CellTiter-Glo® Reagent (Promega, Germany) equal to the volume of cell culture media present was added to the cells as recommended by the manufacturer. The luminescent signal was recorded with a Tecan Infinite M100 plate reader. The viability was calculated based on the average luminescent signal intensity (n = 3) for the non-treated cells.

Statistical analysis. GraphPad Prism v9.02 was used for the statistical analysis of the cellular uptake extent. The p-values generated after an unpaired t-test (n = 3) were used to determine the significance of the difference between samples. Values $p > 0.12$ were considered non-significant, p-values < 0.033 were reported with $*$, p-values < 0.002 were reported with $**$, and p-values < 0.001 were reported with $***$.

2.4 Results and discussion

To establish the stability of the nanoparticles in the plasma solution, we measured the change in hydrodynamic diameter after coating at different temperatures or with different concentrations of plasma. To ensure that free proteins did not interfere with the measurements, the particles were centrifuged after the formation of the protein corona and washed with PBS. We observed that upon exposure to a concentration of 25% plasma or higher, the size of the nanoparticle increases from 130 nm on average to 160-170 nm indicating the formation of a protein corona around them (Tab. S2.1). For low plasma concentrations (10%) the size of CTMA_NH2, Lut, and SDS_COOH nanoparticles increased to 470, 221, and 226 nm, respectively. The larger size at 10% hP indicates the presence of aggregates, possibly due to the lower protein concentration surrounding the NPs at any given time. For highly charged NPs this means that the stabilization provided by the proteins is overcome by the destabilization brought on by the salts present in the buffer. Nevertheless, the size of the nanoparticles stabilized with 25% plasma. This could be a first hint that the protein corona around the nanoparticle changes with different plasma concentrations. In addition to the increased mean diameter of the NPs with protein corona, the presence of plasma, even at low concentration or low temperature, resulted in a negative ζ-potential around -18 mV, independently of the original ζ-potential of the pristine nanoparticles (Tab. S2.2). All these parameters confirmed that the coated nanoparticles are stable in solution (except for 10% hP) for future cellular uptake experiments. All NPs were synthesized with Bodipy 523 as fluorophore for cellular uptake tracking.

After we have ensured the quality of the coated NPs, we tested the uptake of the five polystyrene nanoparticles by HUVEC cells after 24 h incubation in media without proteins. First, we focused on the impact of citrate plasma dilution on the cellular uptake (Fig. 2.1A). The pre-coating of the NPs was always done at 37 °C for this series of experiments. We observed that the coating of the NPs induced a reduction of the uptake and was dependent on the plasma concentration of the coating solution (Fig. 2.1B-F). For the Lutensol-stabilized NPs, the uptake is similar across surface functionalization when the NPs are coated with 40% up to 100% plasma. Indeed, the broad range of uptake extent seen for the pristine NPs based on their surface modification subsides in the presence of increasing protein in the coating solution. Additionally, the trend observed for Lutensol-stabilized NPs is also observed for CTMA- and SDS- stabilized NPs. For all NPs tested, the increase of the protein concentration in the coating solution led to a significant decrease of the uptake in HUVECs.

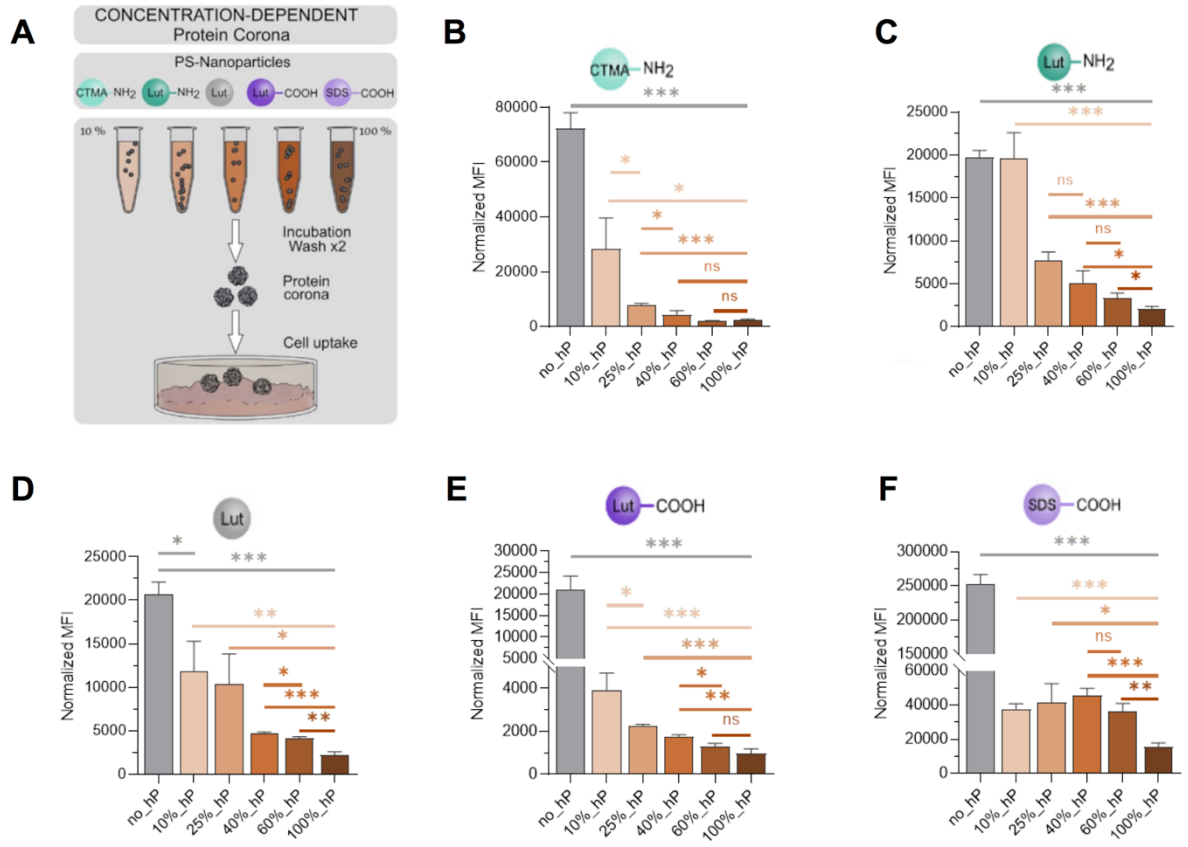

Figure 2.1: Uptake of pre-coated NPs with different plasma concentrations by HUVECs after 24 h incubation at 37 °C. (A) Schematic representation of the coating procedure leading to the cellular uptake displayed. **(B-F)** HUVECs were incubated for 24 h in media without protein with 40 µg ml^{-1} pre-coated polystyrene nanoparticles. The pre-coating of the NPs was done at 37 °C here. The „no_hP" corresponds to pristine NPs incubated with the cells. The difference of intrinsic fluorescence intensity of the NPs tested was accounted for by normalizing the median fluorescence intensity recording by the flow cytometer based on the fluorescence intensity of the "Lut" NPs. The statistical significance of the difference between samples was determined by unpaired t-test. P-values > 0.12 were non-significant (n.s.), p-values < 0.033 correspond to *, p-values < 0.002 correspond to **, and p-values < 0.001 correspond to *** (data are shown as mean ± SD, n = 3).

We also verified the absence of toxicity induced by the NPs and confirmed good cell viability after incubation for all conditions, even though the pristine NPs tend to be more toxic to the cells (Fig. S2.1).

Next, we investigated the protein corona composition to explain the uptake pattern observed. The change in uptake between pristine NPs (no_hP) and coated NPs was expected [62, 78, 119]; however the change for plasma concentration of 25% and above was interesting. Since the size and apparent surface charge did not change much within this plasma concentration range (25-100%), we looked into the protein corona composition. First, we checked if the amount of protein adsorbed on the NPs varied with the coating concentration. We found no correlation

between the original protein concentration and the amount adsorbed on each NPs. The amount varied based on the surfactant and surface functionalization as expected (Fig. S2.2A). We also checked the protein corona composition by SDS-PAGE analysis. We observed a clear difference in the composition of the protein corona for the carboxy-functionalized NPs compared to the amino- or un-functionalized ones. The differences between the concentrations were not as obvious. For example, for the CTMA_NH2 NPs we could see a decrease in the band intensity for the serum albumin at 62 kDa. However, since the staining method used here is a non-quantitative method, it is not possible to draw a direct conclusion from the band intensities to the protein concentration in the protein corona. Overall, no new band appeared at different concentrations for any NPs (Fig. S2.2B) which suggests that no new proteins are appearing but rather that the relative concentration of each proteins in the protein corona may be changing.

Therefore, we moved on to proteomic analysis of the whole protein corona recovered from the NPs. For the Lutensol-stabilized NPs, we observed that the fraction of clusterin in the corona increases with increased plasma concentration (Fig. 2.2B-D). However, it does not account for the same fraction of the corona for each NPs. Here, the surface modification has a higher impact compared to the cellular uptake. Apolipoproteins constitute a large part of the proteins identified, with clusterin and ApoE found in the top10 identified proteins across all five NPs. The Lut_COOH NP has the most complex corona out of the three Lutensol-stabilized NPs in terms of the category to which the most abundant proteins belong. Indeed, for the other two, about 60 to 80% of the corona was made of apolipoproteins leaving little space for other types of proteins. In contrast, the corona evolved quite interestingly for the Lut_COOH NPs with a change from coagulation proteins (fibrinogen) at low plasma concentrations to a tripartite composition involving coagulation proteins, apolipoproteins, and vitronectin at higher concentrations (Fig. 2.2D). A similar trend is observed with SDS_COOH NPs for which when the proportion of coagulation proteins decreases, the proportion of vitronectin increases with the plasma concentration (Fig. 2.2E). For these NPs as well as the CTMA_NH2, apolipoproteins account for a very small portion of the corona (Fig. 2.2A/E). Taking into account that for the SDS_COOH nanoparticles the cellular uptake decreases with increasing plasma concentration, we would expect to see an increasing concentration of apolipoproteins and especially of clusterin which is known to reduce the cellular uptake of nanoparticles [78, 118]. However, for this type of nanoparticle apolipoproteins and clusterin play only a minor role in the protein corona.

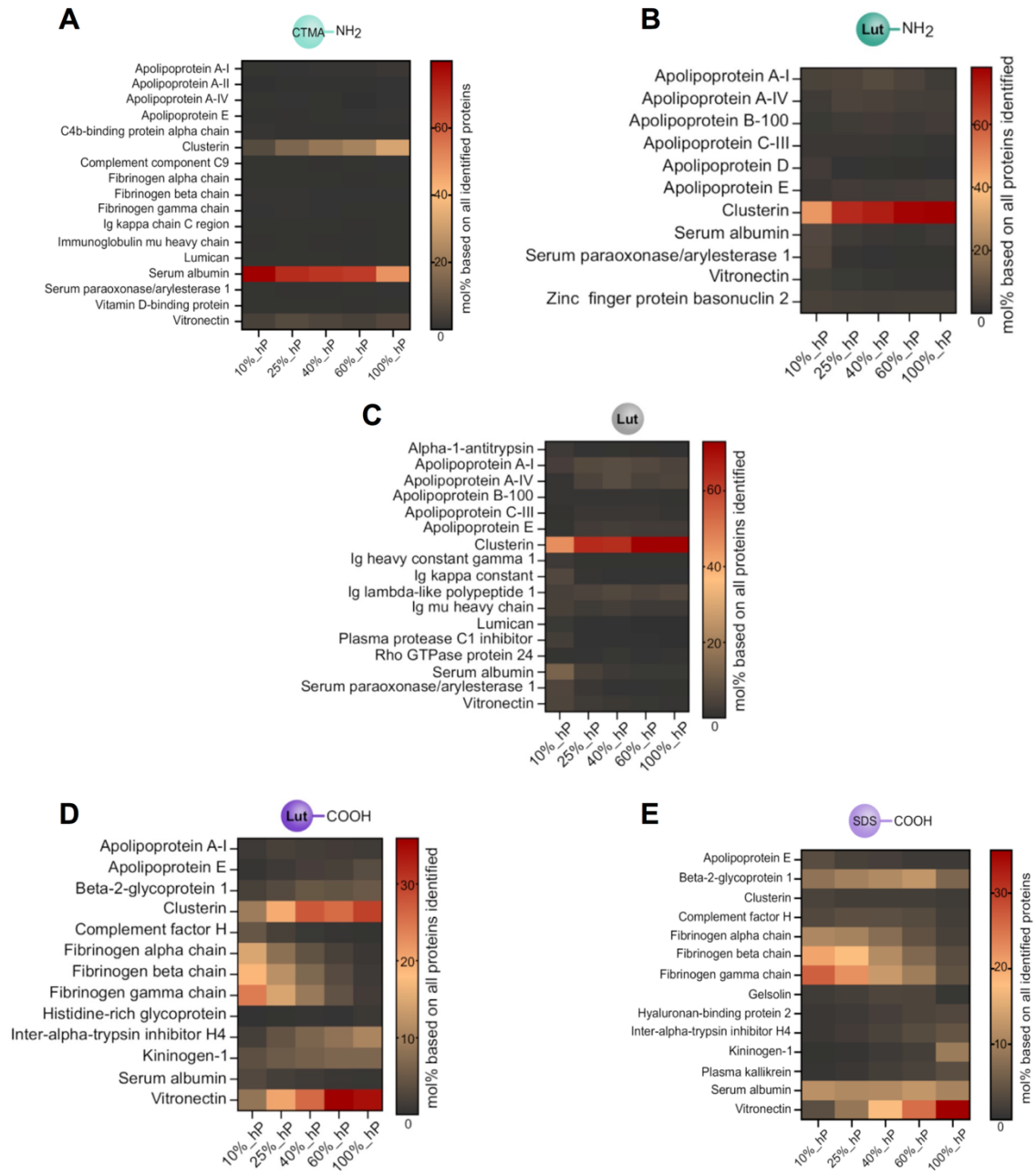

Figure 2.2: Combined top10 proteins identified in the corona of the NPs after incubation in different plasma concentrations. The top10 proteins for each condition for CTMA_NH2 NPs **(A)**, Lut_NH2 NPs **(B)**, Lut NPs **(C)**, Lut_COOH NPs **(D)**, and SDS_COOH NPs **(E)**, respectively, were combined to the final heatmap shown here. Values are represented as the mole percentage based on all identified proteins.

We can conclude that for all the NPs tested, the composition of the protein corona evolves with the amount of plasma in the coating solution (Fig. S2.3). It is worth noting that the use of Lutensol, a non-ionic PEGylated surfactant, led to a protein corona enriched with apolipoproteins for all the NPs. The corona composition seems to be dictated as much by the surfactant as by the surface functionalization. Indeed, the carboxy-functionalized NPs showed

enrichment with coagulation proteins compared to the amino ones. Based on these observations, we propose that the presence of carboxy-groups on the NPs are more important than the surfactant, while the surfactant is more important than the presence of amino-groups on the NPs.

Besides the influence of different plasma concentrations on the protein corona, we also focused on different incubation temperatures. Here we kept the concentration of plasma for the pre-coating stable at 100% (Fig. 2.3A). The coating of the nanoparticles with human plasma induces a reduction of the uptake in HUVECs. For Lutensol-stabilized NPs, it can be seen that the uptake is reduced with increasing temperature (Fig. 2.3C-E). Additionally, this trend is observed for CTMA-stabilized NPs (Fig. 2.3B). For these NPs the decrease of the uptake from 4 °C to 37 °C is mainly significant while the difference between 4 °C to 25 °C and 25 °C to 37 °C is only minor. For the SDS-stabilized carboxylic NPs a different trend can be observed. As for the other particles, a reduced uptake from pristine to coated particles can be seen. However, with increasing temperature an increase in cellular uptake was observed (Fig. 2.3F). We tested the toxicity induced by the NPs as well for these conditions. For most conditions, we additionally confirmed here the absence of toxicity to both cell types (Fig. S2.4). For the pristine CTMA-stabilized amine particle we saw a toxic effect. The toxic effect is no longer present when a protein coating was applied.

To investigate the reason for the uptake change, we analyzed the protein corona composition. Since the size and surface charge do not change significantly between the different temperatures, we focused on the protein analysis of the protein corona on the particles. Protein quantification with Pierce assay resulted in no obvious correlation between temperature and amount of protein adsorbed except for the CTMA-stabilized amine NPs (Fig. S2.5A). For the CTMA_NH2 NPs the highest protein amount desorbed can be observed at 4 °C and it decreases at 37 °C. However, SDS-PAGE analysis showed a temperature-dependent difference in protein composition on the particles (Fig. S2.5B). Especially for the SDS-stabilized carboxylic and the CTMA-stabilized amine particles, an increase of the band intensity at 38 kDa was observed. But also for the Lutensol-stabilized NPs a slight increase of the band intensity between 38 kDa and 49 kDa was observed. However, a clear appearance or disappearance of the bands cannot be observed. Comparing the different particles, as expected, a difference in protein corona composition can be seen between the different surface functionalization’s but also between different surfactants.

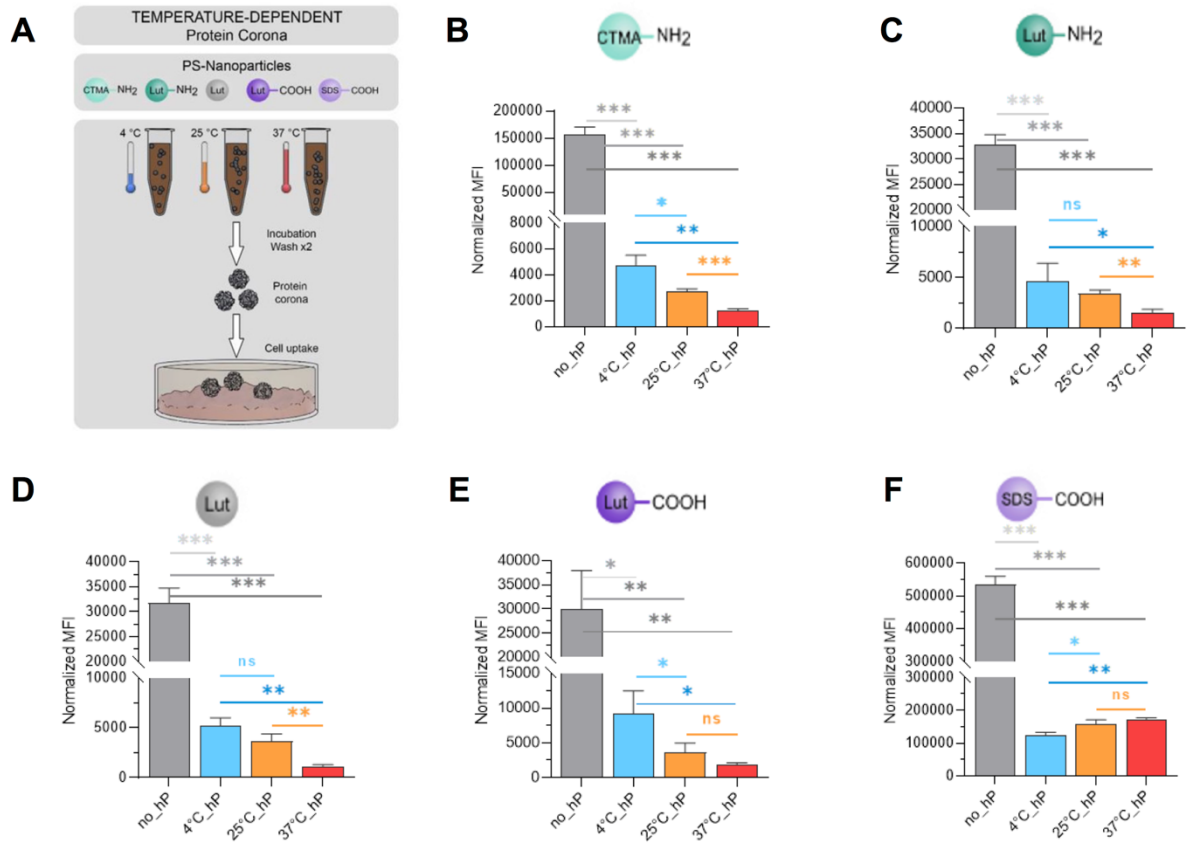

Figure 2.3: Uptake of pre-coated NPs at different temperatures by HUVECs after 24 h incubation at 37 °C. (A) Schematic representation of the coating procedure leading to the cellular uptake displayed. **(B-F)** HUVECs were incubated for 24 h in media without protein with 40 µg ml^{-1} pre-coated polystyrene nanoparticles. Pre-coating was done in 100% plasma. The „no_hP" corresponds to pristine NPs incubated with the cells. The difference of intrinsic fluorescence intensity of the NPs tested was accounted for by normalizing the median fluorescence intensity recording by the flow cytometer based on the fluorescence intensity of the "Lut" NPs. The statistical significance of the difference between samples was determined by unpaired t-test. P-values > 0.12 were non-significant (n.s.), p-values < 0.033 correspond to *, p-values < 0.002 correspond to **, and p-values < 0.001 correspond to *** (data are shown as mean ± SD, n = 3).

Afterwards, we had a deeper look at the composition of the protein corona via LC-MS analysis. As already shown previously, the surface modification had a huge influence on the composition of the protein corona (Fig. 2.4). However, it can be seen that for the Lutensol-stabilized nanoparticles the amount of clusterin in the protein corona increased with increasing temperature while the amount of ApoA1, ApoE, and fibrinogen decreased with increasing temperature. Interestingly, for the Lutensol-stabilized carboxylic nanoparticles we saw an additional increase in the amount of vitronectin in the protein corona. While the coagulation proteins were the dominant protein group in the protein corona at 4 °C, the lipoproteins and the vitronectin were the dominant proteins in the protein corona at 37 °C (Fig. S2.6). This trend

can also be observed for the SDS-stabilized carboxylic nanoparticle. The CTMA-stabilized amine nanoparticles showed additionally a temperature-dependent increase of serum albumin in the protein corona with increasing temperature (Fig. S2.4A/E). From that, we can conclude that the protein corona composition is temperature dependent.

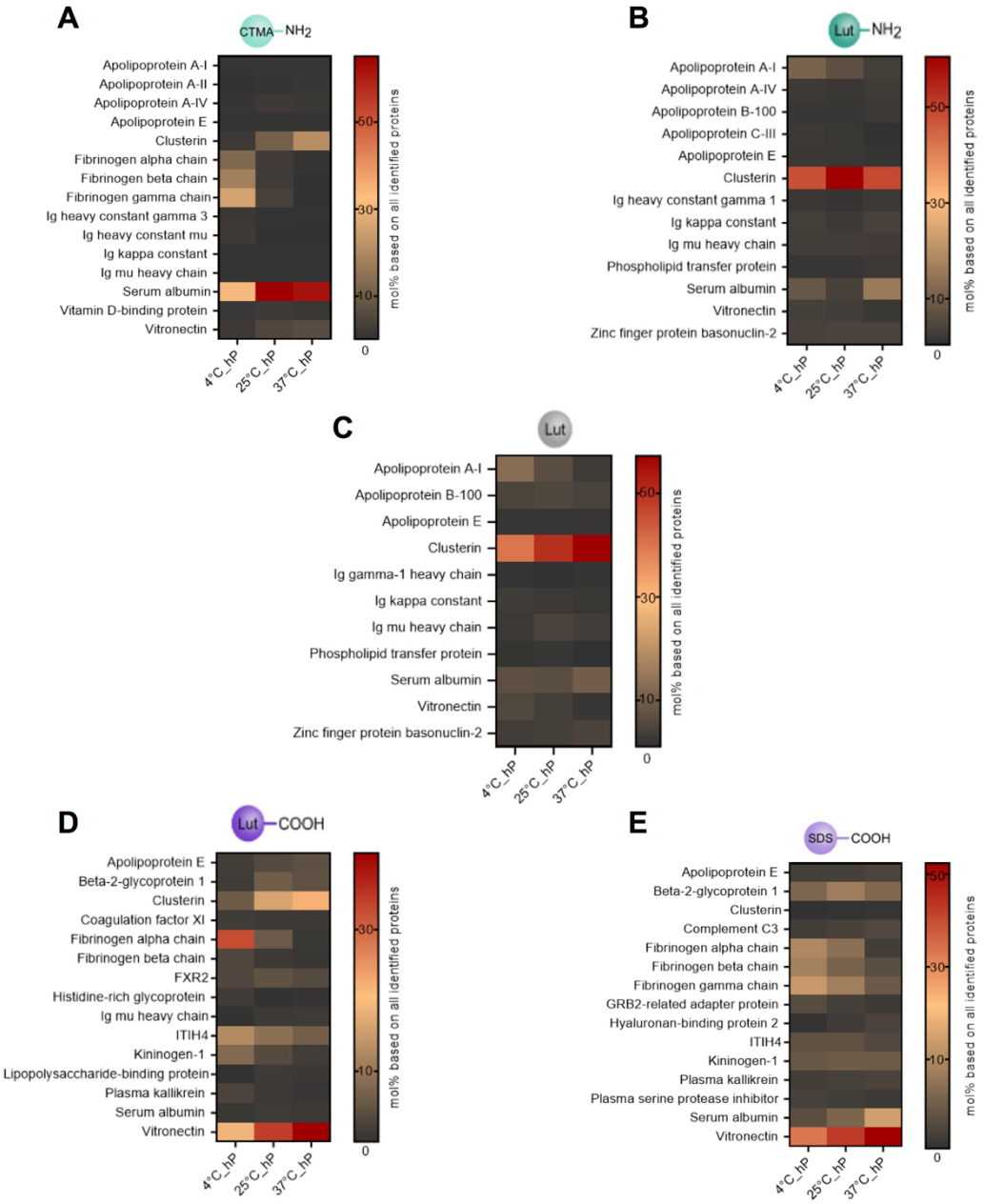

Figure 2.4: Combined top10 proteins identified in the corona of the NPs after incubation in plasma at three different temperatures. The top10 proteins for each condition for CTMA_NH2 NPs **(A)**, Lut_NH2 NPs **(B)**, Lut NPs **(C)**, Lut_COOH NPs **(D)**, and SDS_COOH NPs **(E)**, respectively, were combined to the final heatmap shown here. Values are represented as the mole percentage based on all identified proteins.

We demonstrated that the cellular uptake of pre-coated polystyrene NPs by endothelial cells steadily decreases with increasing plasma concentration in the coating solution. This stealth effect appears to be more pronounced at low protein concentrations, with the extent of uptake flattening above 40% of plasma. Given our results here, it would be a good practice to not go below 40% plasma in a medium when pre-coating or actively incubating NPs with cells. This highlights the need to choose a sufficiently high plasma concentration when performing in vitro studies aiming to mimic in vivo conditions. In the human body, blood is composed of about 55% plasma with cells accounting for the other 45% [121]. We would like to point out that this 45% of non-plasma volume is not readily accessible for NPs and therefore we would argue that the NPs "see" only the pure plasma (100%). Although we still observe a statistically significant difference in uptake at a high plasma concentration, the difference between 40% and 100% does not appear to be clinically relevant, meaning that the uptake is more uniform at this point and using any plasma concentration above 40% should not drastically alter the outcome of the cellular uptake. If diluent is used this introduces an additional variability and hence, using 100% of plasma could solve the issue of the diluent without bias to the resulting cellular uptake.

Still, the decrease of the uptake could not be explained by the change in size of surface charge and is therefore due to the evolution of the protein corona. The increase of plasma concentration leads to an increase of clusterin in the corona for most NPs, except for SDS_COOH. The proportion of clusterin in the corona varies from NP to NP, but the trend endures. Clusterin is a well-known dysopsonin protein and was shown to improve the stealth of nanoparticles in macrophages [78, 118]. Yet, clusterin alone cannot explain the trend observed for the SDS_COOH NPs. Indeed, the percentage of clusterin in the corona of this NP is very low (about 2%) and the same at all concentrations. However, the percentage of fibrinogen and vitronectin fluctuates greatly based on the concentration and could be somehow involved in the change of cellular uptake. We could also point out to the difference in coverage of the nanoparticles with proteins at the different coating concentrations to explain the change in cellular uptake. The question of the protein density would in turn raise the question of the orientation of the absorbed proteins, which could change depending on the densely or sparsely populated protein regions. However, the analysis of single proteins on the surface of nanoparticles is challenging, even more so for a complex protein mixture and is beyond the scope of the present study. Other groups performed studies to evaluate the impact of low or high plasma concentrations on the protein corona as well [69, 109, 111]. Salvati's group showed a higher uptake of silica nanoparticles with a lower plasma concentration and the group of Dawson demonstrated changes in the protein corona composition with different plasma concentrations [109, 111]. However, in most cases these studies were only performed on one type of nanoparticles and the impact on the cellular uptake was not always shown.

Besides the concentration-dependent uptake of PS nanoparticles in the cells, we also showed that the uptake of NPs in HUVECs decreases with increasing temperature during protein corona formation. For a protein corona formed at 4 °C, the uptake of the Lutensol-stabilized nanoparticles was significantly higher than for a protein corona formed at 37 °C. This also applies to the CTMA-stabilized amine nanoparticles. However, for the SDS-stabilized carboxylic nanoparticles a slightly increased uptake has been observed at the highest temperature of 37 °C. In most studies, protein corona formation and cellular uptake of nanoparticles are performed at 37 °C in order to be as close as possible to the in vivo conditions. Nevertheless, especially when working at low temperatures [71-72] or when working with temperature sensitive materials, this must be taken into account [113, 115].

Furthermore, we showed that the protein corona changes with the incubation temperature and that this is very likely the reason for the temperature-dependent uptake behavior. At 4 °C, we observed a low amount of lipoproteins but an increased amount of coagulation proteins in the protein corona. This changed when we increased the temperature to 37 °C. At this temperature, the lipoproteins, serum albumin, and vitronectin became more prominent in the protein corona. However, it can also be seen that the protein corona of the Lutensol- and SDS-stabilized carboxylic as well as the CTMA-stabilized amine nanoparticles show a stronger dependence on temperature than the Lutensol-stabilized unfunctionalized and amine nanoparticles. Since the amount of total proteins bound in the protein corona does not differ much between the different incubation temperatures, we assume that the difference in the protein corona is not due to a reduced interaction of the proteins with the nanoparticles. It is more likely that the affinity of specific proteins for the nanoparticles is temperature dependent. It is known that proteins can consist of multiple binding sites which can interact with surfaces and that conformational stability of proteins depends on temperature, among other factors [122]. However, the protein corona consists of different proteins, and for most of them the protein structure is not yet known. A prediction of binding affinities in dependence on temperature, therefore, remains challenging. Yet, this field is relatively unexplored and requires further research. Moreover, we analyzed here the proteins bound in the hard protein corona. When considering protein affinities, we could also suggest that with a change in the hard protein corona the protein affinities in the soft corona could change. However, the analysis of the soft protein corona remains complicated. Previously it has been shown that for a short incubation time the uptake of pre-coated liposomes did not differ between hard and soft protein corona [123]. We therefore do not expect an impact of the soft protein corona and its difference with temperature or concentration on the uptake of the nanoparticles.

2.5 Conclusion

We demonstrated that the protein corona composition varies with plasma concentration and temperature. Five NPs with different surface functionalization and surfactants were similarly impacted proving the universality of the effect. Additionally, the change in the protein corona composition directly affected the extent of cellular uptake of the precoated NPs. In endothelial cells, a decrease of the uptake was observed with the increase of the plasma concentration of the coating solution. Hence, we recommend always performing experiments using a plasma content of at least 40% to ensure the full stealth effect induced by a mature protein corona. This recommendation is aimed at pre-clinical studies to provide consistent results when proceeding with animal-based studies. We have also shown a decrease in the cellular uptake of the nanoparticles with an increase in temperature during protein coating. This should be considered when using different incubation temperatures for precoating and in in vitro experiments.

2.6 Supplementary information

Table S2.1: Mean hydrodynamic diameter (nm) of the pre-coated NPs treated as for cellular uptake experiment. The "no hP" condition corresponds to the pristine NCs dispersed in DPBS before coating with plasma. The nanoparticles with protein corona were centrifuged and washed with DPBS after formation of the protein corona in plasma (data are shown as mean ± SD, value in parenthesis corresponds to SD, n = 3).

	no hP (37°C)	10% (37°C)	25% (37°C)	40% (37°C)	60% (37°C)	100% (37°C)	100% (25°C)	100% (4°C)
CTMA-NH_2	124 (1.5)	470 (35)	178 (2.7)	166 (1.5)	167 (1.6)	164 (3.9)	169 (0.5)	144 (16.8)
Lut-NH_2	125 (3.5)	197 (2.5)	161 (1.4)	159 (1.1)	154 (3.1)	151 (3.8)	150 (2.4)	162 (18.8)
Lut	136 (0.8)	221 (9.6)	199 (5.4)	192 (9.2)	188 (1.4)	165 (9.1)	162 (3.0)	185 (2.7)
Lut-COOH	131 (3.8)	170 (3.7)	168 (0.6)	162 (3.5)	166 (3.4)	164 (2.4)	156 (1.6)	143 (14.1)
SDS-COOH	102 (1.3)	226 (4.2)	165 (0.4)	157 (2.2)	158 (2.2)	160 (4.8)	151 (1.6)	141 (14.2)

Table S2.2: Mean ζ-potential (mV) of the pre-coated NPs treated as for cellular uptake experiment. The "no hP" condition corresponds to the pristine NCs dispersed in DPBS before coating with plasma. The nanoparticles with protein corona were centrifuged and washed with DPBS after formation of the protein corona in plasma (data are shown as mean ± SD, value in parenthesis corresponds to SD, n = 3).

	no hP (37°C)	10% (37°C)	25% (37°C)	40% (37°C)	60% (37°C)	100% (37°C)	100% (25°C)	100% (4°C)
CTMA-NH_2	33.3 (0.5)	-19.8 (1.2)	-21.3 (1.1)	-21.9 (1.0)	-21.1 (0.7)	-21.0 (0.3)	-13.8 (0.6)	-12.0 (0.8)
Lut-NH_2	-1.1 (0.9)	-14.1 (1.3)	-16.5 (0.6)	-14.9 (0.9)	-13.5 (1.5)	-13.2 (1.7)	-12.8 (1.1)	-13.2 (0.9)
Lut	-1.3 (0.4)	-18.6 (1.2)	-23.0 (1.3)	-22.6 (1.5)	-21.5 (0.9)	-20.8 (0.8)	-20.0 (1.3)	-8.7 (0.6)
Lut-COOH	-8.3 (0.5)	-11.3 (1.3)	-12.2 (0.5)	-11.3 (0.7)	-15.0 (1.5)	-16.2 (1.0)	-12.6 (1.3)	-20.5 (0.4)
SDS-COOH	-42.4 (1.5)	-21.3 (1.0)	-21.4 (0.6)	-14.6 (0.6)	-20.8 (1.2)	-19.4 (1.4)	-15.8 (0.6)	-13.2 (0.9)

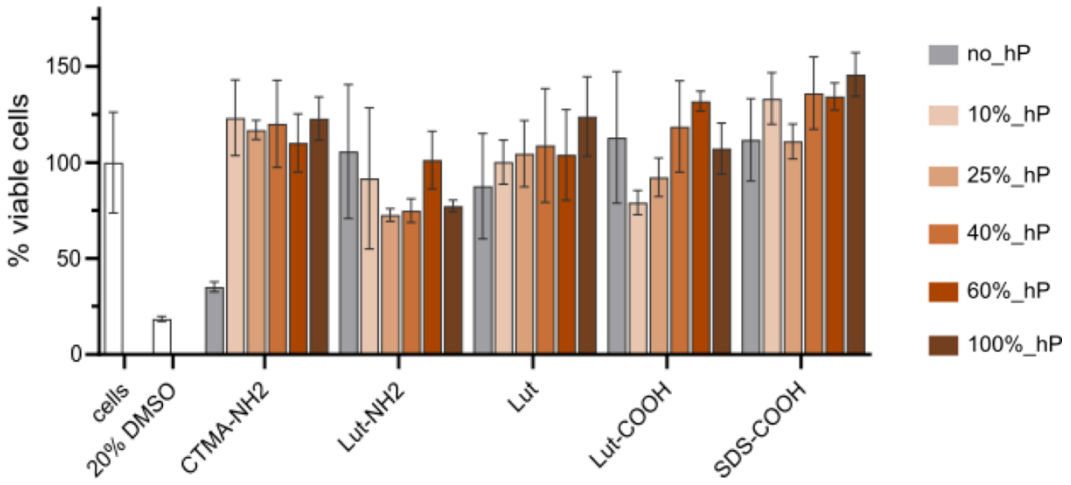

Figure S2.1: Cellular viability after incubation for 24 h in presence of 40 µg ml^{-1} NPs after coating with five different plasma concentrations. The sample labeled "cells" corresponds to the untreated cells incubated in DMEM media without NPs, the sample labelled "20% DMSO" corresponds to cells treated for 24 h with a DMEM media containing 20% DMSO. These samples are used as controls to validate the assay (data are shown as mean ± SD, n = 3).

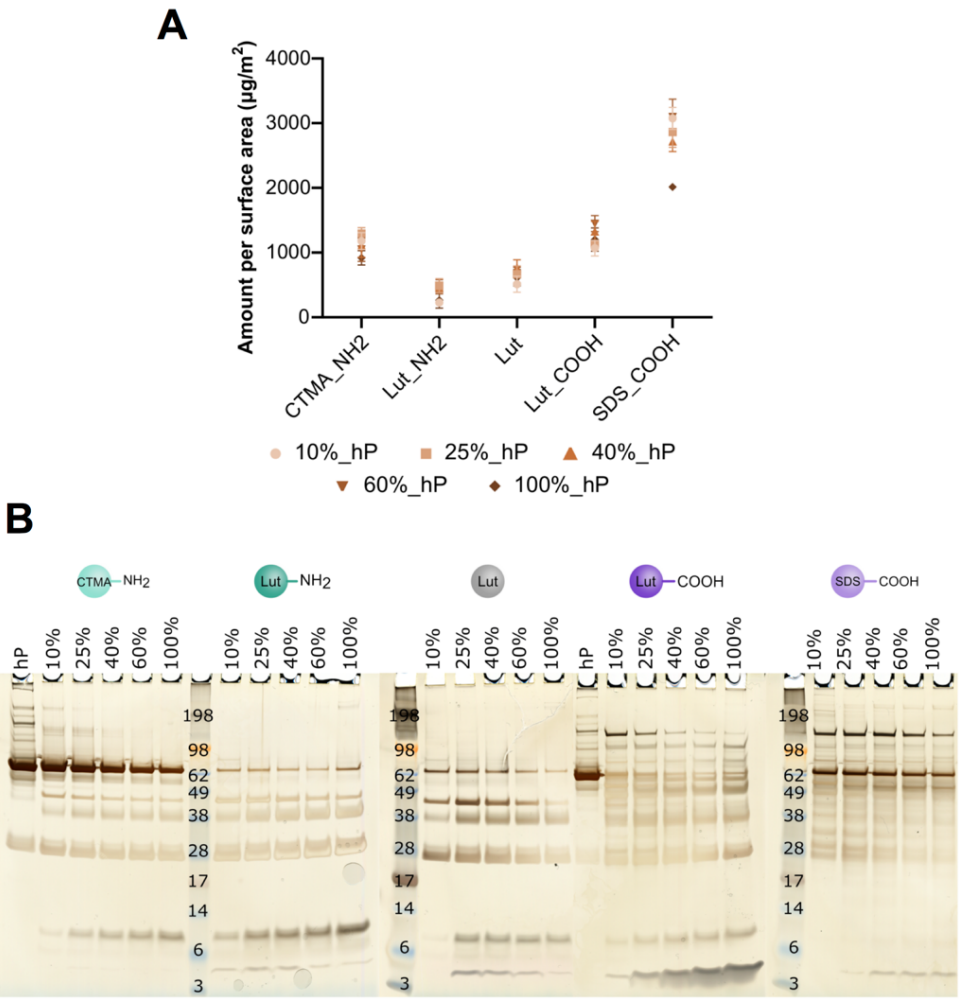

Figure S2.2: Hard corona protein amount and composition recovered from the nanoparticles after coating in different concentrations of plasma. (A) The proteins were desorbed with 2% SDS and quantified by Pierce 660 nm Protein Assay Reagent. For accurate comparison between conditions, the amount of proteins is normalized based on the surface area. The nanoparticles were incubated with 10% hP (dot), 25% hP (square), 40% hP (triangle), 60% hP (inverted triangle), and 100% hP (diamond) (data are shown as mean ± SD, n = 3). **(B)** Separation of the hard corona proteins by SDS-PAGE revealed by silver staining. The lanes labeled as "hP" correspond to loading of pure plasma. The samples were loaded from left to right based on an increased amount of plasma (10%, 25%, 40%, 60%, and 100%) used in the NPs coating step.

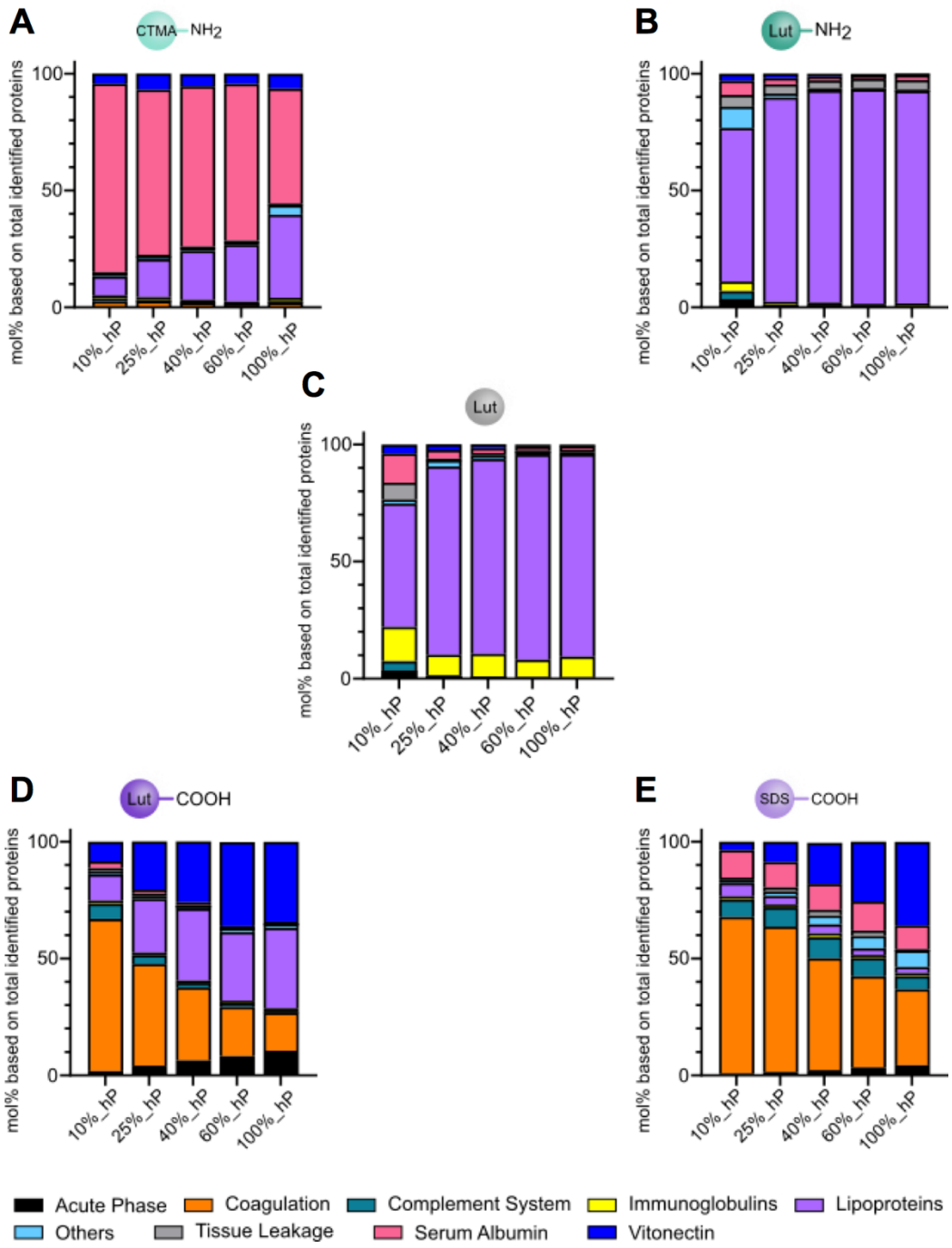

Figure S2.3: LC-MS analysis of the hard protein corona of NPs after coating with five different plasma concentrations. All the proteins recovered from the surface of CTMA_NH2 NPs **(A)**, Lut_NH2 NPs **(B)**, Lut NPs **(C)**, Lut_COOH NPs **(D)**, and SDS_COOH NPs **(E)** and measured by LC-MS were identified and sorted based on their affiliation to one of the following categories: Acute Phase, Coagulation, Complement System, Immunoglobulins, Lipoproteins, Others, Tissue Leakage (staked from bottom to top on the graphics). Additionally, 2 single proteins (Serum Albumin and Vitronectin) with a high mol% present in the protein corona were also plotted.

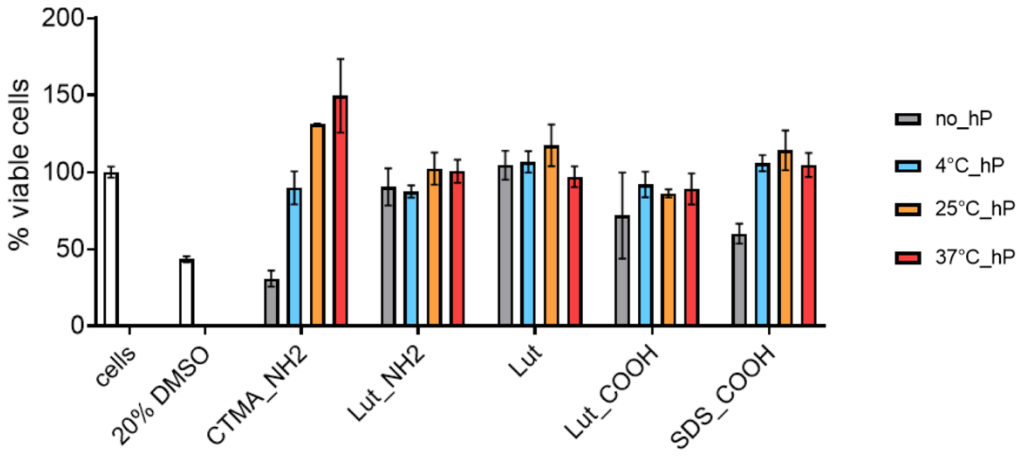

Figure S2.4: Cellular viability after incubation for 24 h in presence of 40 µg ml^{-1} NPs after coating at different temperatures with plasma. The sample labeled “cells” corresponds to the untreated cells incubated in DMEM media without NPs, the sample labelled “20% DMSO” corresponds to cells treated for 24h with a DMEM media containing 20% DMSO. These samples are used as controls to validate the assay (data are shown as mean ± SD, n = 3).

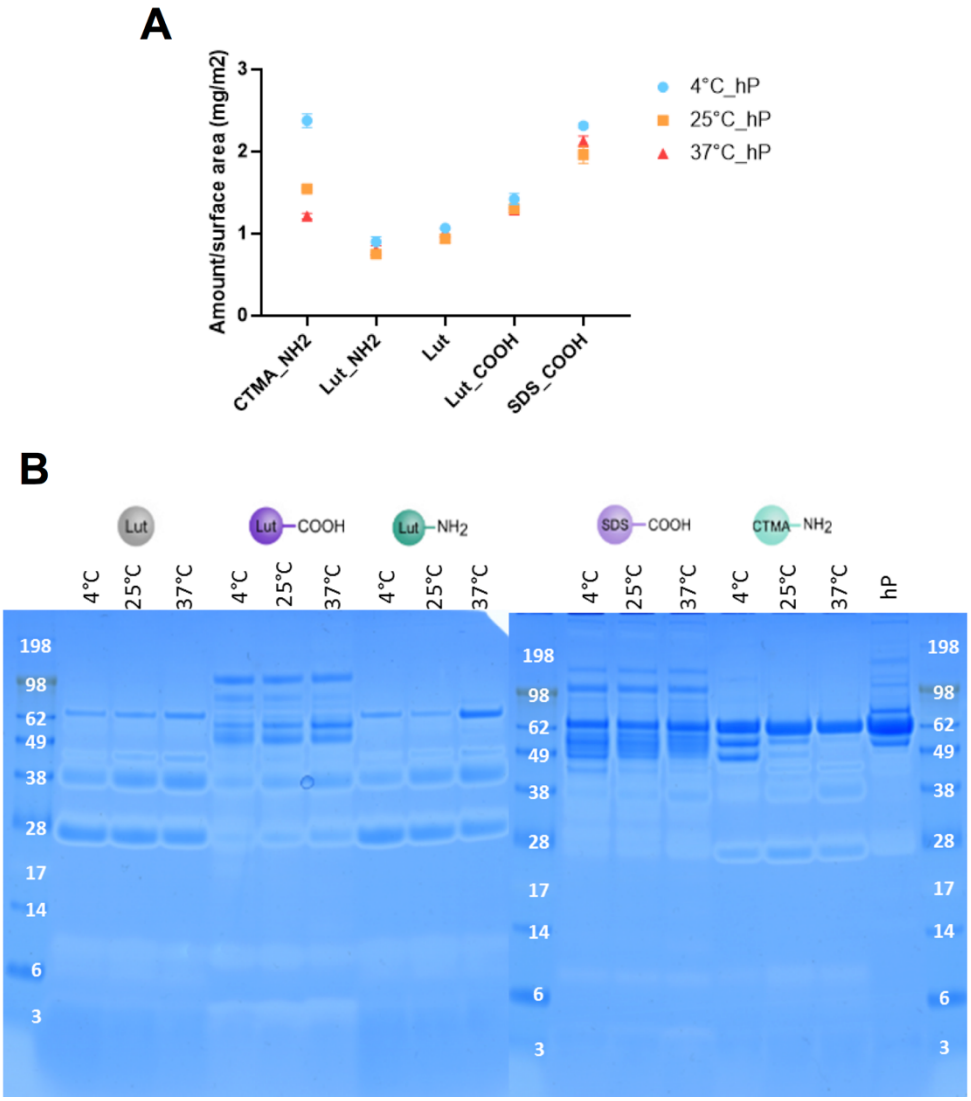

Figure S2.5: Hard corona protein amount and composition recovered from the nanoparticles after coating at different temperatures with plasma. (A) The proteins were desorbed with 2% SDS and quantified by Pierce 660 nm Protein Assay Reagent. For accurate comparison between conditions, the amount of proteins is normalized based on the surface area. The nanoparticles were incubated at 4 °C hP (blue dot), 25 °C hP (orange square), and 37 °C hP (red triangle) (data are shown as mean ± SD, n = 3). **(B)** Separation of the hard corona proteins by SDS-PAGE revealed by Coomassie Blue. The lane labeled as "hP" corresponds to loading of pure plasma. The samples were loaded from left to right based on an increased temperature (4 °C, 25 °C, and 37 °C) used in the NPs coating step.

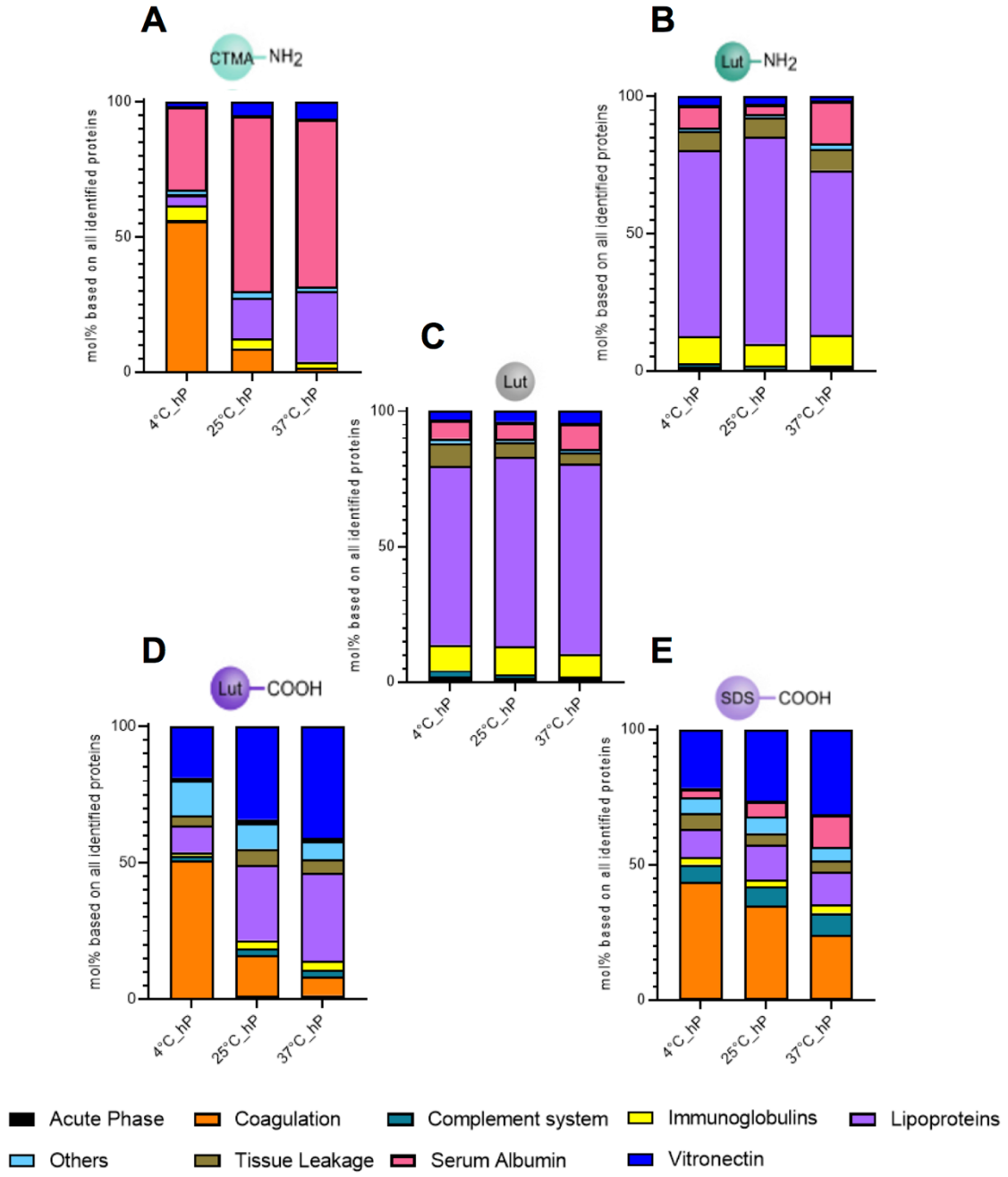

Figure S2.6: LC-MS analysis of the hard protein corona of NPs after coating with plasma at three different temperatures. All the proteins recovered from the surface of CTMA_NH2 NPs **(A)**, Lut_NH2 NPs **(B)**, Lut NPs **(C)**, Lut_COOH NPs **(D)**, and SDS_COOH NPs **(E)** and measured by LC-MS were identified and sorted based on their affiliation to one of the following categories: Acute Phase, Coagulation, Complement System, Immunoglobulins, Lipoproteins, Others, Tissue Leakage (staked from bottom to top on the graphics). Additionally, two single proteins (Serum Albumin and Vitronectin) with a high mol% present in the protein corona were also plotted.

Chapter B - The protein corona in the intracellular environment

Chapter B consists of four subchapters. Subchapter 3 introduces mechanisms of the cellular uptake, also endocytosis of nanoparticles. Furthermore, the intracellular trafficking, and then the cellular exclusion, also exocytosis of nanoparticles are explained. Next, subchapter 4 presents study **[2]** that investigated the intracellular separation of a pre-adsorbed protein corona from NPs and their fate. Study **[2]** is, at the time being, accepted by reviewers for the publication in a peer-reviewed journal and undergoes editorial revision. Study **[2]** is presented as a verbatim reproduction with slight adaptions. Subchapter 5 presents study **[3]** that analyzed the intracellular evolution of the protein corona composition and its possibilities in explaining the uptake and intracellular trafficking. Study **[3]** was submitted to a peer-reviewed journal. Last, subchapter 6 presents publication **[4]**, in which the analysis of the intracellular protein corona was utilized to detail the exocytosis processes of gold NPs for imaging purposes. Publication **[4]** was previously published in a peer-reviewed journal and was shortened and edited to highlight my contribution to the work.

[2] ___, **da Costa Marques, R.***, ___, ___, ___, ___, ___, ___. Endosomal sorting results in a selective separation of the protein corona from nanoparticles. *Nature Communication.* (*shared first, accepted by reviewers, under editorial revision)

[3] **da Costa Marques, R.**, ___, ___, ___, ___, ___. Proteomics-guided intracellular trafficking analysis reveals time-dependent protein corona changes and the intracellular pathway. *Nanoscale Horizons*. (submitted)

[4] ___, ___, ___, **da Costa Marques, R.**, ___, ___, ___, ___, ___, ___. Higher Loading of Gold Nanoparticles in PAD Mesenchymal-like Stromal Cells Leads to a Decreased Exocytosis. *Cells*, **2022**, *11*(15), 2323.

3. Theoretical Background

3.1 Cellular uptake mechanisms of nanoparticles

As described in the previous chapter, efficient nanomedicine requires precise knowledge about the nano-bio interactions. Nevertheless, the interactions of NPs are not only limited to biomolecules. Another challenge for most NPs is the cell membrane, a barrier composed of a lipid bilayer and equipped with proteins and other biomolecules [124]. This barrier must be overcome if the desired nanomedical goal should be achieved intracellularly. This is the case for NPs in therapeutic drug delivery and imaging applications [5, 124]. As these applications constitute two major nanomedical fields [5-6], the cellular uptake of NPs remains an important and widely studied phenomenon [124]. More so, the uptake mechanism can define the following intracellular fate [125], successful drug delivery [126], and the eventual biological response [124, 127].

Cellular uptake mechanisms that do not rely on diffusion or direct transport through the lipid bilayer are termed endocytosis [128]. Endocytosis is a cellular energetic-active process that includes re-shaping the cellular membrane and employing protein-driven mechanisms to engulf extracellular substances [128-129]. The extracellular substance is subsequently packed into intracellular lipid bilayer vesicles which are broadly classified as endocytic vesicles or endosomes [124, 129]. Cellular uptake of NPs is mostly driven by endocytosis, as most NPs cannot bypass the lipid bilayer directly, unlike most small or hydrophobic molecules [128]. Endocytosis is broadly divided into two categories: pinocytosis and phagocytosis [128-129]. Pinocytosis is a collective term for endocytosis mechanisms that take up extracellular fluid with dissolved molecules or small particles [128-129]. Particularly, pinocytosis can be further categorized into macropinocytosis, clathrin-mediated endocytosis (CME), caveolin-mediated (CAV) endocytosis, and endocytosis mechanisms that are independent of clathrin and caveolin [129-130]. Conversely, phagocytosis is the endocytosis mechanism by which the cell engulfs larger (> 0.5 µm) solid particles [130-131]. Phagocytosis is employed by specialized cell types referred to as phagocytes. Typical phagocytes are e. g. monocytes, macrophages, and dendritic cells [130-131]. The most relevant endocytosis mechanisms for NPs are shown in Figure 3.1.

Clathrin-mediated endocytosis (CME), the best-characterized endocytosis pathway yet, is common to all cell types [131]. This pathway is required for nutrient collection, such as iron via transferrin or cholesterol via low-density lipoproteins [131-132]. CME occurs via ligand binding of receptors, such as transferrin receptors [133] or low-density lipoprotein receptors [134] but also can occur as receptor-independent [130]. Upon receptor binding, the adaptor protein 2 (AP2) complex is recruited to the cytosolic cell membrane side, initiating the formation of clathrin-coated pits [131-132, 135]. These pits resemble membrane invaginations, stabilized by the name-

giving protein, clathrin, which is linked to the membrane via AP2 [132, 136]. Clathrin forms a three-legged triskelion structure composed of three heavy and three light chains [136-137]. These triskelions assemble to a polyhedral lattice on the cytosolic membrane side, contributing to the pit stabilization [130, 136-137]. The pits are then closed by the GTPase dynamin, resulting in clathrin-coated vesicles [130, 136]. These vesicles appear as “fuzzy” spherical intracellular vesicles in EM imaging, with an average size of 120 nm [130, 138]. The clathrin coat is eventually disintegrated for recycling upon vesicle fusion with early endosomes (EE) to deliver the internalized cargo [130]. NPs with sizes around 100 nm, synthesized from poly(ethylene glycol)-polylactide and poly(lactic-co-glycolic acid) were shown to enter epithelial cells and smooth muscle cells by CME [139-140]. Additionally, NP surface modifications with mannose-6-phosphate, transferrin, and nicotinic acid were shown to target CME [141].

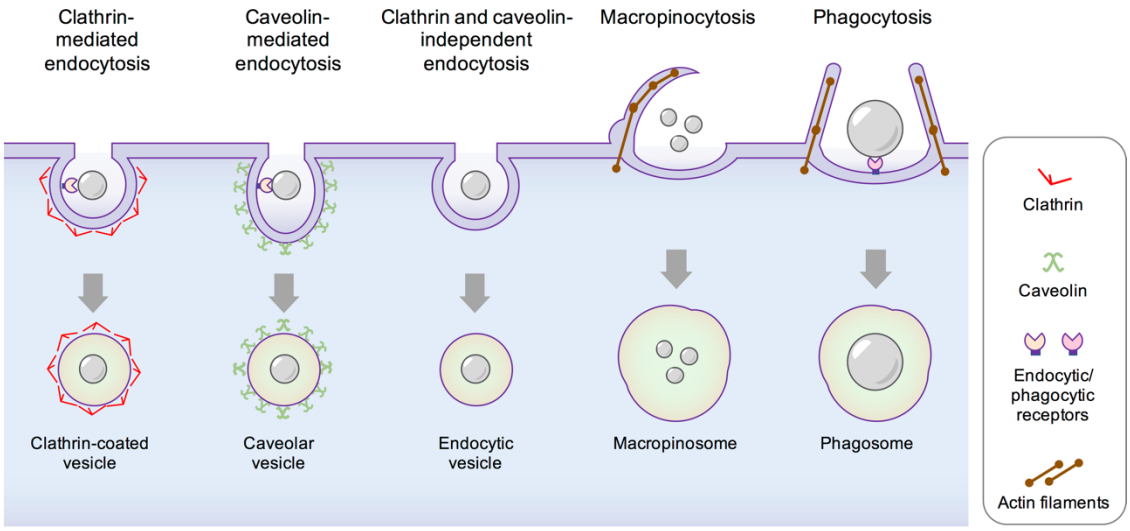

Figure 3.1: Cellular mechanisms for nanoparticle uptake. The five most common endocytosis mechanisms for NPs with associated vesicles are depicted.

Caveolin-mediated (CAV) endocytosis, common in many cell types, particularly in endothelial cells [130], is characterized by flask-shaped membrane invaginations, the so-called caveolae [142]. The caveolae are stabilized through dimeric caveolin and internalize cargo via receptor-binding [142]. Typical ligands for the caveolae-associated receptors are folic acid, albumin, and glycosphingolipids [142]. Similar to CME, the fission of the vesicles is dynamin-assisted [142]. Upon the formation of the 50-100 nm caveolar vesicles [132], the cargo can be delivered to EEs or through the formation of a caveosome to the Golgi apparatus or transported out of the cell [142-144]. The latter fate is connected to tissue transport, such as transcytosis through the endothelium [145]. NP surface modifications to address CAV endocytosis are folic acid and albumin [146-147].

Besides CME and CAV endocytosis, there are several clathrin and caveolin-independent pathways. These newly emerging pathways include several mechanistically distinct endocytosis routes, such as fast endophilin-mediated endocytosis (FEME) and clathrin-independent carrier / glycosylphosphatidylinositol-anchored protein enriched early endocytic compartment (CLIC/GEEC) endocytosis [131]. These routes generate endocytic vesicles not larger than 100 nm [131] and remain to be closer investigated for their cell and NP-specific purposes in nanomedical applications.

The last presented type of pinocytosis, macropinocytosis, relies on the actin-driven formation of cell membrane protrusions [130, 148]. The protrusions collapse on the cell, incorporating large amounts of extracellular fluid in 1-5 µm large vacuoles, termed macropinosomes [130]. The formed macropinosomes undergo gradual shrinking and acidification [148]. Macropinocytosis is common in various cell types, such as macrophages, dendritic cells, and endothelial cells [149]. Macropinocytosis is an unspecific process that does not rely on specific membrane coating or receptor-binding [130, 150].

Phagocytosis focuses primarily on the uptake of larger, solid substances of 0.5 µm and above [131]. However, it is not ruled out that NPs smaller than 0.5 µm can be engulfed by this mechanism as well [131]. Phagocytosis is only performed by phagocytes. Phagocytes are specialized cell types, such as macrophages or dendritic cells, which are part of the cellular immune system [151]. The main function of the phagocytic pathway is the clearance of pathogens, apoptotic cells, and foreign substances [151]. This also includes previously reported NP clearance through the bloodstream by macrophages [152]. Notably, phagocytosis is highly driven by the process of opsonization. Here, specific blood proteins, so-called opsonins, adsorb to the surface of the to-be-phagocytosed solid substances [151]. Phagocytosis is then initiated upon binding specific receptors, which include Fc receptors, mannose receptors, scavenger receptors, and complement receptors [124, 151]. The receptor binding initiates a Rho-family GTPase-involved intracellular signal cascade, leading to actin-driven membrane re-shaping to a phagocytotic cup [130, 151]. Finally, the cup-shaped protrusions engulf the extracellular substance, resulting in vesicular phagosomes, which eventually connect to the endolysosomal system [130].

Selected types of NPs and applications allow NP internalization without endocytic mechanisms [124]. For example, inorganic NPs below 10 nm and with a zwitterionic surface chemistry were shown to enter the cell via direct translocation [153-154]. Moreover, liposomes can fuse with the plasma membrane, delivering their content directly into the cytosol [155].

Overall, the above-mentioned endocytosis mechanisms are highly regulated and require complex protein machinery to drive them. Certain mechanisms are very exclusive to a few cell types, making them prominent targets in specific NP-based drug delivery or imaging

approaches. On the other hand, the physio-chemical properties of NPs can crucially address or prevent specific uptake routes. Typical properties that influence NPs to a certain uptake pathway are size [156], material [124], charge [154], and surface modifications [154]. As a matter of fact, protein adsorption via the formation of the protein corona also determines the NPs' uptake pathway [157]. In all cases, NPs will be internalized into the cell, enabling access to intracellular structures.

3.2 Intracellular trafficking of nanoparticles

Succeeding the cellular uptake through one of the diverse endocytosis mechanisms, NPs will be internalized into the cell via different subsets of endocytic vesicles. However, NPs are eventually introduced into the endolysosomal system, which represents various subsets of tubulovesicular compartments [132]. The trafficking of these compartments is highly regulated, interconnected to various organelles, and fulfills its purpose in nutrient processing, clearance of extracellular material, and storage [144]. Potential outcomes of the intracellular trafficking of NPs are recycling through the cell, degradation in lysosomes, translocation to the cytosol, and transport through the cell [124, 132]. The latter fate is particularly interesting for transcytosis applications of NPs, leading NPs to traverse through tissue barriers [132]. Determining and controlling the fate of NPs within the cell is influential in controlling drug release. As many drugs rely on transports via NPs due to their chemical nature, e. g. being very hydrophobe or acid unstable, the drug release should occur within specific subcellular compartments, such as the lysosome or the cytoplasm. Achieving the precise control of the NP trafficking within the endolysosomal system remains another challenge in nanomedicine, but is ultimately crucial for efficient drug delivery [124].

The intracellular trafficking of NPs through the endolysosomal system is schematically presented in Figure 3.2. The first station is the early endosome (EE), which arises from the fusion of endocytic vesicles upon internalization [144]. Located closely to the cell membrane, EEs are small and heterogeneous in appearance and show a weekly acidic pH value (pH 6.8-5.9) [144]. The EEs serve as a sorting platform and can direct cargo towards recycling endosomes (REs) for a recycling pathway, return the cargo directly back to the membrane, and carry cargo to the endolysosomal pathway for eventual degradation [124, 144]. Here, the sorting is mainly driven by acidification during the maturation of the EEs [132]. In fact, different cargo bound to endosomal receptors dissociates at different pH values, which results in an earlier or later receptor release of the cargo [132]. If the cargo is released early, the endosome recycles the cargo back to the membrane, whereas tight ligand (cargo)-receptor complexes

are transported deeper into the endolysosomal pathway. This sorting is further facilitated by the tubulation of EEs [158-159]. Cargo destined to be recycled accumulates in the tubules, which results in REs after budding. Notably, these REs endosomes keep the elongated, tube-like structure and recycle NPs back to the surface [158-159].

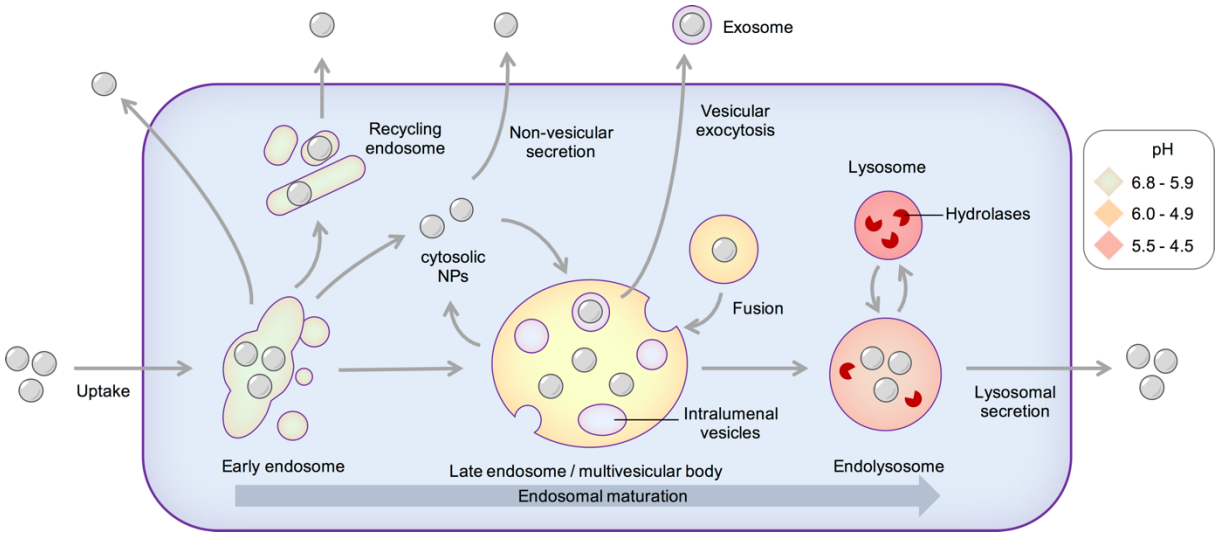

Figure 3.2: Endolysosomal trafficking of nanoparticles. The figure depicts the trafficking routes of NPs through the cell via the endolysosomal system. This includes early endosomes (EEs), recycling endosomes (REs), late endosomes (LEs) or multivesicular bodies (MVBs). Eventually, the endosomal system leads to the fusion of LEs with lysosomes (LY), forming endolysosomes (ELs). The vesicle colors indicate the pH values within the endosomal vesicles, as shown in the table. The values were retrieved from the literature [144, 160-161].

The cargo, which is not destined for recycling, resides in the central vacuolar part of the EEs and follows the endosome during its maturation [132]. During the endosomal maturation, the EE progresses to a late endosome (LE), and eventually fuses with the lysosome (LY), becoming the endolysosome (EL) [144]. These endosomal stages hold different molecular and functional identities [132]. However, these identities are volatile because of the gradual maturation process. First, the maturation includes gradual acidification of the endosomal lumen [132, 144]. This acidification is driven primarily by the v-type vacuolar H^+ ATPase in the vesicular membrane, pumping hydrogen ions into the endosome [132, 162]. Second, the ionic environment changes, increasing specifically the Cl^- concentration [144]. Third, the endosomes acquire a different morphology, losing the tubular features and instead becoming larger and rounder [144]. Last, specific proteins are recruited, which mark the new identity of the endosome. The most prominent protein family here is the Rab GTPase family, which mediates the fusion of endosomes with other vesicles, organelles, and the cell membrane [132, 163]. A switch of Rab proteins allows endosomes to further mature, i. e. by switching from EEs with Rab5 to LEs with

Rab7 [132, 164]. From here, only vesicles with recruited Rab7 are able to form endolysosomes by fusing with lysosomes [132, 144].

Through endosomal maturation, the NPs transit from EEs to LE [124, 144]. LEs are formed from the vacuolar domain of EEs and move around the perinuclear area of the cell [144]. Furthermore, the lumen shows a lower pH value (pH 6.0-4.9) [144, 160]. LEs grow in size to 250-1000 nm due to homotypic fusion events and the acquisition of intralumenal vesicles (ILVs) [144]. LEs with visible IVLs are also named multivesicular bodies (MVBs). ILVs can be formed through the inclusion of cytosolic substances or via vesicle fusion [144]. ILVs play a role in vesicular NP exclusion (more in subchapter 3.3). Eventually, LEs, containing NPs fuse with LYs [124]. LYs are the main proteolytic compartment of the cell, containing a variety of hydrolases to enzymatically degrade biomolecules, such as proteins, triglycerides, and nucleic acids [165-166], and resemble therefore, the last station of endosomal degradation [144]. Several models of endosomal and lysosomal communication are currently discussed, among which one model demonstrates the heterotypic fusion of LY with LEs to form ELs [144, 166-167]. LYs and ELs are, among others, characterized by the lysosome-associated membrane glycoproteins (LAMPs) and show the lowest pH values (pH 5.5-4.5) within the endolysosomal system [144, 160]. If NPs are not recycled or excluded from the cell at this point, they will face enzymatic degradation at this point [49, 124].

The endolysosomal compartments harbor different receptors, which remain interesting targets to address. Notably, toll-like receptors and major histocompatibility complex II reside within the endolysosomal system and are valuable targets for immunotherapy [124]. On the other hand, other drug delivery applications require to address the endosomal system. NPs or NP cargo need to be released in the cytosol to evade lysosomal degradation or to access other organelles, such as the Golgi Apparatus, mitochondria, or the nucleus [124]. Here, smart NP design choices allow endosomal escape of NP in order to enter the cytosol [124, 168]. For instance, NPs modified with poly(ethyleneimine) were shown to disrupt the endosomal membrane and enter the cytosol [124, 169]. Another example are NPs with pH-sensitive polymers or enzyme-sensitive linkers which split during the endosomal maturation, releasing the payload, and accessing the cytosol [124, 170-171]. Overall, these examples highlight the urgent need for smart NP design. However, just by understanding the interactions of NPs and the intracellular environment, this smart NP design can be realized. Only then, the desired control over the drug delivery process can be achieved.

3.3 Exocytosis of nanoparticles

While endocytosis plays a big role in NP targeting and drug delivery, the exclusion of NPs from cells, termed exocytosis, is crucial for the eventual removal of the NPs [124, 172]. In cellular homeostasis, exocytosis is responsible for receptor recycling, waste removal, and secretion of signal molecules, such as hormones or proteins [124, 173-174]. Exocytosis is also part of transcytosis [124]. Understanding the exocytosis kinetics of NPs might improve toxicity studies of potential toxic NPs [172] or drug delivery studies towards a prolonged drug release [124, 175]. Furthermore, imaging applications with NPs as contrast agents can profit from a longer cellular internalization, which makes studying exocytosis a necessary endeavor [173]. However, unlike endocytosis of NPs, exocytosis of NPs remains less studied [124, 172].

Several pathways for NPs exocytosis exist (Fig. 3.2). From the EEs, NPs can be transported directly to the cell membrane [124, 144]. In addition, NPs can be sorted from EEs into REs which transport NPs to the cell membrane [124, 144]. Both mechanisms expel the NPs with endosomal luminal contents into the extracellular fluid without vesicle formation around the NPs. Here, the direct transport from EEs occurs faster than over REs [158]. However, the exact molecular mechanisms and driving factors of direct recycling compared to REs recycling are poorly understood [158]. Another pathway for NPs that escaped the endosome and are in the cytosol is the non-vesicular secretion [172]. Yet, this pathway requires NP to be able to cross cellular lipid bilayer by inherent physicochemical properties. Additionally, cytosolic NPs can also be subjected to inclusion into ILVs [172]. The inclusion into ILVs of NPs can optionally occur via LE fusion events [144]. From here on, MVBs carrying the NP-loaded ILVs fuse with the cell membrane, releasing ILVs with NPs in a vesicular exocytosis [172, 176]. The resulting vesicles are up to 100 nm-sized exosomes, and function as biological signaling molecule carriers for intercellular communication [176]. Finally, NPs can be released by the cell via lysosomal secretion [172, 177]. Here, endolysosomes fuse with the cell membrane, eliminating NPs from the cell.

Similar to endocytosis, exocytosis behavior is highly dependent on the cell type [124, 178] and the physicochemical properties of NPs, such as size or shape [172, 179]. In this regard, studies demonstrated a higher exocytosis rate for rod-shaped gold NPs over spherical gold NPs [179]. Additionally, decreasing the NPs size correlated with a higher exocytosis rate [179]. These findings in the less investigated field of NP exocytosis demonstrate that NP design and intracellular studies are indeed beneficial to nanomedical research.

4. Endosomal sorting results in a selective separation of the protein corona from nanoparticles

Aim:

Previous research on the protein corona has extensively focused on its formation in extracellular environments and its consequences on cellular uptake. However, once internalized into the cell, the intracellular fate of a pre-formed protein corona and its potential detachment from the NPs remains elusive. This work presents the intracellular separation and the subsequent fate of the protein corona from NPs. The work explains the findings through time-based flow-cytometry experiments and high-resolution microscopic techniques.

Copyright:

Subchapter 4 contains a verbatim reproduction with slight adaptions of article **[2]** that is accepted by reviewers for the publication in a peer-reviewed journal and undergoes editorial revision at the time of the preparation of the thesis.

[2] ___, **da Costa Marques, R.***, ___, ___, ___, ___, ___, ___. Endosomal sorting results in a selective separation of the protein corona from nanoparticles. *Nature Communication.* (*shared first, accepted by reviewers, under editorial revision)

Contributions:

___ and I performed the protein labeling, the protein corona preparation, the protein quantification, SDS-PAGE, the cell culture methods, and the flow cytometry measurements. ___ performed the LC-MS sample preparation and LC-MS measurements. I evaluated the LC-MS data. ___ and ___ conducted the CLEM experiments. ___ created Figures 4.3, 4.5, 4.6, S4.4, S4.8, and S4.12-S4.14. ___ performed cLSM, the CLEM connectivity analysis, and created Figures S4.6 and S4.7. ___ performed the FCCS measurements. ___ and I wrote the manuscript. I created all figures not described above and edited all figures. ___ synthesized the polystyrene nanoparticles. ___ and ___ assisted in the preparation of the CLEM samples and performed EM. ___ assisted with the in-gel fluorescence measurement. ___ assisted in the cell culture preparations. The project was supervised by ___, ___, and ___.

4.1 Abstract

The formation of the protein corona is a well-known effect when nanoparticles (NP) are exposed to biological environments. The protein corona is the most important factor, which determines the rate and route of endocytosis, and decisively impacts cellular processes and even the release of the active pharmaceutical ingredient from the nanoparticles. While many studies concentrate on the effect of the protein corona formation extracellularly or the uptake consequences, little is known about the fate of the protein corona inside of cells. Here, we reconstruct for the first time the separation of the protein corona from the NPs by the cell and their further fate. Ultimately, the NPs and protein corona are separated from each other and end up in morphologically different cellular compartments. The cell directs the NPs towards recycling endosomes, whereas the protein corona gathers in multivesicular bodies. From this, we conclude that the NPs are prepared for subsequent exocytosis, while the protein corona remains in the cell and is finally metabolized there.

4.2 Introduction

While classical drug development for small molecules tweaks the pharmacokinetic by changing the drug itself, nanomedicine is a fundamentally different approach in which active pharmaceutically ingredients (API) are incorporated into smart, nanoparticulate systems in order to achieve this. For example, the RNA-based Covid-19 vaccine from BioNTech/Pfizer is based precisely on this nanotechnology and shows the tremendous success of this concept [8-9]. The problem of stability of the mRNA outside of cells, as well as the uptake of a large mRNA molecule, is solved by a clever design of nanomedical packaging. After the application to the organism, the nanoparticles (NPs) will finally enter the targeted cells to release their API and achieve the desired pharmaceutical effect. Before that, however, the NPs need to be introduced into the body and hence come immediately into contact with a biological environment, which contains proteins and other biomolecules. As a result, a coat of biomolecules adsorbs instantaneously on the NPs termed protein corona [11]. This protein corona alters the NP surface from a chemical into a biological identity, which can impact blood circulation [180], cellular uptake [78, 107], cytotoxicity [76], and the release of the API from the NP [181-182]. Consequently, researchers aimed to form the protein corona in a controlled way to achieve tailored effects. These artificial protein coronas have been shown to actively induce cell type [81] and tissue targeting [82] or even prevent cellular uptake [80], demonstrating the possibilities of pre-adsorbed proteins for nanoparticle modification.

However, it is yet unknown what happens to the protein corona after a NP is taken up by a cell, although detailed knowledge of the intracellular fate of the NP-associated protein corona is crucial for the understanding and development of any drug delivery system. Previous studies have highlighted the dynamic nature of the protein corona and the continuous exchange of the adsorbed proteins after the transition of the NPs to different protein-containing media. These studies demonstrate the exchange of proteins in both, single protein solutions and complex protein mixtures [60-61]. The protein exchange of the protein corona occurs also within the confined subcellular environment after internalization of the NPs with a distinct protein corona composition [183]. Eventually, Bertoli et. al. found evidence for the intracellular degradation of the protein corona from the NP in lysosomes using optical microscopy methods [184]. These studies rely on staining distinct subcellular compartments but lack the ultrastructural aspects as detailed in electron microscopy. Here, we use a fluorescence staining technique combined with electron microscopy, termed correlative light and electron microscopy (CLEM). This allows us to obtain unbiased information about the subcellular fate of NPs and the protein corona. Moreover, even the unlabeled cellular environment of the protein corona becomes visible due to the unspecific imaging capacities supplied by the electron microscopy technique.

Here, we demonstrate the co-internalization and the subsequent in-cell separation of the protein corona from the NP in murine macrophages by combining confocal laser scanning microscopy (cLSM) with electron microscopy (EM). To realize a trackable protein corona, we fluorescently labeled murine plasma proteins and formed a fluorescent protein corona on NPs. For the first time, we performed single-cell volume CLEM to visualize the protein corona and the NPs in 3D within the cell with high resolution and reveal their subcellular location and fate by fluorescence.

After co-internalization of the fluorescently labeled NPs together with the likewise fluorescently labeled protein corona, we observe a distinct decrease of the fluorescence signals over time and a spatial separation of the NPs from the protein corona signal in cLSM. To increase the resolution and also obtain information about the non-labeled cellular environment, we additionally performed EM studies and correlated them for the very same cells with the cLSM data (CLEM). In particular, we have been able to reconstruct the volume of complete cells using CLEM array tomography, utilizing fluorescence data to localize the protein corona and NPs. These volume reconstructions clearly show an enrichment of the NPs and the protein corona in morphologically different compartments 24 hours after incubation: The NPs are found in recycling endosomes (REs) whereas the protein corona is preferably found in multivesicular bodies (MVBs). Moreover, we found evidence for a subsequent exocytosis of the separated NPs and protein corona. Hence, these observations might impact the further design of drug delivery systems.

4.3 Materials and methods

Synthesis of carboxy-functionalized polystyrene nanoparticles. A macroemulsion was prepared with a continuous phase containing 600 mg Lutensol AT50 (BASF, Germany) solution in 24 ml Milli-Pore water as surfactant and a dispersed phase containing 5.88 g distilled styrene, 251 mg hexadecane (Acros Thermo Fisher, Germany) as hydrophobe, 153 mg distilled acrylic acid for the introduction of carboxy-functionalities, 6.1 mg BODIPY methacrylate as fluorescent dye and 100 mg 2,2'azobis(2methylbutyronitrile) V59 (Wako, Germany) as oilsoluble azo initiator. The dispersed phase was mechanically stirred. The continuous phase was slowly added to the dispersed phase to achieve homogenization. The macroemulsion was stirred for 1 h at the highest speed. The macroemulsion was then ultrasonicated with a Branson Sonifier (1/2" tip, 6.5 nm diameter) for 2 min at 450 W 90% amplitude under ice cooling to obtain a miniemulsion. The miniemulsion was transferred into a 50 ml flask and heated to 72 °C in an oil bath under stirring. The polymerization was performed for 11 h. Subsequently, the dispersion was centrifuged for 1.5 h at 13 000 rpm, 5 times for purification. The supernatant was removed after each centrifugation and the pellet redispersed in Milli-pore water. Nanoparticles were characterized by dynamic light scattering for the average diameter. The zeta potential was measured by diluting particles in a 1 mM potassium chloride solution. Dynamic light scattering and zeta potential were measured by a Malvern Zetasizer nano-s90 (Malvern Instruments, Germany).

Fluorescent labeling of murine plasma proteins with Cy5. Cyanin5(Cy5)-NHS ester (Lumiprobe, Germany) was added to murine plasma (GeneTex, U.S.A.) with a molar excess of 1.6 to one amino group, assuming all proteins in the plasma to be serum albumin. The reaction was carried out for 1 h at room temperature, shaking. Purification of labeled proteins and removal of unreacted free dye was performed with Zeba™ Spin 7 kDa MWCO columns (Thermo Fisher, Germany), following the manufacturer's instructions.

Protein corona preparation. Protein corona preparation was performed according to a previously published protocol [62]. Briefly, to form the protein corona, 1 mg of carboxy-functionalized polystyrene nanoparticles, which corresponds roughly to a surface of 0.01 m^2, was added to 1 ml of unlabeled or Cy5labeled murine plasma and incubated at 37 °C for 1 h, shaking. After the incubation, samples were centrifuged at 20 000*g* for 30 min at 4 °C (5804R, Eppendorf, Germany), the supernatant removed and the pellet resuspended in 1 ml PBS (Sigma-Aldrich, Germany). To remove non-adsorbed and low-affinity proteins, one wash step was performed for cellular uptake experiments and three wash steps for protein analysis. For

protein analysis, proteins were desorbed with 100 µl of desorption buffer (2% (w/v) SDS, 62.5 mM Tris-HCl) after incubation at 95 °C for 5 min, shaking and one centrifugation step as described above.

Protein quantification. The Protein concentration was quantified by Pierce™ 660 nm Protein Assay Reagent (Thermo Scientific, Germany) following the manufacturer's instructions. Ionic Detergent Compatibility Reagent (Thermo Scientific, Germany) was added to the assay reagent to measure samples containing SDS. A standard calibration curve was prepared with bovine serum albumin (Sigma-Aldrich, Germany). Absorption was measured with an Infinite M1000 plate reader (Tecan, Switzerland) at 660 nm.

SDS-PAGE, silver staining, and in-gel fluorescence detection. To perform SDS-PAGE, 2 µg of protein was diluted with deionized water to a volume of 26 µl. To this sample dilution, 4 µl of NuPAGE™ Sample Reducing Agent and 10 µl of NuPAGE™ LDS Sample Buffer (both Invitrogen, Germany) were added and incubated at 70 °C for 10 min for protein denaturation. The samples were loaded on a Bolt™ 10% Bis-Tris Plus gel using NuPAGE™ MES SDS Running Buffer (both Invitrogen, Germany). Protein electrophoresis was run for 1 h at 200 V. SeeBlue™ Plus2 Pre-Stained Standard (Invitrogen, Germany) was used as a molecular weight marker. SilverQuest™ Silver Staining Kit (Invitrogen, Germany) was used to stain the gels according to the manufacturer's instructions. Pictures of the developed gels were taken with a View Pix 1100 scanning system (Biostep, Germany). The in-gel fluorescence was detected by an IVIS Spectrum CT (PerkinElmer, U.S.A.) with an excitation wavelength of 650 nm, an emission wavelength of 680 nm, and an exposure time of 3 s.

In-solution tryptic digestion. Proteins were forwarded to an in-solution tryptic digest for LC-MS measurements, which was performed in previous studies [52, 183]. Before starting the digestion protocol, SDS was removed from samples with Pierce™ Detergent Removal Spin Columns (Thermo Scientific, Germany) according to the manufacturer's instructions. After SDS removal, 25 µg of protein per sample were precipitated with ProteoExtract Protein Precipitation Kit (CalBioChem, Germany), following the manufacturer's instructions. The precipitated proteins were isolated by centrifugation at 10 000*g* for 10 min at RT and two wash steps. The supernatant was finally removed and the pellet dried for 5 to 10 min. To solubilize the dried protein pellet, 0,1% RapiGest SF surfactant (Waters Corporation, Germany), dissolved in 50 mM ammonium carbonate buffer was added and incubated at 80 °C for 15 min. A dithiothreitol (Sigma, Germany) solution was added in a final concentration of 5 mM to reduce protein disulfide bonds. The reaction was run at 56 °C for 45 min. To alkalize the

proteins, 500 mM iodoacetamide (Sigma, Germany) solution was added for a final concentration of 15 mM. The reaction was run at RT for 1 h in the dark. To initiate digestion, a trypsin (Promega, Germany) solution was added in the mass ratio of 50 : 1 (protein : trypsin). After digestion for 16 h at 37 °C, 2 µl of hydrochloric acid (Sigma, Germany) was added to stop the digest and incubated further for 45 min at 37 °C. Finally, the aggregated degradation products were removed by centrifugation at 13 000*g* for 15 min at 4 °C. The supernatant containing peptides was transferred into new tubes.

Liquid chromatography coupled to mass spectrometry (LC-MS). Digested samples were diluted with LC-MS grade water (Merck, Germany) containing 0.1% formic acid (Sigma, Germany). To perform an absolute quantification according to a previously established protocol [185], samples were additionally spiked with 50 fmol μl^{-1} HI3 Ecoli Standard (Waters Corporation, Germany). The samples were measured by a nanoACQUITY UPLC system, installed with a C18 nanoACQUITY trap column (5 µm, 180 µm × 20 mm) and a C18 analytical reversed-phase column (1.7 µm, 75 µm × 150 mm; all Waters Corporation, Germany). The mobile phases used for separation consisted of (A) 0.1% (v/v) formic acid in water and (B) 0.1% (v/v) formic acid in acetonitrile (Biosolve, Germany). A gradient of 2% to 37% of mobile phase B over 70 min was performed. The samples flow rate was set to 0.3 µl min^{-1} and the flow rate of the referent components Glu-Fibrinopeptide and LeuEnkephalin (both Sigma, Germany) were set to a flow rate of 0.5 µl min^{-1}. The nanoACQUITY UPLC system was connected to a Synapt G2Si mass spectrometer (Waters Corporation, Germany) with electrospray ionization (ESI). The NanoLockSpray source was set to positive mode. The measurements were performed in resolution mode and data-independent acquisition (MS^E). Following settings were used: mass to charge range of 50–2 000 Da, scan time of 1 s, ramped trap collision energy from 20 to 40 V, and data acquisition of 90 min. Technical replicates were measured for each sample. The system was operated by the software MassLynx 4.1 (Waters Corporation).

Protein identification. Measured peptides and assigned proteins were processed with the software Progenesis QI 2.0 (Nonlinear Dynamics). The settings and procedure were described in previous studies [78]. Briefly, we defined the noise reduction threshold for low energy, elevated energy, and peptide intensity as 120, 25, and 750 counts, respectively. The murine proteome database with reviewed proteins was retrieved from uniport (swiss prot). The protein sequence information for the standard protein, Hi3 E. coli standard, was added to perform absolute quantification. The identification runs were performed with the following settings: one missed cleavage, maximum protein mass of 600 kDa, fixed carbamidomethyl modification for cysteine,

variable oxidation for methionine, a minimum of three assigned fragments per peptide, a minimum of two assigned peptides per protein, a minimum of five assigned fragments per protein, and a score parameter below 4.

RAW264.7 cell culture. The murine macrophage cell line RAW264.7 was cultivated with Dulbecco's Modified Eagle Medium, supplemented with 10% FBS, 100 U ml^{-1} penicillin, and 100 mg ml^{-1} streptomycin (all Gibco/Thermo Fisher, Germany). The cells were cultured in an incubator (CO_2 Incubator C200, Labotect, Germany) at 37 °C, 5% CO_2, and 95% relative humidity. For subculturing and harvesting, RAW264.7 cells were briefly washed with PBS prior to adding 0.25% Trypsin-EDTA (Gibco/Thermo Fisher, Germany) for detachment. Cells were collected after incubation for 5 min at 37 °C, 5% CO_2, and 95% relative humidity. The same volume of cell culture medium was added and the cells were sedimented by a centrifugation step of 300*g* for 5 min. The supernatant was removed. The cell viability and count were measured by an automated cell counter (TC10, Bio-Rad, Germany). The cells were diluted in cell culture medium for the next passage or experiment.

Cell uptake analysis with flow cytometry. After harvesting the cells, 150 000 RAW264.7 cells were seeded per well in a 24 well plate. To induce cell attachment, cells were incubated at 37 °C and 5% CO_2 overnight. On the next day, the medium was removed and the cells were washed once with 1 ml of PBS. Carboxy-functionalized PS NPs were diluted to a concentration of 150 µg ml^{-1} in DMEM without FBS and added to the cells in a volume of 200 µl. For a control experiment, Cy5-labeled murine plasma proteins were added in a comparable amount to the protein corona to the cells, which corresponded to 9 µg ml^{-1}. Uptake after different incubation times was measured by flow cytometry. To harvest the cells, the culture medium was removed and the cells washed once with 1 ml of PBS. Subsequently, 250 µl 0.25% Trypsin-EDTA was added and the cells incubated for 5 min at 37 °C and 5% CO_2 to induce detachment. After detachment, 250 µl DMEM without FBS was added and the cells were transferred to 1.5 ml tubes. The cells were centrifuged at 300*g* for 5 min. The supernatant removed and the cells resuspended in 1 ml of PBS. The flow cytometry measurements were performed with an Attune NxT (Thermo Fisher, Germany). To detect BODIPY (Carboxy-functionalized PS NPs) a 488 nm excitation laser was employed with a 530/30 nm band-pass filter. To detect Cy5 (labeled murine plasma proteins) a 638 nm excitation laser was used with a 670/14 nm band-pass filter. Cells were analyzed by forward scatter and sideward scatter to discriminate cellular debris and identify the cell population. Next, fluorescence properties of the identified cell population were analyzed as the percentage of gated fluorescent events or as the median

fluorescent intensity (MFI). Processing of flow cytometry data was performed with Attune NxT Software (Thermo Fisher, U.S.A).

F**luorescence cross-correlation spectroscopy (FCCS).** Protein corona preparation was performed as described above with one wash step to be comparable with the cell experiments. After the wash step, the PS NPs with the Cy5-labeled protein corona were resuspended in DMEM with different pH values (all without FBS). Hydrochloric acid (1N, Honeywell™ Fluka™, Germany) was used to adjust the pH value of DMEM. The pH values were measured with a pH electrode (Lab 855, SI Analytics, Germany). The stability of the Cy5-labeled protein corona on the BODIPY labeled PS NPs was studied by performing FCCS experiments [186-187] at different time intervals at the respective pH. An eight-well polystyrene, chambered cover glass (Laboratory-Tek, Nalge Nunc International) was used as a sample cell. The FCCS experiments were performed on a commercial setup (LSM 880, Carl Zeiss, Jena, Germany). For excitation of the BODIPY and Cy5 labeled species an argon ion laser (488 nm) and a He/Ne-laser (633 nm) were used respectively. The excitation light was focused into the studied solution by a high numerical aperture water immersion objective (C-Apochromat 40x/1.2 W, Carl Zeiss, Jena, Germany). The fluorescence was collected with the same objective and after passing through a confocal pinhole, directed to a spectral detection unit (Quasar, Carl Zeiss). In this unit, emission was spectrally separated by a grating element on a 32 channel array of GaAsP detectors operating in a single photon counting mode. The emission of BODIPY was detected in the spectral range 500-550 nm and that of Cy5 in the range 640-700 nm. The recorded experimental auto- and cross-correlation curves were fitted with the theoretical model function for freely diffusing fluorescence species [186-187]. The fits yielded the diffusion coefficients and the concentrations of the BODIPY labeled, Cy5 labeled and double labeled species. To evaluated the stability of the protein corona on the PS NPs, we calculated the ratio of the concentration of the Cy5 labeled species (all plasma proteins) to the concentration of the double labeled species (plasma proteins on the PS NPs) and monitored the time dependence of this ratio (Fig. S4.15).

Data Representation. GraphPad Prism 8 (GraphPad Software, USA) was utilized for data visualization. The data are shown as means ± standard deviation (SD) of the values.

Correlative light and electron microscopy (CLEM) sample preparation. RAW264.7 macrophages were seeded onto 3 mm sapphire disks (M. Wohlwend GmbH, Switzerland). Sapphire disks were pre-coated with a 10 nm-thick carbon layer using an EM MED020 instrument (Leica, Germany). The coated sapphire disks were dried and sterilized in an oven

at 120 °C overnight before use. Macrophages were seeded onto sapphire disks in 12 well plates overnight for cell attachment. Nanoparticles were added in a concentration of 150 µg ml^{-1} to the macrophages and incubated in a humidified incubator at 37 °C and 5% CO2. The incubation time points are indicated for each figure showing CLEM images. After the incubation, each sapphire disk was collected from the 12 well plates and slightly immersed into 1-hexadecene before placing them between two aluminum plates (3 mm, Plano). The aluminum 'sandwich' structure was placed into a specimen holder for high pressure freezing in a Wohlwend HPF Compact 01 high pressure freezer with a pressure of 2100 bar for 2-3 s. The specimen holder was withdrawn from the freezer and immersed into liquid nitrogen to release the sample. The frozen sample was then labeled and stored in a container filled with liquid nitrogen. Frozen sapphire discs were carefully removed from the aluminum 'sandwich' and transferred into 1 ml pre-cooled freeze substitution medium (0.2% (w/v) osmium tetroxide, 0.1% (w/v) uranyl acetate, 5% (v/v) distilled water in acetone) and kept in a freeze substitution unit (AFS2, Leica, Germany). Samples were then slowly warmed up to 0 °C over a period of 20 h in the unit. After being warmed up, the freeze-substituted samples were brought to room temperature, then the substitution medium was removed and the discs were washed 3 times with acetone at half an hour intervals. Then the discs were infiltrated sequentially in gradient epoxy resin-acetone mixture (1;1, 1:2, and 2:1) for 1 h. Samples were then infiltrated in 100% epoxy resin overnight. Finally, each sample was transferred into a new Eppendorf tube containing fresh epoxy resin for polymerization at 60 °C for 24 h.

Serial sectioning and CLEM imaging. After polymerization, sapphire discs were detached using liquid nitrogen. Afterward, resin blocks were trimmed for later serial sectioning. Trimmed resin blocks were sectioned by an ultra 45° Jumbo diamond knife (Diatome, Switzerland) with a home-made water draining setup. An ITO coated coverslip (SPI) was placed and fixed at the other end of the diamond knife. Diluted glue was placed on either top or bottom side of the trimmed resin block to make sure the sections stay attached in the correct order while sectioning. Section band was carefully moved to the coverslip with an eyelash brush until one end of the band touched the coverslip. Afterward, the water level was carefully lowered with the draining setup until the whole section band was slowly attached to the coverslip. The coverslip was then placed on a preheated hotplate to dry completely. The dried coverslip was then imaged in cLSM (SP5, Leica, Germany) with a 20X 0.75 NA dry objective for overviews or 63X 1.4 NA oil immersion objective to capture images of selected areas. The same coverslip was later mounted onto a clap holder to be imaged in HITACHI SU8000 with 2.5 V landing voltage 15 mA and a HA-BSE detector. Image registration and alignment of light and electron microscopy images were accomplished in Fiji and icy with eC-CLEM plugin.

Fluorescence connectivity measurement . To identify the separation of the Cy5-labeled protein corona from the PS NPs, we developed a macro that measures the connectivity of red and green signals using ImageJ. The ijm file of the used ImageJ macro is included in the supplementary information. We evaluated 12-73 cells per time point. The outlines of the cells were defined manually in the reflected light channel or EM images. In some cases, several adjacent images were used to include enough cells for the evaluation. Thresholds were defined to identify NP and protein corona objects and their signal intensities were evaluated using the ParticleAnalyzer plugin. A protein corona object was counted as connected to a PS NP object if its box overlapped or touched a box of PS NP object. The connected signal intensity of the connected protein corona were was compared with the total signal intensity of protein corona for each cell and a percentual fraction of connected signal intensity was calculated. The connectivity was determined as the mean for all cells in a region of adjacent cells having at least five green and three red objects. The cell-based standard deviation was plotted with the mean of the connectivity.

4.4 Results and discussion

The formation of a fluorescent protein corona

In order to form the protein corona and study its fate after cellular internalization, we synthesized and carboxyl-functionalized polystyrene nanoparticles (PS NPs). The synthesized PS NPs were stabilized with Lutensol, fluorescently labeled with BODIPY, and showed an average diameter of 116 nm and a zeta potential of 7.21 mV (Tab. S4.1). We labeled the murine plasma proteins with Cy5 by NHS-chemistry and formed the protein corona on the NPs with both, unlabeled and labeled proteins (Fig. 4.1A).

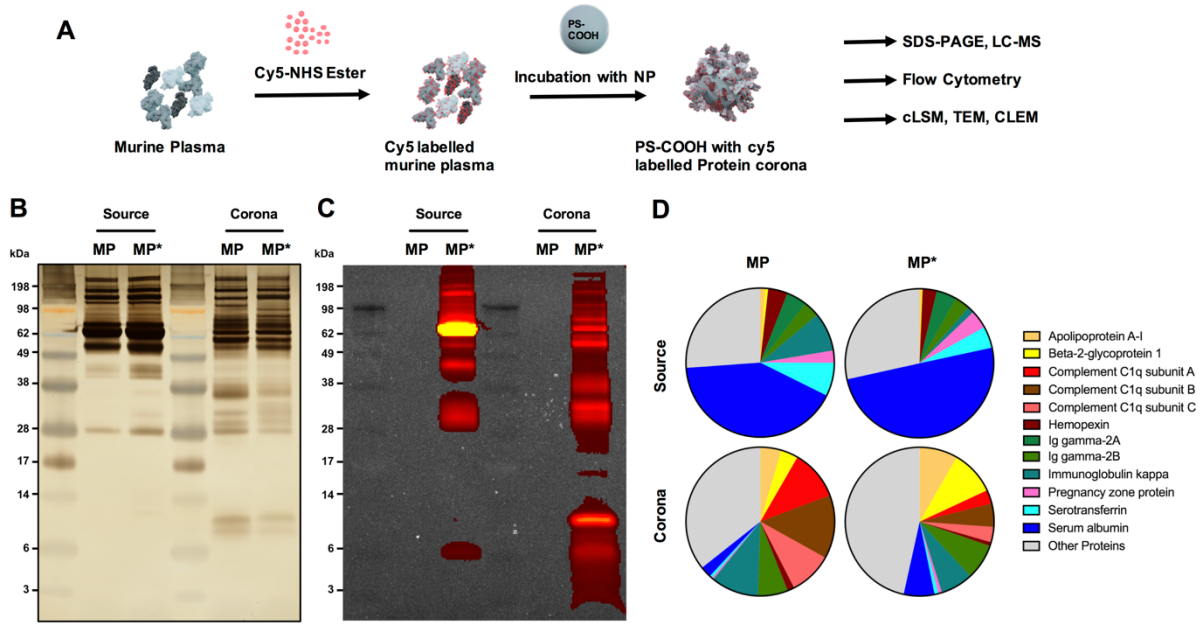

Figure 4.1: Protein analysis of unlabeled and Cy-5-labeled murine plasma and protein corona. **(A)** Murine plasma proteins were labeled with Cy5 by NHS-chemistry. Carboxyl-functionalized PS NPs were incubated in unlabeled and Cy5-labeled murine plasma, respectively, to form a protein corona. **(B)** Unlabeled murine plasma (MP), Cy5-labeled murine plasma (MP*), and associated protein corona samples were analyzed by SDS-PAGE and silver staining. Corona proteins were obtained after incubation of carboxyl-functionalized PS NPs in plasma, washing, and desorption with 2% of SDS. **(C)** Analysis of in-gel fluorescence. The Cy5-fluorescence was imaged by IVIS at an excitation wavelength of 640 nm and an emission wavelength of 680 nm. **(D)** Quantitative LC-MS proteomic analysis. The pie charts display the proteins with at least 4% presence in the proteome. Values are represented as the percentage based on all identified proteins.

Subsequently, we quantified the proteins and characterized the composition in the unlabeled and labeled plasma and unlabeled and labeled protein corona. The protein corona samples showed a comparable protein amount after desorption. We measured 51.79 (± 1.14) µg for the

unlabeled protein corona and 60.47 (± 2.8) µg for the Cy5-labeled corona (protein amounts as mean ± SD, n = 2, amounts correspond to 0.01 m^2 NP surface). Additionally, we observed similar band patterns on the SDS-PAGE by silver staining between unlabeled and labeled samples, respectively (Fig. 4.1B, Fig. S4.1). We detected the fluorescent labeling via in-gel fluorescence measurements by IVIS. Here we observed a high similarity between the band patterns of the silver-stained SDS-Page and the in-gel fluorescence (Fig. 4.1C). This similarity confirmed the high degree of fluorescent labeling of the proteins of different molecular weights.

Next, we employed quantitative LC-MS measurements to further detail the protein composition. Overall, the protein composition was slightly changed in quantitative measures after the Cy5-labeling. Serum albumin was measured as the highest abundant protein in both, unlabeled and labeled murine plasma, followed by immunoglobulin kappa in the unlabeled plasma and serotransferrin in the labeled plasma as the second-highest proteins, respectively. For the unlabeled protein corona, we measured complement C1q subunit B and complement C1q subunit A as the two most abundant proteins. In the labeled protein corona we identified beta-2-glycoprotein and apolipoprotein A1 as the two most abundant proteins. After the Cy5-labeling, we observed changes in the protein composition of the murine plasma, such as a ~6 fold decrease of immunoglobulin kappa and a ~2.7 fold decrease of apolipoprotein A1. In the case of the protein corona samples, we determined a ~2.7 fold to ~3.6 fold decrease of the complement C1q subunits and a ~2.7 fold increase of serum albumin after labeling (Fig. 4.1D). For the remaining most abundant proteins, however, we observed smaller quantitative differences, as the ones mentioned. As a consequence, we accepted the described quantitative changes after the labeling and assumed that the labeling would not alter the outcome of a fluorescently labeled protein corona compared to an untreated protein corona. Nevertheless, we included the NPs with an unlabeled protein corona as a control in the following uptake experiments.

Co-internalization of PS NPs and the protein corona

Next, we employed flow cytometry to understand the uptake of both, PS NPs and the protein corona. Murine macrophages RAW264.7 were incubated with untreated PS NPs, PS NPs with an unlabeled protein corona, and PS NPs with a Cy5-labeled protein corona (Fig. 4.2A). After an incubation of 2 h with the nanoparticles, almost 100% of the cells were BODIPY-positive, indicating the uptake of the PS NPs by most cells (Fig. 4.2B). Almost all measured cells were Cy5-positive, if the cells were incubated with PS NPs with a Cy5-labeled protein corona (Fig. 4.2C). A control uptake experiment with only Cy5-labeled proteins showed that no or a fairly small amount of Cy-5 proteins were taken up when compared to the uptake of Cy5-labeled proteins on the protein corona on PS NPs. This difference was confirmed by flow

cytometry and cLSM (Fig. 4.2D/E). Therefore, our findings prove a co-internalization of the PS NPs and the associated protein corona.

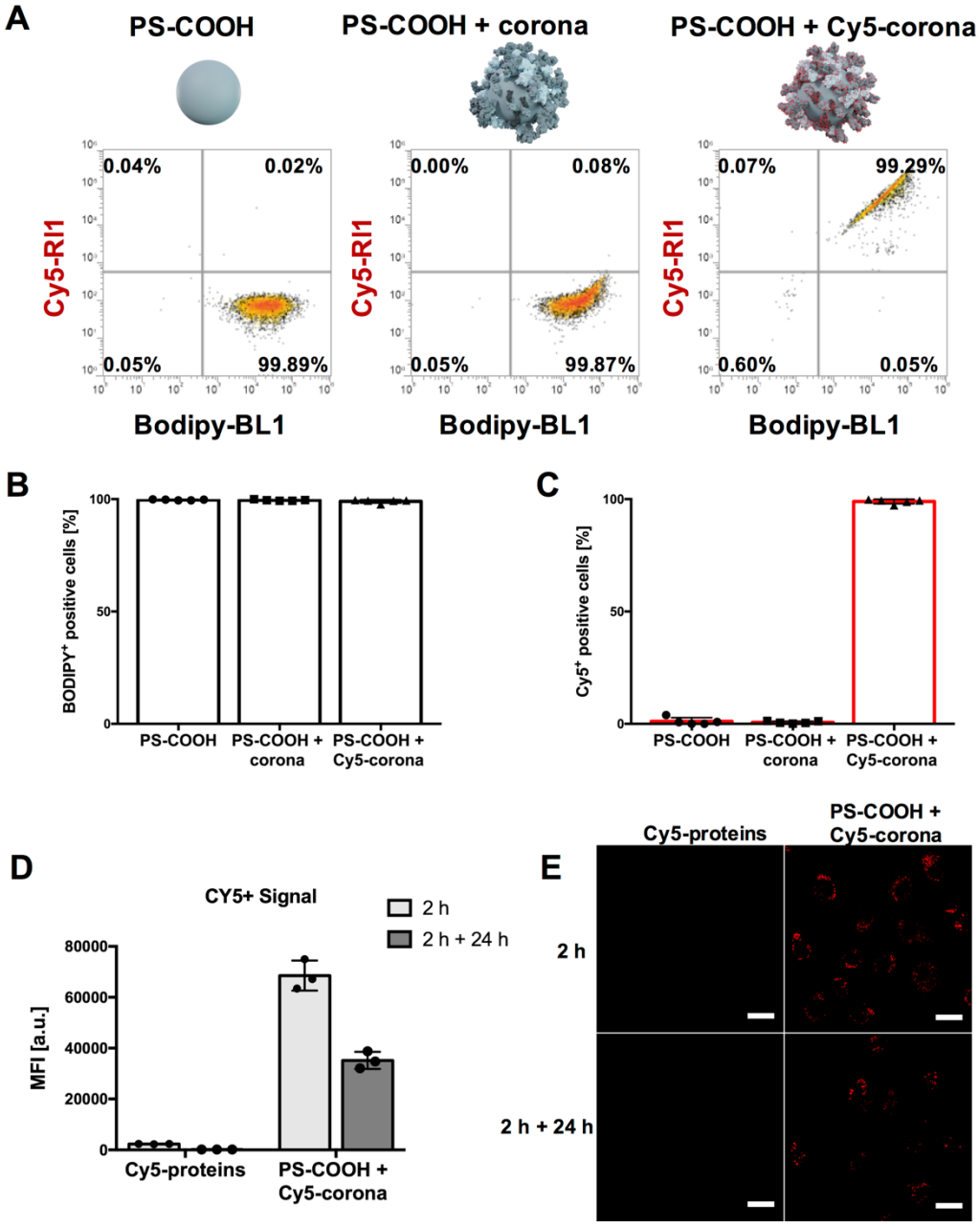

Figure 4.2: Cy-5-labeled protein corona is detectable after uptake in murine macrophages. RAW264.7 cells were incubated with 150 µg ml^{-1} of carboxyl-functionalized PS NPs for 2 h. Untreated NPs, NPs with an unlabeled protein corona, and NPs with a Cy5-labeled protein corona were used for the uptake experiment. **(A)** Flow cytometry was performed to measure BODIPY (PS NPs) fluorescence and Cy5 (labeled corona proteins) fluorescence. Values are shown as the percentage of measured events regarding the fluorescence. **(B)** The percentage of BODIPY-positive cells is shown. **(C)** The percentage of Cy5-positive cells is shown (data are shown as mean ± SD, n = 5). **(D)** As a control experiment, RAW264.7 cells were incubated with 9 µg mL^{-1} Cy5-labeled murine plasma proteins and

150 µg mL^{-1} of PS NPs with a Cy5-labeled protein corona, respectively. The amount of 9 µg mL^{-1} corresponds to the amount of proteins on the protein corona. The uptake was evaluated after 2 h and 2 h + 24 h. Flow cytometry was performed to measure the median fluorescence intensity (MFI) of Cy5 (proteins or protein corona; data is shown as mean ± SD, n = 3). The gating strategy for flow cytometry is provided in Supplementary Figure S4.2. **(E)** The uptake was analyzed by cLSM. Red represents the Cy5-labeled protein corona. The green signal is not included for a better overview of the red signal. Scale bars: 20 µm.

Visualizing PS NPs and protein corona within the cells

In order to study the intracellular behavior of the protein corona, we performed volume CLEM in RAW264.7 macrophages with a Cy5-labeled protein corona on BODIPY-labeled PS NPs. Volume CLEM is an imaging technique that is applied to visualize the three-dimensional information of biological samples (e.g. cells, tissues) by combining the strength of light microscopy and electron microscopy. The imaging process is performed on serial sections. After 24 h of co-incubation of protein corona coated PS NPs with macrophages, samples were immediately vitrified by high pressure freezing (HPF) to preserve the native structures. After undergoing the preparation steps of freeze substitution and EPON embedding, samples were finally sectioned and investigated in cLSM and SEM sequentially (see material and methods). In total 15 EPON sections (100 nm each) were imaged in both microscopic modalities and the images from both microscopes were superimposed as previously described (Fig. 4.3A, Fig. S.4.3) [188]. CLEM images of each section were aligned in the correct order and eventually segmented for the reconstruction model with a volume of 1.5 µm (Fig. 4.3I). Each object was segmented in a different color for better distinction. Totally, 1446 BODIPY-labeled PS NPs were segmented in green (Fig. 4.3B/F) and they were found within 172 endocytotic vesicles (Fig. 4.3C/F). Furthermore, 20 endocytotic vesicles containing separated Cy5-labeled protein corona (Fig. 4.3E/F) were segmented within the PS-vesicles complex (Fig. 4.3C), and 271 objects of protein corona (Fig. 4.3D/F) were segmented according to CLEM images. In addition, 12 mitochondria (Fig. 4.3G/H) were found within the vesicle complex. Vesicles containing the separated protein corona and vesicles containing PS NPs were closely located together with mitochondria. Within the vesicles containing the separated protein corona, a few PS NPs were found.

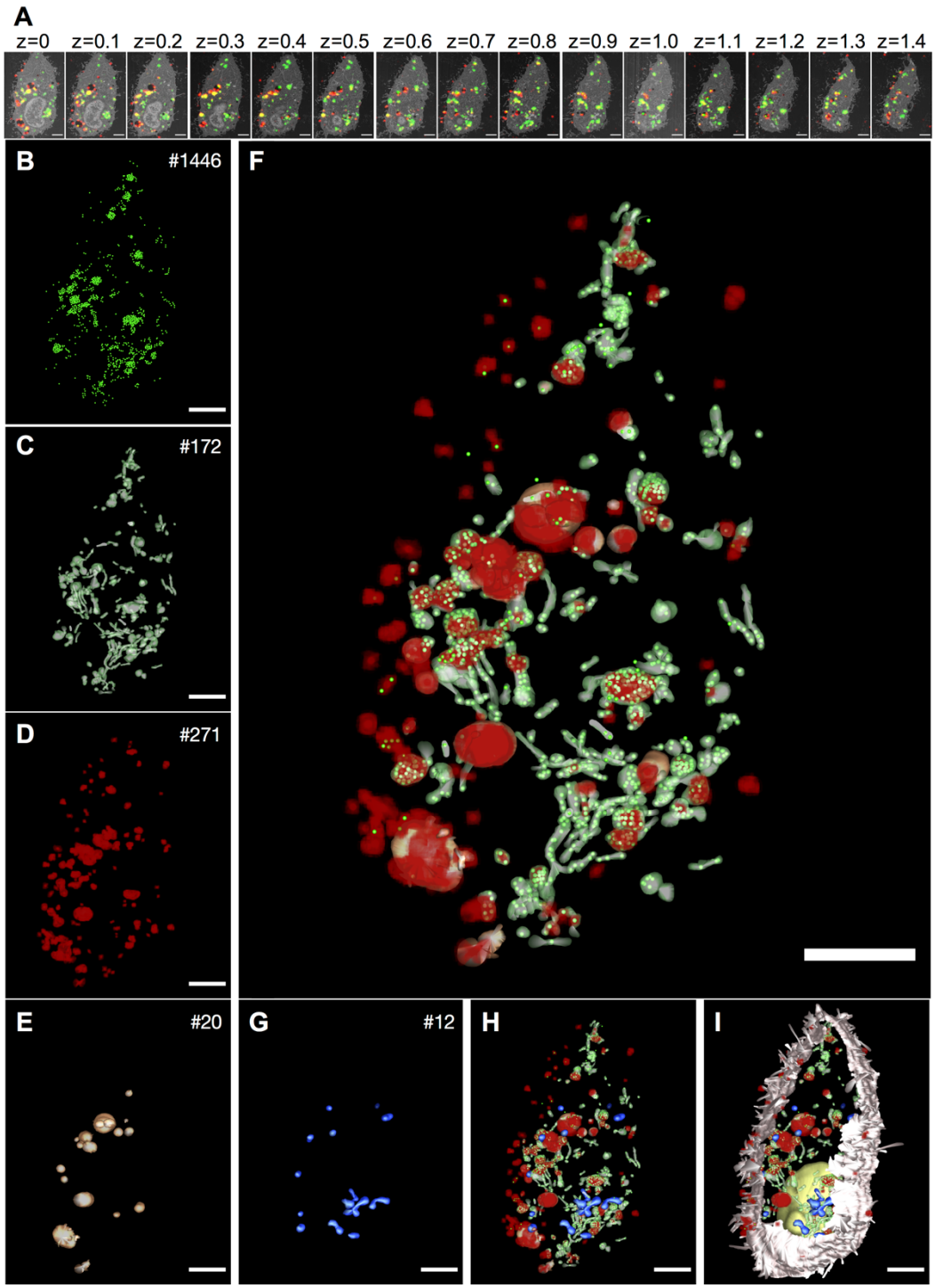

Figure 4.3: Volume CLEM of one cell and segmented model. PS NPs with Cy5-labeled protein corona were incubated with RAW264.7 cells and imaged in CLEM after 2 h + 24 h. **(A)** CLEM micrographs of 15 physical EPON sections (100 nm each). z represents the relative depth of each section in µm. Red represents the Cy5-labeled protein corona, green represents BODIPY-labeled PS NPs, yellow represents the overlay of the protein corona and PS NPs. The enlarged images are provided in Figure S4.4. **(B-I)** Segmented model of individual or combined objects with the number of segmented objects (upper right corner). **(B)** PS NPs. **(C)** Vesicles containing PS NPs. **(D)** Protein corona. **(E)** Vesicles containing protein corona. **(F)** Combined objects of the protein corona, PS NPs,

vesicles containing PS NPs, vesicles containing protein corona. **(G)** Mitochondria. **(H)** Objects in F with mitochondria. **(I)** Objects in H with cell membrane (light pink) and nucleus (yellow). Scale bars: 2 µm.

Separation of PS NPs and protein corona in the cell

We conducted additional flow cytometry analysis at different time points to investigate the fate of the internalized PS NPs and protein corona. For this, we retrieved the NPs-containing supernatant on RAW264.7 macrophages after an incubation time of 2 h and evaluated the BODIPY and Cy5 signal by flow cytometry after different additional incubation times. This procedure was performed for untreated PS NPs, PS NPs with an unlabeled protein corona, and PS NPs with a Cy5-labeled protein corona. Similar to the uptake analysis after 2 h, almost all measured cells were positive for BODIPY at every time point. If the cells were incubated with PS NPs with a Cy5-labeled protein corona we also detected that almost all measured cells were positive for Cy5 at every time point (Fig. S4.4). Additionally, we evaluated the median fluorescence intensity (MFI) to understand the intensity of the signal after different incubation times and link this intensity to the fate of the NPs and the protein corona. Overall, the MFI for BODIPY decreased over time, indicating a lowering amount of PS NPs in the cells with time. This decrease can be partially explained by cell division, which was shown to reduce the amount of nanoparticles in a growing cell population over time [189]. However, the release of PS NPs was previously shown in different cell lines and contributes additionally to the signal decrease [190-191]. This decrease of PS NPs with time was observed for all three conditions of PS NPs (Fig. 4.4A). In general, the MFI of the samples with protein corona, unlabeled and Cy5-labeled showed a lower MFI than the PS NPs without protein corona. We observed a similarly reduced uptake for PS NPs with protein corona in past studies, which might be a result of adsorbed dysopsonin proteins [117]. The MFI for Cy5 showed a similar decrease over time for cells that were incubated with PS NPs with a Cy5-labeled protein corona compared to an unlabeled protein corona (Fig. 4.4B). To compare the decrease of the BODIPY and Cy5 signal in the case of the uptake of PS NPs with a Cy5-labeled protein corona, we calculated a percentual MFI. This percentual MFI is based on the normalization of the MFI value compared to the highest MFI value (the MFI value of 2 h). Interestingly, we observed that the MFI of Cy5 decreased faster than the MFI of BODIPY (Fig. 4.4C). Accordingly, we state that the macrophages metabolize or exocytose the fluorescent corona protein faster or process it by a different pathway than the PS NPs.

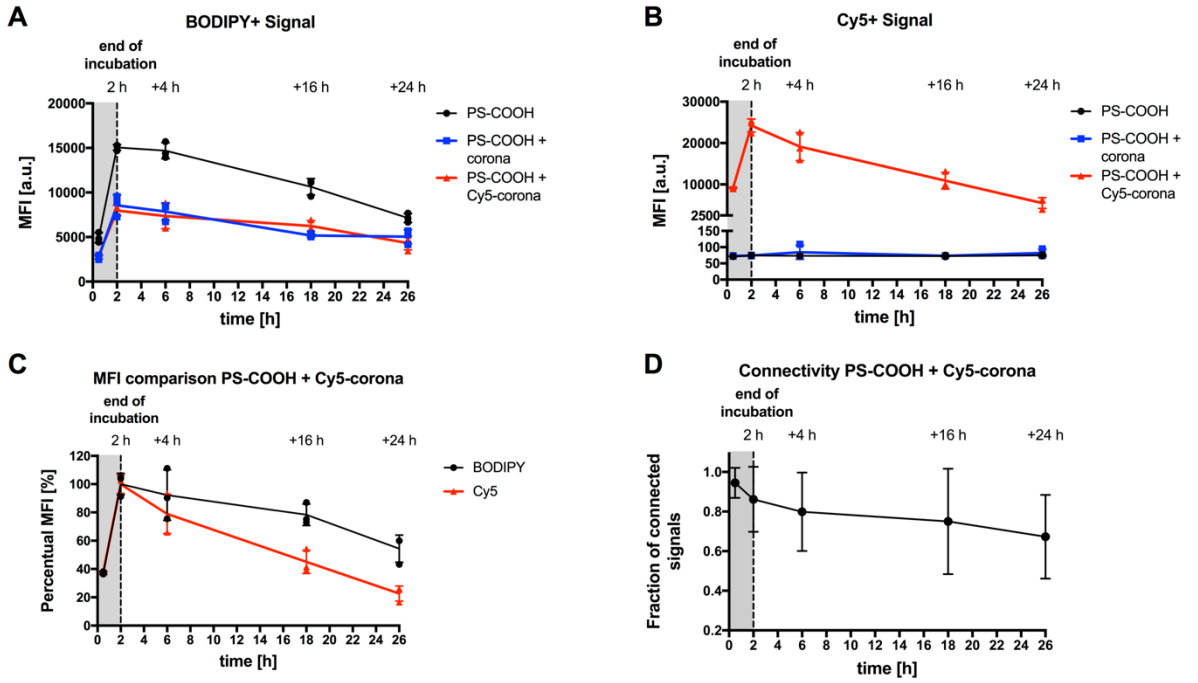

Figure 4.4: Flow cytometry and CLEM connectivity analysis reveal a slow separation of NP and protein corona after cell uptake. RAW264.7 cells were incubated with 150 µg ml^{-1} of carboxyl-functionalized PS NPs. Untreated NPs, NPs with an unlabeled protein corona, and NPs with a Cy5-labeled protein corona were used for the uptake experiment. The cells were incubated with the NPs for 2 h (dotted line). Subsequently, the NP-containing supernatant was removed and replaced with fresh culture medium without NPs. **(A)** Flow cytometry was performed to measure the median fluorescence intensity (MFI) of BODIPY (PS NPs). **(B)** The MFI of Cy5 (labeled corona proteins) was measured for the same events. The gating strategy for flow cytometry is provided in Figure S4.2. **(C)** The percentual MFI was plotted for the BODIPY and the Cy5 fluorescence in the case of the uptake of NPs with a Cy5-labeled corona. The percentual MFI value was calculated for each time point, comparing it to the highest MFI value measured (here: 2 h; data are shown as mean ± SD, n = 3). **(D)** The connectivity of BODIPY and Cy5 signals was analyzed for the uptake of NPs with a Cy5-labeled corona on CLEM images after different time points. The connectivity analysis was conducted by using an in-house ImageJ macro, calculating the fraction of connected signal intensities compared to the total intensities (data are shown as mean ± SD; n(0.5 h = 28, n(2 h) = 67, n(2 h + 4 h) = 73, n(2 h + 16 h) = 14, n(2 h + 24 h) = 12).

To support the flow cytometry findings, we analyzed the connectivity of the BODIPY and Cy5 signal on the embedded sections for CLEM (Fig. 4.4D). Here, we investigated multiple cells to generate reliable values. The connected signals were evaluated with an ImageJ macro (see material and methods). In brief, the cell outlines were identified and defined on the section with cells with internalized PS NPs after different time points (Fig. S4.5). Subsequently, thresholds were defined to identify the BODIPY signals (PS NPs) and Cy5 signals (protein corona; Fig. S4.6) A protein corona object was counted as connected to a nanoparticle if its box overlapped or touched a box of a PS NP object. The intensities of the connected signals were

then compared with the total signal intensities and a percentual fraction of connected signal intensity was calculated for each cell. We observed a decrease in the signal connectivity over the same time frame as in the flow cytometric experiment. Therefore, we conclude that the fluorescently labeled protein corona must be separated from the PS NP after the uptake. This separation is a process that takes several hours.

The evolution of the protein corona after cellular uptake

The intracellular fate of the protein corona and PS NPs was further revealed by the serial CLEM images. The protein corona (Cy5, red) and PS NPs (BOPDIPY, green) were mostly localized in round endosomes (Fig. 4.5B/B', yellow), whereas the separated protein corona signal was exclusively found in multivesicular bodies (MVBs) (Fig. 4.5D/D', MVBs in Fig. S4.7, red). These events were repeatedly observed in various cells (Fig. S4.8). In fact, the protein corona was exclusively observed within vesicular boundaries at 2 h and 2 h + 24 h (Fig. S4.9), which excludes the Cy5-labeled proteins translocating to the cytosol or to other compartments outside the endo-lysosomal system during the trafficking. We also localized elongated tubular vesicles around MVBs containing only PS NPs. These tubular vesicles can be morphologically identified as recycling endosomes (REs) (Fig. 4.5E/E') [159]. We confirmed that PS NPs without protein corona were also transported to REs (Fig. S4.10). Upon the observation that the protein corona and PS NPs were distributed separately in morphologically different endosomes, we further identified the sorting and separation event (Fig. 4.5C/C') by investigating the CLEM images where two signals were closely connected but not overlapped. Depending on the EM micrograph (Fig. 4.5C'), the endosome containing the protein corona exhibited a ruffling towards the endosome containing PS NPs (Fig. 4.5C', white arrow), indicating a possible division and thus formation of two distinctly loaded endosomal vesicles. Meanwhile, the endosome that contained only the protein corona (Fig. 4.5C, red) was found to be developed into an MVB in later sections (Fig. 4.6A). This finding confirms the earlier observation of the separated protein corona. Additionally, we observed exocytosis of separated PS NPs (Fig. 4.5F/F') in another cell (Fig. S4.12, Fig. S4.13), implying that PS NPs could be exocytosed by REs after being separated from the protein corona.

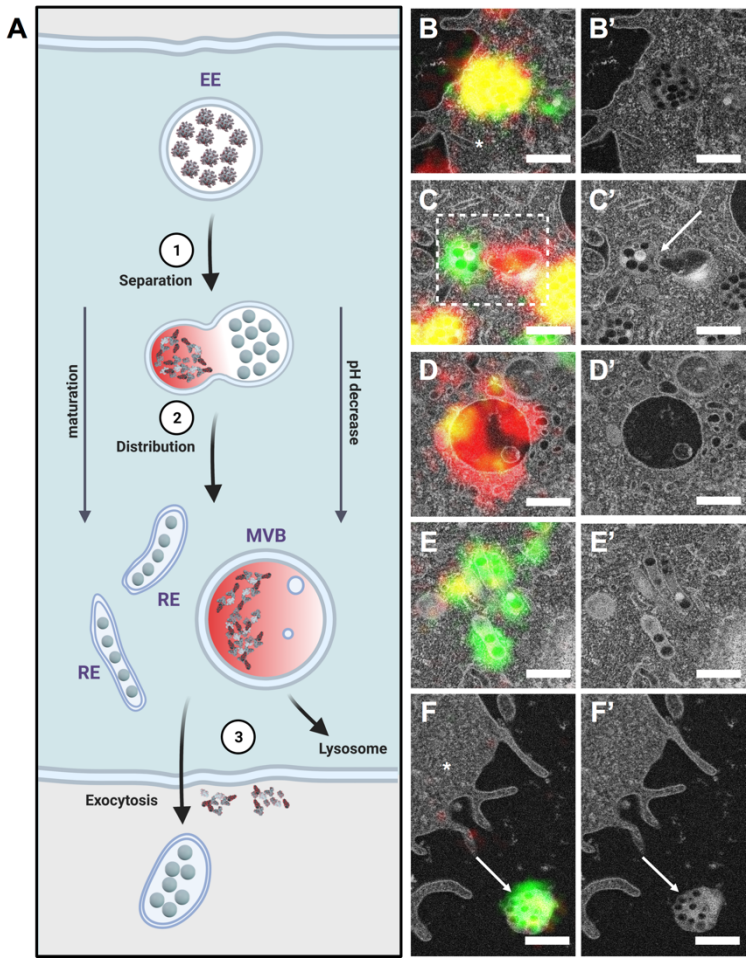

Figure 4.5: Intracellular fate of the protein corona and PS NPs illustrated by CLEM and EM micrographs. (A) Scheme of intracellular separation of the protein corona and PS NPs and exocytosis of NPs. Scheme was created with Biorender.com. **(B/B')** Protein corona coated PS NPs in an endosome after internalization. Intracellular space is indicated with a star symbol. **(C/C')** Separation of the protein corona and PS NPs. Separation event is highlighted with a dotted square and an arrow. **(D/D')** Distribution of separated protein corona in an MVB. **(E/E')** Distribution of separated PS NPs in tubular recycling endosomes. **(F/F')** Exocytosis of separated PS NPs. Exocytosis of naked PS NPs is indicated by an arrow and intracellular space is indicated with a star symbol. Red represents the Cy5-labeled protein corona, green represents BODIPY-labeled PS NPs, yellow represents the overlay of the protein corona and PS NPs. Scale bars: 500 nm.

To further demonstrate the separation event and the distribution of separated protein corona in MVBs, serial CLEM images of areas in Figure 4.5C and Figure 4.5D were shown in detail accordingly (Fig. 4.6A, Fig. 4.6B). The segmented models (Fig. 4.6A'/A''/A''') of Figure 4.6A showed the close spatial relationship between an endosome containing separated PS NPs (green) and an MVB containing the separated protein corona (red). An endosome with protein corona coated PS NPs and tubular REs with separated PS NPs were located next to the MVB indicating the separation might be an ongoing process. The segmented model (Fig. 4.6B'/B''/B''') of Figure 4.6B revealed dimensionally that several REs containing

separated PS NPs were located close to the MVB containing separated protein corona. The spatial information from both models further hinted that the separation and distribution of protein corona and PS NPs were closely related to the functions of different endosomes.

According to our CLEM results, the protein corona-coated PS NPs were mainly located in crowded round-shaped endosomes, whereas the separated protein corona was exclusively located in MVBs, and the separated PS NPs were found in tubular REs (Fig. S4.7, Fig. S4.8). Because our flow cytometry results showed the successful co-internalization of the protein corona and NPs, we assume that the endosomes with the protein corona-coated NPs were the primary or early endosomes (EEs). At the same time, it is known that EEs are crucial for sorting functions [158-159, 192] and are able to generate tubular REs for further transportation or recycling [159, 193]. Therefore, we consider that the separation or sorting of the protein corona and PS NPs starts at the site of early endosomes when REs containing PS NPs begin to form while the protein corona begins to separate from NPs. Furthermore, we observed the separated protein corona only in large MVBs containing intraluminal vesicles [194-195]. These MVBs mature from EEs [194] and more specifically from the main bodies of the EEs after the formation of REs [158, 192]. We hypothesize that during the maturation of the EEs after internalization, NPs start to separate from the protein corona and are transported into REs. As the maturation of the EEs into MVBs completes, most NPs are then transported into REs leaving behind the protein corona within the matured MVBs (Fig. 4.5A). This hypothesis correlates with the endosome maturation during the endocytic pathway and is supported by our CLEM results. Exocytosed NPs within a vesicle were also observed at the same condition (Fig. S4.12), and this phenomenon has been reported in different cell lines [190-191]. We speculate that the exocytosis might happen via the recycling of REs to the plasma membrane after protein corona separation. On the other hand, depending on the MVB maturation, the separated protein corona in the MVBs might eventually accumulate in lysosomes [195] or exocytose via exosomes [196]. Degradation of the protein corona in lysosomes is predictable and was previously observed [184]. Nevertheless, we have captured the Cy5 signals around the plasma membrane, either co-localizing with some membranous vesicles or on the membrane ruffling (Fig. S.4.11). These Cy5 signals outside of the cell might be the evidence of the exocytosed protein corona from MVBs and suggest an alternative destiny of the separated protein corona.

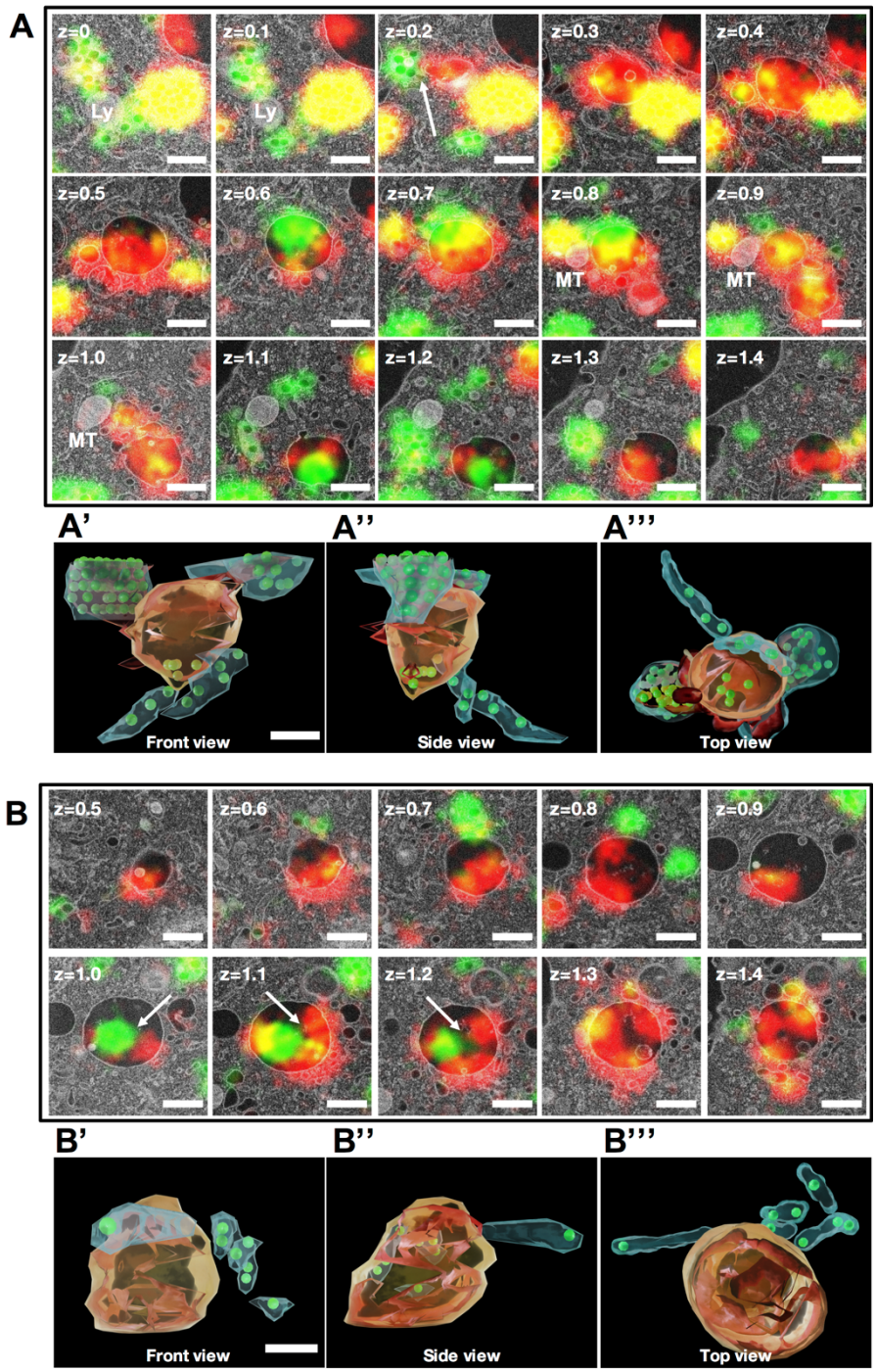

Figure 4.6: Volume CLEM and segmented models of the separation of the protein corona and PS NPs. PS NPs with Cy5-labeled protein corona were incubated with RAW264.7 cells and imaged in CLEM after 2 h + 24 h. **(A)** Volume CLEM of the separation of protein corona and PS NPs in endosomes. **(A')** Front view of the segmented model in A. **(A'')** Side view of the segmented model in A. **(A''')** Top view of the segmented model in A. **(B)** Volume CLEM of an MVB with separated protein corona and PS NPs. **(B')** Front view of segmented model in B. **(B'')** Side view of segmented model in B. **(B''')** Top view of segmented model in B. Red represents the Cy5-labeled protein corona, green represents BODIPY-labeled PS NPs, yellow represents the overlay of the protein corona and PS NPs. Scale bars: 500 nm.

We can point out various potential reasons for the separation of the protein corona from the NPs. One reason behind the separation of the protein corona and NPs might be related to the changing acidification within different endosomes. To investigate the role of the acidification, we conducted a fluorescence cross-correlation spectroscopy (FCCS) evaluation of the stability of the Cy5-labeled protein corona on the PS NPs in cell culture medium at different pH values. The FCCS results suggested that the protein corona on NPs remained stable in the range of pH 7.6-pH 5.5. At pH 4.5 the Cy5 and BODIPY signals separated over a time span of 24 h indicating disintegration of the protein corona (Fig. S4.14). The pH value in different endosomes decreases, thus the endosomes acidifies, along the endocytic pathway during the endosomal maturation [158, 161]. It is well understood for in vitro situations that the composition and stability of the protein corona are strongly affected by the environmental pH [197-198]. We suggest, that due to the decreased pH from EEs to MVBs, the proteins on the protein corona might lose their affinity to the surface of the NPs because the evolution of protein corona is dynamic under a fickle environment [199-200]. Additionally, the acidification might cause conformation changes of the adsorbed proteins [197, 201] which can consequently influence and alter protein-protein and most protein-NP interactions of the protein corona. However, our in-vitro experiment showed a disintegration at pH 4.5 and not at higher pH values (Fig. S4.14). Particularly, endosomes before the late endosomal stage show pH values of 6.5-5.5 [160]. Therefore, acidification can only be seen as one possible reason for the separation of the fluorescent-labeled protein corona from the PS NPs.

Furthermore, the protein corona-coated NPs transit through dynamic biological environments, being subjected to changes of the ionic environment and being confronted with new, intracellular proteins which were not originally present in the plasma. Endosomal maturation involves a constant efflux of cations, such as Ca^{2+}, Na^{+}, and K^{+}, and an influx countering Cl^{-} anions [144]. The importance of the ionic environment for the formation of the protein corona was previously explored [202], making it possible that continuous changes in the ionic environment could contribute to the displacement or rearrangement of the protein corona. Other studies highlighted the dynamic behavior of the protein corona after transitioning through different biological fluids [61] and within cells [203-204]. It is possible that intracellular proteins exhibit a higher affinity towards the NPs' surface and, therefore, adsorb on the NPs surface intracellularly and replace the previous proteins, leading to a newly formed protein corona. Additionally, protein degradation via late-endosomal proteases is likely to contribute to the identity change of the protein corona on NPs if they surpass the early endosomal stage [184]. Thus, this highly dynamic molecular environment might further contribute to the separation of the fluorescently labeled plasma proteins from the corona.

Ultimately, with our work we identified the separation process in a time-dependent manner with the strong support of high-resolution images. Nevertheless, future investigations must uncover

the exact molecular aspects behind the separation. Here, we see potential in stable isotope-labeling of amino acids to precisely track the protein corona and related peptides by degradation in the intracellular environment. In addition, these studies will profit from staining intracellular compartments, e. g. by transfection or antibodies, and including state-of-the-art microscopic techniques, such as cryogenic electron microscopy (cryo-EM) for structural studies or super-resolution live imaging.

4.5 Conclusion

Our results demonstrate the progressive separation of PS NPs from an associated protein corona that occurs over a timeframe of several hours. We visualized these events within the cell by volume CLEM and propose an intracellular pathway for the hereby used nanoparticular system that includes (1) the mutual internalization into the endosomal system, (2) the separation of NPs and the protein corona by early endosomal sorting mechanisms, (3) the presence of NPs in elongated REs and the protein corona in MVBs, and (4) the exocytosis of PS NPs and while the protein corona remains in the endo-lysosome. However, all these findings are based on the examination of one cell line. But in order to be able to make a general statement on the intracellular processing of the protein corona, it is of course necessary to examine a wide variety of different cell lines. With these findings, we should ultimately be able to understand engineered artificial protein coronas on NPs and optimize the release of the API towards a more sophisticated design of nanotherapeutics.

4.6 Supplementary Information

Table S.4.1: Characterization of carboxy-functionalized polystyrene nanoparticles. The used surfactant, fluorescent dye with excitation and emission wavelength, average nanoparticle diameter D_Z, and zeta potential ζ are listed. The average diameter was measured by dynamic light scattering. The average diameter and zeta potential were measured by a Malvern Zetasizer nano-s90 .

Name	Surfactant	Fluorescent Dye λ (Excitation/Emission) [nm]	D_Z [nm]	ζ [mV]
PS-COOH	Lutensol	BODIPY (523/536)	116	-7.21

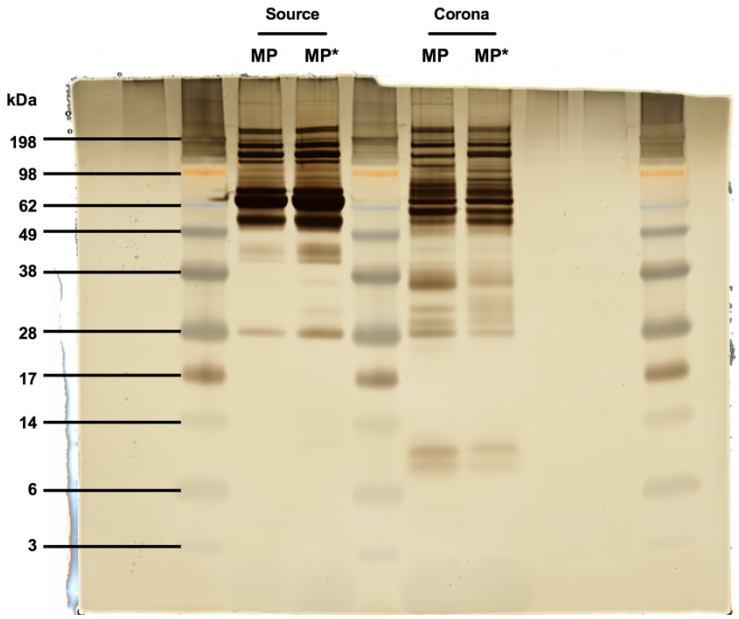

Figure S4.1: SDS-PAGE of murine plasma and protein corona samples. Unlabeled murine plasma (MP), Cy5-labeled murine plasma (MP*), and associated protein corona samples were analyzed by SDS-PAGE and silver staining. Corona proteins were obtained after incubation of carboxyl-functionalized PS NPs in plasma, washing, and desorption with 2% of SDS.

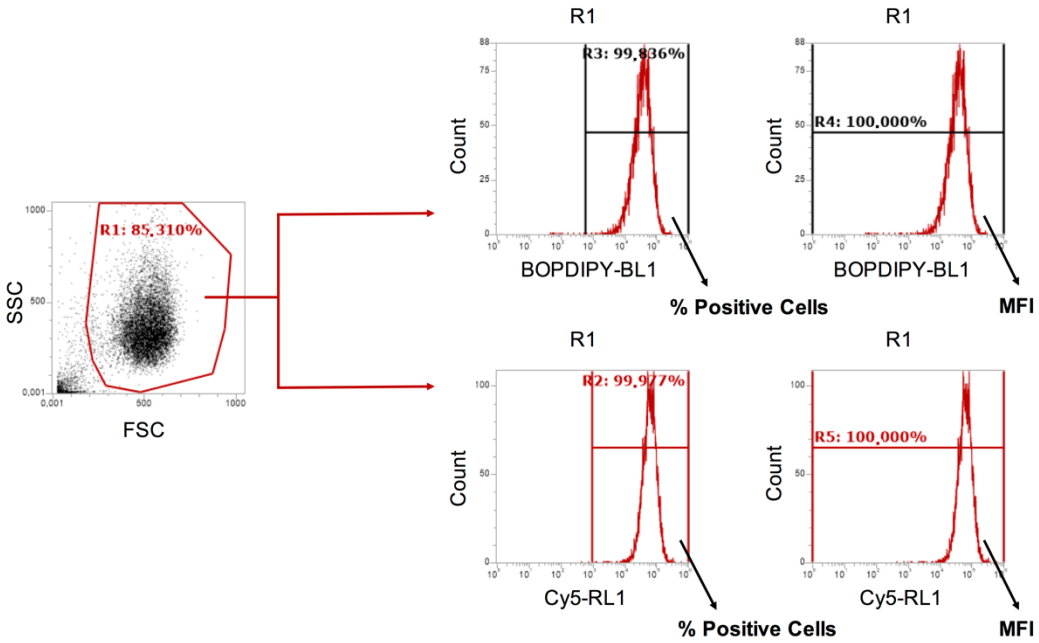

Figure S4.2: Gating strategy of the flow cytometry experiments. RAW264.7 cells were analyzed by forward scatter and sideward scatter to identify the cell population of interest and exclude cell debris. The cell population of interest was gated (R1). The events of the gate R1 were analyzed for their fluorescence of BODIPY of the PS NPs with the channel BL-1 (excitation: 488 nm, band-pass filter: 530/30 nm) and of Cy5 of the labeled protein corona with the channel RL-1 (excitation: 638 nm, band-pass filter: 670/14 nm). The percentage of BODPIY- and Cy5-positive cell populations were identified with a histogram by comparison with a cell-only control. The MFI was measured for all events of R1.

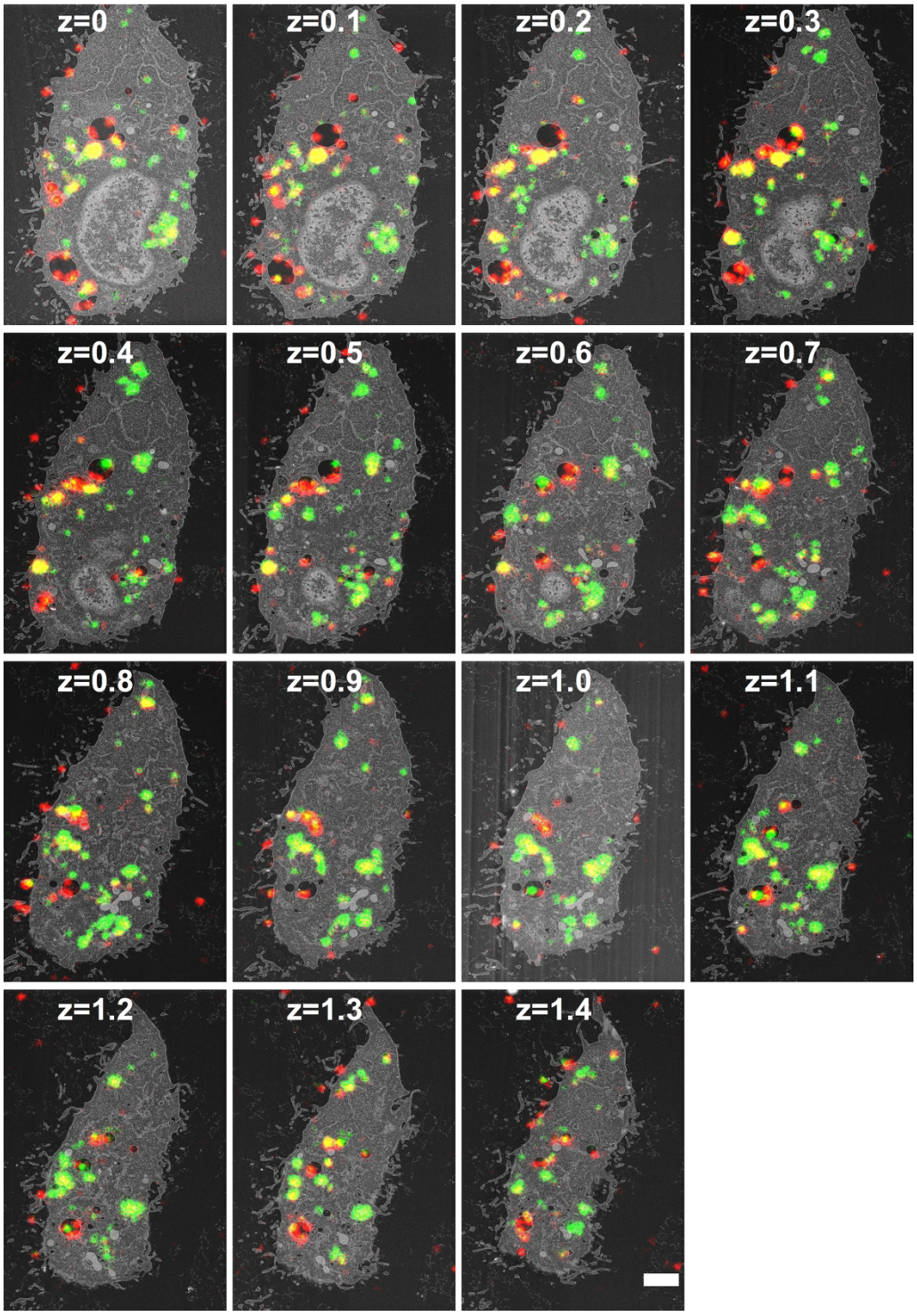

Figure S4.3: Volume CLEM of a RAW macrophage with internalized PS NPs with Cy5-labeled protein corona. PS NPs with Cy5-labeled protein corona were incubated with RAW264.7 cells and imaged in CLEM after 2 h + 24 h. z represents the relative depth of each section in µm. Red represents the Cy5-labeled protein corona, green represents BODIPY-labeled PS NPs, yellow represents the overlay of the protein corona and PS NPs. Scale bars: 2 µm.

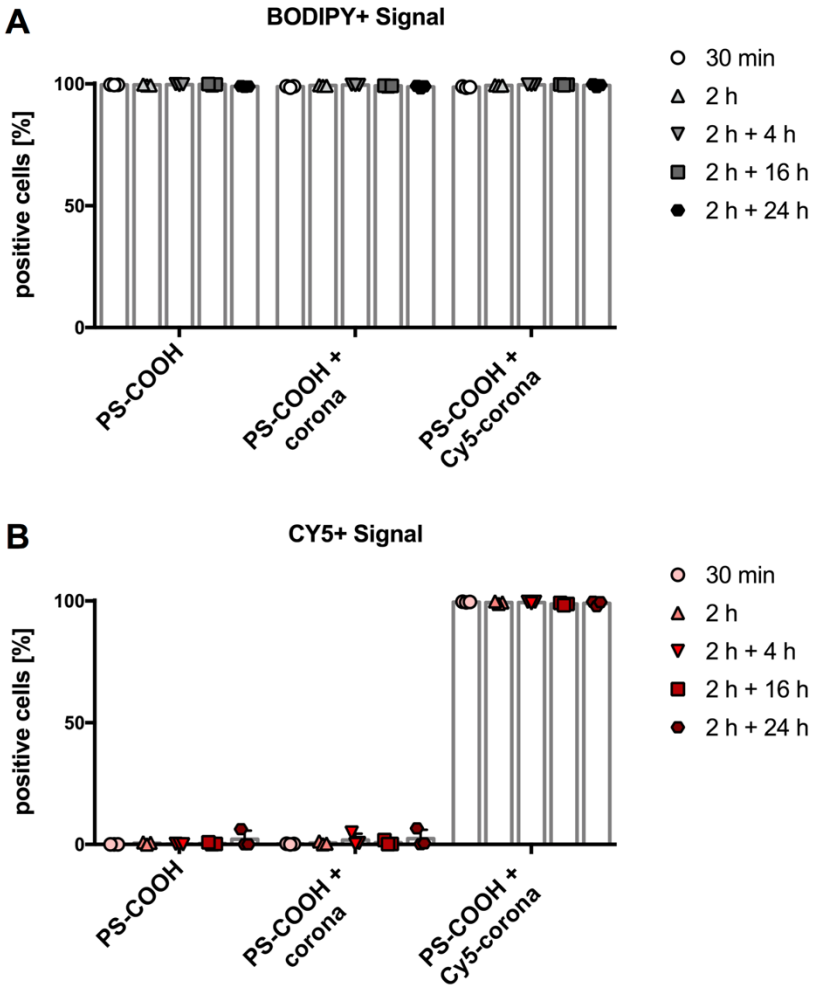

Figure S4.4: Murine macrophages show a very high uptake of differently treated NPs after various time points. RAW264.7 cells were incubated with 150 µg ml^{-1} of carboxyl-functionalized PS NPs. Untreated NPs, NPs with an unlabeled protein corona, and NPs with a Cy5-labeled protein corona were used for the uptake experiment. The cells were incubated with the NPs for 30 min or 2 h. Subsequently, the NP-containing supernatant was removed after 2 h and replaced with fresh culture medium without NPs. **(A)** Flow cytometry was performed to measure the percentual amount of BODIPY (PS NPs) fluorescent cells. Values are shown as the percentage of measured events in regards to the fluorescence. **(B)** Percentage of Cy5-positive cells (labeled protein corona) are shown (data are shown as mean ± SD, n = 3). The gating strategy for flow cytometry is provided in Figure S4.2.

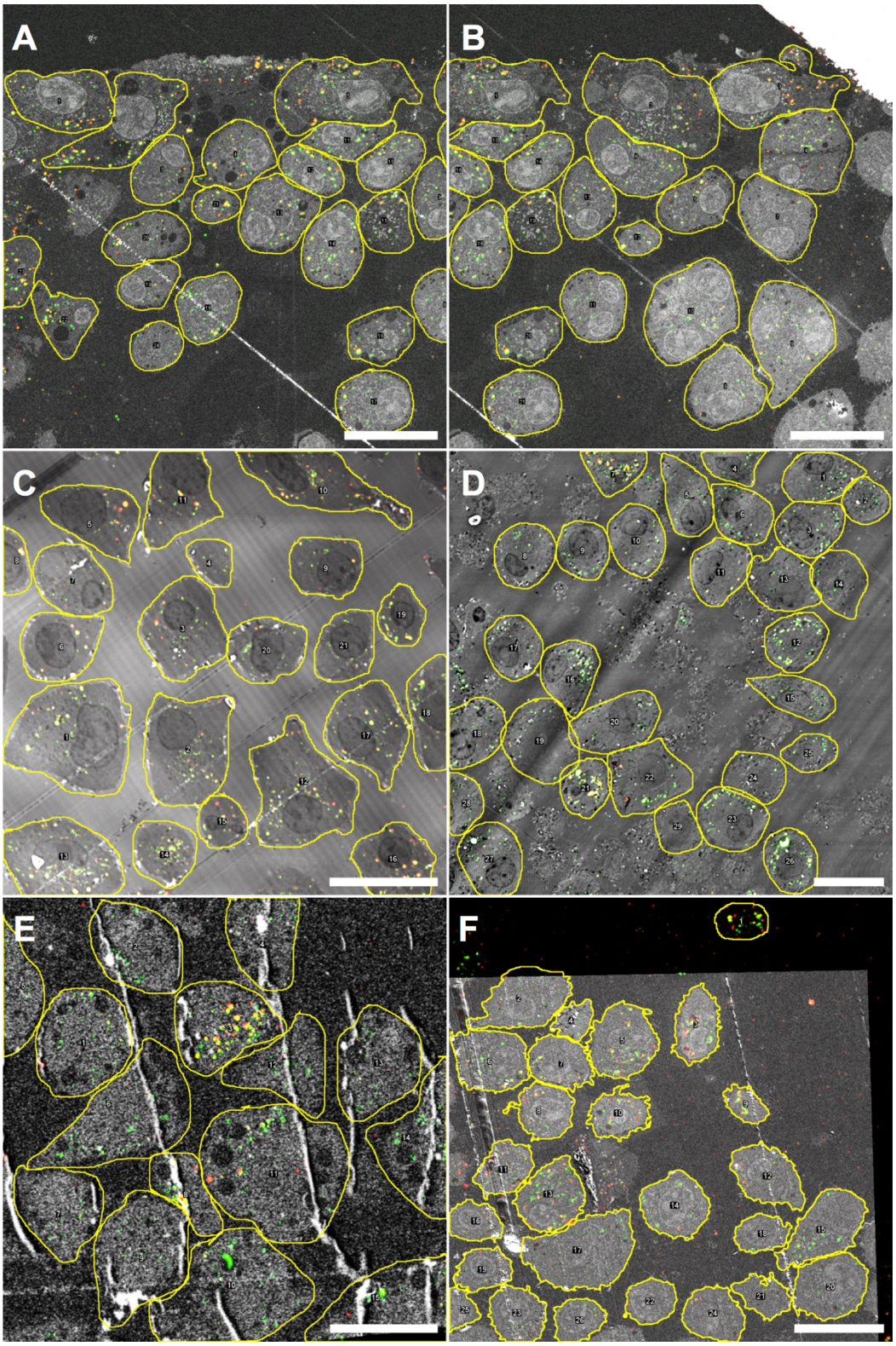

Figure S4.5: Exemplary images of cell selection in connectivity measurements. Identification of cells for a cell-based evaluation of the connectivity of BODIPY and Cy5 signals. **(A/B)** Cell selection at 30 min. **(C)** Cell selection at 2 h. **(D)** Cell selection at 2 h + 4 h. **(E)** Cell selection at 2 h + 16 h. **(F)** Cell selection at 2 h + 24 h. Scale bars: 20 µm.

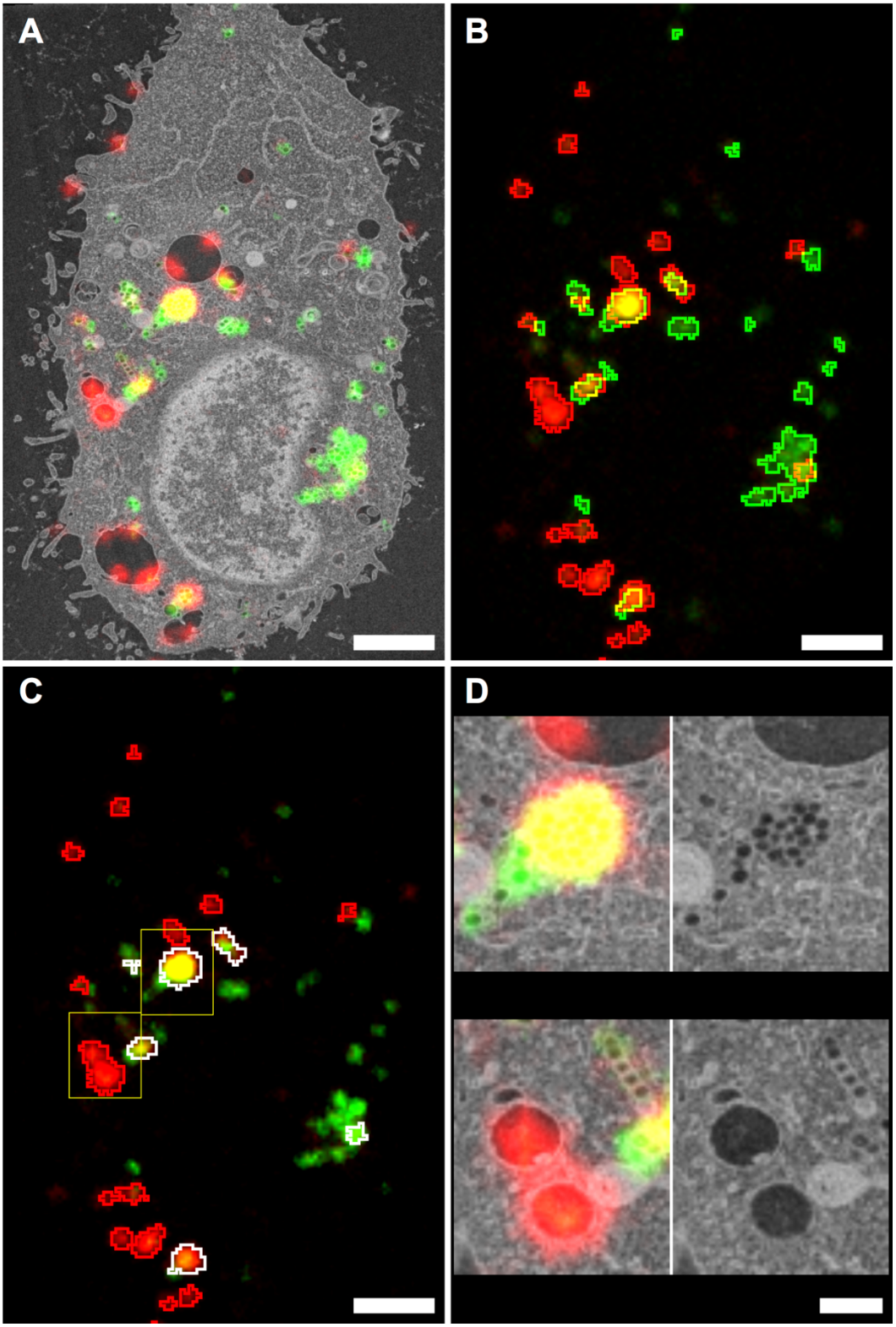

Figure S4.6: Workflow for connectivity measurements. (A) Cell to be evaluated. **(B)** Thresholding to identify protein and nanoparticle objects. **(C)** Classification as connected (white) and not connected (red) protein signal. **(D)** Insets of C, showing high-resolution EM images of incomplete (upper) and complete (lower) separation of protein corona from PS NPs Red represents the Cy5-labeled protein corona, green represents BODIPY-labeled PS NPs, yellow represents the overlay of the protein corona and PS NPs. Scale bars A-C: 2 µm. Scale bar D: 500 nm.

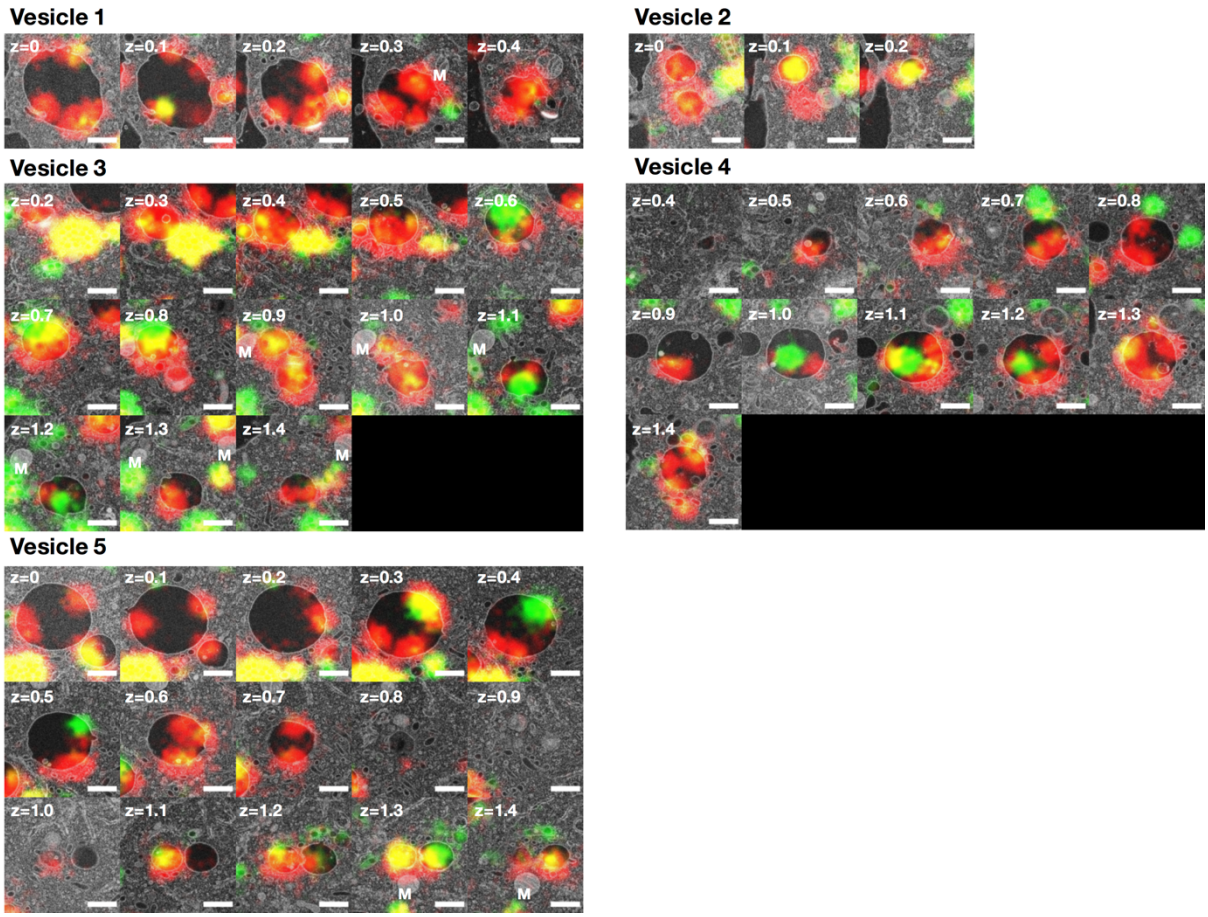

Figure S4.7: Multivesicular bodies (MVBs) containing Cy5-labeled protein corona signal. PS NPs with Cy5-labeled protein corona were incubated with RAW264.7 cells and imaged in CLEM after 2 h + 24 h. z represents the relative depth of the section. M represents mitochondria Red represents the Cy5-labeled protein corona, green represents BODIPY-labeled PS NPs, yellow represents the overlay of the protein corona and PS NPs. Scale bars: 500 nm.

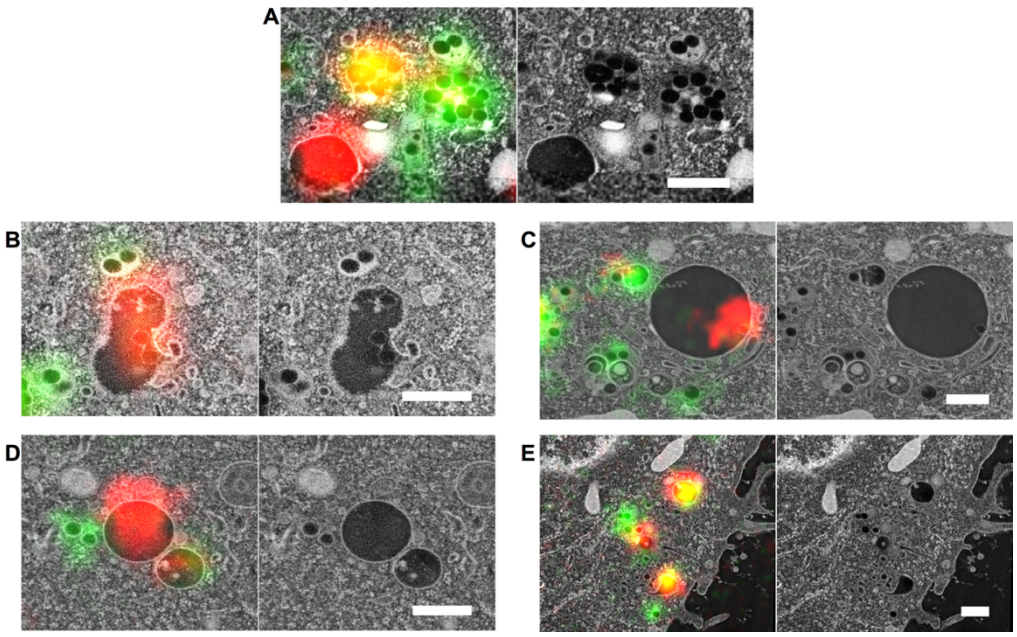

Figure S4.8: Events of separated PS NPs and protein corona in different cells. PS NPs with Cy5-labeled protein corona were incubated with RAW264.7 cells and imaged in CLEM after 2 h + 24 h. **(A-E)** Events within five different cells, showing the protein corona-coated PS NPs in crowded round-shaped endosomes, the separated protein corona in MVBs, and the separated PS NPs in tubular recycling endosomes (REs). Red represents the Cy5-labeled protein corona, green represents BODIPY-labeled PS NPs, yellow represents the overlay of the protein corona and PS NPs. Scale bars: 500 nm.

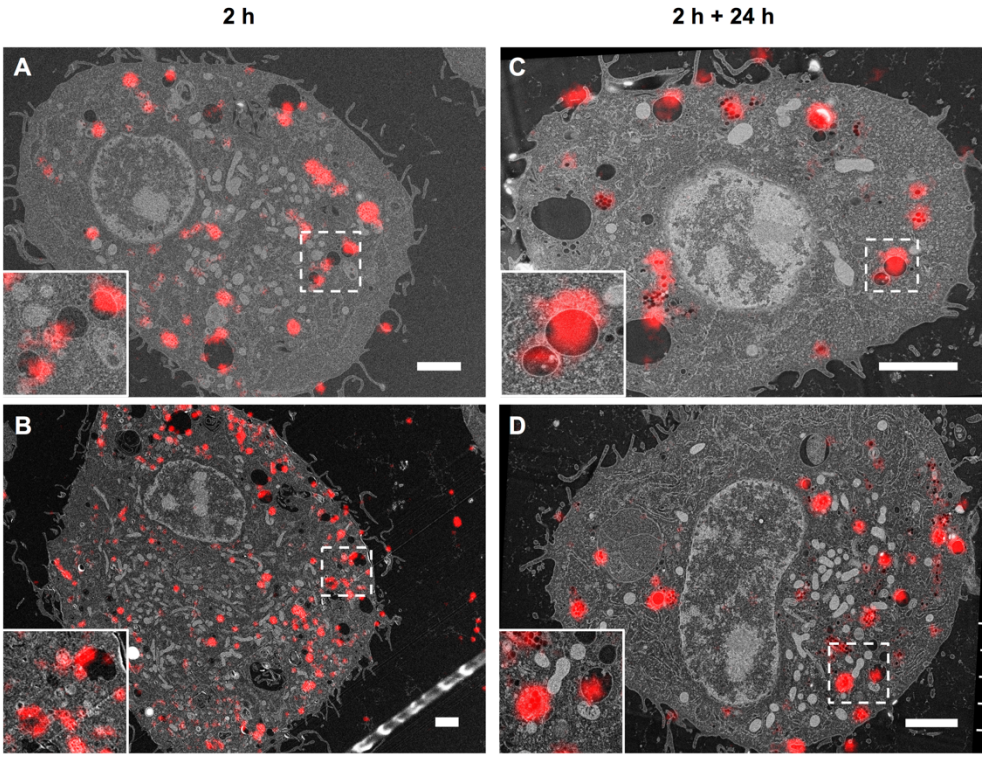

Figure S4.9: Cy5-labeled protein corona at two different time points. PS NPs with Cy5-labeled protein corona were incubated with RAW264.7 cells and imaged in CLEM. **(A/B)** Cy5-labeled protein

corona located in vesicles after 2 h. **(C/D)** Cy5-labeled protein corona located in vesicles after 2 h + 24 h. The sections in the dotted squares were enlarged to highlight the presence of the Cy5 signal within vesicles. Red represents the Cy5-labeled protein corona. The green signal is not included for a better overview of the red signal. Scale bars: 2 µm.

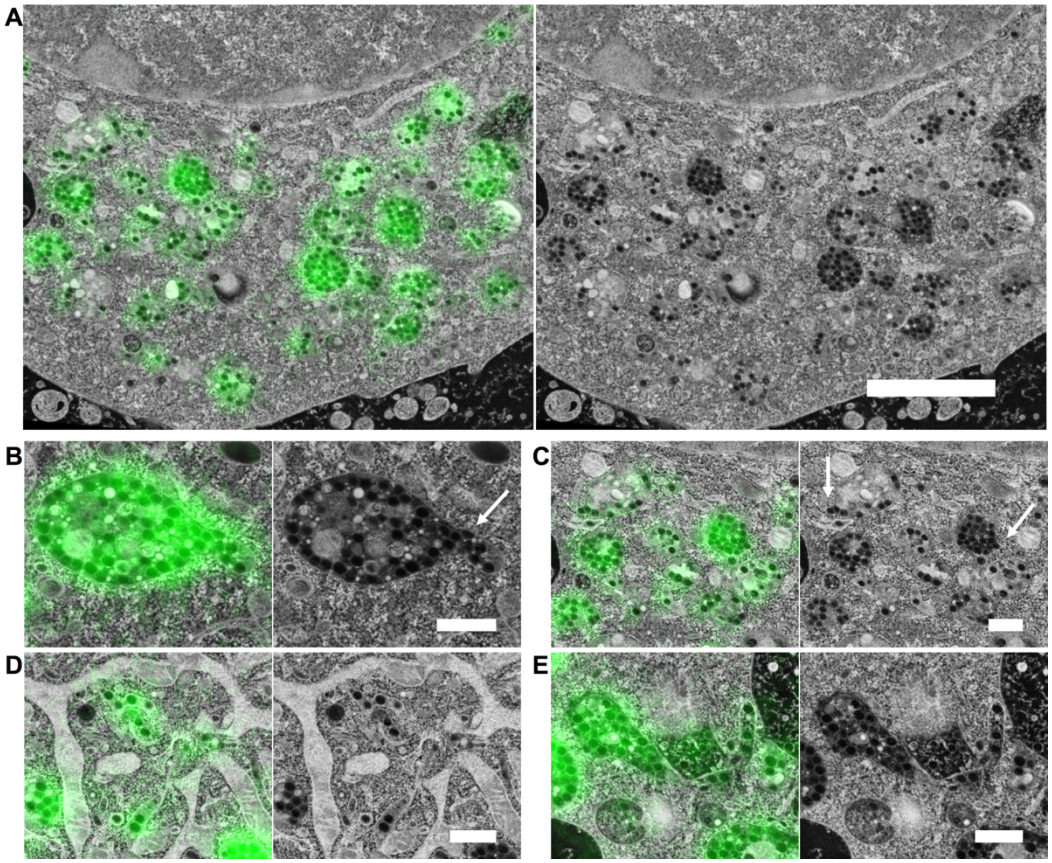

Figure S4.10: Control uptake experiment with PS NPs without protein corona. PS NPs without protein corona were incubated with RAW264.7 cells and imaged in CLEM after 2 h + 24 h. **(A)** PS NPs in endosomal vesicles. **(B/C)** Vesicles with PS NPs undergo budding and sorting. The white arrows indicate the budding within the vesicles. **(D/E)** PS NPs in tubular-shaped REs. Green represents BODIPY-labeled PS NPs. Scale bar A: 2 µm. Scale bars B-E: 500 nm.

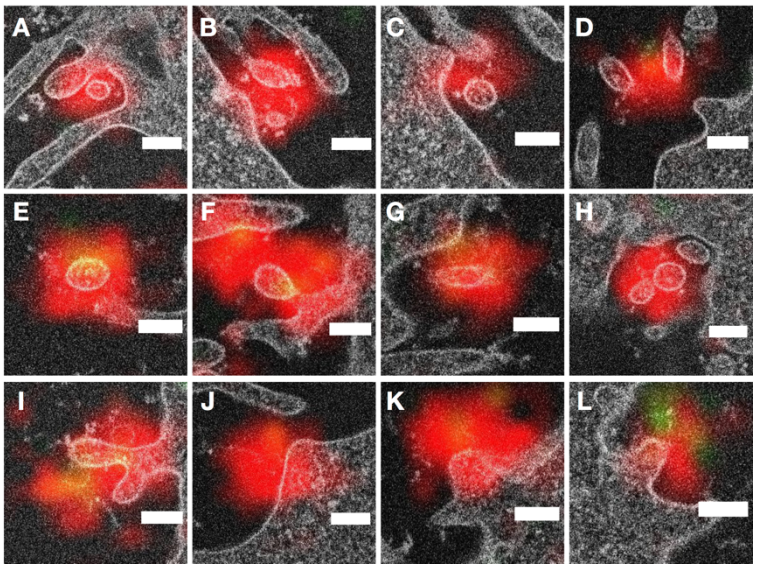

Figure S4.11: CLEM micrographs of extracellular Cy5-labeled protein corona close to the plasma membrane. PS NPs with Cy5-labeled protein corona were incubated with RAW264.7 cells and imaged in CLEM after 2 h + 24 h. **(A-H)** Cy5-labeled protein corona located within extracellular vesicles. **(I-L)** Cy5-labeled protein corona located next to the plasma membrane. Red represents the Cy5-labeled protein corona. Scale bars: 200 nm.

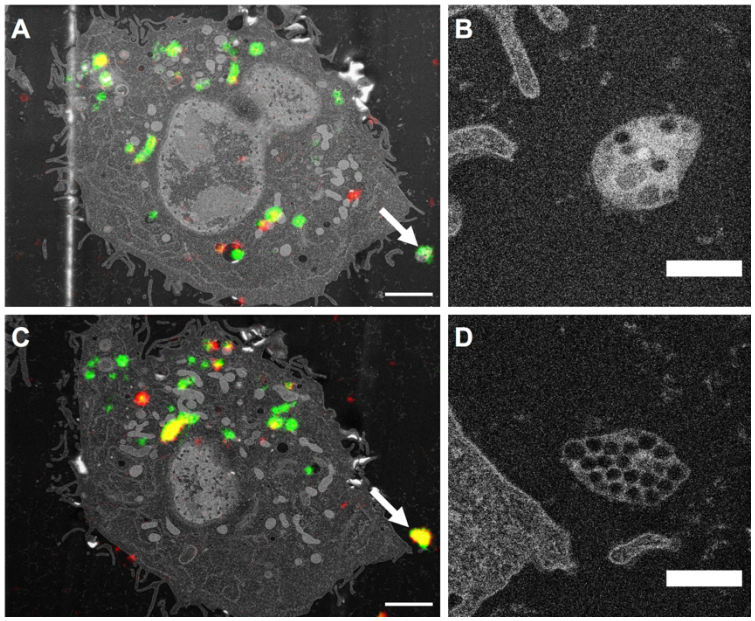

Figure S4.12: Exocytotic vesicles with PS NPs. PS NPs with Cy5-labeled protein corona were incubated with RAW264.7 cells and imaged in CLEM after 2 h + 24 h. **(A)** A RAW264.7 macrophage after 2 h + 24 h, arrow indicated the extracellular vesicle with PS NPs nanoparticles. **(B)** Zoom-in image of the vesicle in A. **(C)** A second macrophage, arrow indicated the extracellular vesicle with protein corona-covered PS NPs. **(D)** Zoom-in image of the vesicle in C. Red represents the Cy5-labeled protein corona, green represents BODIPY-labeled PS NPs, yellow represents the overlay of the protein corona and PS NPs. Scale bars: A and C: 2 µm, B and D: 500 nm.

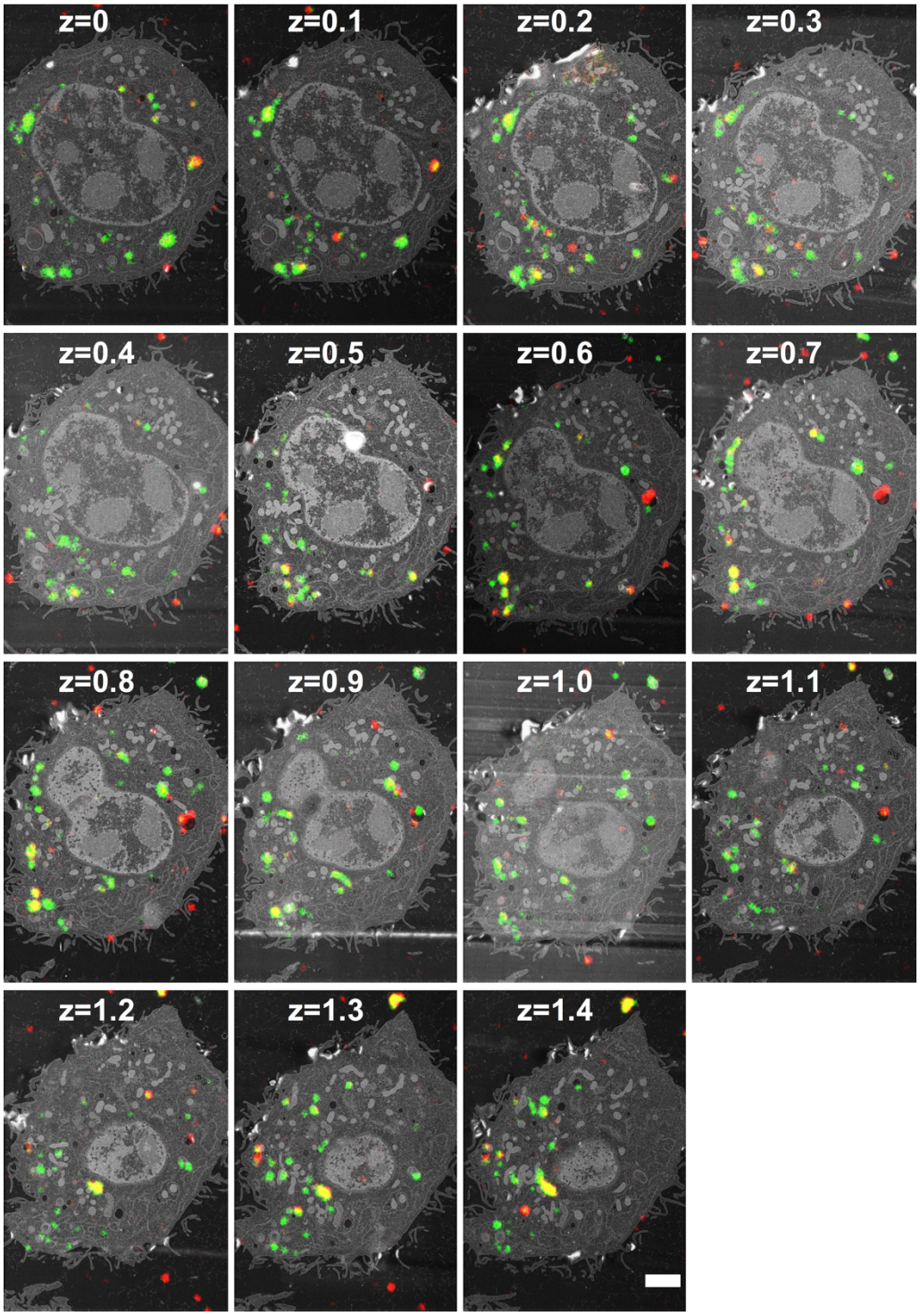

Figure S4.13: Volume CLEM of another cell. PS NPs with Cy5-labeled protein corona were incubated with RAW264.7 cells and imaged in CLEM after 2 h + 24 h. A second cell was inspected with volume CLEM. Figure S4.13A is from z=0.9, Figure S4.13C is from z=1.4. z represents the relative depth of the sections. Red represents the Cy5-labeled protein corona, green represents BODIPY-labeled PS NPs, yellow represents the overlay of the protein corona and PS NPs. Scale bars: 2 µm.

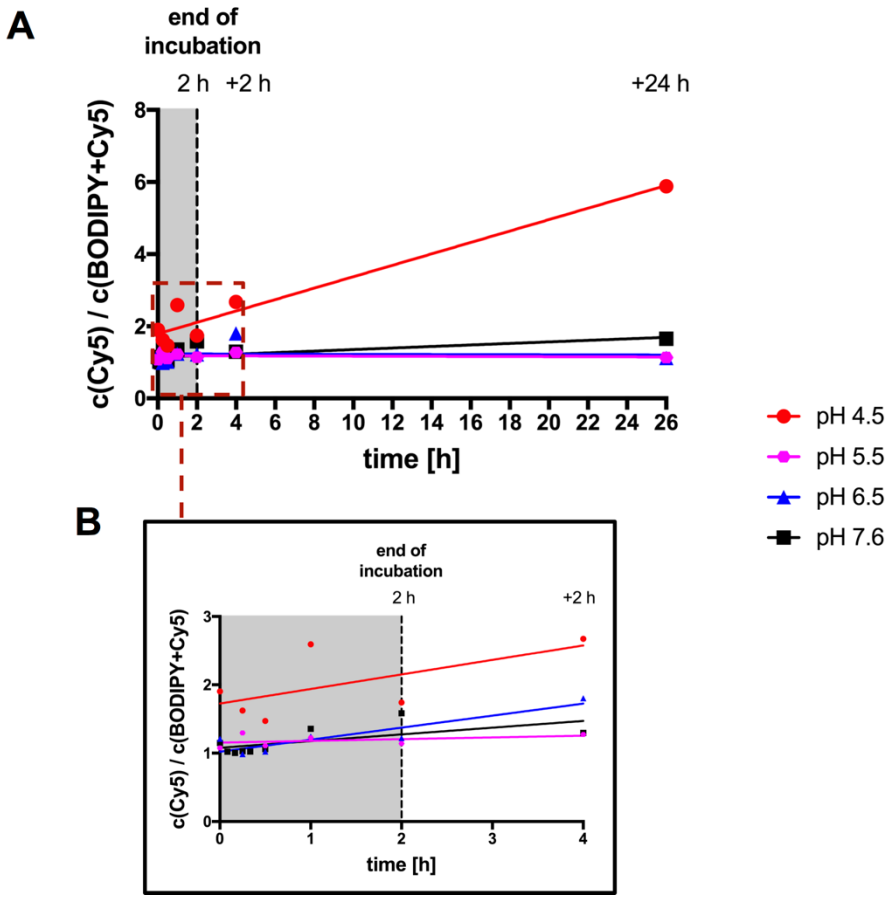

Figure S4.14: Acidification contributes to the separation of the protein corona from PS NPs. PS NPs (BODIPY labeled) with a murine plasma protein corona (Cy5 labeled) were resuspended in cell culture medium with different pH values. The signal correlation was measured by FCCS at various time points **(A)** Ratio of the concentrations of Cy5 labeled species (all plasma proteins) to the concentration of the double labeled species (PS NPs with protein corona) vs. incubation time in DMEM at the respective pH. An increase of this ratio indicates partial separation of the protein corona from the nanoparticles. **(B)** The data within the dotted square in A were enlarged to show the measurements in the time frame from 0 h to 4 h. Linear regression was fitted with the data to visualize the correlation progression over time

5. Proteomics-guided intracellular trafficking analysis reveals time-dependent protein corona changes and the intracellular pathway

Aim:

Despite the efforts of past protein corona research, the composition of the protein corona that forms in an intracellular environment remains poorly studied. This study analyzed the endocytosis pathways and the intracellular trafficking of two biocompatible nanocarrier systems. Label-free quantitative LC-MS proteomics was included to unravel the intracellular protein corona. Further, the composition of the protein corona was analyzed in a time-dependent manner to generate information on the intracellular protein corona evolution and annotated to intracellular compartments to reveal a molecular view of the intracellular trafficking of the nanocarriers.

Copyright:

Subchapter 5 contains a verbatim reproduction with slight adaptions of study **[3]**, which was submitted to a peer-reviewed journal.

[3] **da Costa Marques, R.**, ___, ___, ___, ___, ___. Proteomics-guided intracellular trafficking analysis reveals time-dependent protein corona changes and the intracellular pathway. *Nanoscale Horizons*. (submitted)

Contributions:

I characterized the magnetic hydroxyethyl starch nanoparticles. I performed the cell culture methods and the cell uptake experiments for flow cytometry, TEM, and cLSM. I performed flow cytometry and cLSM. I prepared the intracellular protein corona, quantified the protein samples, and performed SDS-PAGE. I prepared the samples for LC-MS, performed the measurements, and evaluated the LC-MS data. ___ synthesized and characterized the magnetic human serum albumin nanocapsules. ___ performed the ICP-OES measurements, edited the cLSM images, and created Figures 5.4, S5.2, and S5.6-5.9. I wrote the manuscript and created all other figures. I edited the figures. ___ performed TEM for nanocarrier characterization and cellular studies for uptake and intracellular trafficking. The project was supervised by ___, ___, and ___.

5.1 Abstract

The intracellular protein corona remains poorly investigated within the field of nanotechnology-biology (nano-bio) interactions. To deeply understand the intracellular protein corona formation and dynamics, we established a workflow to isolate the intracellular protein corona of different nanoparticles - magnetic hydroxyethyl starch nanoparticles (HES-NPs) and magnetic human serum albumin nanocapsules (HSA-NCs) - and after different uptake time points. This intracellular protein corona defines the direct molecular contact partners of the nanocarrier and is, therefore, a prime target for further drug development We performed label-free quantitative LC-MS proteomics to analyze the composition of this intracellular protein corona and correlated our findings to conventional methods for intracellular trafficking of nanocarriers, such as flow cytometry, transmission electron microscopy (TEM), and confocal microscopy (cLSM). In sum, we demonstrated the evolution of intracellular protein corona. The protein corona differed within the different timepoints for the HES-NPs with a slow uptake but less for the HSA-NCs with a rapid uptake. Furthermore, we selectively identified proteins of interest for intracellular trafficking. These proteins served as an effective “fingerprint” and allowed for a more detailed intracellular pathway reconstruction than the conventional methods. Thus, the analysis of the intracellular protein corona will provide a powerful resource in investigating the intracellular trafficking of nanocarriers for efficient drug delivery or intracellular applications.

5.2 Introduction

The nanotechnology-biology (nano-bio) interactions determine nanocarriers' properties, destination, and effect, and therefore remain a key factor in efficient nanomedicine [1, 51]. Nanomedicine creates smart nanoscale materials to improve diagnosis and therapy [5]. Selected nanomedicines, beyond liposomal Doxil® (Janssen), have successfully translated into the clinical field with examples like Abraxane® (Celgene) and the COVID-19 (mRNA-1273) vaccine (Pfizer/BioNTech) [6]. Notably, these materials achieved the desired cargo delivery and crucially enable or change the delivery of the active pharmaceutical ingredient. This highlights the so far underrated importance of effective and directed intracellular release of active pharmaceutical ingredients. However, achieving this time- and spatial-controlled cargo release still remains a challenging but highly desirable goal [124, 205]. To reach this goal, we must precisely investigate the intracellular nano-bio interactions [124, 205].

On a sub-organism level, the nano-bio interactions occur predominantly between tissues, cells, nanocarriers, and biomolecules. Whereas on a sub-cellular level these interactions are mainly based on nanocarriers and biomolecules [124]. Upon the contact of a nanocarrier with a biomolecule-containing fluid, the biomolecules adsorb spontaneously to the nanocarrier's surface and lower the surface free energy [1]. Ultimately, the formation of this biomolecular corona influences the nanocarriers' properties, their cellular interaction, pharmacokinetics, tissue penetration, biodistribution, and the release of active pharmaceutical ingredients [205]. The biomolecular corona, also described as protein corona when investigating adsorbed proteins, forms in both extracellular protein-containing fluids and within the cell [1, 124]. While the protein corona has been studied extensively in several body fluids [1, 15-16], the impact of the intracellular environment on the formation or change of the protein corona remains a novelty.

Research started to focus on the formation of the protein corona within cells. Indeed, our group isolated intracellular vesicles containing nanocarriers to investigate the vesicular protein milieu to elucidate intracellular trafficking [183]. Other studies specifically elucidated the composition of the intracellular protein corona as a "fingerprint" to explain intracellular trafficking. Among these works, magnetic silica nanoparticles were analyzed in A549 cells or gold nanoparticles in Caco2 cells or HepG2 cells [203, 206-207]. These works utilized different strategies to isolate and identify the proteins of interest within this fingerprint. Moreover, these works emphasized the value of proteomic investigation for the intracellular trafficking of nanocarriers. However, the number of studies is limited and the strategies to isolate the protein corona from intracellular nanocarriers remain pioneering work within the field of nano-bio interactions.

To understand the evolution and informational value of the intracellular protein corona, we conducted an investigative intracellular workflow. This workflow was performed on magnetic

hydroxyethyl starch nanoparticles (HES-NPs) and magnetic human serum albumin nanocapsules (HSA-NCs). We chose these two as they are promising materials for future nanocarrier design toward a targeted and site-specific cargo release [47-50, 208]. The uptake and trafficking were investigated in DC2.4 cells, a murine dendritic cell line. Dendritic cells are antigen-presenting cells and a promising cell type for targeting in immunotherapeutic research due to their central role in adaptive and innate immunity [209]. Moreover, dendritic cells can process and present antigens through different uptake and intracellular pathways [209].

First, we used established methods, such as flow cytometry, transmission electron microscopy (TEM), and confocal microscopy (cLSM) to characterize uptake and intracellular trafficking. Furthermore, we established a protocol to isolate the nanocarriers after the cellular uptake. We conducted label-free quantitative LC-MS proteomics to reveal the composition of the intracellularly-formed protein corona. We compared this protein composition at several time points to study the intracellular evolution of the protein corona between the nanocarrier systems. To put the proteomic data in the context of intracellular trafficking, we performed protein annotation and identified intracellular proteins of interest. Here, we reconstructed intracellular pathways to detail the intracellular trafficking of the nanocarriers.

5.3 Materials and methods

Magnetic hydroxyethyl starch nanoparticles. The magnetic hydroxyethyl starch nanoparticles (HES-NPs) were purchased from micromod Partikeltechnologie (Germany) as BNF-Starch-redF. According to the manufacturer, the core-shell nanoparticles consist of a 75-80% (w/w) magnetic iron oxide core with a shell of crosslinked hydroxyethyl starch. The synthesis of similar core-shell HES-NPs was described in the literature [48, 208]. The HES-NPs were obtained with an amino-functionalization and red-fluorescent labeling (redF, excitation: 552 nm, emission: 580 nm).

Magnetic human serum albumin nanocapsules.

Synthesis of iron oxide nanoparticles. The synthesis of oleic acid-coated iron oxide nanoparticles (Fe_3O_4 NPs) by co-precipitation was adapted with modifications from a previous work of our group [210]. First, Iron(III) chloride hexahydrate (24.36 g, 90 mmol, Acros, Germany) and Iron(II) chloride tetrahydrate (12.01 g, 60 mmol, Merck, Germany) were dissolved in 100 ml demineralized water. An aqueous ammonia solution (40 ml, 28 wt%) was added dropwise under stirring. Next, oleic acid (4.00 g, 14 mmol, Sigma-Aldrich, Germany) was added, followed by mechanical stirring at 70 °C for 1 h and then at 110 °C for 2 h. The iron oxide NPs were rinsed several times with demineralized water and dried in an oven at 65 °C. Next, the iron oxide NPs were dispersed in 10 wt% tetramethylammonium hydroxide solution (TMAOH, Sigma-Aldrich, Germany) in an ultrasonication bath (Bandelin Sonorex, Germany) for 1 h, followed by a centrifugation at 1400 rpm for 1 h. The supernatant was removed, and the pellet was redispersed in 0.1 wt% TMAOH solution. CMPVA (100 mg, in-house synthesized) was dissolved in 50 ml hot, demineralized water and added dropwise to the dispersion of iron oxide NPs, followed by vigorous stirring overnight. The dispersion was centrifuged at 1400 rpm for 1 h and washed with demineralized water. This washing step was repeated three times to obtain CMPVA-coated iron oxide nanoparticles for encapsulation. **Synthesis of human serum albumin nanocapsules (HSA-NCs) and encapsulation of iron oxide nanoparticles.** The performed synthesis is based on a previously published work of our group and was modified as described [47]. Human serum albumin (50 mg, Sigma-Aldrich, Germany) was dissolved in 0.2 ml of demineralized water. Iron oxide nanoparticles (200 µl) were added for magnetic properties and 100 µl of Cy5-Oligo (0.1 nmol μl^{-1}, excitation: 649 nm, emission: 670 nm IBA Lifesciences GmbH, Germany) or an in-house synthesized Cy5-PEG5K conjugate were added for fluorescent labeling. To this aqueous solution, we added an organic solution consisting of the surfactant poly((ethylene/butylene)-block-(ethylene oxide)) (P((E/B)-b-EO)) (35.7 mg, in-house synthetized), dissolved in cyclohexane (7.5 g, HPLC Grade, VWR,

Germany). The two phases were homogenized by ultrasonication (70% amplitude, 3 min, 20 s pulse, 10 s pause) under constant cooling. P((E/B)-b-EO) (10.7 mg) and the crosslinker toluene diisocyanate (TDI, 10 mg, TCI chemicals, Germany) were dissolved in 5 g of cyclohexane, and the resulting organic solution was added dropwise to the above-mentioned miniemulsion. The polyaddition reaction was performed at 25 °C for 24 h. Next, we centrifuged the formed nanocapsules at 1 500*g* for 30 min at 20 °C, removed the supernatant, and redispersed the nanocapsules in cyclohexane. This washing step was performed three times to remove the excess surfactant and TDI. To transfer the nanocapsules into an aqueous solution, we added 500 µl of the concentrated, organic nanocarrier dispersion dropwise to 5 ml 0.1 wt% SDS solution under constant shaking in an ultrasonication bath. The process was performed for 3 min, followed by regular stirring in an open reaction vessel to evaporate the organic solvent overnight. The resulting emulsion was centrifuged at 500*g* for 30 min at 20 °C with Amicon Ultra-2 centrifugal filters (MWCO 50 kDa, Merck, Germany), and the supernatant was removed. The pellet was redispersed in demineralized water. The washing was repeated three times to obtain the HSA-NCs. The HSA-NCs were sonicated for 5 min in an ultrasonication bath before each experiment.

Nanocarrier Characterization. The HES-NPs and HSA-NCs were characterized for the average diameter and polydispersity index (PDI) via dynamic light scattering (DLS). A 1:100 dilution of the HES-NPs in PBS (Sigma-Aldrich, Germany) and a 1:4 dilution of the HES-NPs in demineralized water were measured at 20 °C with the detector at a 90 degrees angle on a Malvern Zetasizer nano-s90 (Malvern Instruments, Germany). The measurements were performed in triplicates. The zeta potential was measured by diluting HES-NPs 1:100 and HSA-NCs 1:4 with a 1 mM potassium chloride solution at 20 °C. The measurements were performed in triplicates on a Malvern Zetasizer nano-s90. The morphology of the nanocarriers was visualized by transmission electron microscopy (TEM). One drop of undiluted nanocarrier suspension was added on a carbon-coated copper grid and then blotted with filter paper. The visualization of the samples was performed on a JEOL JEM1400 transmission electron microscope (JEOL, Japan), equipped with a 120 kV tungsten emitter. The iron concentration was analyzed by inductively coupled plasma-optical emission spectrometry (ICP-OES, SPECTROGREEN, SPECTRO/AMETEK, Germany). The calibration curve was prepared by using 0.1, 0.5, 1, 5, and 20 ppm iron standard solutions (stock 1 000 mg l^{-1} Fe, Certipur®, Merck) in 10% hydrochloric acid (37%, Merck, Germany).

DC2.4 cell culture. The murine dendritic cell line DC2.4 (Merck) was kept for cultivation in Iscove's Modified Dulbecco's Medium (IMDM, Sigma-Aldrich, Germany) that was

supplemented with 5% fetal bovine serum (FBS), 100 U ml^{-1} penicillin, 100 mg ml^{-1} streptomycin, 2 mM glutamine, and 550 nM 2-Mercaptoethanol (all Gibco/Thermo Fisher, Germany). For harvesting, cells were rinsed once with PBS and then detached by adding 2 mM EDTA (AppliChem, Germany) in PBS and incubated at 4 °C for 10 min. Next, the cells were collected in a tube with the same volume of culture medium and sedimented by centrifugation at 300*g* for 5 min. Afterward, the supernatant was removed, and the cells were either used for experiments or subcultured. For the subculture, the cell pellet was resuspended in culture medium. Of this suspension, 20 µl were mixed with the same volume of Trypan Blue (Sigma-Aldrich, Germany). The cell viability and cell number were measured with an automated cell counter (TC10, Bio-Rad, Germany), and the cells were diluted appropriately and added into a fresh cell culture flask (Greiner Bio-One, Austria). The cells were utilized below a passage number of 20 and, if not in active use, kept in an incubator (CO_2 Incubator C200, Labotect, Germany) at 37 °C, 5% CO_2, and 95% relative humidity.

Uptake inhibitors. All small molecule inhibitors were obtained from Merck, Germany. Dansylcadaverine, dynamin inhibitor I (dynasore), 5-(N-Ethyl-N-isopropyl)amiloride (EIPA), genistein, and nocodazole were solved in DMSO (Hybri-Max™/BioReagent, Merck Germany) to obtain stocks with a 100-fold concentration for cell experiments. chlorpromazine, cytochalasin D, filipin III, LY294002, and p21-activated kinase inhibitor III (IPA 3) were solved in DMSO to create stock solutions with a 1 000 fold concentration. Wortmannin was solved in DMSO to create a stock solution with a 200 000 fold concentration. Methyl-β-cyclodextrin was solved in sterile, demineralized water to create a stock solution with a 1 000 fold concentration.

Flow cytometry for cell uptake and uptake inhibition. The harvested DC2.4 cells were seeded in 24 well plates (Greiner Bio-One, Austria) with a cell number of 150 000 cells per well and incubated at 37 °C and 5% CO_2 overnight for adherence. The next day, the culture medium was removed and the cells carefully rinsed once with PBS. The nanocarrier suspension was added with a concentration of 250 µg ml^{-1}, and the uptake was monitored at different time points within 24 h to reconstruct the uptake kinetic. Additionally, the nanocarrier suspension was removed after 2 h, and the uptake was monitored at various time points within 24 h. For uptake inhibition experiments, cells were pretreated with different uptake inhibitors and a DMSO control (1%) and incubated at 37 °C and 5% CO_2 for 30 min. The supernatant was then removed, and the cell were rinsed once with PBS before adding the nanocarrier suspension with a concentration of 250 µg ml^{-1} to analyze the uptake after 4 h. To analyze the uptake of nanocarriers with flow cytometry, the cells were harvested as stated above and collected in 1.5 ml tubes. After centrifugation at 300*g* for 5 min, the supernatant was removed

and the cells resuspended in 1 ml of PBS per sample including LIVE/DEAD™ Fixable Green Dead Cell Stain (Invitrogen/Thermo Fisher, Germany). This viability stain was prepared according to the manufacturer's instructions. The flow cytometry measurements were carried out with an Attune NxT (Thermo Fisher, Germany). The LIVE/DEAD™ Fixable Green Dead Cell Stain was excited with the 488 nm laser and detected with the BL1 channel, employing a 530/30 nm band-pass filter. The red fluorescent dye of the HES-NPs was excited with the 561 nm laser and detected with the YL1 channel, using a 585/16 nm band-pass filter. Cy5 of the HSA-NCs was excited with the 638 nm excitation laser and detected with the RL1 channel, with a 670/14 nm band-pass filter. For the flow cytometry analysis, the cells were discriminated from debris and artifacts by employing the forward and sideward scatter. Next, this cellular population was evaluated by its fluorescent properties, outputting the percentual value of gated fluorescent events and as the median fluorescent intensity (MFI). The device operation and data evaluation was performed with Attune NxT Software (Thermo Fisher, U.S.A).

TEM for uptake and intracellular trafficking visualization. A 24 well plate was loaded with 3 mm plasma-sterilized sapphire discs (M. Wohlwend GmbH, Switzerland) covered with a 20 nm carbon layer. After harvesting, 150 000 DC2.4 cells were seeded per well on the sapphire discs and incubated at 37 °C and 5% CO_2 overnight for attachment. The next day, the culture medium was removed, the cells carefully rinsed once with PBS, and the nanocarrier suspension was added with a concentration of 250 µg ml^{-1}, diluted with culture medium. After the respective incubation times (30 min, 2 h, 24 h, and 2 h + 24 h), cells were prepared for TEM imaging. The sapphire discs containing the cells were collected and immersed in 1-hexadecene before placing them between two aluminum plates of 3 mm. This assembly was subjected to high pressure freezing by a Wohlwend HPF Compact 01 high pressure freezer (M. Wohlwend GmbH, Switzerland) with a pressure of 2100 bar. The sample was immersed in liquid nitrogen for storage at this point. The sapphire discs were removed from the aluminum plates and placed in pre-cooled (-87 °C) freeze substitution medium consisting of 0.2% (w/v) osmium tetroxide, 0.1% (w/v) uranyl acetate, 5% (v/v) demineralized water in acetone in a freeze substitution device (AFS2, Leica, Germany). The samples were slowly warmed up to room temperature within 20 h. The substitution medium was removed and the discs were washed 3 times with acetone before infiltrating the samples sequentially with a gradient of an epoxy resin-acetone mixture. Eventually, the samples were infiltrated with 100% epoxy resin overnight. The polymerization was carried out at 60 °C for at least 24 h. Ultrathin sections were created with an Ultramicrotome (Leica, Germany) and monitored with a JEOL JEM1400 transmission electron microscope, equipped with a 120 kV tungsten emitter. Fiji was utilized to edit the images and add the scale bars [211].

Confocal laser scanning microscopy. The harvested DC2.4 cells were seeded in µ-Slide 8 well ibidi slides (ibiTreat, ibidi GmbH, Germany) with a cell number of 50 000 cells per well. The cells were incubated at 37 °C and 5% CO_2 overnight for attachment. The next day, the culture medium was removed and the cells rinsed once with PBS. The nanocarrier suspension was added with a concentration of 250 µg ml^{-1} and incubated at 37 °C and 5% CO_2. After 2 h or 24 h of incubation, the nanocarrier containing supernatant was removed and the cells rinsed once with PBS. To stain the low pH intracellular compartments, including lysosomes, LysoTracker™ Green (Thermo Fisher, Germany) was diluted 1:20 000 in culture medium (final concentration 75 mM) and added to the cells. After incubation at 37 °C and 5% CO_2 for 5 min, the supernatant was removed, the cells were washed once with PBS, and culture medium was added to the cells. For the plasma membrane staining, the cells were fixated with 4% formaldehyde (Carl Roth GmbH, Germany) for 15 min. The formaldehyde solution was removed and the cells were washed once with PBS. The plasma membranes were stained by adding a 1:1 000 dilution of Cell Mask (DeepRed for HES-NPs and Orange for HSA-NCs, both Thermo Fisher, Germany) in PBS to the cells. The cells were incubated in the dark for 5 min. The staining was removed, the cells were washed twice with PBS, and directly analyzed by microscopy. For the antibody staining, the cells were fixated and then permeabilized with 0.2% Triton X100 (Sigma-Aldrich, Germany) in PBS for 10 min, followed by a wash step with PBS and blocking with BSA at room temperature for 1 h. After the wash step, the primary antibodies for clathrin heavy chain (1:500, polyclonal GTX132976, GeneTex, U.S.A.), RAB5 (1:100, polyclonal PA5-29022, Thermo Fisher, Germany), RAB7 (1:100, polyclonal PA5-52369, Thermo Fisher, Germany), and LAMP1 (1:100 clone EPR21026, ab208943, abcam, U.K.) were added to the cells and incubated at 4 °C overnight. The antibody solution was removed and the cells were washed three times with PBS. Next, a secondary goat-anti-rabbit FITC (1:1 000, polyclonal F-2765, Thermo Fisher, Germany) antibody was applied at room temperature for 1 h. Finally, the supernatant was removed, the cells were rinsed once with PBS and kept in PBS for observation. Confocal laser scanning microscopy (cLSM) was performed with an LSM SP5 STED Leica Laser Scanning Confocal Microscope (Leica, Germany), composed of an inverse fluorescence microscope DMI 6000CS equipped with a multi-laser combination using an HCA PL APO CS2 63 x 1.2 water objective. FITC and LysoTracker™ Green were excited with the 488 nm laser and detected at 500 nm - 550 nm. CellMask Orange and the red fluorescent dye of the HES-NPs were excited at 561 nm and detected at 570-625 nm. CellMask Deep Red and Cy5 in the HSA-NCs were excited with the 633 nm laser and detected at 645-720 nm. Fiji was utilized to edit the images, add the scale bars, and create the montages [211].

Intracellular protein corona preparation. To obtain intracellular protein corona proteins on HES-NPs and HSA-NCs, DC2.4 cells were seeded in a cell number of 3 000 000 cells per well in a 6 well plate and incubated at 37 °C and 5% CO_2 overnight for attachment. The next day, the nanocarrier suspension was added with a concentration of 250 µg ml^{-1} and incubated at 37 °C and 5% CO_2 for different time points. Eventually, the cells were harvested as described above but using IMDM without FBS during the process. Also, to obtain enough intracellular nanocarriers, the cells of 3 wells were pooled for one sample. The supernatant was removed after the centrifugation, and the cells were resuspended in 4 °C-cold PBS with Halt™ protease inhibitor (Thermo Fisher Scientific) and 5 mM EDTA. The cells were lysed by sonification, employing a Q800R3 sonicator (QSonica) and performing the sonication with an amplitude of 70% at 4 °C for 7 min with pulse cycles of 30 sec. The lysis of the cells was confirmed by observation through a CKX41 inverted microscope (Olympus). The nanocarriers were isolated by magnetic separation for 10 min, and the supernatant was discarded. Next, the magnetic nanocarrier pellet was resuspended in 1 ml of 4 °C-cold PBS with Halt™ protease inhibitor and 5 mM EDTA. The HES-NPs were centrifuged at 20 000*g*, and the HSA-NCs were centrifuged at 10 000*g* at 4 °C for 5 min, respectively. Two more wash steps were applied before adding a desorption buffer to the nanocarriers. The desorption buffer consisted of 2% (w/v) SDS and 62.5 mm Tris*HCl in demineralized water and was previously used in our group to desorb hard-corona proteins from different nanomaterial's surfaces [16, 62]. The desorption step was performed at 95 °C for 5 min. Finally, the nanocarriers were centrifuged once more, and the supernatant that contained the proteins was transferred to fresh tubes for protein analysis.

Protein quantification and SDS-PAGE. The protein concentration was measured by using Pierce™ 660 nm Protein Assay Reagent (Thermo Scientific, Germany) with added Ionic Detergent Compatibility Reagent (both Thermo Scientific, Germany) according to the manufacturer's instructions. The standard calibration curve was prepared with bovine serum albumin (Sigma-Aldrich, Germany). The adsorption was analyzed at 660 nm with an Infinite M1000 plate reader (Tecan, Switzerland). For SDS-PAGE, we diluted 2 µg of protein with demineralized water to a total volume of 26 µl. The samples were prepared with 4 µl of NuPAGE™ Sample Reducing Agent and 10 µl of NuPAGE™ LDS Sample Buffer (both Invitrogen/Thermo Fisher, Germany) and denaturized at 70 °C for 10 min. Protein electrophoresis was performed on a Bolt™ 10% Bis-Tris Plus gel using NuPAGE™ MES SDS Running Buffer (both Invitrogen/Thermo Fisher, Germany) at 200 V for 1 h. SeeBlue™ Plus2 Pre-Stained Standard (Invitrogen/Thermo Fisher, Germany) was loaded on the gel as a molecular weight ladder. Protein staining was performed with SilverQuest™ Silver Staining Kit (Invitrogen/Thermo Fisher, Germany), following the manufacturer's instructions. The developed gels were scanned with a View Pix 1100 scanning system (Biostep, Germany).

In-solution tryptic digestion. The protein samples were processed to peptides for LC-MS analysis by in-solution tryptic digestion as previously described [183]. First, SDS was removed from the protein corona samples by utilizing Pierce™ Detergent Removal Spin Columns (Thermo Scientific, Germany) according to the manufacturer's instructions. Next, 10 µg of proteins were precipitated with the ProteoExtract Protein Precipitation Kit (CalBioChem, Germany), following the instructions of the manufacturer. The protein pellet was eventually solubilized with 0,1% RapiGest SF surfactant (Waters Corporation, Germany), dissolved in 50 mM ammonium bicarbonate buffer at 80 °C for 15 min. Disulfide bonds were reduced with 5 mM dithiothreitol (Sigma-Aldrich, Germany) at 56 °C for 45 min. Thiols were alkalized with 15 mM iodoacetamide (Sigma-Aldrich, Germany) at room temperature in the dark for 1 h. The digestion was performed with trypsin (Promega, Germany) in a ratio of 50 : 1 of the mass of protein to trypsin at 37 °C between 16 h to 18 h. The digestion was stopped with the addition of 2 µl of hydrochloric acid and incubation at 37 °C for 45 min. Aggregation products were removed by centrifugation at 13 000*g* for 15 min at 4 °C and transferring the supernatant into fresh tubes.

Liquid chromatography coupled to mass spectrometry (LC-MS). The LC-MS method was adapted from previous works of our group with modifications [16, 62]. The samples were diluted with 0.1% formic acid (Sigma-Aldrich, Germany) in LC-MS grade water (Merck, Germany) and spiked with 50 fmol μl^{-1} HI3 E.coli Standard (Waters Corporation, Germany) to allow absolute quantification according to an established work from the literature [185]. Ultra-performance liquid chromatography (UPLC) was performed on a nanoACQUITY UPLC system, equipped with a C18 nanoACQUITY trap column (5 µm, 180 µm × 20 mm) and a C18 analytical reversed-phase column (1.7 µm, 75 µm × 150 mm; all Waters Corporation, Germany). The solvents for chromatography were (A) 0.1% (v/v) formic acid in water and (B) 0.1% (v/v) formic acid in acetonitrile (Biosolve, Germany). The separation was performed with a gradient of 5% to 40% of mobile phase B over 90 min. The sample flow rate was set to 0.3 µl min^{-1}, and the flow rate of the referent components Glu-Fibrinopeptide and Leu-Enkephalin (both Sigma-Aldrich, Germany) was set to 0.5 µl min^{-1}. The UPLC system was coupled to a Synapt G2Si mass spectrometer (Waters Corporation, Germany). Compound ionization was performed via electrospray ionization (ESI) with a NanoLockSpray source that was set to positive mode. The samples were measured in resolution mode with employed ion-mobility separation and data-independent acquisition (IMS-MS^E/$HDMS^E$). The measurements were carried out in technical replicates for a mass to charge range of 50–2 000 Da, a scan time of 1 s, a ramped trap collision energy from 20 V to 40 V, and the data acquisition of 120 min. The LC-MS was operated with MassLynx 4.1 (Waters Corporation).

Protein identification. The LC-MS proteomics analysis was executed with the software Progenesis QI 2.0 (Nonlinear Dynamics, U. K.), following a protocol from Schöttler et al. with modifications [78]. The noise reduction threshold for low energy, elevated energy, and peptide intensity was set to 120, 25, and 750 counts, respectively. A reviewed data bank (Swiss-Prot) of the murine proteome was downloaded from Uniprot (https://www.uniprot.org), and the protein sequence for the spike protein Hi3 E.coli standard was added to this list. The identification was performed with one missed cleavage, a maximum protein mass of 600 kDa, fixed carbamidomethyl modification for cysteine, variable oxidation for methionine, a minimum of one assigned fragment per peptide, a minimum of one assigned peptide per protein, a minimum of three assigned fragments per protein, and a score parameter below 4.

Protein enrichment, Venn diagrams and annotation. The enriched intracellular protein corona proteins were determined by calculating all 1.5-fold enriched proteins compared to the cell lysate proteins. The Venn diagrams were created with Venny 2.1 [212]. The enriched proteins were analyzed with the functional annotation tool collection DAVID (Version 6.8, https://david.ncifcrf.gov/home.jsp) [213-214]. Functional annotation clustering was performed under the database GOTERM_CC_FAT, using a medium classification stringency. The GOTERMs *cytosol*, *nucleosome*, *endoplasmic reticulum*, *organelle envelope*, *microtubule cytoskeleton*, *mitochondrion*, *plasma membrane region*, *side of membrane*, *Golgi apparatus*, *endosome*, *lysosome*, *secretory vesicles*, and *exocytotic vesicles* were selected for the annotation diagram in Figure 5.4. The proteins in the intracellular trafficking network in Figure 5.5 are based on the proteins of the of GOTERMs *plasma membrane region*, *side of membrane*, *Golgi apparatus*, *endosome*, *lysosome, secretory vesicle*, and *exocytotic vesicle*.

Data Representation. Data visualization was created with GraphPad Prism 8 (GraphPad Software, USA). The presented data are shown as means ± standard deviation (SD) of the values.

5.4 Results and discussion

Differences in cellular uptake kinetics and mechanism

We chose to investigate magnetic hydroxyethyl starch nanoparticles (HES-NPs) and magnetic human serum albumin nanocapsules (HSA-NCs) due to their promising perspectives as biocompatible and biodegradable nanocarrier platforms for drug delivery [47-50, 208]. The core-shell HES-NPs displayed a diameter of 130.5 ± 0.20 nm and a slightly negative Zeta potential of -3.36 ± 0.49 mV (Fig. 5.1A). The HSA-NCs were distinctively larger at 370.5 ± 4.14 nm and more negatively charged at 23.7 ± 0.92 mV (Fig. 5.1B). Both nanocarrier systems were fluorescently labeled for flow cytometry measurements and confocal microscopy (cLSM) visualization. Additionally, the nanocarrier systems consisted of a magnetic iron oxide core (HES-NPs) or contained encapsulated magnetite iron oxide particles (HSA-NCs). Both nanocarrier systems did not affect the cell viability of the murine dendritic cell line DC2.4 in various tested concentrations (50, 125, 250, 500 µg ml^{-1}; Fig. S5.1A/B).

The cellular uptake in DC2.4 of both nanocarrier systems was analyzed by flow cytometry, measuring the median fluorescence intensity (MFI) at different time points. We performed a continuous uptake experiment and an experiment that included the removal of the nanocarrier suspension after 2 h of uptake and replacing it with fresh medium. Both nanocarrier systems demonstrated different uptake kinetics in both experimental settings over a timespan of 24 h. The HES-NPs showed a constant uptake and did not reach saturation after 24 h (Fig. 5.1C, Fig. S5.1C). We attribute this slow uptake rate of the HES-NPs to the stealth properties that were found for HES nanocarriers by previous studies [48, 208]. After removing the nanocarrier suspension, we observed a rapid decrease of the MFI so that for the 2 + 22 h condition it returned to a similar value as after 30 min. Conversely, the HSA-NCs reached uptake saturation after 6 h in the continuous uptake experiment (Fig. 5.1D, Fig. S5.1D). Upon removal of the HSA-NC suspension, the MFI remained stable for at least 2 h and started then to decrease to an MFI, similar to the 30 min value. We confirmed by cLSM and cell membrane staining that both nanocarrier systems were indeed incorporated into the cells. Furthermore, the trend from the flow cytometry measurements was visible for three selected time points (2 h, 24 h, and 2 + 22 h; Fig. S5.2A/B). Interestingly, the HSA-NC were weakly co-localized with the membrane at 2 h, followed by a stronger co-localization after 24 h (Fig. S5.2B). Eventually, at 2 + 22 h, the nanocarriers were not visible at the cell membrane but only within the cell. We did not observe a cell membrane co-localization with HES-NPs. We correlate the increased uptake rate of the HSA-NCs and the delayed signal decrease after nanocarrier retrieval to this contact of protein nanocapsules with the cell membrane. Indeed, albumin is naturally recognized by dendritic cell-expressed neonatal Fc-receptors (FcRn), which has been

exploited for nanoparticle targeting in the past [215-216]. Therefore, we assume a likely receptor-based recognition of the HSA-NCs in our experiment.

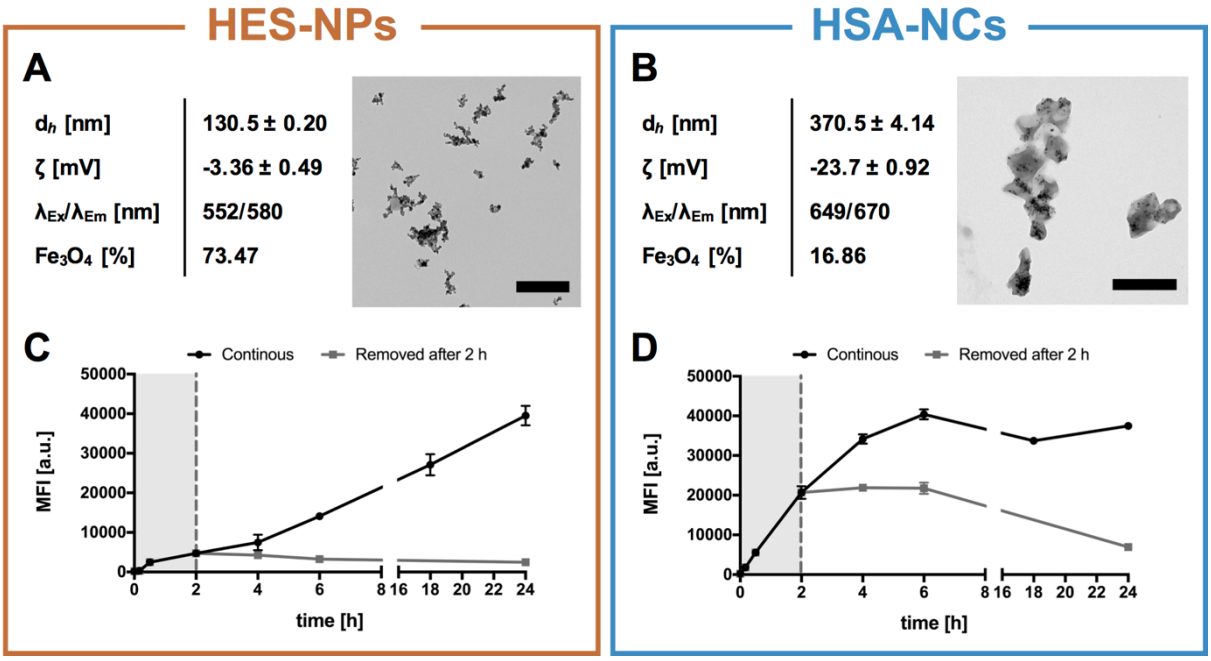

Figure 5.1: Nanocarrier characterization and uptake analysis in murine dendritic cells. HES-NPs **(A)** and HSA-NCs **(B)** were characterized for their physicochemical properties such as size, zeta-potential, fluorescence, and magnetite content (d_h and ζ is shown as mean ± SD, n = 3). The nanocarriers' morphology was visualized by TEM. The scale bars represent 500 nm. Murine dendritic cells DC2.4 were incubated with 250 µg ml^{-1} HES-NPs **(C)** and HSA-NCs **(D)** continuously and discontinuously for various time points. For a continuous incubation, the nanocarrier suspension was left on the cells for all incubation times (10 min, 30 min, 2 h, 4 h, 6 h, 18 h, and 24 h). Additionally, nanocarrier suspension was removed after 2 h and replaced with cell culture medium for the discontinuous incubation (2 h + 2 h, 2 h + 4 h, 2 h + 22 h). The cell uptake was analyzed by flow cytometry, measuring the median fluorescent intensity (MFI) of the events (data are shown as mean ± SD, n = 3).

Next, we pretreated DC2.4 with twelve different uptake inhibitors and analyzed the uptake of HES-NPs and HSA-NCs by flow cytometry. The uptake inhibitor treatment did not affect the cell viability (Fig. S5.3). In total, the uptake of the HES-NPs was reduced by five of the twelve uptake inhibitors: Dynasore, filipin III, wortmannin, 5-(N-Ethyl-N-isopropyl)amiloride (EIPA), and cytochalasin D (Fig. 5.2A). Dynasore inhibits the GTPase activity of dynamin and thus blocks dynamin-dependent cellular mechanisms, such as clathrin-mediated endocytosis [131, 217]. However, previous studies described off-target effects, such as the inhibition of actin assembly and the interference of membrane ruffling, which are necessary for micropinocytosis and phagocytosis [131, 218-219]. Filipin III inhibits the formation of caveolae in the caveolin-dependent

(CAV) endocytosis by cholesterol depletion of the cell membrane [220-221]. Wortmannin, EIPA, and cytochalasin D are all inhibitors of macropinocytosis and phagocytosis, but the inhibition relies on different mechanisms: Wortmannin inhibits the phosphoinositide 3-kinase (PI3 kinase) activity [222], EIPA inhibits sodium channels [223], and cytochalasin D disrupts the polymerization of actin [131, 224]. The other ten inhibitors did not reduce the uptake of HES-NPs in our experiment: Dansylcadaverine and chlorpromazine are inhibitors of clathrin-mediated endocytosis [131, 225-226]. Methyl-ß-cyclodextrin and genistein are inhibitors of CAV endocytosis [131, 227-229]. LY294002 and p21-activated kinase inhibitor III (IPA-3) are inhibitors of macropinocytosis and phagocytosis [230-232]. Nocodazole binds tubulin and prevents microtubule formation [233].

Only two of the twelve inhibitors reduced the uptake of the HSA-NCs: dynasore and methyl-ß-cyclodextrin (Fig. 5.2B). Latter inhibitor sequesters cholesterol from the cell membrane, inhibiting CAV endocytosis [131, 227]. The other ten inhibitors did not reduce the uptake of the HSA-NCs. The small number of effective inhibitors could be explained by the observed cell contact or even possible receptor binding of the HSA-NCs. Notably, measurements by flow cytometry do not discriminate between membrane-associated nanoparticles or internalized nanoparticles.

To further explain these results, we visualized the uptake by transmission electron microscopy (TEM). The iron oxide content of both nanocarrier types facilitated the visualization at the cell membrane and within the cell. For both nanocarrier types, we predominantly observed the formation of vesicles at the cell membrane that contained the nanocarriers and that were larger than 500 nm (Fig. 5.2C/D, nanocarrier marked with white arrows). Vesicles of this size indicate macropinocytosis or phagocytosis [130-131, 234]. The vesicle formation around the HES-NPs resembled a collapsing and invaginated cell membrane as described previously for macropinocytotic events (Fig. 5.2C, Fig. 5.3A.1, and Fig. S5.4A right picture) [130, 234-235]. In contrast, we observed protrusions, zipping up along the HSA-NCs (Fig. 5.2D, Fig. 5.3B.2) which we identified as phagocytotic cups, a common event in phagocytosis [130, 151, 234].

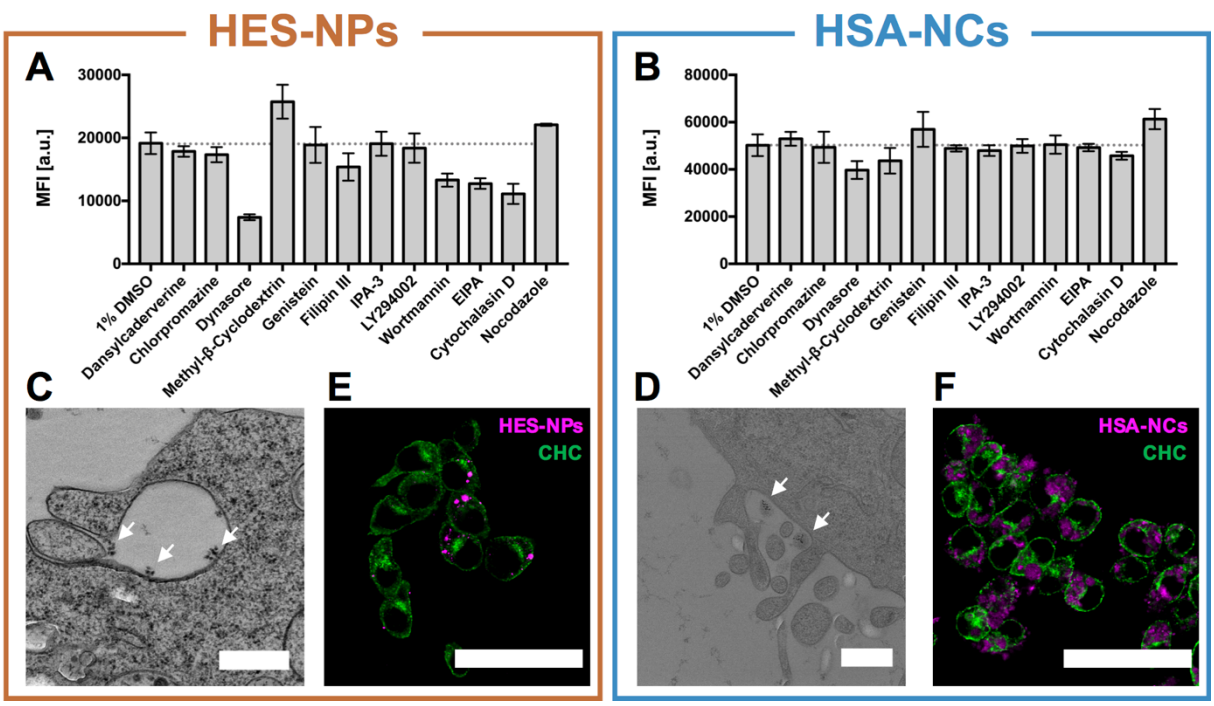

Figure 5.2: HES-NPs and HSA-NCs enter the cell by distinct uptake mechanisms. DC2.4 cells were pretreated with twelve different small molecule inhibitors for 30 min to block various uptake pathways. Next, the cells were incubated with 250 µg ml^{-1} HES-NPs **(A)** and HSA-NCs **(B)** for 4 h. As some inhibitors were solved in DMSO, a control with 1% DMSO (the highest DMSO concentration in the samples) was included to exclude DMSO toxic effects. The cell uptake was analyzed by flow cytometry, measuring the median fluorescent intensity (MFI) of the events (data are shown as mean ± SD, n = 3). The uptake events were imaged by TEM for HES-NPs **(C)** and HSA-NCs **(D)** after 10 min exposure to the cells, respectively. The white arrows indicate the nanocarriers. The scale bars represent 500 nm. **(E/F)** Clathrin heavy chain (CHC) was stained via antibody staining and analyzed by cLSM with HES-NPs and HSA-NCs after 2 h exposure to the cells. Green represents the antibody staining, and magenta represents the nanocarriers. The scale bars represent 50 µm.

Additionally, we performed antibody staining to visualize the clathrin heavy chain by cLSM to understand the strong uptake inhibition by dynasore. We did not observe colocalization events of clathrin heavy chain and both nanocarrier types in the early phase of the uptake, therefore excluding an uptake through clathrin-mediated endocytosis (Fig. 5.2E/F). This assumption was further supported by observing various empty clathrin vesicles close to nanocarrier-filled vesicles by TEM (Fig. S5.4A/B, white arrows). Instead, we argue that dynasore did evoke an off-target effect on the actin-based uptake mechanisms (predominantly macropinocytosis for HES-NPs and phagocytosis for HSA-NCs).

However, for the HES-NPs, we observed the formation of smaller vesicles, roughly 100 nm, that incorporated the NPs into the cell (Fig. S5.4C). We identified these vesicles as caveolin-

vesicles. The formation of caveolin vesicles was also observed in DC2.4 treated with HSA-NCs but the vesicles remained empty (Fig. S5.4D).

Thus, we concluded that HES-NPs and HSA-NCs differed in uptake kinetics and the mode of uptake. The HES-NPs were taken up comparably slower than HSA-NCs. The process was dependent on dynamin, cholesterol, and various factors contributing to macropinocytosis. Morphologically we observed macropinocytosis and CAV endocytosis. The phagocytotic uptake of the HSA-NCs was dynamin-dependent but overall weakly affected by other inhibitors.

Microscopy of the intracellular trafficking

We observed the internalization of HES-NPs through collapsing membrane ruffles into 0.5-1 µm large macropinosomes (Fig. 5.3A.1/A.2). Next, the vesicles displayed tubular shapes and demonstrated vesicle division that we attributed to early endosomes (EE, Fig. 5.3A.3). We also observed the presence of smaller vesicles of ~100 nm filled with HES-NPs, which we attribute to CAV endocytosis (Fig. S5.5A.1). Notably, these smaller vesicles were fusing with the larger vesicles (Fig. S5.5A.2/A.3, small vesicle marked with white arrow). Eventually, we detected the nanocarriers in late endosomes (LE), which fused with other LEs and lysosomes (LY) to form endolysosomes (EL, Fig. 5.3A.4, Fig. S5.5A.4). The ELs displayed a variable morphology. Indeed, we observed large vesicles of more than 1 µm filled with loosely packed HES-NPs (Fig. 5.3A.5, lower left vesicle) or with HES-NPs packed in intraluminal vesicles (Fig. 5.3A.5, lower right vesicle). The latter EL type seemed to be a successor of a multivesicular body, which is a subset of LEs containing intraluminal vesicles [236]. Furthermore, we observed smaller vesicles with densely packed HES-NPs, which could meet the fate of exocytosis (Fig. 5.3A.5, upper vesicle) as shown by similar experiments with iron oxide-containing NPs in the past [168, 172, 237]. Based on the different appearances of ELs it is likely that the HES-NPs are exocytosed by lysosome excretion or vesicle-related secretion after the engulfment in intraluminal vesicles.

The HSA-NCs were identified in ~500 nm large phagosomes after internalization through the above-mentioned formation of a phagocytotic cup (Fig. 5.3B.1/B.2, Fig. S5.5B.1). Similar to the HES-NPs, these phagosomes fused with smaller vesicles (Fig. S5.5B.1) and eventually exhibit characteristics of EEs (Fig. 5.3B.3). The vesicles gradually matured to LEs and fused with LYs (Fig. 5.3B.4). Parallelly, we observed the fusion of LEs, but unlike the HES-NPs, we identified the HSA-NCs within the formation of multilamellar vesicles (Fig. 5.3B.2/B.3). These multilamellar vesicles were described as another subtype of late endosomes, similar to multivesicular bodies but instead containing various membrane layers with a concentric orientation. A past study had shown that the depletion of ras-related protein Rab9 (RAB9) impacted the maintenance of multilamellar vesicles and therefore connected RAB9 as a

marker to this LE subset [238]. Finally, the HSA-NCs or the iron oxide NPs were found in ELs with a comparable smaller (~500 nm) and darker morphology (Fig. 5.3B.5, Fig. S5.5B.4) than in the case of the HES-NPs. Here, we observed degradation of the protein capsule within the ELs. In fact, the degradation of bovine serum albumin nanocapsules was visualized in ELs by electron microscopy before [49]. From this step on, we expect the eventual exocytosis of the iron oxide NPs via lysosome secretion based on the lysosome appearance and the missing intraluminal vesicles.

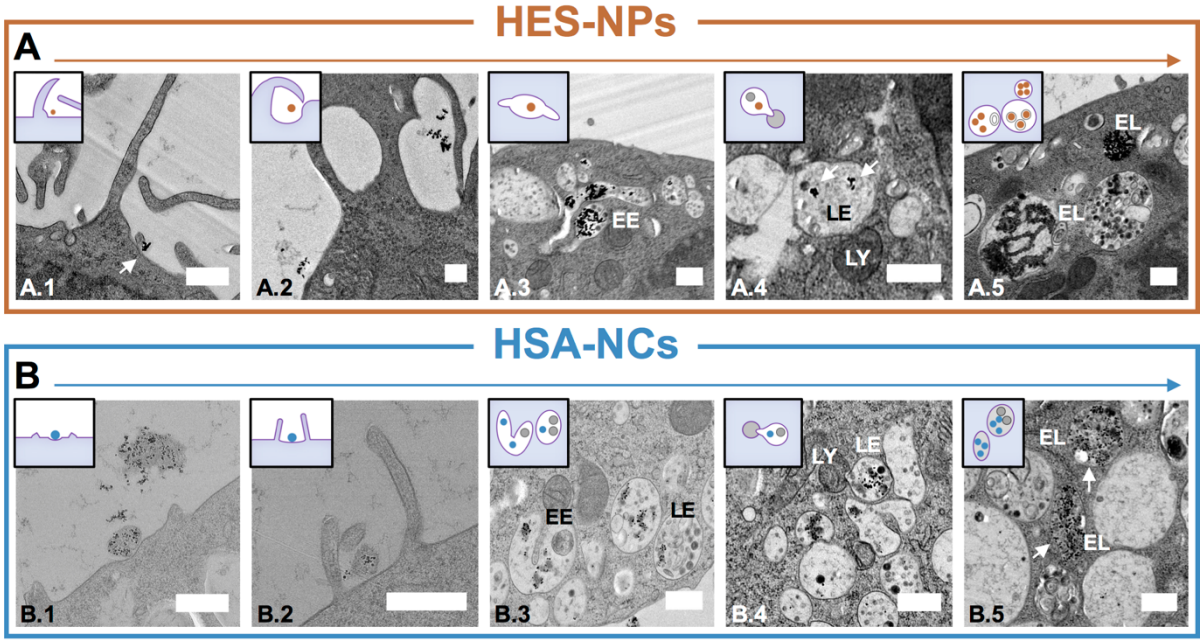

Figure 5.3: Intracellular trafficking visualized by TEM for HES-NPs and HSA-NCs. (A) DC2.4 cells internalize HES-NPs (white arrow) by collapsing membrane ruffles via micropinocytosis (A.1, A.2; 10 min - 2 h). The HES-NPs traffic through the tubular-shaped early endosome (EE, A.3; 2 h). Next, HES-NPs reach the late endosomes (LE) filled with intraluminal vesicles, which fuse with lysosomes (LY, A.4; 24 h). Finally, HES-NPs accumulate in endolysosomes (EL, A.5; 2 h + 22 h). **(B)** HSA-NCs were observed to create contact with the membrane before being engulfed by a phagocytotic cup for phagocytosis (B.1, B.2; 10 min). The HSA-NCs are then found in EE (B.3, 2 h) and LE (B.4, 2 h). Finally, HSA-NCs are localized in EL (white arrows, B.5, 2 h + 22 h). The scale bars represent 500 nm.

Furthermore, we conducted cLSM with LysoTracker, a dye for acidic intracellular compartments, and with antibody-staining of endolysosomal markers. The HES-NPs colocalized only weakly with LysoTracker after 2 h but colocalized progressively stronger at the later time points, 24 h and 2 + 22 h, especially at 2 + 22 h (Fig. 5.4a, Fig. S5.6). In the case of the HSA-NCs, we observed colocalization already after 2 h with an increasing colocalization after 24 h (Fig. 5.4B, Fig. S5.7). Previous colocalization experiments with bovine serum albumin nanocapsules proved a rapid transfer of the protein nanocapsules to LysoTracker-

stained acidic compartments within 1 h [49]. The colocalization decreased after 2 + 22 h. The earlier transport of the HSA-NCs than HES-NPs into acidic compartments correlates with the comparably rapid uptake and indicates accelerated endolysosomal processing. In addition, the lower co-localization for HSA-NCs at 2 + 22 h seemed to indicate an earlier endolysosomal degradation.

Next, we applied antibody staining for the EE marker RAB5, the LE marker RAB7, and the EL marker lysosomal-associated membrane protein 1 (LAMP1). First, we observed a weak RAB5 colocalization for both nanocarrier systems at 2 h but not after 24 h (Fig. 5.4C/D, Fig. S5.8, Fig. S5.9). A colocalization with RAB7 was observed for both time points, 2 h and 24 h for both nanocarriers. The HES-NPs colocalized with LAMP1 after 2 h and 24 h but the HSA-NCs colocalized with LAMP1 only after 2 h.

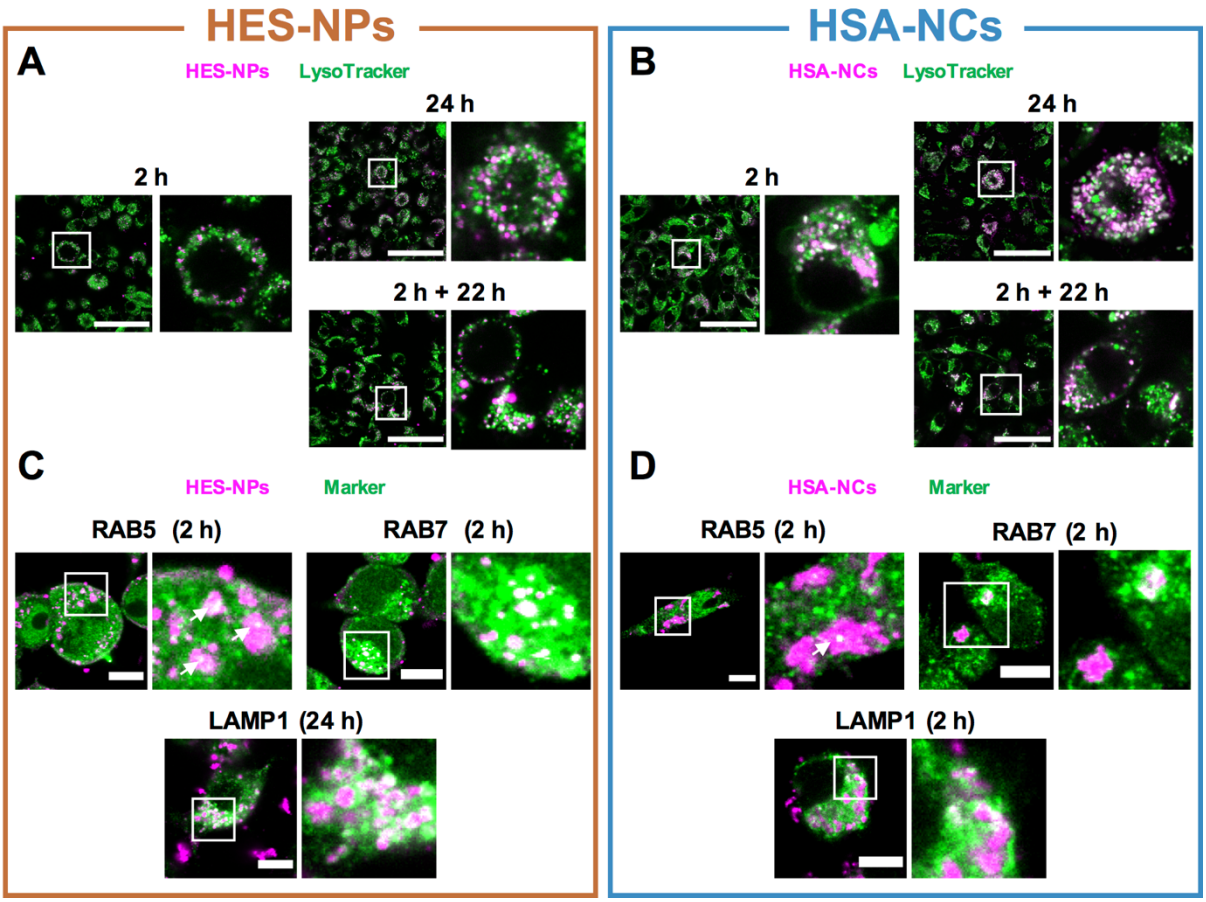

Figure 5.4: Confocal microscopy supports different processing times between the nanocarrier systems. DC2.4 cells were incubated with 250 µg ml^{-1} HES-NPs **(A)** and HSA-NCs **(B)** for different time points (2 h, 24 h, 2 h + 22 h). The acidic compartments were stained with LysoTracker. The samples were analyzed by cLSM. Green represents LysoTracker, and magenta represents the nanocarriers. The scale bars represent 50 µm. Antibody staining was performed to stain RAB5, RAB7, and LAMP1 and to observe co-localization with HES-NPs **(C)** and HSA-NCs **(D)**. Green represents the antibody staining,

and magenta represents the nanocarriers. The scale bars represent 10 µm. Transmission light images, single-channel images, and complement time points (for antibody staining) can be found in Figures S5.6-S5.9.

In short, we visualized the morphology of the uptake and the intracellular trafficking by TEM. By cLSM experiments, we could support this morphological evidence that HES-NPs and HSA-NCs were indeed processed by the endolysosomal system of the DC2.4 cells. However, sole microscopic studies, particularly of certain intracellular markers, underlie a previous selection of markers to investigate. Moreover, the exact antibodies need to be available or transfected cells need to be created for the study. Compelling microscopic analysis in these terms can therefore be time-consuming and selective in the representation of the uptake and intracellular trafficking details.

Proteomics detail the intracellular trafficking

Consequently, we evaluated the protein composition that adsorbed during the internalization and trafficking of the nanocarriers in the cell to complement our abovementioned results. Therefore, we incubated DC2.4 with HES-NPs and HSA-NCs for three time points (2 h, 24 h, and 2 + 22 h; Fig. 5.5A). Afterward, the cells were harvested and lysed by sonification. The nanocarriers were magnetically separated from the cell debris and the protein corona was isolated as described in the methods section. As for the controls, we incubated nanoparticles in fetal bovine serum (FBS) to study the protein corona in cell culture medium (termed as ‘medium corona’). Additionally, we performed the protein corona preparation without nanocarriers, studying possible contaminations by the experiment itself (termed as ‘negative control’).

After the preparation and quantification of the protein samples, we observed a similar trend for both nanocarrier systems by comparing the desorbed protein amounts. The intracellular protein corona concentrations were measured in a range of 20-69 µg ml^{-1} (in 100 µl each). The sample concentration increased in the following order: 2 h, 24 h, and 2 + 22 h (Fig. S5.10A/B). For the cell lysate, we measured 1.5-2.1 mg ml^{-1} protein (in 1 ml). The medium corona and negative control generated less protein than the intracellular protein corona samples. We detected a 10-24 µg ml^{-1} range for these control samples (in 100 µl). To visualize the overall protein composition, we performed SDS-PAGE. The pattern composition of the intracellular protein corona samples was overall complex but differed significantly from the lysate as its original protein source (Fig. S5.11, Fig. S5.12C). This observation confirmed that the protein corona composition differed from the pure lysate, and only specific proteins adsorbed to the surface of the nanocarriers. The band pattern of the protein corona for the HES-NPs appeared

significantly different at 2 h when compared to the patterns at 24 h or 2 + 22 h (Fig. S5.11A). In contrast, we observed a similar band pattern for the HSA-NCs at all three time points (Fig. S5.11B). This difference indicated that the HES-NPs-protein corona differed when the NPs traversed the cell for 2 h versus later time points. This time point-dependency was obviously not the case for the HSA-NCs. The band pattern for the medium corona of both nanocarriers was much simpler (Fig. S5.12A/B), with a notable band at 66 kDa. We assigned this band to serum albumin by comparison with the literature [239].

For an unbiased look, at which proteins adsorbed on the nanocarriers during their intracellular trafficking, we performed label-free quantitative LC-MS proteomics. Overall, the composition of the most abundant proteins on the protein corona was quantitatively different from the lysate (Fig. S5.13A/B). This difference supported the observations of the SDS-PAGE that these analyzed proteins adsorbed specifically on the retrieved nanocarriers. We measured abundant amounts of four different types of histones on the protein corona for both types of nanocarriers. These histones were identified as H2A, H2B, H3, and H4. For the HES-NPs at 2 h, we identified high amounts of the ER junction formation protein lunapark, which decreased at later time points (Fig. S5.13A). Instead, we observed an increase of Dolichyl-diphospho-oligosaccharide-protein glycosyltransferase 48 kDa subunit (DDOST) at the later time points. For the protein corona of the HSA-NCs, the highly abundant protein composition remained overall comparable (Fig. S5.13B). We measured 2 proteins on the protein corona formed with HES-NPs in medium and 15 proteins on the protein corona formed with HSA-NCs in medium (Fig. S5.14A/B). These numbers were overall lower when compared to the number of proteins on the protein corona that formed within the cells (218 proteins for HES-NPs, 164 proteins for HSA-NCs). This difference reflects the great changes in interaction partners that the protein corona undergoes, once the nanocarriers are introduced into the cell. In the case of the negative control, we identified 3 proteins, which were histones H2A, H2B, and H3 (Fig. S5.14C). Therefore, it is likely that these proteins were enriched on the corona by the performed preparation steps.

To further select proteins of interest regarding intracellular trafficking, we identified all proteins with a 1.5-fold higher abundance in comparison to the lysate proteins. These proteins were termed enriched proteins (Tab. S5.1, Tab. S5.2). We analyzed the enriched proteins regarding the time points and used Venn diagrams to display the differences. In the case of the enriched proteins of the HES-NPs protein corona, we identified 5 proteins for 2 h, 16 for 24 h, 1 for 2 h and 2 + 22 h, 60 for both later time points, and 38 for all time points to be enriched (Fig. 5.5B). For the HSA-NCs, we identified 16 proteins for 2 h, 2 for 24 h, 14 for 2 h and 2 + 22 h, and 56 for all time points (Fig. 5.5C). In other words, the protein corona on HES-NPs changed between 2 h and both of the later time points. This change was in accordance with distinct band patterns observed by SDS-PAGE and the prolonged uptake measured by flow cytometry.

In comparison, we observed the opposite case for the HSA-NCs which displayed the highest number at 2 h and did not change but rather loose proteins over time. This course indicates that the protein corona evolved with prolonged trafficking for the HES-NPs but stayed overall the same for the HSA-NCs which were internalized and processed faster.

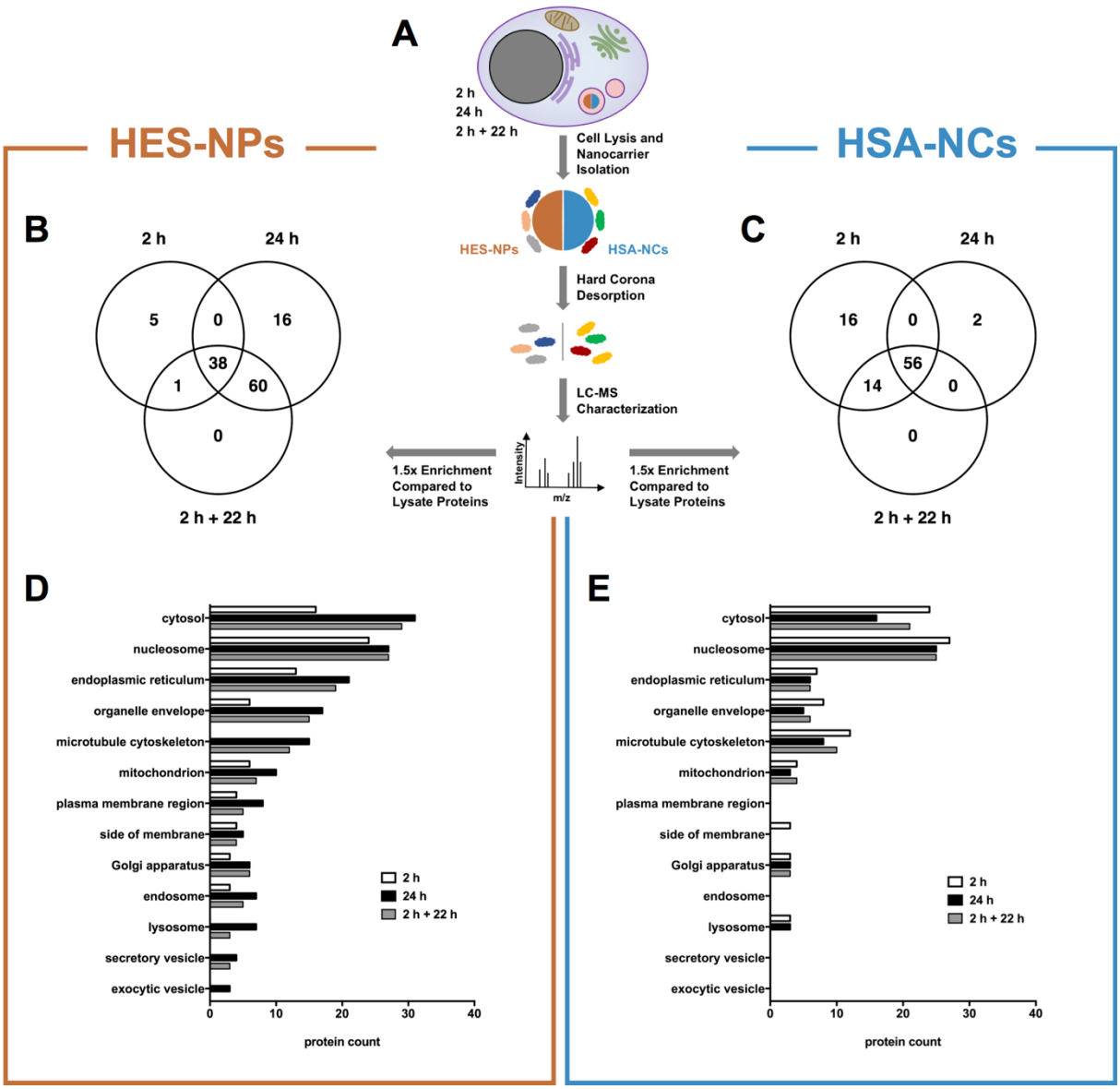

Figure 5.5: LC-MS proteomics reveals nanocarrier- and time-dependent differences of the protein corona during intracellular trafficking. (A) Workflow for the isolation of the intracellular protein corona samples. DC2.4 cells were incubated with 250 µg ml^{-1} nanocarriers for different time points (2 h, 24 h, 2 h + 22 h). The cells were harvested and lysed by sonification. The nanocarriers were magnetically separated from the cell debris and washed three times with PBS and centrifugation. The proteins were desorbed with 2% SDS and forwarded to LC-MS proteomic analysis. The corona proteins were compared to lysate proteins, and only the 1.5-fold enriched proteins were further analyzed. The enriched corona proteins associated with HES-NPs **(B)** and HSA-NCs **(C)** were compared in regard to the time points by Venn diagrams. A detailed list of the proteins in the Venn diagrams with their uniport identifiers

is shown in Figures S5.15 and S5.16. The enriched corona proteins associated with HES-NPs **(D)** and HSA-NCs **(E)** were forwarded to annotation analysis utilizing DAVID (Version 6.8). Functional annotation clustering was performed with the database GOTERM_CC_FAT. The protein counts for the different time points are listed for fifteen selected GOTERMs.

Next, we utilized protein annotation analysis to further categorize the proteins according to their subcellular compartments. We observed the overall trends from the Venn diagrams when comparing the protein count between the time points. There was a noticeable change for the HES-NPs between the early and the late time points (Fig. 5.5D) but a general similarity in the protein count within the time points for the HSA-NCs (Fig. 5.5E). Overall, most of the proteins were attributed to the categories or GOTERMs of *cytosol*, *nucleosome*, and *endoplasmic reticulum*. Other approaches to isolate intracellular nanoparticles for protein corona analysis or nanoparticle-containing vesicles have similarly reported the presence of proteins from the nucleus or non-endosomal organelles [183, 203]. We specifically included GOTERMs based on compartments of importance for the intracellular trafficking. These GOTERMs were *plasma membrane region*, *side of membrane*, *Golgi apparatus*, *endosome*, *lysosome*, *secretory vesicle*, and *exocytotic vesicle*. In the case of the HES-NPs, we identified proteins within all these GOTERMs with a protein count per time point between 3 and 7. Conversely, we obtained fewer proteins for the HSA-NCs. Here we determined proteins only in the categories of *side of membrane*, *Golgi apparatus*, and *lysosome* with a protein count of 3. We attribute the decreased protein count in the case of the HSA-NCs to the different affinity of the proteins for the HSA-NCs' surface and the advanced intracellular degradation of the HSA-NCs.

To identify the proteins that are specifically related to the intracellular trafficking of the nanocarriers, we selected all proteins annotated by the above-mentioned intracellular trafficking GOTERMs (Fig. 5.6A/B). In total, we found 20 proteins for the HES-NPs and 10 proteins for the HSA-NCs that we defined as intracellular trafficking proteins. The two lists contain the proteins from all time point conditions for the respective nanocarriers but are also given with a time point dependency depicted by Venn diagrams (red highlighted proteins in Fig. S5.15, Fig. S5.16). The identified intracellular trafficking proteins were used in combination with our previous results to reconstruct an intracellular pathway for the nanocarriers (Fig. 5.6C/D).

We describe the HES-NPs trafficking by proteomics as follows: The HES-NPs are mainly internalized via macropinocytosis and to a smaller extent by CAV endocytosis. Indeed, we identified ras-related C3 botulinum toxin substrate 1 (RAC1), Arf-GAP with SH3 domain_ANK repeat and PH domain-containing protein 2 (ASAP2), and caveolae-associated protein 2 (CAVN2, also SDPR) that support this assumption. RAC1 is a small GTPase molecular switch that resides in the plasma membrane to participate in membrane ruffling for

macropinocytosis [240]. ASAP2 belongs to the Arf GTPase-activating protein family, which function as actin regulators, being involved in both actin-based endocytosis processes, macropinocytosis and phagocytosis [241]. In fact, RAC1 and ASAP2 both interact with ADP-ribosylation factor 6 (ARF6, not found in our measurements) which assists in the formation of macropinosomes [241-242]. CAVN2 induces membrane curvature and, thus, the formation of caveolin vesicles [243]. Furthermore, we identified sodium/calcium exchanger 2 (NAC2, also Ncx2), a transmembrane cation exchange channel [244]. Next, the HES-NPs are transported to EEs. We measured ras-related protein Rap 1A (RAP1A), nicastrin (NICA), and V-type proton ATPase subunit d 1 (VA0D1). RAP1A and NICA reside both in vesicles of the endolysosomal system [245-246] and VA0D1 contributes to the endosomal acidification by proton transport into the vesicles [247]. Notably, RAP1A, NICA, and VA0D1 are not confined to EEs but are rather present throughout the endolysosomal pathway, which also includes LEs and ELs. Additionally for the LEs, we identified ADP-ribosylation factor-like protein 8A (ARL8A), and macrosialin (CD68). ARL8A and CD68 are predominantly present in Lys and ELs, but also LEs [248-249]. Finally, the HES-NPs reach the ELs. By proteomics, we further identified the lysosomal marker LAMP1, cathepsin K (CATK), and heat shock protein HSP 90-beta (HS90B). CATK is a lysosomal protease and HS90B is a chaperone that preserves the stability of lysosomal membrane proteins, such as LAMP2 [250-251].

The intracellular trafficking of the HSA-NCs is described as follows: We identified ASAP2, which retains a role in phagocytosis in regards to the cellular entry of the HSA-NCs. For the subsequent EEs, we identified unconventional myosin Vb (MYO5B) which was identified as a regulator of endosomal size and was also connected to RAB11-based recycling endosomes (RAB11 was not found in our measurements) [252-253]. For the LEs we measured CD68 and ARLA8. The ELs were additionally connected to CATK and NPC intracellular cholesterol transporter 2 (NPC2). Latter protein regulates the cholesterol levels in the LYs and ELs [254].

Furthermore, we measured intracellular proteins that were assigned to the vesicular transport between the endoplasmic reticulum (ER), the Golgi apparatus, and the endolysosomal pathway. These proteins were DYHC2, SAR1A, CANT1, RYR1, and RYR2 for the HES-NPs and AKAP9 and AT2A2 for the HSA-NCs. However, we did not observe enough evidence by TEM to fully support the presence of the nanocarriers within a vesicular transport between the Golgi apparatus and the ER.

In sum, we developed a strategy to isolate and identify intracellularly adsorbed proteins on nanocarriers with analytical importance. The time point-related distribution of these proteins demonstrated that the intracellular corona changed for a slower trafficking, as for the HES-NPs. Additionally, the detected intracellular proteins offered us a complementary and detailed view of the cellular uptake and intracellular trafficking.

HES-NPs

A

Uniprot Accession	Uniprot ID	Protein Name
Q8VEH3	ARL8A	ADP-ribosylation factor-like protein 8A
Q7SIG6	ASAP2	Arf-GAP with SH3 domain_ ANK repeat and PH domain-containing protein 2
P97929	BRCA2	Breast cancer type 2 susceptibility protein homolog
P55097	CATK	Cathepsin K
Q63918	CAVN2	Caveolae-associated protein 2
Q45VK7	DYHC2	Cytoplasmic dynein 2 heavy chain 1
O88833	CP4AA	Cytochrome P450 4A10
P36536	SAR1A	GTP-binding protein SAR1a
P11499	HS90B	Heat shock protein HSP 90-beta
P10922	H10	Histone H1.0
P11438	LAMP1	Lysosome-associated membrane glycoprotein 1
P31996	CD68	Macrosialin
P57716	NICA	Nicastrin
P63001	RAC1	Ras-related C3 botulinum toxin substrate 1
P62835	RAP1A	Ras-related protein Rap-1A
E9PZQ0	RYR1	Ryanodine receptor 1
E9Q401	RYR2	Ryanodine receptor 2
Q8K596	NAC2	Sodium/calcium exchanger 2
Q8VCF1	CANT1	Soluble calcium-activated nucleotidase 1
P51863	VA0D1	V-type proton ATPase subunit d 1

HSA-NCs

B

Uniprot Accession	Uniprot ID	Protein Name
Q70FJ1	AKAP9	A-kinase anchor protein 9
Q8VEH3	ARL8A	ADP-ribosylation factor-like protein 8A
Q7SIG6	ASAP2	Arf-GAP with SH3 domain_ ANK repeat and PH domain-containing protein 2
P55097	CATK	Cathepsin K
B2RSH2	GNAI1	Guanine nucleotide-binding protein G(i) subunit alpha-1
P10922	H10	Histone H1.0
P31996	CD68	Macrosialin
Q9Z0J0	NPC2	NPC intracellular cholesterol transporter 2
O55143	AT2A2	Sarcoplasmic/endoplasmic reticulum calcium ATPase 2
P21271	MYO5B	Unconventional myosin-Vb

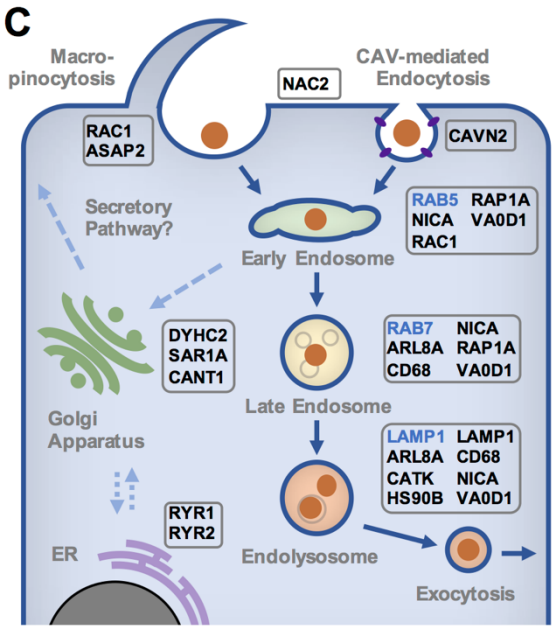

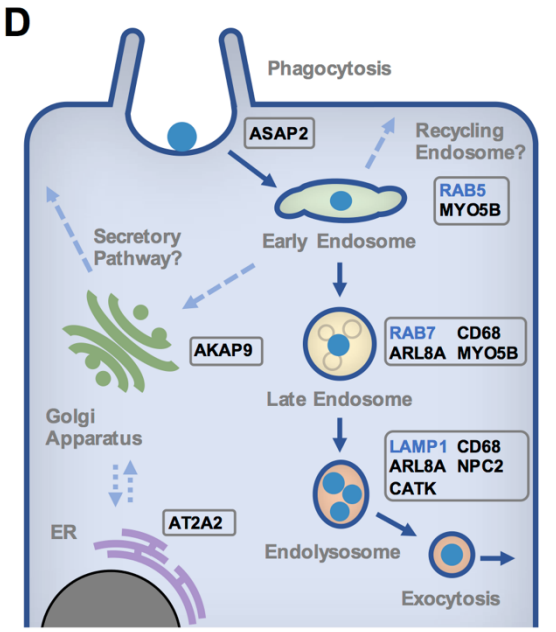

Figure 5.6: Intracellular trafficking proteins and network for HES-NPs and HSA-NCs. Intracellular trafficking proteins for HES-NPs **(A)** and HSA-NCs **(B)** were retrieved from GOTERMs *plasma membrane region, side of membrane, Golgi apparatus, endosome, lysosome, secretory vesicle, and exocytotic vesicle* and are listed with uniport accession, uniport id, and protein name. The LC-MS identified proteins were linked to intracellular compartments (as seen in black) and combined with the findings of TEM and cLSM (RAB5, RAB7, and LAMP1; seen in blue) to recreate an intracellular trafficking network for HES-NPs **(C)** and HSA-NCs **(D)**, respectively.

5.5 Conclusion

We studied the uptake mechanisms and the intracellular trafficking of HES-NPs and HSA-NCs. Conventional methods, such as flow cytometry, TEM, and cLSM proved to be fundamental methods to identify the nature and differences of uptake kinetics and morphology of the intracellular events. However, the study of the intracellular protein corona by quantitative LC-MS proteomics offered detailed insights into the possible molecular events during the uptake and intracellular trafficking. We demonstrated that a comparable slow uptake for the HES-NPs correlated with a time point-depending protein corona. A faster uptake of the HSA-NCs correlated with a stable protein corona with minor time-dependent changes. Thus, the flow cytometry analysis was in accordance with our proteomic measurements. The microscopic methods visualized the morphology of the uptake and trafficking of both nanocarriers. Furthermore, by identifying proteins of high importance for endosomal trafficking, we were able to construct nanocarrier-specific intracellular pathways that detail the events after the cellular uptake. Proteomic-driven or complemented investigations improve, therefore, the research on the uptake and intracellular trafficking of nanocarriers. This strategy will prove beneficial when investigating altered intracellular routes through nanomaterial modification and targeting.

5.6 Supplementary information

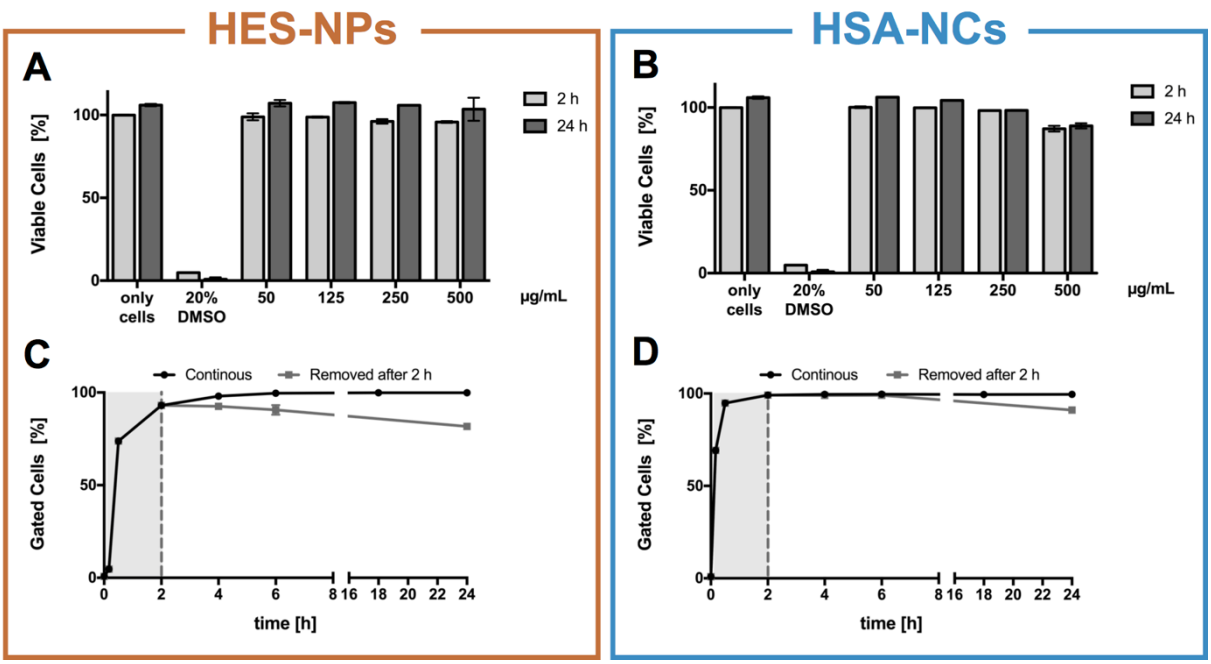

Figure S5.1: DC2.4 cell viability and uptake analysis in murine dendritic cells. Murine dendritic cells (DC2.4) were incubated with various concentrations of HES-NPs **(A)** and HSA-NCs **(B)** for 2 h and 24 h. The cell viability was analyzed by flow cytometry using LIVE/DEAD Fixable Green Dead Cell Stain. A control with 20% DMSO in the medium was included to demonstrate toxic effects (data are shown as mean ± SD, n = 2). For cell uptake analysis, we incubated DC2.4 cells with 250 µg ml^{-1} HES-NPs **(C)** and HSA-NCs **(D)** continuously and discontinuously for various time points. For a continuous incubation, the nanocarrier suspension was left on the cells for all incubation times (10 min, 30 min, 2 h, 4 h, 6 h, 18 h, and 24 h). Additionally, nanocarrier suspension was removed after 2 h and replaced with cell culture medium for the discontinuous incubation (2 h + 2 h, 2 h + 4 h, 2 h + 22 h). The cell uptake was analyzed by flow cytometry measuring the percentual amount of the events positive for fluorescence by the nanocarriers (data are shown as mean ± SD, n = 3).

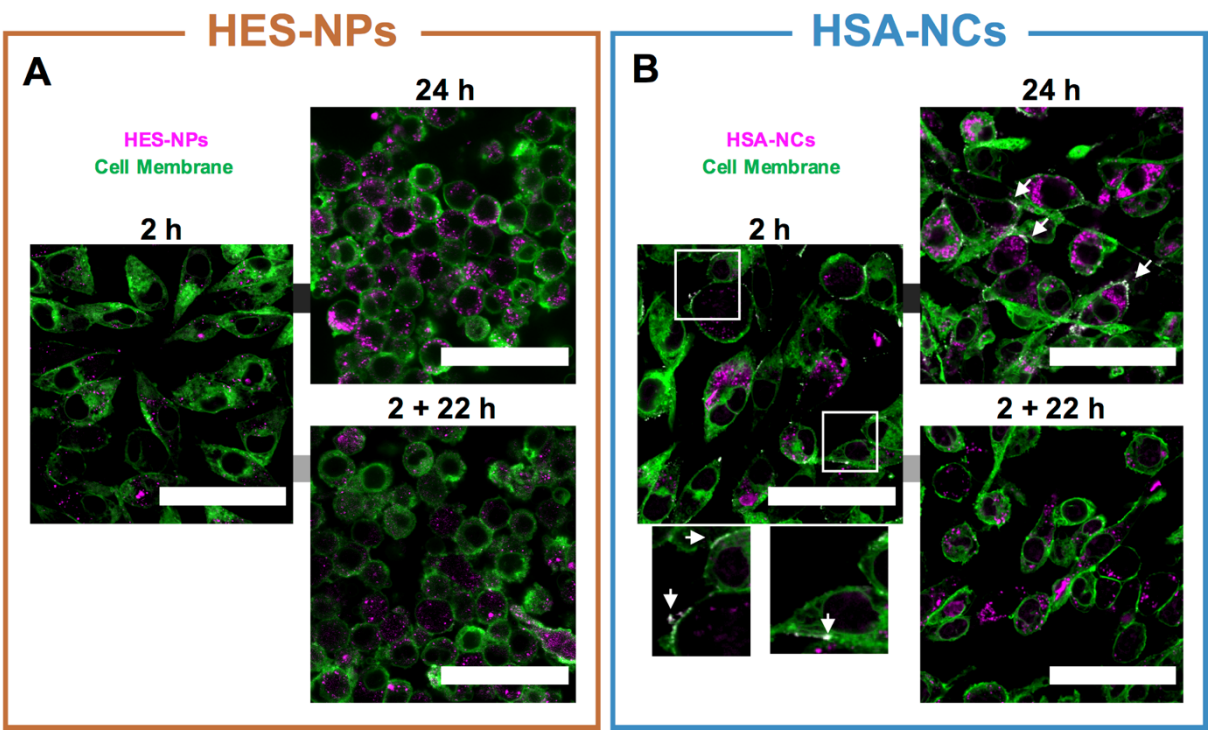

Figure S5.2: HSA-NCs establish contact with the cell membrane. DC2.4 cells were incubated with 250 µg ml^{-1} HES-NPs **(A)** and HSA-NCs **(B)** for different time points (2 h, 24 h, 2 h + 22 h). The cell plasma membrane was stained with CellMask. The samples were analyzed by cLSM. White arrows indicate colocalization events of nanocarriers (here: HSA-NCs) with the cell membrane. Green represents CellMask, and magenta represents the nanocarriers. The scale bars represent 50 µm.

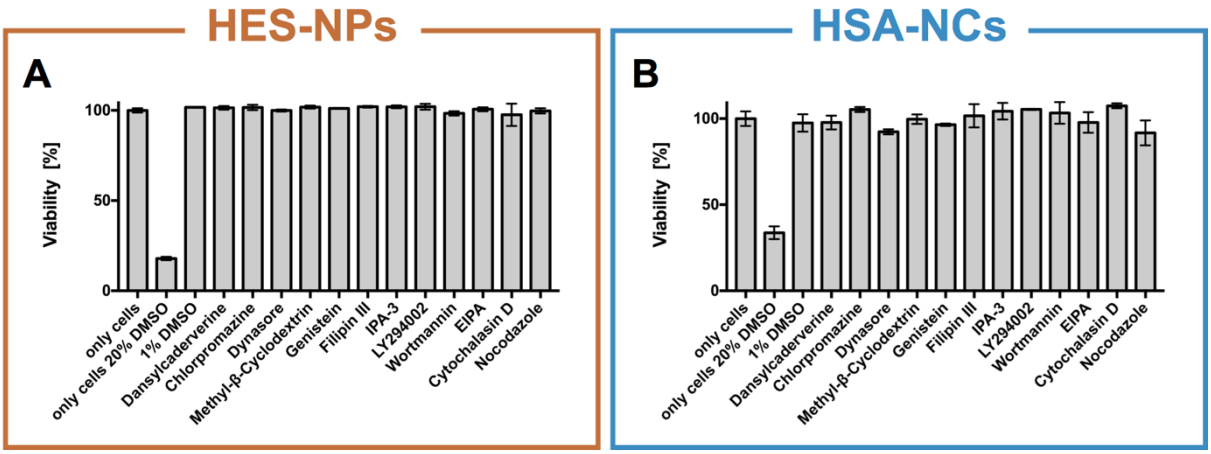

Figure S5.3: DC2.4 cell viability for uptake inhibitor experiments. DC2.4 were pretreated with twelve different small molecule inhibitors for 30 min to block various uptake pathways. Next, the cells were incubated with 250 µg ml^{-1} HES-NPs **(A)** and HSA-NCs **(B)** for 4 h. As some inhibitors were solved in DMSO, a control with 1% DMSO (the highest DMSO concentration in the samples) was included to exclude DMSO toxic effects. The cell viability was analyzed by flow cytometry using LIVE/DEAD Fixable Green Dead Cell Stain. A control with 20% DMSO in the medium was included to demonstrate toxic effects (data are shown as mean ± SD, n = 2).

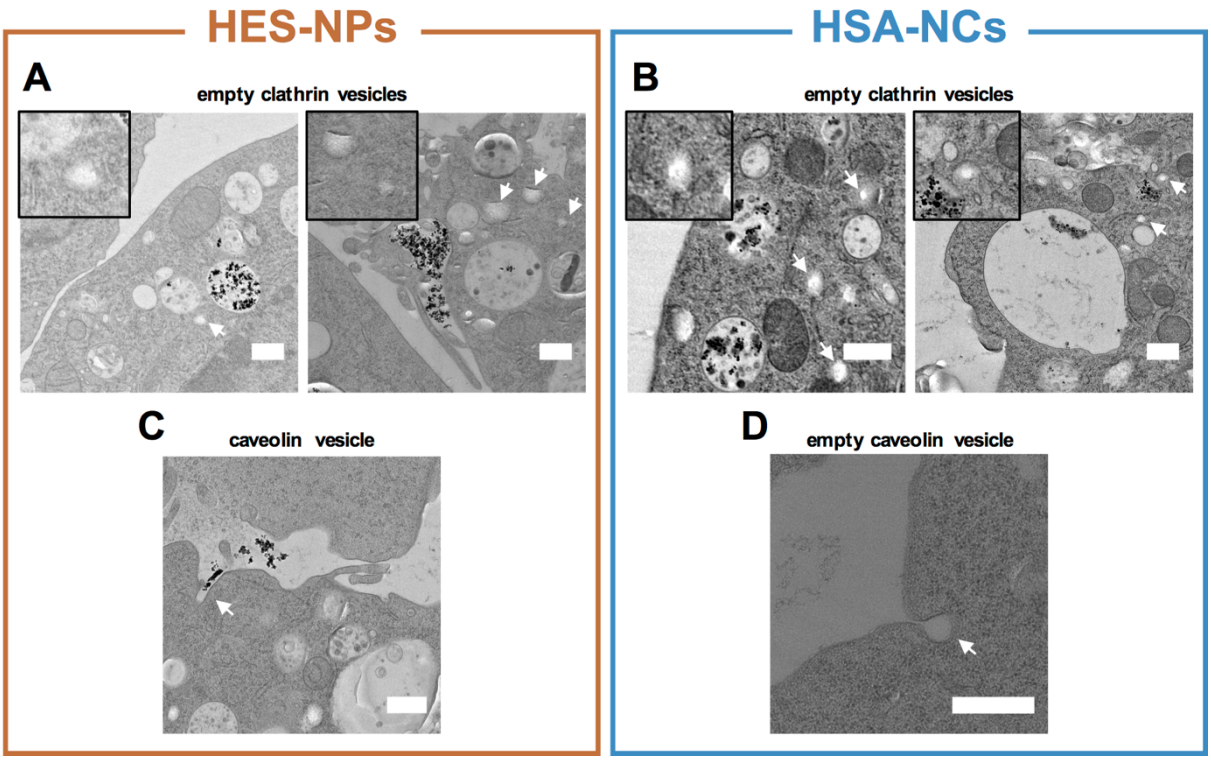

Figure S5.4: TEM micrographs of clathrin and caveolin vesicles. Images of empty clathrin vesicles in close vicinity to vesicles filled with HES-NPs **(A)** and HSA-NCs **(B)**. The events were visualized by TEM after a 2 h exposure of nanocarriers to the cells. The white arrows indicate the empty clathrin vesicles. The scale bars represent 500 nm. Images of a caveolae-associated uptake for HES-NPs **(C)** after 2 h and an empty caveolae vesicle for HSA-NCs **(D)** exposed cells after 10 min. The white arrows indicate the caveolae uptake and vesicle. The scale bars represent 500 nm.

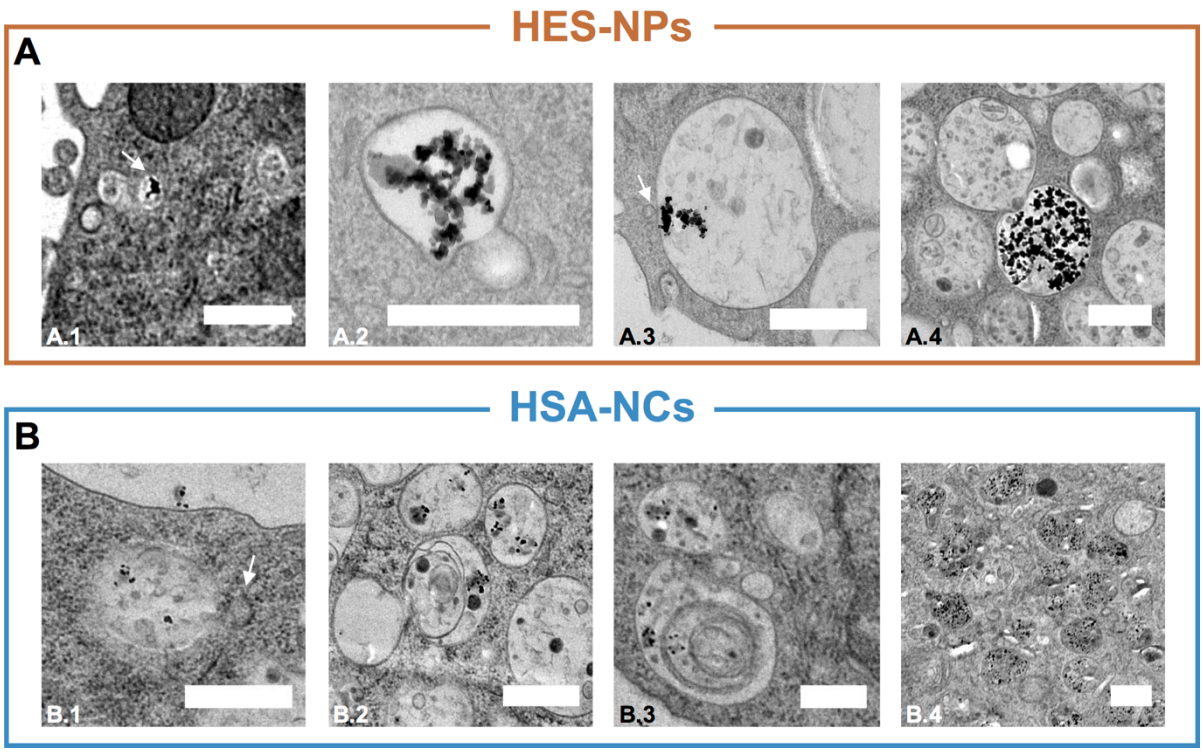

Figure S5.5: Additional events during intracellular trafficking visualized by TEM. (A) DC2.4 cells internalize HES-NPs parallelly over small, caveolae-like vesicles (white arrow) (A.1; 2 h). The small vesicles fuse with larger vesicles containing HES-NPs (A.2, A.3; 2 h). HES-NPs-filled late endosomes (LE) fuse with, empty LE (A.4; 2 h). **(B)** Small vesicles fuse with larger vesicles containing HSA-NCs (B.1; 2 h). HSA-NCs-containing endosomes establish contact with other endosomal vesicles (B.2; 2 h) and possibly form multilamellar vesicles (B.3; 2 h). HSA-NCs are localized in endolysosomes (B.4, 24 h). The scale bars represent 500 nm.

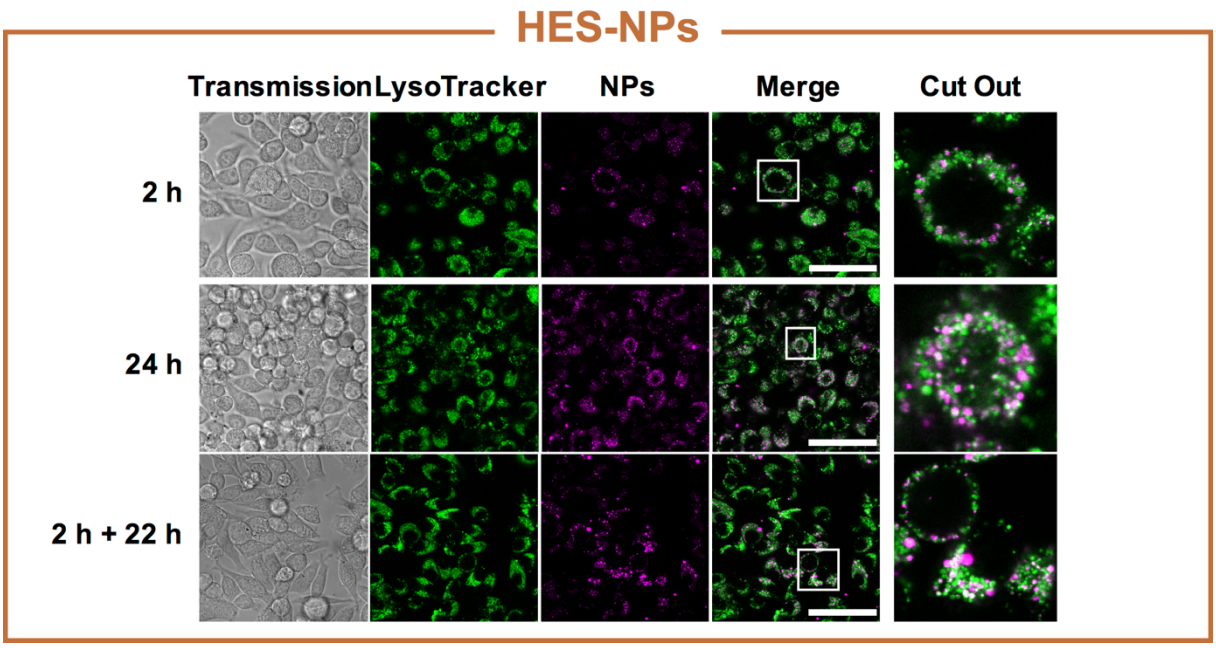

Figure S5.6: Single channel montage for cLSM analysis with LysoTracker and HES-NPs. DC2.4 cells were incubated with 250 µg ml^{-1} HES-NPs for different time points (2 h, 24 h, 2 h + 22 h). The acidic compartments were stained with LysoTracker. The samples were analyzed by cLSM. Green represents LysoTracker, and magenta represents the nanocarriers. The scale bars represent 50 µm.

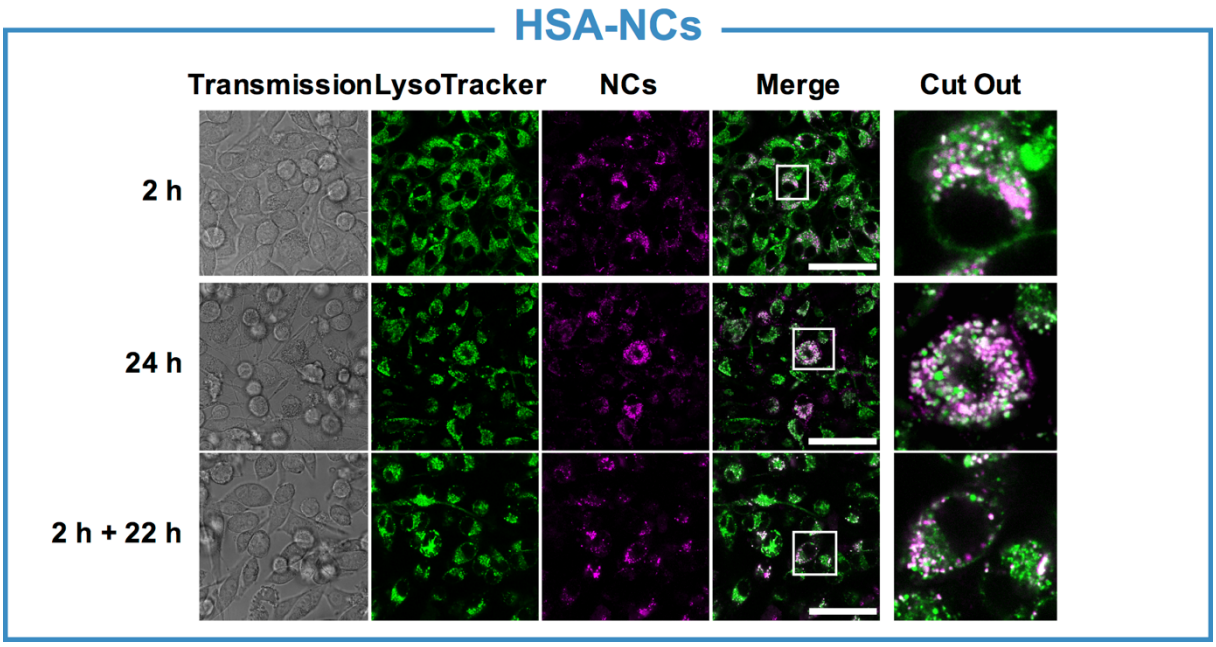

Figure S5.7: Single channel montage for cLSM analysis with LysoTracker and HSA-NCs. DC2.4 cells were incubated with 250 µg ml^{-1} HSA-NCs for different time points (2 h, 24 h, 2 h + 22 h). The acidic compartments were stained with LysoTracker. The samples were analyzed by cLSM. Green represents LysoTracker, and magenta represents the nanocarriers. The scale bars represent 50 µm.

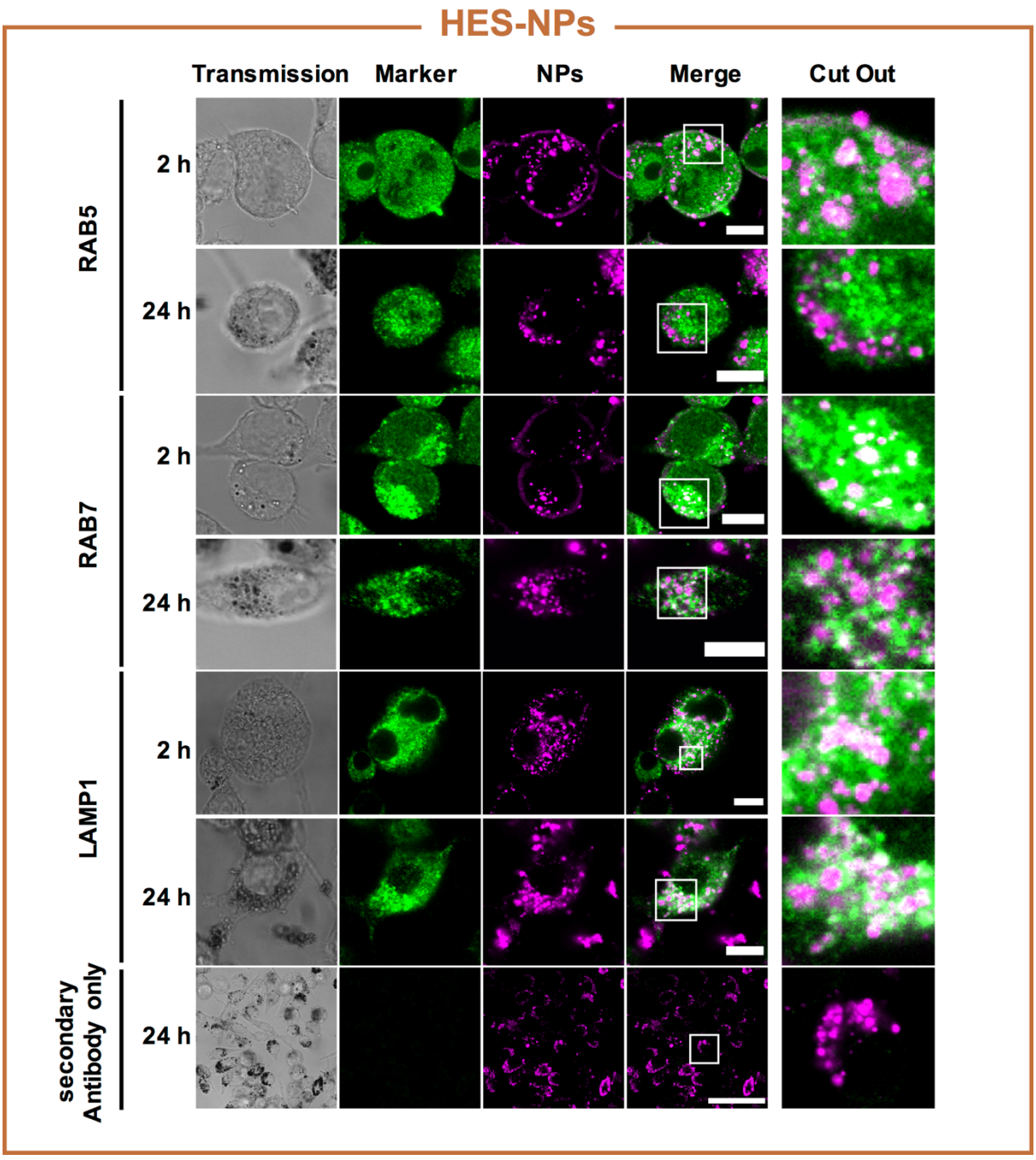

Figure S5.8: Single channel montage for cLSM analysis with antibody staining for RAB5, RAB7, LAMP, and HES-NPs. DC2.4 cells were incubated with 250 µg ml^{-1} HES-NPs for different time points (2 h and 24 h). Antibody staining was performed to visualize RAB5, RAB7, and LAMP1 and to observe potential co-localization with HES-NPs. The samples were analyzed by cLSM. Green represents the antibody staining, and magenta represents the nanocarriers. The scale bars for the RAB5, RAB7, and LAMP1 images represent 10 µm. The scale bar for the secondary antibody only-control represents 50 µm.

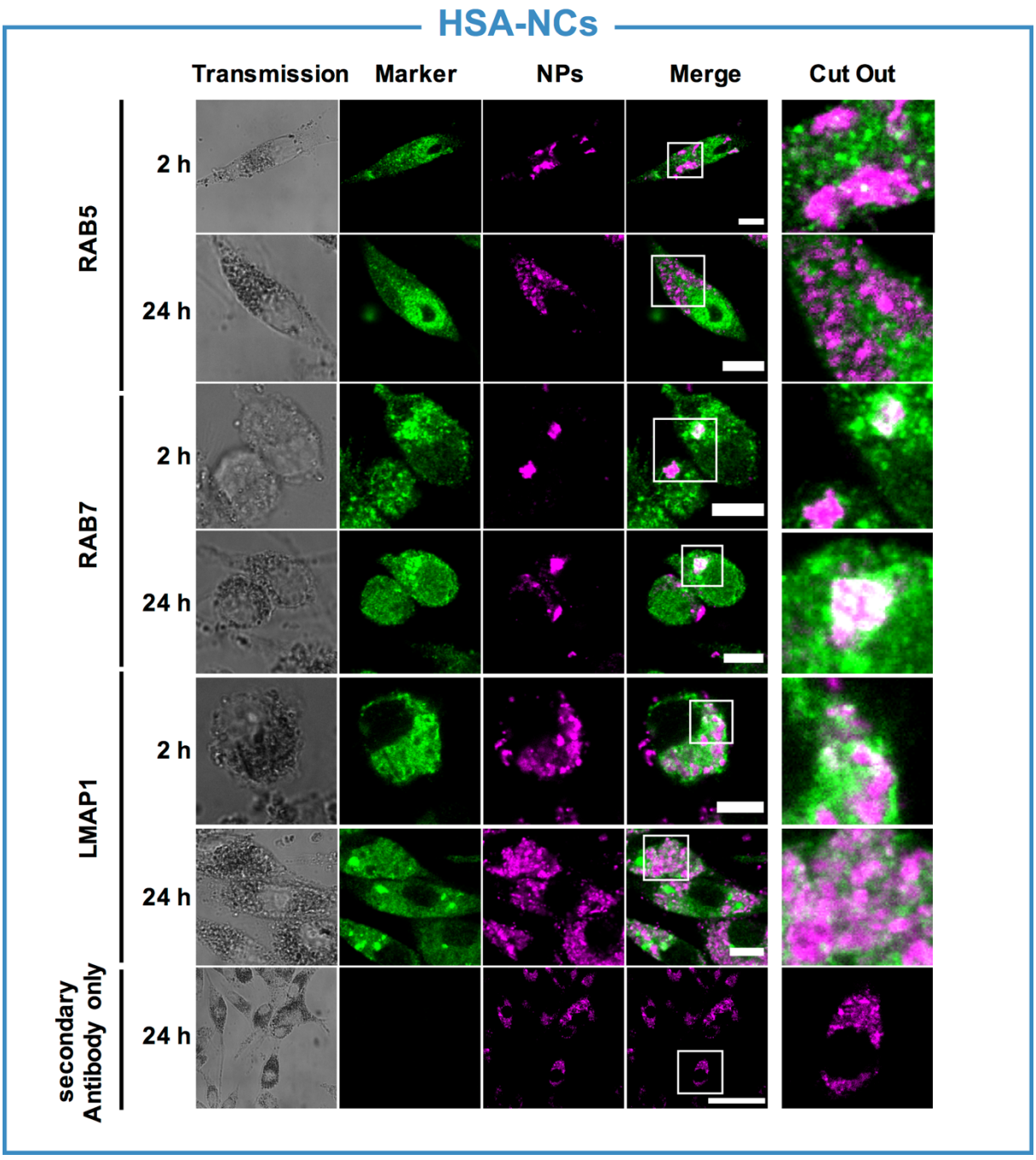

Figure S5.9: Single channel montage for cLSM analysis with antibody staining for RAB5, RAB7, LAMP, and HSA-NCs. DC2.4 cells were incubated with 250 µg ml^{-1} HSA-NCs for different time points (2 h and 24 h). Antibody staining was performed to visualize RAB5, RAB7, and LAMP1 and to observe potential co-localization with HSA-NCs. The samples were analyzed by cLSM. Green represents the antibody staining, and magenta represents the nanocarriers. The scale bars for the RAB5, RAB7, and LAMP1 images represent 10 µm. The scale bar for the secondary antibody only-control represents 50 µm.

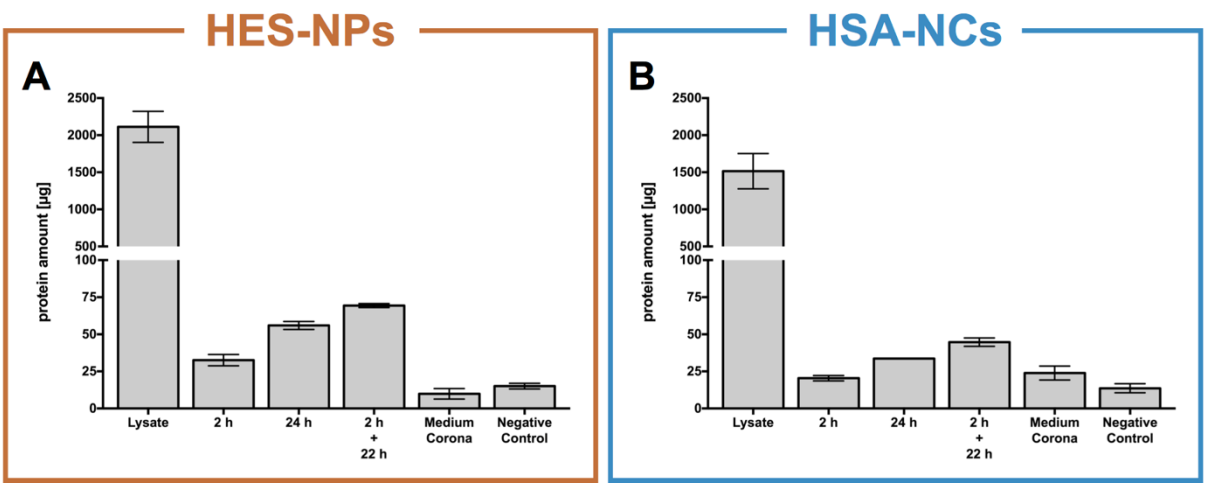

Figure S5.10: Protein quantification of cell lysate and protein corona samples. DC2.4 were incubated with 250 µg ml^{-1} HES-NPs **(A)** and HSA-NCs **(B)** for different time points (2 h, 24 h, 2 h + 22 h). The cells were harvested and lysed by sonification. Lysate corresponds to untreated lysed cells. For the protein corona samples, the nanocarriers were magnetically separated from the cell debris and washed three times with PBS and centrifugation. Protein corona preparations in cell culture medium served as the medium corona sample. Protein corona preparation with no nanocarriers served as the negative control. The proteins were desorbed with 2% SDS. The proteins were quantified by Pierce 660 nm Protein Assay Reagent (data are shown as mean ± SD, n = 2).

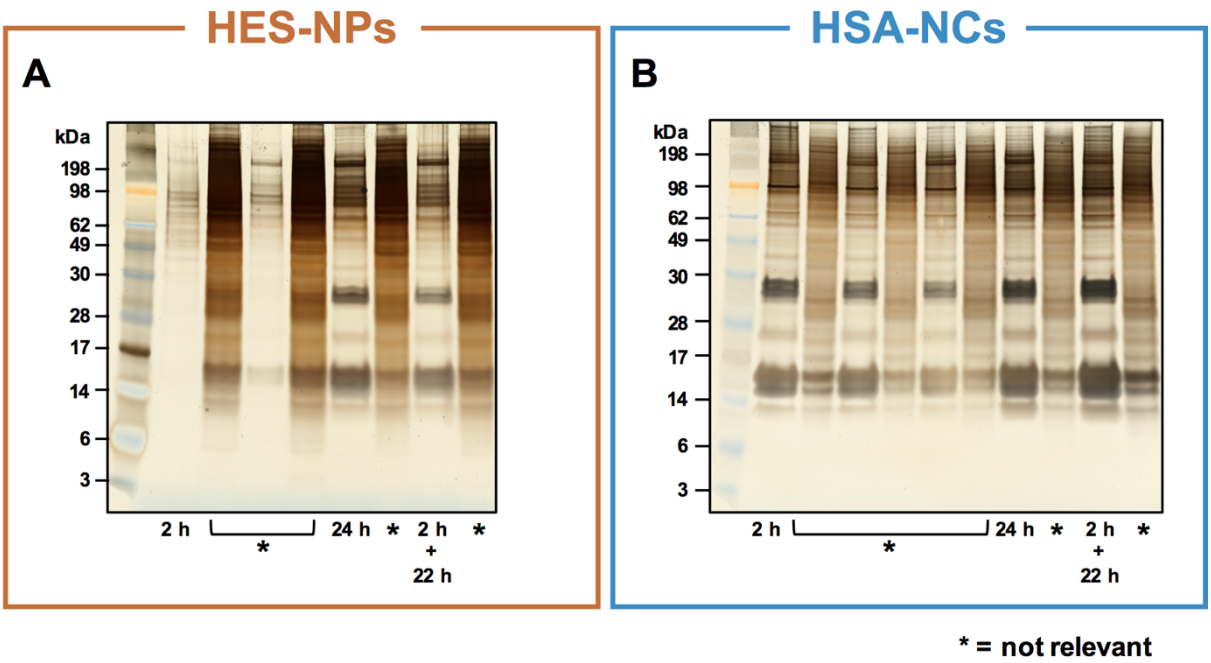

Figure S5.11: SDS-PAGE of protein corona samples. Protein corona samples associated with HES-NPs **(A)** and HSA-NCs **(B)** were analyzed by SDS-PAGE and silver staining. Samples marked with an asterisk (*) are not relevant for the experiment but were included for completeness of the gel.

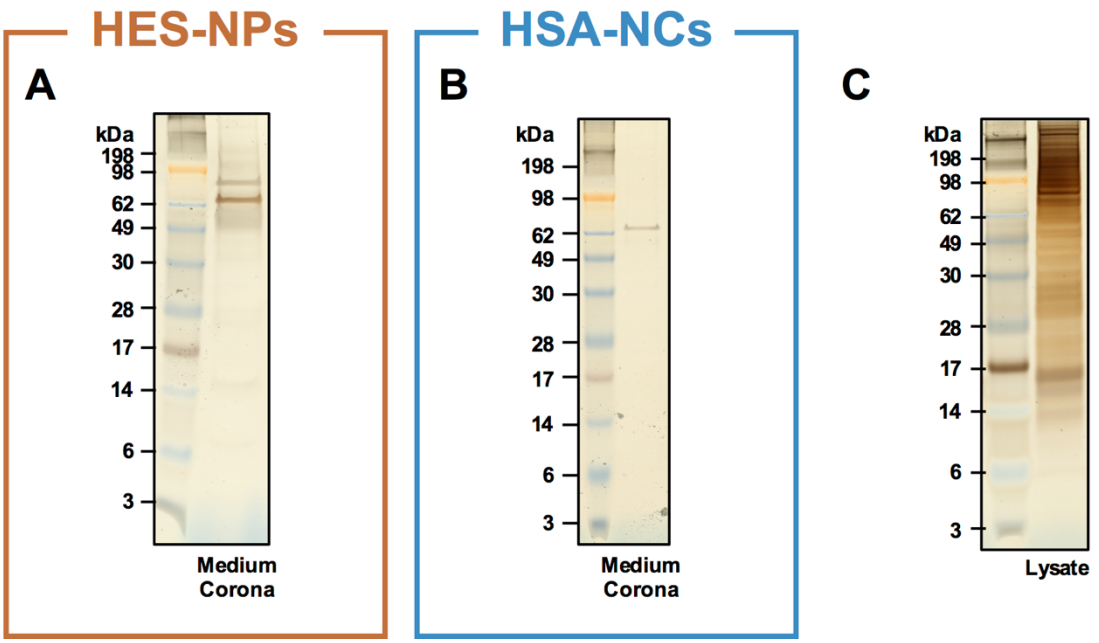

Figure S5.12: SDS-PAGE of control samples and cell lysate. HES-NPs **(A)** and HSA-NCs **(B)** were incubated in cell culture medium to prepare a protein corona as a control. The control samples and the cell lysate **(C)** were analyzed by SDS-PAGE and silver staining.

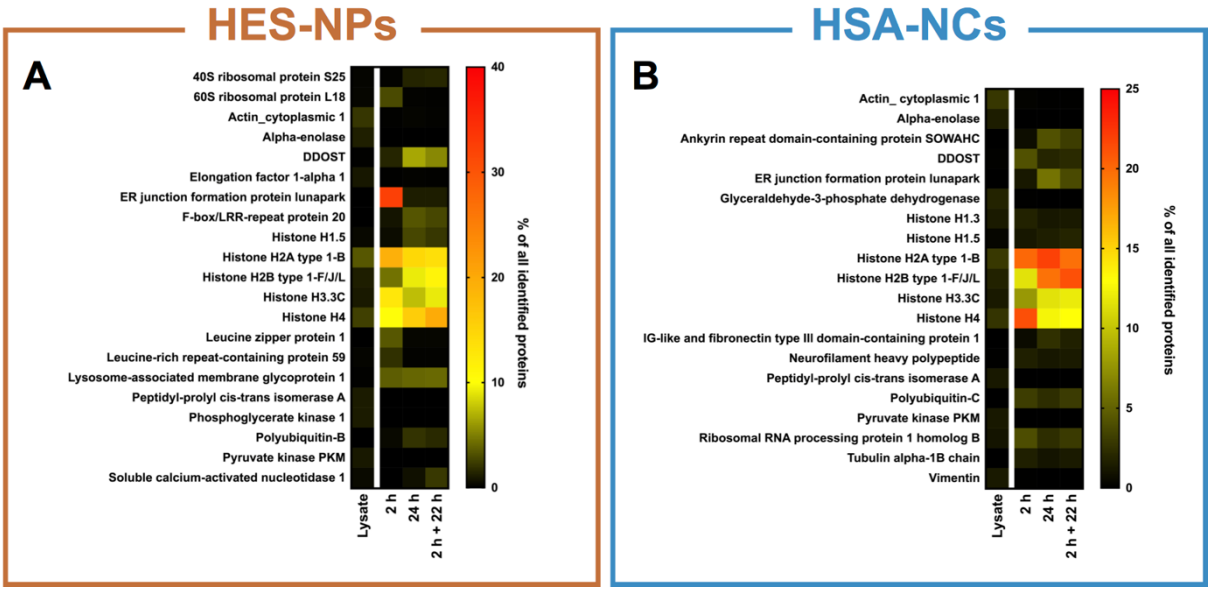

Figure S5.13: TOP proteins identified in lysate and protein corona samples by quantitative LC-MS proteomics. DC2.4 cells were incubated with 250 µg ml^{-1} HES-NPs **(A)** and HSA-NCs **(B)** for different time points (2 h, 24 h, 2 h + 22 h). The cells were harvested and lysed by sonification. The nanocarriers were magnetically separated from the cell debris and washed three times with PBS and centrifugation. The proteins were desorbed with 2% SDS and forwarded to LC-MS proteomic analysis. Cell lysate without nanoparticles, as obtained after lysis, served as a control. The heat maps list the 10 most abundant proteins for each condition, resulting in 21 top proteins for HES-NPs and 20 top proteins for HSA-NCs. The values are shown as the percentage of all identified proteins.

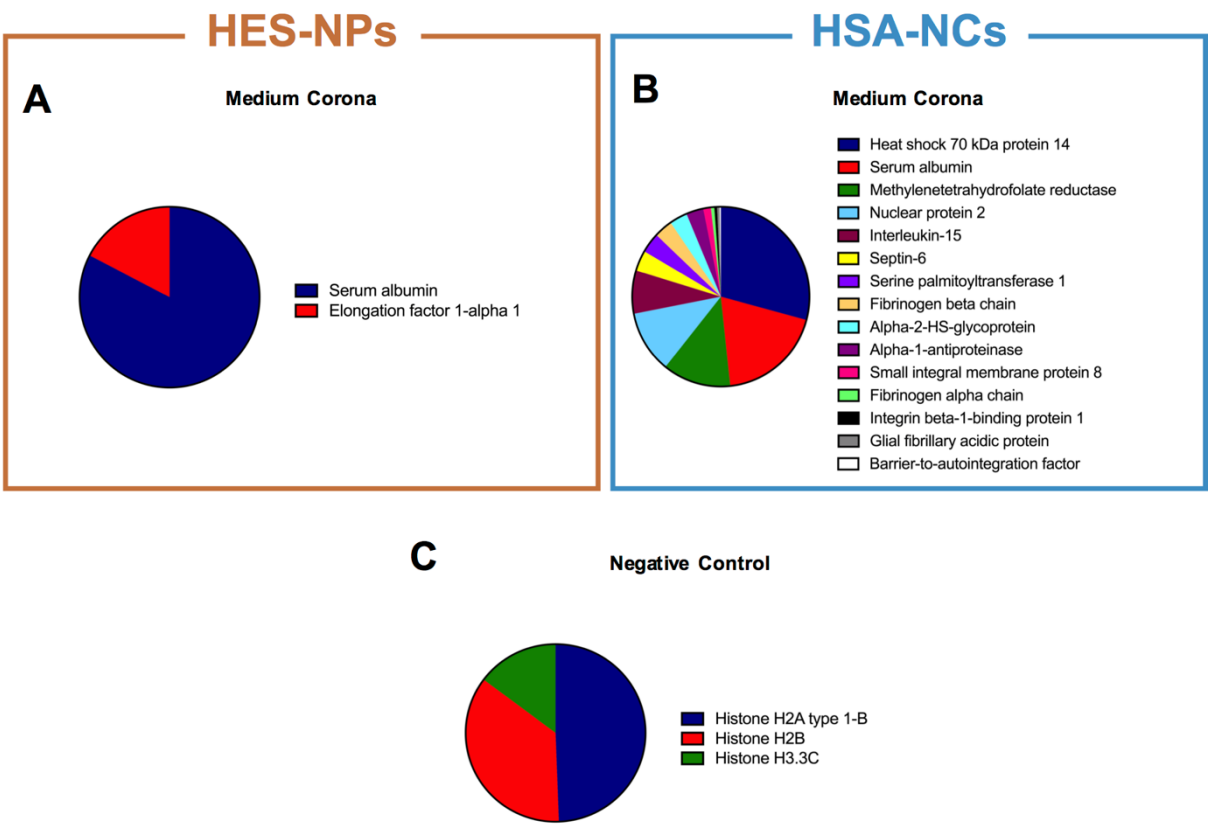

Figure S5.14: Quantitative LC-MS proteomics analysis of control samples. HES-NPs **(A)** and HSA-NCs **(B)** were incubated in the cell culture medium to prepare a protein corona as a control. For the negative control **(C)**, the protein corona workflow was performed, but without nanocarriers. The pie charts show all proteins detected in the samples.

Table S5.1: List of enriched proteins associated with the protein corona formed on HES-NPs. The proteins associated with the protein corona on HES-NPs were compared to the proteins identified in the cell lysate without nanoparticle incubation. All proteins enriched 1.5-fold compared to the lysate proteins are listed with their respective Uniprot accession, Uniprot ID, and protein name.

HES-NPs

Uniprot Accession	Uniprot ID	Protein Name
Q9CY73	RM44_MOUSE	39S ribosomal protein L44_ mitochondrial
P62264	RS14_MOUSE	40S ribosomal protein S14
P62270	RS18_MOUSE	40S ribosomal protein S18
P62852	RS25_MOUSE	40S ribosomal protein S25
P62862	RS30_MOUSE	40S ribosomal protein S30
P53026	RL10A_MOUSE	60S ribosomal protein L10a
P35980	RL18_MOUSE	60S ribosomal protein L18
Q8BP67	RL24_MOUSE	60S ribosomal protein L24
Q9D1R9	RL34_MOUSE	60S ribosomal protein L34
P61514	RL37A_MOUSE	60S ribosomal protein L37a
Q8VEH3	ARL8A_MOUSE	ADP-ribosylation factor-like protein 8A
P48962	ADT1_MOUSE	ADP/ATP translocase 1
Q8C0J6	SWAHC_MOUSE	Ankyrin repeat domain-containing protein SOWAHC
P30355	AL5AP_MOUSE	Arachidonate 5-lipoxygenase-activating protein
Q7SIG6	ASAP2_MOUSE	Arf-GAP with SH3 domain_ ANK repeat and PH domain-containing protein 2
Q8CDM1	ATAD2_MOUSE	ATPase family AAA domain-containing protein 2
O54962	BAF_MOUSE	Barrier-to-autointegration factor
Q8BHX3	BOREA_MOUSE	Borealin
P97929	BRCA2_MOUSE	Breast cancer type 2 susceptibility protein homolog
Q8BM92	CADH7_MOUSE	Cadherin-7
P55097	CATK_MOUSE	Cathepsin K
Q63918	CAVN2_MOUSE	Caveolae-associated protein 2
P28033	CEBPB_MOUSE	CCAAT/enhancer-binding protein beta
Q9CXS4	CENPV_MOUSE	Centromere protein V
Q6P5D4	CP135_MOUSE	Centrosomal protein of 135 kDa
Q924Z4	CERS2_MOUSE	Ceramide synthase 2
P23198	CBX3_MOUSE	Chromobox protein homolog 3
Q61686	CBX5_MOUSE	Chromobox protein homolog 5
E9Q5M6	CFA44_MOUSE	Cilia- and flagella-associated protein 44
Q9QYC3	BHA15_MOUSE	Class A basic helix-loop-helix protein 15
Q9QZQ8	H2AY_MOUSE	Core histone macro-H2A.1
O88833	CP4AA_MOUSE	Cytochrome P450 4A10
Q45VK7	DYHC2_MOUSE	Cytoplasmic dynein 2 heavy chain 1
Q8BMK4	CKAP4_MOUSE	Cytoskeleton-associated protein 4
Q04750	TOP1_MOUSE	DNA topoisomerase 1
Q01320	TOP2A_MOUSE	DNA topoisomerase 2-alpha
Q64511	TOP2B_MOUSE	DNA topoisomerase 2-beta
Q91WN1	DNJC9_MOUSE	DnaJ homolog subfamily C member 9
O54734	OST48_MOUSE	Dolichyl-diphosphooligosaccharide--protein glycosyltransferase 48 kDa subunit
Q91YQ5	RPN1_MOUSE	Dolichyl-diphosphooligosaccharide--protein glycosyltransferase subunit 1
P61804	DAD1_MOUSE	Dolichyl-diphosphooligosaccharide--protein glycosyltransferase subunit DAD1
P46978	STT3A_MOUSE	Dolichyl-diphosphooligosaccharide--protein glycosyltransferase subunit STT3A
O70263	LNX1_MOUSE	E3 ubiquitin-protein ligase LNX
Q7TPM3	TRI17_MOUSE	E3 ubiquitin-protein ligase TRIM17
Q5XFR0	EPAB2_MOUSE	Embryonic polyadenylate-binding protein 2
Q7TQ95	LNP_MOUSE	Endoplasmic reticulum junction formation protein lunapark
P10630	IF4A2_MOUSE	Eukaryotic initiation factor 4A-II
Q8R1B4	EIF3C_MOUSE	Eukaryotic translation initiation factor 3 subunit C
Q9CZV8	FXL20_MOUSE	F-box/LRR-repeat protein 20
Q920B9	SP16H_MOUSE	FACT complex subunit SPT16
Q08943	SSRP1_MOUSE	FACT complex subunit SSRP1
P36536	SAR1A_MOUSE	GTP-binding protein SAR1a
Q9CY66	GAR1_MOUSE	H/ACA ribonucleoprotein complex subunit 1
Q9CRB2	NHP2_MOUSE	H/ACA ribonucleoprotein complex subunit 2
Q9ESX5	DKC1_MOUSE	H/ACA ribonucleoprotein complex subunit DKC1
Q9CQN1	TRAP1_MOUSE	Heat shock protein 75 kDa_ mitochondrial
P11499	HS90B_MOUSE	Heat shock protein HSP 90-beta
P17095	HMGA1_MOUSE	High mobility group protein HMG-I/HMG-Y
Q5SVQ0	KAT7_MOUSE	Histone acetyltransferase KAT7
P10922	H10_MOUSE	Histone H1.0
P15864	H12_MOUSE	Histone H1.2
P43277	H13_MOUSE	Histone H1.3
P43276	H15_MOUSE	Histone H1.5
C0HKE1	H2A1B_MOUSE	Histone H2A type 1-B
P0C0S6	H2AZ_MOUSE	Histone H2A.Z
P70696	H2B1A_MOUSE	Histone H2B type 1-A
P10853	H2B1F_MOUSE	Histone H2B type 1-F/J/L
Q64524	H2B2E_MOUSE	Histone H2B type 2-E
P02301	H3C_MOUSE	Histone H3.3C
P62806	H4_MOUSE	Histone H4
Q3U9G9	LBR_MOUSE	Lamin-B receptor
Q61033	LAP2A_MOUSE	Lamina-associated polypeptide 2_ isoforms alpha/zeta
Q8R4U7	LUZP1_MOUSE	Leucine zipper protein 1
Q922Q8	LRC59_MOUSE	Leucine-rich repeat-containing protein 59
P11438	LAMP1_MOUSE	Lysosome-associated membrane glycoprotein 1
P31996	CD68_MOUSE	Macrosialin
Q91VE6	MK67I_MOUSE	MKI67 FHA domain-interacting nucleolar phosphoprotein
Q64669	NQO1_MOUSE	NAD(P)H dehydrogenase [quinone] 1
P57716	NICA_MOUSE	Nicastrin
Q99P88	NU155_MOUSE	Nuclear pore complex protein Nup155
E9Q5C9	NOLC1_MOUSE	Nucleolar and coiled-body phosphoprotein 1
Q9D6Z1	NOP56_MOUSE	Nucleolar protein 56
P25976	UBF1_MOUSE	Nucleolar transcription factor 1
Q99JF8	PSIP1_MOUSE	PC4 and SFRS1-interacting protein
Q8BU03	PWP2_MOUSE	Periodic tryptophan protein 2 homolog
P0CG49	UBB_MOUSE	Polyubiquitin-B
P48678	LMNA_MOUSE	Prelamin-A/C
Q6PGB8	SMCA1_MOUSE	Probable global transcription activator SNF2L1
E9PVX6	KI67_MOUSE	Proliferation marker protein Ki-67
Q8CJF7	ELYS_MOUSE	Protein ELYS
Q6PKN7	INCA1_MOUSE	Protein INCA1
Q6NS46	RRP5_MOUSE	Protein RRP5 homolog
Q9JLR1	S61A2_MOUSE	Protein transport protein Sec61 subunit alpha isoform 2
Q9CQS8	SC61B_MOUSE	Protein transport protein Sec61 subunit beta
Q3UZD5	PRDM6_MOUSE	Putative histone-lysine N-methyltransferase PRDM6
P63001	RAC1_MOUSE	Ras-related C3 botulinum toxin substrate 1
P62835	RAP1A_MOUSE	Ras-related protein Rap-1A
Q8VE37	RCC1_MOUSE	Regulator of chromosome condensation
Q99M28	RNPS1_MOUSE	RNA-binding protein with serine-rich domain 1
Q8CJ40	CROCC_MOUSE	Rootletin
P35550	FBRL_MOUSE	rRNA 2'-O-methyltransferase fibrillarin
E9PZQ0	RYR1_MOUSE	Ryanodine receptor 1
E9Q401	RYR2_MOUSE	Ryanodine receptor 2
Q6ZWQ7	SPCS3_MOUSE	Signal peptidase complex subunit 3
P47758	SRPRB_MOUSE	Signal recognition particle receptor subunit beta
Q8K596	NAC2_MOUSE	Sodium/calcium exchanger 2
Q8VCF1	CANT1_MOUSE	Soluble calcium-activated nucleotidase 1
Q9R0M3	SRPX_MOUSE	Sushi-repeat-containing protein SRPX
Q91ZW3	SMCA5_MOUSE	SWI/SNF-related matrix-associated actin-dependent regulator of chromatin subfamily A member 5
Q62465	VAT1_MOUSE	Synaptic vesicle membrane protein VAT-1 homolog
Q8C1A5	THOP1_MOUSE	Thimet oligopeptidase
Q921T2	TOIP1_MOUSE	Torsin-1A-interacting protein 1
P05213	TBA1B_MOUSE	Tubulin alpha-1B chain
Q9Z277	BAZ1B_MOUSE	Tyrosine-protein kinase BAZ1B
Q8C7V3	UTP15_MOUSE	U3 small nucleolar RNA-associated protein 15 homolog
Q8R3Y5	CS047_MOUSE	Uncharacterized protein C19orf47 homolog
E9Q634	MYO1E_MOUSE	Unconventional myosin-Ie
P51863	VA0D1_MOUSE	V-type proton ATPase subunit d 1
Q3TWF6	WDR70_MOUSE	WD repeat-containing protein 70
Q5HZG9	ZN488_MOUSE	Zinc finger protein 488

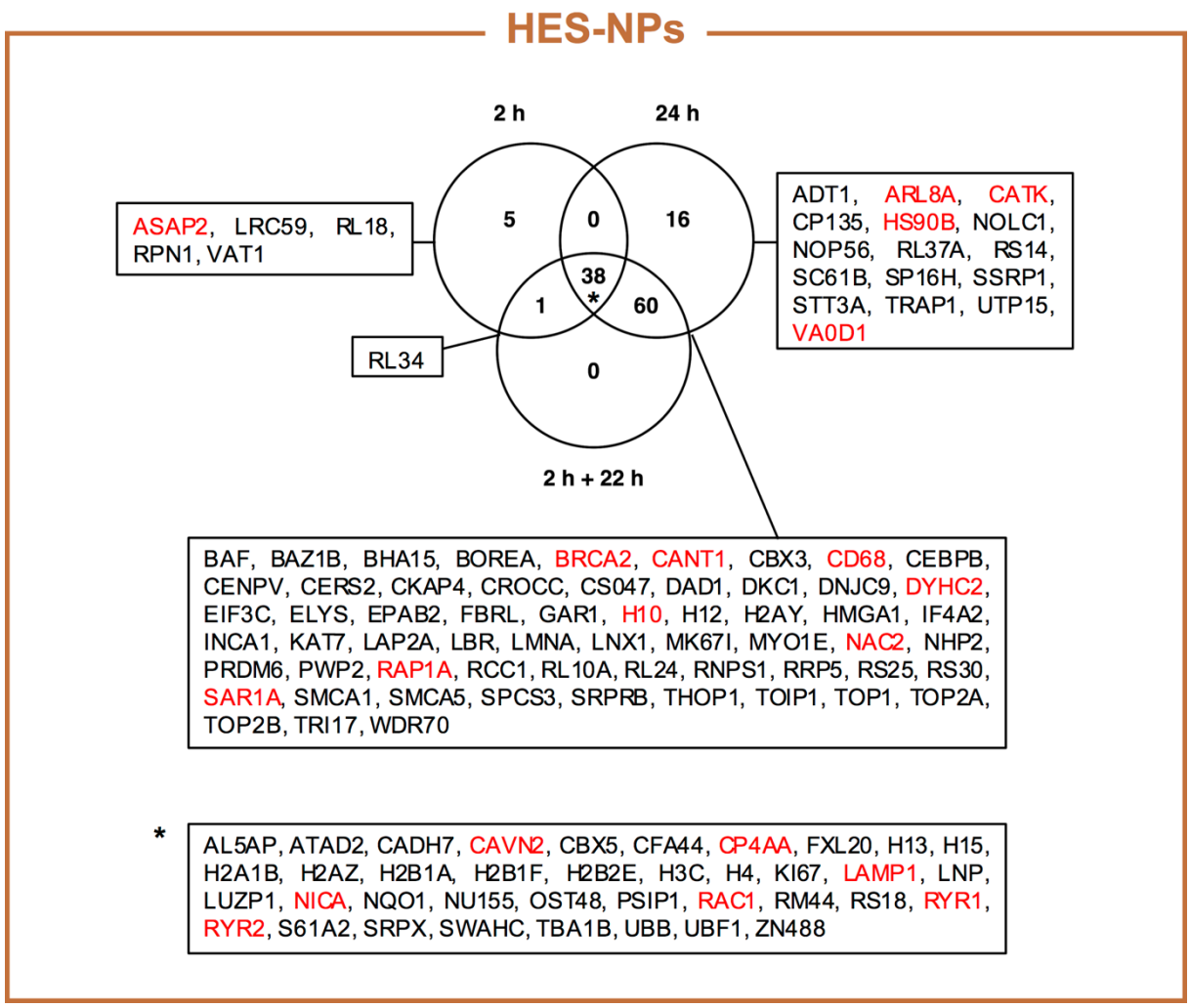

Figure S5.15: Enriched proteins of the HES-NP protein corona compared between time points. The enriched corona proteins associated with HES-NPs were compared in regards to the time points by a Venn diagram. The proteins unique to each section of the Venn diagram are listed with their Uniprot ID. The intracellular trafficking proteins, as seen in Figure 5.5 are marked in red.

Table S5.2: List of enriched proteins associated with the protein corona formed on HSA-NCs. The proteins associated with the protein corona on HSA-NCs were compared to the proteins identified in the cell lysate without nanoparticle incubation. All proteins enriched 1.5-fold compared to the lysate proteins are listed with their respective Uniprot accession, Uniprot ID, and protein name.

HES-NPs

Uniprot Accession	Uniprot ID	Protein Name
P63276	RS17_MOUSE	40S ribosomal protein S17
P62270	RS18_MOUSE	40S ribosomal protein S18
P62852	RS25_MOUSE	40S ribosomal protein S25
P61514	RL37A_MOUSE	60S ribosomal protein L37a
Q70FJ1	AKAP9_MOUSE	A-kinase anchor protein 9
Q8VEH3	ARL8A_MOUSE	ADP-ribosylation factor-like protein 8A
E9Q4F7	ANR11_MOUSE	Ankyrin repeat domain-containing protein 11
Q8BLB8	AN34C_MOUSE	Ankyrin repeat domain-containing protein 34C
Q8C0J6	SWAHC_MOUSE	Ankyrin repeat domain-containing protein SOWAHC
P30355	AL5AP_MOUSE	Arachidonate 5-lipoxygenase-activating protein
Q7SIG6	ASAP2_MOUSE	Arf-GAP with SH3 domain_ ANK repeat and PH domain-containing protein 2
O54962	BAF_MOUSE	Barrier-to-autointegration factor
P97929	BRCA2_MOUSE	Breast cancer type 2 susceptibility protein homolog
Q80TJ1	CAPS1_MOUSE	Calcium-dependent secretion activator 1
P55097	CATK_MOUSE	Cathepsin K
Q99LM2	CK5P3_MOUSE	CDK5 regulatory subunit-associated protein 3
Q61686	CBX5_MOUSE	Chromobox protein homolog 5
P59242	CING_MOUSE	Cingulin
Q9QYC3	BHA15_MOUSE	Class A basic helix-loop-helix protein 15
Q810N9	CC172_MOUSE	Coiled-coil domain-containing protein 172
Q810U5	CCD50_MOUSE	Coiled-coil domain-containing protein 50
Q9QZQ8	H2AY_MOUSE	Core histone macro-H2A.1
Q04750	TOP1_MOUSE	DNA topoisomerase 1
Q01320	TOP2A_MOUSE	DNA topoisomerase 2-alpha
Q64511	TOP2B_MOUSE	DNA topoisomerase 2-beta
O54734	OST48_MOUSE	Dolichyl-diphosphooligosaccharide--protein glycosyltransferase 48 kDa subunit
Q8K4Q6	NEIL1_MOUSE	Endonuclease 8-like 1
Q7TQ95	LNP_MOUSE	Endoplasmic reticulum junction formation protein lunapark
Q920B9	SP16H_MOUSE	FACT complex subunit SPT16
Q00422	GABPA_MOUSE	GA-binding protein alpha chain
B2RSH2	GNAI1_MOUSE	Guanine nucleotide-binding protein G(i) subunit alpha-1
Q8K259	GIN1_MOUSE	Gypsy retrotransposon integrase-like protein 1
Q9CY66	GAR1_MOUSE	H/ACA ribonucleoprotein complex subunit 1
Q9CRB2	NHP2_MOUSE	H/ACA ribonucleoprotein complex subunit 2
Q9ESX5	DKC1_MOUSE	H/ACA ribonucleoprotein complex subunit DKC1
P16627	HS71L_MOUSE	Heat shock 70 kDa protein 1-like
P17095	HMGA1_MOUSE	High mobility group protein HMG-I/HMG-Y
P10922	H10_MOUSE	Histone H1.0
P15864	H12_MOUSE	Histone H1.2
P43277	H13_MOUSE	Histone H1.3
P43276	H15_MOUSE	Histone H1.5
Q07133	H1T_MOUSE	Histone H1t
C0HKE1	H2A1B_MOUSE	Histone H2A type 1-B
P0C0S6	H2AZ_MOUSE	Histone H2A.Z
P27661	H2AX_MOUSE	Histone H2AX
P10853	H2B1F_MOUSE	Histone H2B type 1-F/J/L
P02301	H3C_MOUSE	Histone H3.3C
P62806	H4_MOUSE	Histone H4
Q3KNY0	IGFN1_MOUSE	Immunoglobulin-like and fibronectin type III domain-containing protein 1
Q80WE4	KI20B_MOUSE	Kinesin-like protein KIF20B
Q52KG5	KI26A_MOUSE	Kinesin-like protein KIF26A
Q3U9G9	LBR_MOUSE	Lamin-B receptor
Q61029	LAP2B_MOUSE	Lamina-associated polypeptide 2_ isoforms beta/delta/epsilon/gamma
Q8R4U7	LUZP1_MOUSE	Leucine zipper protein 1
P31996	CD68_MOUSE	Macrosialin
Q91VE6	MK67I_MOUSE	MKI67 FHA domain-interacting nucleolar phosphoprotein
P19246	NFH_MOUSE	Neurofilament heavy polypeptide
Q9Z0J0	NPC2_MOUSE	NPC intracellular cholesterol transporter 2
E9Q5C9	NOLC1_MOUSE	Nucleolar and coiled-body phosphoprotein 1
Q9D6Z1	NOP56_MOUSE	Nucleolar protein 56
P25976	UBF1_MOUSE	Nucleolar transcription factor 1
P09405	NUCL_MOUSE	Nucleolin
P70206	PLXA1_MOUSE	Plexin-A1
P70208	PLXA3_MOUSE	Plexin-A3
P11103	PARP1_MOUSE	Poly [ADP-ribose] polymerase 1
P0CG50	UBC_MOUSE	Polyubiquitin-C
Q921N6	DDX27_MOUSE	Probable ATP-dependent RNA helicase DDX27
E9PVX6	KI67_MOUSE	Proliferation marker protein Ki-67
Q8CG70	P3H3_MOUSE	Prolyl 3-hydroxylase 3
Q6PKN7	INCA1_MOUSE	Protein INCA1
Q6NS46	RRP5_MOUSE	Protein RRP5 homolog
Q8VE37	RCC1_MOUSE	Regulator of chromosome condensation
Q91YK2	RRP1B_MOUSE	Ribosomal RNA processing protein 1 homolog
P35550	FBRL_MOUSE	rRNA 2'-O-methyltransferase fibrillarin
O55143	AT2A2_MOUSE	Sarcoplasmic/endoplasmic reticulum calcium ATPase 2
Q61045	SIM1_MOUSE	Single-minded homolog 1
Q8BZX4	SREK1_MOUSE	Splicing regulatory glutamine/lysine-rich protein 1
Q91ZW3	SMCA5_MOUSE	SWI/SNF-related matrix-associated actin-dependent regulator of chromatin subfamily A member 5
Q7TMY4	THOC7_MOUSE	THO complex subunit 7 homolog
Q921T2	TOIP1_MOUSE	Torsin-1A-interacting protein 1
P05213	TBA1B_MOUSE	Tubulin alpha-1B chain
Q91WQ3	SYYC_MOUSE	Tyrosine--tRNA ligase_ cytoplasmic
Q9Z277	BAZ1B_MOUSE	Tyrosine-protein kinase BAZ1B
Q921Y2	IMP3_MOUSE	U3 small nucleolar ribonucleoprotein protein IMP3
P21271	MYO5B_MOUSE	Unconventional myosin-Vb
Q3TWF6	WDR70_MOUSE	WD repeat-containing protein 70
E9Q784	ZC3HD_MOUSE	Zinc finger CCCH domain-containing protein 13
Q80SU3	ZAR1_MOUSE	Zygote arrest protein 1

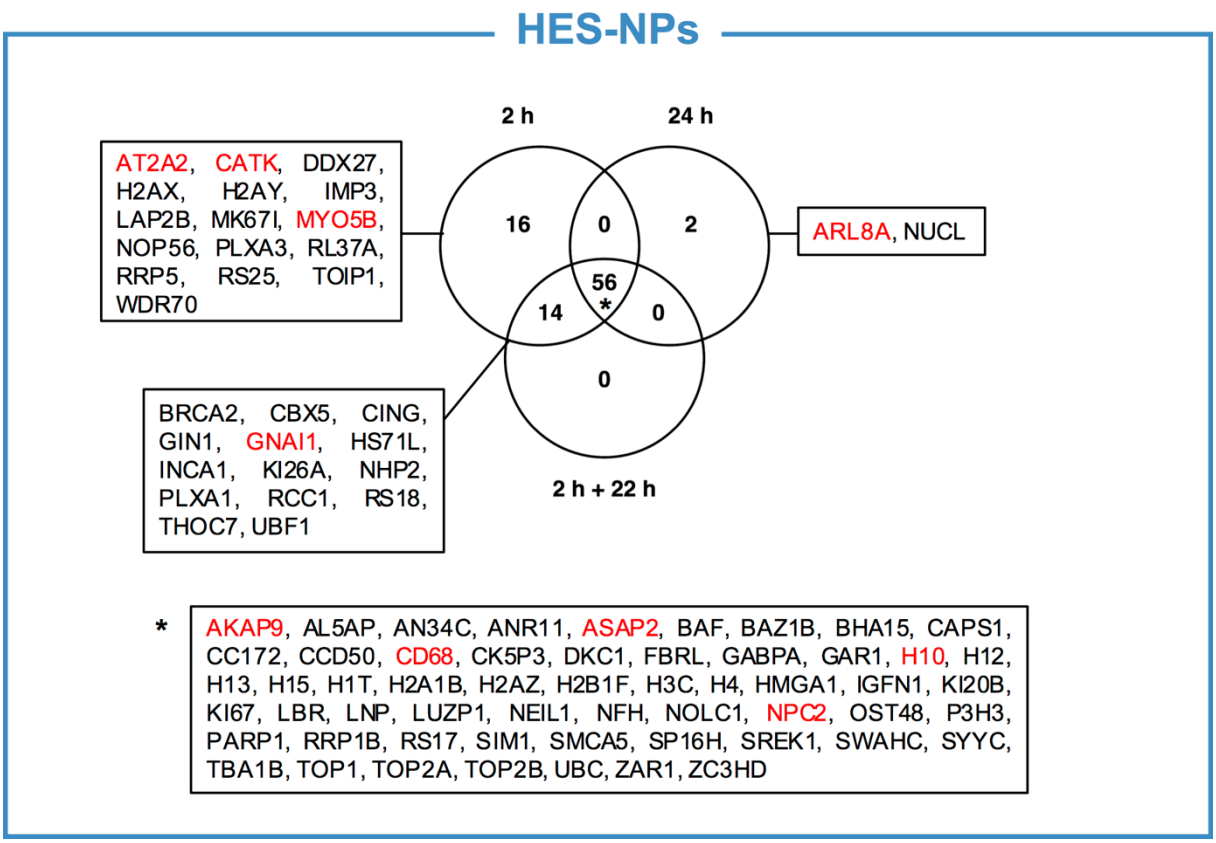

Figure S5.16: Enriched proteins of the HSA-NC protein corona compared between time points. The enriched corona proteins associated with HSA-NCs were compared in regards to the time points by a Venn diagram. The proteins unique to each section of the Venn diagram are listed with their Uniprot ID. The intracellular trafficking proteins, as seen in Figure 5.5 are marked in red.

6. Higher loading of gold nanoparticles in PAD mesenchymal-like stromal cells leads to a decreased exocytosis

Aim:

Exocytosis of NPs is an important cellular process that needs to be kept reduced for cell labeling with NPs for visualization purposes. This study compared two loading protocols of gold NPs regarding exocytosis in stromal cells. The protocols varied the uptake time and the loading amount. To explain the different exocytosis routes in both protocols, label-free quantitative LC-MS proteomics was used to investigate the intracellular protein corona.

[4] ___, ___, ___, **da Costa Marques, R.**, ___, ___, ___, ___, ___, ___. Higher Loading of Gold Nanoparticles in PAD Mesenchymal-like Stromal Cells Leads to a Decreased Exocytosis. *Cells*, **2022**, *11*(15), 2323.

Contributions:

I performed the preparation of the intracellular protein corona and LC-MS data evaluation. I created Figures 6.3, 6.4, and Tables S6.1-6.10 in the following version. ___ conducted the Zeta-potential measurements, the cell experiments for uptake and exocytosis, the ICP-OES measurements, protein quantification, SDS-PAGE, LC-MS sample preparation, and the LC-MS measurements. ___ wrote the manuscript and created all other figures in the following version. ___ edited the figures for the original manuscript. I edited all the figures for the following version. ___, ___, and ___ provided the nanoparticles. ___ and ___ provided the cells. ___ performed the DLS measurements. ___ performed the TEM imaging. The project was supervised by ___, ___, ___, and ___.

6.1 Abstract

Cell therapy is an important new method in medicine and is being used for the treatment of an increasing number of diseases. The challenge here is the precise tracking of cells in the body and their visualization. One method to visualize cells more easily with current methods is their labeling with nanoparticles before injection. However, for a safe and sufficient cell labeling, the nanoparticles need to remain in the cell and not be exocytosed. Here, we test a glucose-PEG-coated gold nanoparticle for the use of such a cell labeling. To this end, we investigated the nanoparticle exocytosis behavior from PLX-PAD cells, a cell type currently in clinical trials as a potential therapeutic agent. We showed that the amount of exocytosed gold from the cells was influenced by the uptake time and loading amount. This observation will facilitate the safe labeling of cells with nanoparticles in the future and contribute to stem cell therapy research.

6.2 Introduction

The idea of using cells as a therapeutic agent for various diseases has widely expanded over the past years [255]. However, the therapeutic mechanisms and the distribution of the cells in the organism often remain unclear. As methods for tracking cells in the human body are very limited, imaging and contrast agents like nanoparticles have been developed to increase the visibility of the cells in vivo [256-258]. To date, cell tracking is often performed using either radionuclides for scintigraphy, PET (positron emission tomography), and SPECT (single photon emission computer tomography), or using superparamagnetic iron oxide nanoparticles for MRI (magnetic resonance imaging) [259-261]. Radionuclide imaging has the main advantage of high sensitivity and very small amounts of label can be detected. However, radionuclides with short half-lives make this method very expensive and make long-term tracking impossible [260]. On the other hand, MRI does not use ionizing radiation and tissue can be well visualized. Nevertheless, this method is also relatively cost-intensive and the acquisition time is slow [260-261]. Therefore, there is increasing effort to develop cell tracking markers for CT (computed tomography). These have the benefit that the technology is cost-effective with a fast temporal resolution [261]. Thereby, gold nanoparticles or gold-iron nanoparticles have proven to be very promising tracking tools. Gold features strong contrast properties for CT imaging and, in combination with iron for MRI, a wide range of analysis methods can be covered when combining both materials [257]. Furthermore, gold nanoparticles are already very well studied materials of low toxicity to cells, making them even more promising as a contrast agent for cell therapy labeling [262-264]. However, for good CT tracking, a high amount of gold nanoparticles need to be taken up by the cells and, for long-term tracking, the nanoparticles need to remain stable in the cells [265]. While high loading of cells could previously be achieved, the reduction of the exocytosis of gold nanoparticles from cells still remains a challenge [265-267].

One type of cell that is currently considered as a potential therapeutic agent against different diseases is the PLX-PAD cell [268-278]. PLX-PAD cells are a cell therapy product under development containing placental expanded (PLX) placenta-derived mesenchymal-like adherent stromal cells [270, 275, 279]. It has previously been shown that these cells secrete relevant factors as a response to muscle trauma or inflammation to trigger the natural repair mechanisms of the body [270]. Therefore, these cells are currently used in different clinical studies for the treatment of injured muscle.

For a combination of particles and cells to be effective as a therapeutic and imaging reagent, the particles must remain stable in the cells. One factor that can influence the uptake in cells is the so-called protein corona. Furthermore, surface modifications and the size and shape of the particles - among other things - can affect the uptake and exocytosis rate of particles [173,

[280-281]. When nanoparticles come into contact with biological fluids, proteins directly attach to the surface of the particles and form a protein corona. Previously, it has been shown that the protein corona can alter the uptake of particles into cells, but it can also influence the exocytosis rate of particles from cells [78, 173]. To use the nanoparticles as a reliable imaging reagent, it is crucial to keep the exocytosis rate as low as possible to allow long-term tracking of the cells. Besides influencing the uptake into cells, changes in the protein corona composition can also be used to learn about the intracellular pathway followed by the nanoparticles. The type of proteins bound in the corona, therefore, reflects a fingerprint of the intracellular pathway taken by the nanoparticles [183, 203]. This intracellular protein corona can be used to predict whether particles are more likely to be exocytosed or to remain inside the cell.

In this study, we analyzed the exocytosis rate of glucose-coated and PEGylated gold nanoparticles from loaded PLX-PAD cells. As the combination of cells and particles should be used in the future for long-term tracking of cells in the human body, it is important to reach a high loading efficiency together with a low exocytosis rate of the GNPs from the cells. Here, we tested two different in vitro loading protocols - one with a lower loading efficiency and another with a higher loading efficiency of GNPs. Afterwards, we analyzed the amount of exocytosed gold and characterized the intracellular protein corona to predict which protocol reached a more stable loading of nanoparticles in the cells.

6.3 Materials and methods

Synthesis of GNPs. PEGylated and glucose coated gold nanoparticles (GNPs) were synthesized according to previously described methods in a three-step process [257]. The nanoparticles were synthesized by heating $HAuCl_4$ solution (50%; 82.345 ml) in ultrapure water (39.78 l) until boiling. Then sodium citrate solution (10%; 803.556 ml) was introduced and the solution was stirred for 10 min at 1200 rpm. Particles were purified and concentrated via cross-flow filtrations with a 10 kDa PES membrane to a final volume of 1193.4 ml. In a second step PEG (PEG7, 50 mg ml^{-1}, 198.9 ml) was added and together with the particles stirred for 30 min at 1200 rpm followed by an incubation at 4 °C for 24 h. Purification was again performed via cross-flow filtration reaching a final volume of 688.5 ml. In the third step, the glucose was attached to the nanoparticles. Therefore, the PEGylated particles were stirred together with 1-Ethyl-3-(3-dimethylaminopropyl)carbodiimide (EDC; 0.2 M; 68.85 ml) and N-hydroxysuccinimide (NHS; 0.2 M; 344.25 ml) for 30 min at 1200 rpm. Then, the active ester from PEG can react in an amidation reaction with the NH2 groups of the glucosamine (24 mg ml^{-1}; 688.5 ml). After the addition of the glucosamine, the solution was stirred again for 30 min at 1200 rpm and then incubated at 4 °C for 24 h. Final purification was again performed by cross flow filtration and particles were filtrated through a 0.22 µm filter.

Characterization of GNPs. After the synthesis, the gold concentration of the nanoparticles was determined by ICP-OES. The size of the particles was determined via multi-angle DLS and TEM [282]. **DLS.** For multi-angle DLS an ALV spectrometer consisting of a goniometer and an ALV- 5004 multiple-tau full digital correlator (320 channels) was used. This allows measurements over an angular range from 30° to 150°. A He-Ne laser (wavelength of 632.8 nm) was used as the light source. Temperature was adjusted through a thermostat from Julabo. Before the measurement, the GNPs were filtrated through a 0.2 µm filter so that no larger particles or dust interfered with the measurement. **TEM.** TEM images were taken with a Jeol JEM 1400 at 120 kV to determine the primary size. For the drop casting, undiluted GNPs were added on a 300 mash copper grid coated with a 20-30 nm carbon layer. Excess sample dispersion was blotted with a filter paper [282]. The size was determined using Image J software and counting 100 particles. **ICP-OES.** The gold concentration was determined via ICP-OES (SpectroGreen, Spectro/Ametek). 10 µl GNPs were diluted in 1 ml aqua regia (3:1 hydrochloric acid: nitric acid) for digestion of nanoparticles. Afterwards, the samples were diluted up to 10 ml with MiliQ water, and the gold concentration was determined with ICP-OES. The calibration curve was prepared by using 0.1, 0.5, 1, 5, and 20 ppm gold standard solution (stock 1 000 mg l^{-1} Au TraceCERT®, Sigma Aldrich).

Production and Cell Culture of PLX-PAD Cells. PLX-PAD cells were produced by Pluristem Therapeutics, Ltd. (Haifa, Israel). As previously described [268, 279], production of PLX PAD cells was performed in a state-of-the-art clean room facility according to GMP regulations. Human placentas were collected from healthy donors and cut into pieces. After enzymatic digestion of the tissue, cells were seeded as 2D cultures in a culture flask followed by 3D cultivation in a bioreactor. Before characterization of the cells, 3D cultures were harvested and cryopreserved in liquid nitrogen. Characterization was performed by staining the cells with MSC-positive and MSC-negative markers and analyzed by flow cytometry [275].

Cell culture. PLX-PAD cells were cultured in Dulbecco's modified eagle medium (DMEM) supplemented with 10% FBS, 100 U ml^{-1} penicillin, 100 mg ml^{-1} streptomycin, and 2 mM glutamine. Viability and count were measured with trypan blue by an automated cell counter (TC10, Bio-Rad). Cells were grown in a humidified incubator at 37 °C and 5% CO_2. Cells were either thawed one day before the experiment and seeded at the recommended density for the experiments or cultured in flasks and sub-cultured once a week when they reached around 80% confluence.

Uptake and Exocytosis. Two different protocols for the uptake of GNPs were tested. For both protocols, the PLX-PAD cells were seeded at a density of 500 000 cells per well in a six-well plate (Greiner, Pleidelsheim, Germany) and incubated overnight. All incubation steps were performed in a humidified incubator (37 °C, 5% CO_2). Afterwards, the cells were incubated with a nanoparticle solution of 300 µg ml^{-1} in isotone NaCl (B.Braun, Melsungen, Germany) for 30 min (low loading protocol) or with 300 µg ml^{-1} nanoparticles in DMEM (Thermo Fisher Scientific, Waltham, MA, USA) with 10% FBS for 24 h (high loading protocol). After the incubation time, the cells were washed twice with PBS (Thermo Fisher Scientific, Waltham, MA, USA) and then either incubated again in DMEM with 10% FBS for exocytosis measurements or harvested with Trypsin-EDTA (Thermo Fisher Scientific, Waltham, MA, USA) for uptake measurements. The exocytosis of the GNPs was also determined using two different protocols. Either the collected DMEM was not replaced or the DMEM volume collected was replaced. When keeping the same supernatant during the entire time, the DMEM and the corresponding cells were collected after 2, 6, 24, or 48 h (without supernatant replacement). For the second protocol with supernatant replacement, the supernatant was exchanged with fresh supernatant after collecting it from the cells at the same time point as for the protocol without supernatant replacement. Here, the cells and the supernatant were harvested for analysis as well.

ICP-OES Analysis. Before the analysis of the gold content in the cells and in the supernatant, the cells were digested. Therefore, after trypsinization, cells were centrifuged (300*g*, 5 min) and the supernatant was discarded. Afterwards, cells were diluted with 1 ml of aqua regia (3:1 hydrochloric acid/nitric acid) and incubated at room temperature overnight on an orbital shaker (300 rpm) followed by dilution with MiliQ water to 10 ml before measurement. The cell culture supernatants for the determination of exocytosed gold content were collected from the cells and treated with aqua regia followed by incubation and dilution to 10 ml with water. The gold concentration was determined by ICP-OES (SpectroGreen, Spectro/Ametek, Kleve, Germany). The calibration curve was prepared using 0.1, 0.5, 1, 5, and 20 ppm gold standard solution (stock 1 000 mg l^{-1} Au TraceCERT®, Sigma Aldrich, St. Louis, MO, USA). Untreated cells and cell culture media were used to deduct background signals. The amount of gold was calculated using the concentration resulting from the ICP OES and the volume of the sample.

Intracellular Trafficking. For the intracellular trafficking of the GNPs, PLX-PAD cells were seeded at a density of 400 000 cells per well in six-well plates. On the next day, incubation with GNPs was carried out at a GNP concentration of 300 µg ml^{-1} for 4 and 24 h. Additionally, a pulse-chase experiment was performed where the PLX-PAD cells were incubated with the GNPs for 4 h followed by an exchange to fresh cell culture medium and a subsequent 20 h incubation. After the incubation time, cells were harvested with Trypsin-EDTA (Thermo Fisher Scientific, Waltham, MA, USA). For each condition, three wells were pooled after harvesting to reach enough intracellular GNPs. PLX-PAD cells were centrifuged (300*g*, 5 min) and the supernatant was discarded. For cell lysis, cells were suspended in PBS with protease inhibitor (Thermo Fisher Scientific) and EDTA at 4 °C. Cell lysis was carried out through sonication (QSonica Q800R3, QSonica, Newton, CT, USA) at an amplitude of 70% and pulsation frequency of 30 s. Sonication was performed in total for 7 min at 4 °C. Cell debris and nuclei were removed by centrifugation (1 000*g*, 4 °C, 10 min) and, afterwards, the GNPs were collected by centrifugation (5 000*g*, 4 °C, 30 min). To remove unbound and loosely bound proteins, the nanoparticles were washed three times with PBS containing protease inhibitor and EDTA. Afterwards, the hard corona proteins were detached from the nanoparticles using 2% (w/v) SDS and 62.5 mM Tris-HCl, as previously described by our group [62, 119]. Proteins and nanoparticles were separated via centrifugation (5 000*g*, 4 °C, 30 min) and protein-containing supernatant was used for protein quantification, SDS PAGE, and LC-MS analysis.

Protein Quantification and SDS-PAGE. Proteins were quantified by the Pierce 660 nm Protein Assay (Thermo Fisher Scientific) according to the manufacturer's manual. The adsorption was measured with a Tecan Infinite M1000 plate reader using bovine serum

albumin (Merck, Kenilworth, NJ, USA) for a calibration curve. After quantification, the proteins were separated with SDS-PAGE and stained by Silver Staining according to the manufacturer's recommendations. A total of 2 µg protein in 26 µl total volume was mixed with 4 µl NuPage Reducing Agent and 10 ml of NuPage LDS Sample Buffer (Thermo Fisher Scientific). The sample was loaded on a 10% Bis-Tris-Protein Gel using SeeBlue Plus2 Pre-Stained (Invitrogen, Waltham, MA, USA) as a molecular marker and NuPage MES SDS Running Buffer. Gels were stained with Pierce Silver Stain Kit (Thermo Fisher Scientific) according to the manufacturer's protocol.

In-Solution Digestion, Liquid Chromatography-Mass Spectrometry (LC-MS), and Protein Identification. The in-solution digestion, liquid chromatography-mass spectrometry, and protein identification were performed as previously described by our group with slight modifications [62, 80, 119]. Prior to digestion, SDS was removed from the protein mix using Pierce Detergent Removal Spin Columns (Thermo Fisher Scientific). Afterwards, the proteins were precipitated via the ProteoExtract protein precipitation kit (Merck) and solubilized in RapiGest SF (Waters) in ammonium bicarbonate butter (50 mM). The Proteins were reduced with dithiothreitol (5 mM, Sigma-Aldrich) and alkylated with iodoacetamide (15 mM, Sigma-Aldrich) followed by an overnight tryptic digestion at a protein:trypsin ratio of 50:1. To allow absolute protein quantification, samples were diluted with 0.1% formic acid and spiked with 50 fmol μl^{-1} Hi3 E.coli. (Waters), following a published protocol [185]. Peptides were measured using a nanoACQUITY UPLC system coupled to a Synapt G2-Si mass spectrometer. The system was operated in a positive resolution mode, performing data-independent acquisition with additional ion mobility separation (IMS-MS^E) with a mass to charge range of 50-2 000 Da, scan time of 1 s, ramped trap collision energy from 20 to 40 V, and data acquisition of 120 min. The samples were injected with a flow rate of 0.3 µl min^{-1} and as a reference Glu-Fibrinopeptide (150 fmol μl^{-1}) and Leu-Enkephalin (200 pg μl^{-1}) were used and injected with a flow rate of 0.5 µl min^{-1}. Data processing was performed using MassLynx 4.1 and Progenesis GI 2.0 with a reviewed database downloaded from Uniprot. Thresholds for noise reduction were set at 120, 25, and 750 counts for low energy, high energy, and peptide intensity. For protein identification, at least one assigned fragment per peptide, three assigned fragments per protein, and one assigned peptides per protein were required. The TOP3/HI3 approach provided the amount of each protein in fmol [104].

Protein Annotation. After protein identification, we identified all corona proteins with an enrichment of 1.5-fold compared with the lysate proteins. The enriched corona proteins were forwarded to an analysis with the functional annotation tool DAVID (Version 6.8,

https://david.ncifcrf. gov/home.jsp accessed on 15 November 2021) [214, 283]. The enriched proteins were analyzed by functional annotation clustering, implementing the database for GOTERM_CC_FAT with medium classification stringency to consider the cellular compartments. The following GOTERMS were considered for the study: extracellular vesicle, cell surface, secretory vesicle, endoplasmatic reticulum, early endosome, cytoplasmic region, endocytic vesicle, and nucleosome.

6.4 Results and discussion

For the purpose of evaluating the influence of the loading amount on nanoparticles on their exocytosis, glucose-PEG-coated gold nanoparticles (GNPs) were synthesized. In this study, we focused on one type of nanoparticle to demonstrate changes in the nanoparticle exocytosis behavior independently from particle size or surface functionalization. Gold nanoparticles were chosen as a widely used type of nanoparticle and as a particle type that could be used in the future as an imaging reagent for stem cells. To achieve a higher stability of the nanoparticles under physiological conditions, the GNPs were surrounded with HS-PEG-COOH via gold–thiol interactions. Carboxylic functionalization of PEG was then used for coupling of glucose on the nanoparticles to achieve an increased uptake of the GNPs into cells [256]. In Figure 6.1, an illustration of the surface functionalization of the nanoparticles can be seen, as well as a representative transmission electron microscopy (TEM) picture. TEM showed an average size of the gold nanoparticles of 12.0 ± 2.8 nm. Dynamic light scattering (DLS) revealed a significantly larger size of the GNPs of 75 nm. However, using TEM, only the size of the gold nanoparticle core is measured (i.e., without the PEG and glucose coating contributing to the size measurement). In contrast in DLS, where the whole hydrodynamic diameter of the particles is measured. As the PEGylated and glucose-coated nanoparticles show a negative ζ-potential, the particles can, in addition, build up more electrostatic interactions in liquid dispersion, and thus show a larger diameter size than that measured by TEM images.

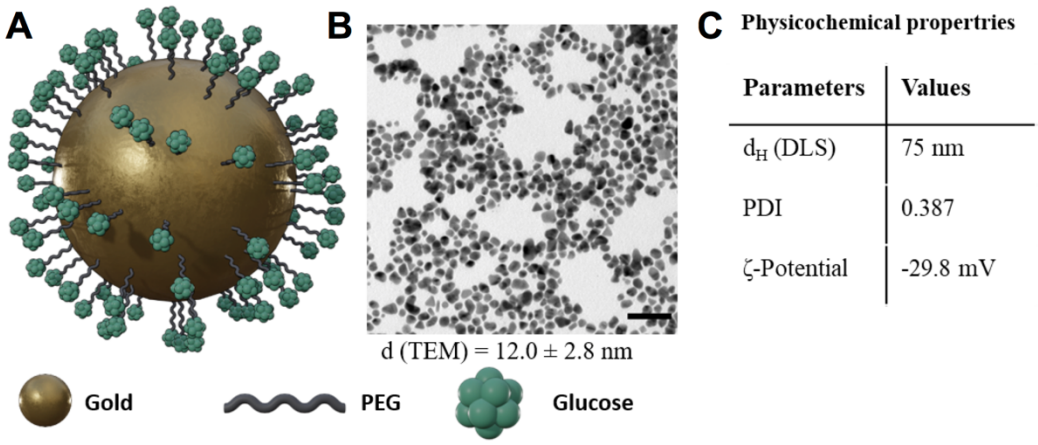

C Physicochemical propertries

Parameters	Values
d_H (DLS)	75 nm
PDI	0.387
ζ-Potential	-29.8 mV

Figure 6.1: Characterization of glucose-PEG-coated gold nanoparticles. (A) Schematic representation of PEGylated and glucose-coated gold nanoparticles. **(B)** Representative TEM images of GNPs. The size of the nanoparticles is given in nm ± SD. The scale bar represents 50 nm. **(C)** Physicochemical properties of the GNPs.

To evaluate the exocytosis of the GNPs from PLX-PAD cells, we used two different uptake and exocytosis protocols. For a lower loading of nanoparticles in the cells, we used a protocol with a short incubation time (30 min). However, to still have a sufficient uptake of nanoparticles in cells for this protocol, we incubated the cells without any proteins in isotone NaCl solution, as it was previously shown that the protein corona that formed in cell culture media with FBS reduces the uptake of nanoparticles into cells [112]. This phenomenon, known as the stealth effect, was intended to be avoided in this protocol by incubating the cells without the presence of proteins in the exposure media [78]. In the second protocol, we incubated the GNPs with the PLX-PAD cells for 24 h in DMEM with FBS. There, we expected to have a higher uptake and intracellular internalization of the nanoparticles because of the longer incubation time, despite the presence of proteins. The FBS was added to the cell culture media to avoid potential damage or change in cell functions due to the long incubation time without proteins.

Determination of the gold concentration in the cells was carried out using ICP-OES. ICP-OES is mainly used to determine the concentration of metals in complex solutions. For the analysis, the samples are first atomized and ionized in an argon plasma. Then, the ions and atoms are excited and emit electromagnetic radiation, which can be assigned to the different elements as discrete lines and by that quantified [284]. For the injection of the samples into the plasma, the samples are sprayed into a nebulizer in order to form small droplets. As cells and cell clumps in the sample could result in an inhomogeneous solution and lead to poor aerosol formation, the cells were previously dissolved overnight in aqua regia. Afterwards, the gold concentration in the cell solutions was determined for both uptake protocols and exocytosis protocols.

In Figure 6.2A, a schematic representation of the different protocols used for the incubation can be seen. Figure 6.2B shows that the different incubation protocols indeed resulted in different amounts of gold in the cell suspension, suggesting that the uptake of GNPs was higher for the high loading protocol than for the low loading protocol. It can be seen at time point 0, which displays the measurement directly after uptake of the nanoparticles, that the amount of gold in the high loading protocol was 165 pg per cell, while for the low loading protocol, it was 15 pg per cell. Therefore, the high loading protocol led to a particle amount 10 times higher in the cell than the low loading protocol.

After uptake of the nanoparticles, the cells were incubated again with DMEM for analysis of the exocytosis of the nanoparticles. First, we determined the amount of gold in the cells when the cell culture media was kept the same the whole time (Fig. 6.2A, grey box left). However, what the behavior might be in vivo should always be considered. There, exocytosed particles would be removed relatively quickly by other cells or body fluids. Thus, it is unlikely that exocytosed particles reabsorb on the cells and are taken up again. The amount of gold in the cells was also analyzed after replacing the supernatant regularly (Fig. 2A grey box right). In

Figure 6.2B, it can be seen that the intracellular gold concentration does not increase or decrease drastically for both protocols. However, looking deeper into the results, it can be seen that the amount of gold increases slightly with time for the low loading protocol both without and with supernatant replacement. This indicates that, after the uptake time, particles could be still attached to the surface of the cells and were available to be taken up with further incubation time. By washing and harvesting for ICP-OES analysis, particles that are attached to the surface might be lost. With supernatant replacement, this increase stopped after 24 h and the intracellular gold concentration leveled off at a gold amount of 17 pg per cell. Without supernatant replacement, the gold amount increases up to 26 pg per cell, which may indicate a further uptake either of exocytosed GNPs or GNPs from the cell surface. For the high loading protocol, no difference could be observed with or without supernatant replacement. Here, a small decrease in the gold amount can be seen after 2 and 6 h. This could be due to a release or exocytosis of nanoparticles from the cells. However, after 24 h, the gold amount increases to the same level as before and decreases afterwards again slightly to 130 pg per cell. The increase in the gold amount could also be due to an uptake of GNPs that were still attached to the surface and reuptake of exocytosed GNPs occurred.

To further determine the exocytosis of the GNPs from PLX-PAD cells, we analyzed the amount of gold in cell culture media after allowing exocytosis from the cells. In Figure 6.2C, the calculated exocytosed gold concentration per cell can be seen. To facilitate a comparison between intracellular gold concentration and that in the supernatant, the amount of gold was also given per cell here. Considering the samples without supernatant replacement, it is noticeable that the amount of gold in the supernatant increased for both protocols (low and high loading) until 6 h, then decreased up to 24 h before it increased again up to 48 h. As the supernatant was kept and harvested at the recommended time point, it is very probable that the particles, which were previously released from the cell, were taken up again. Looking at the intracellular gold concentration, an increase in the concentration for the high loading protocol could be observed, which supports the re-uptake theory when the particles are not removed from the cell culture media. This has also been observed previously for gold particles [280]. There, after a short time, a plateau was reached where exocytosis and re-uptake were in equilibrium [280]. However, under in vivo conditions, it is more probable that the exocytosed particles are removed from the surrounding area of cells by other cells (i.e., phagocytic cells). It is also important to pay attention to additional physiological dynamic removal processes that can occur. Considering this for the protocol, we observed that, with regular supernatant replacement, the amount of exocytosed gold decreased over time. Most of the gold was measured in cell culture media after 2 h and decreased rapidly to 6 h. After 24 h and 48 h, only a small amount of gold was measured in the supernatant. Therefore, in

accordance with previous studies on different cell types, the exocytosis of nanoparticles seems to be fast, but decreases with time [280].

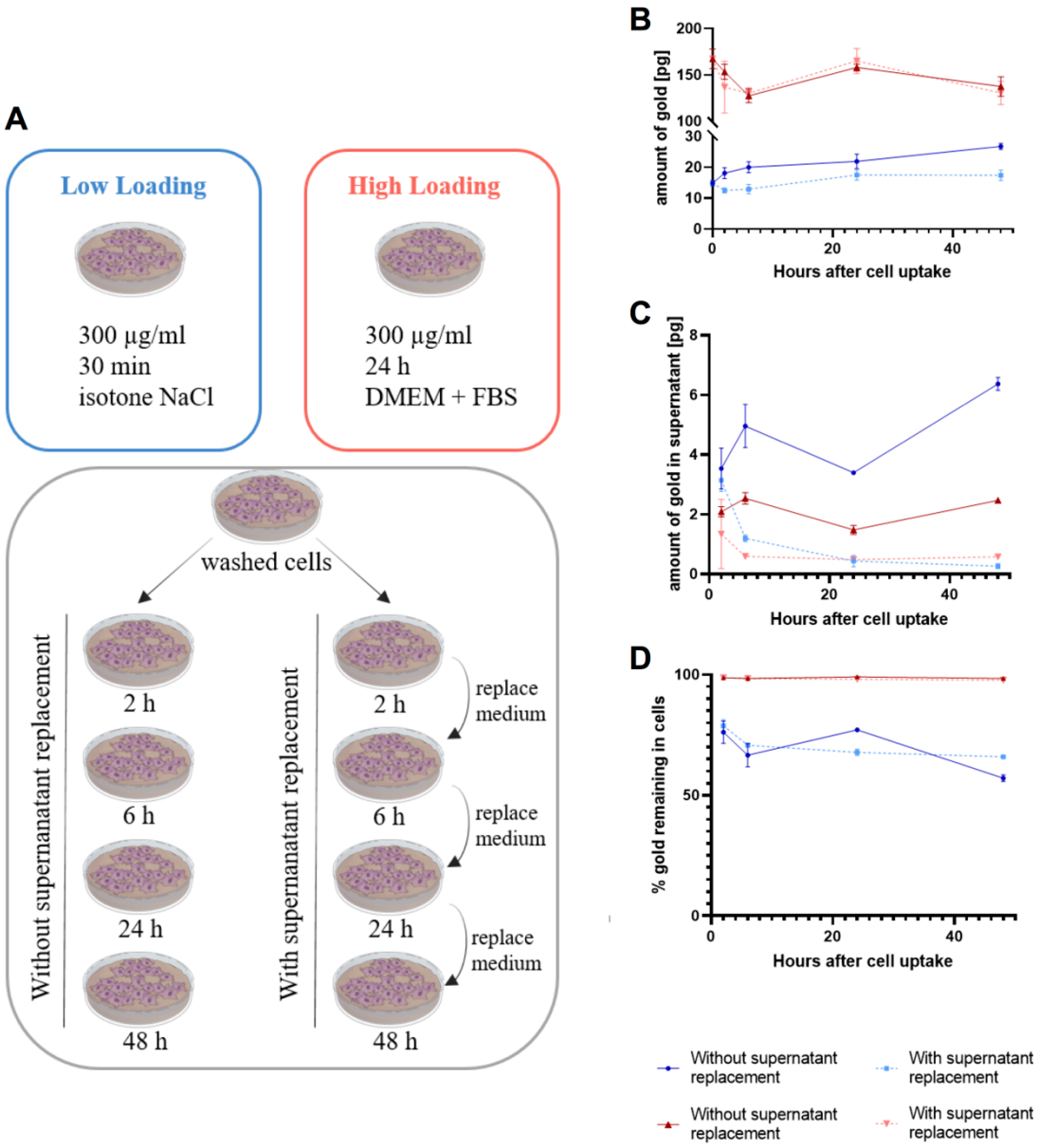

Figure 6.2: Uptake and exocytosis measurements of GNPs in PLX-PAD cells. (A) Schematic representation of the different incubation protocols used for incubation. PLX-PAD cells were incubated either for 30 min with 300 µg ml^{-1} GNPs in isotone NaCl solution (blue) or for 24 h with 300 µg ml^{-1} GNPs in DMEM with FBS (red). After uptake of GNPs, the cells were further incubated in DMEM with FBS for up to 48 h either with regular exchange of the medium (grey box right) or kept in the same medium (grey box left). **(B)** Calculated gold concentration per cell. Cells were harvested after incubation with GNPs and after incubation with DMEM, respectively. Afterwards, cells were analyzed with ICP-OES and the amount of gold per cell was calculated. The low loading protocol is shown in blue and the high loading protocol in red (data are shown as mean ± SD, n = 3). **(C)** Calculated amount of gold in supernatant determined by ICP-OES after incubation of PLX-PAD cells with GNPs and further incubation with cell culture media (data are shown as amount of gold in pg exocytosed per cell as mean ± SD, n = 3).

(D) Calculated gold amount remaining in PLX-PAD cells after allowing for exocytosis given in percent (data are shown as mean ± SD, n = 3).

To allow a better comparison of the exocytosis rate between the different loading protocols, the percent of gold remaining in the cells was calculated (Fig. 6.2D). Therefore, the amount of gold quantified after the uptake of the particles and the amount quantified in the supernatant was used for calculation. While 98% of the gold remained in the cells for the high loading protocol, only 80% remained after 2 h and 66% remained after 48 h for the low loading protocol. Particles could either be released from the cell surface or excreted from the cells. A higher loading of the GNPs in the PLX-PAD cells (by means of a more prolonged incubation protocol) also seems to reduce the exocytosis of the loaded particles from the cells. This can be seen by consideration of the total amount of gold exocytosed and by looking at the amount of exocytosed gold given in percent.

Previously, Yu et al. synthesized temperature-responsive GNPs for long-term tracking of stem cells. Here, by adjusting the temperature, an increased uptake and a reduced exocytosis could be observed. However, still, a non-negligible amount of GNPs was secreted within 24 h, which could lead in vivo to a loss of signal or unspecific signal from other cells [265]. During other studies, GNPs were coated using poly-l-lysin or PEG coupled to a trans-activator of transcription peptide to increase the uptake of GNPs in stem cells, and thereby increase the CT signal. However, increased uptake did not lead to a decreased exocytosis of GNPs, which makes long-term tracking still problematic [266-267]. Using our glucose-PEG-coated GNPs and adapting the incubation protocol, the exocytosis rate was significantly reduced and a high loading of the stem cells could still be achieved. This could be used in the future for better long-term tracking of stem cells.

The next step was to analyze whether proteins attached to the surface of the GNPs indicate if particles stay intracellular or if they are exocytosed. Therefore, we incubated the particles with the PLX-PAD cells, harvested and lysed them, and collected the proteins in the protein corona around the GNPs. The protein corona develops dependently on proteomic milieu around the particle. Therefore, with this method, it is possible to determine the pathway to which the GNPs belong [183, 203]. As it is necessary for this analysis that the nanoparticles were internalized into the cell and were no longer on the surface, the protocol was adapted. Instead of an incubation of 30 min in isotone NaCl solution, the GNPs were incubated for the low loading protocol for 4 h in DMEM with FBS at the same concentration. Therefore, we ensured that we still have a lower and shorter loading of GNPs in the cells, but reach a sufficient amount of particles in the cells to isolate them in the protein corona analysis. Additionally, a 4 + 20 h condition was analyzed to ensure internalization and processing for a possible exocytosis of the GNPs. The proteins were visualized via SDS-PAGE (Fig. S6.1) and analyzed via LC-MS (Fig. 6.3, Fig. 6.4).

No clear differences between the conditions via SDS PAGE were observed. However, a clear distinction between the protein corona composition of the GNPs and the lysate of the PLX-PAD was noticed. This difference confirms that the protein corona of the GNPs was efficiently isolated from the cell lysate.

After the analysis of the SDS-PAGE, the protein corona was additionally analyzed via LC-MS. A bottom-up proteomic approach was used for this protein analysis [285]. Therefore, proteins were desorbed from nanoparticles followed by digestion into peptides with trypsin. Peptides were separated by liquid chromatography and ionized by electrospray ionization. In the mass spectrometer, the mass-to-charge ratio of the ionized peptides was recorded. With the use of a deconvolution software and protein databases, these signals can be assigned to specific proteins, and through this, the composition of protein mixtures can be determined [285]. Here, we used this proteomic approach to analyze the intracellular fate of the GNPs. First, we considered the TOP 10 proteins in the protein corona for all conditions. Thereby, it can be seen that the TOP proteins binding on the GNPs after 4 h differ from the proteins binding after 24 h and 4 + 20 h. After 4 h incubation, serum proteins, namely fibrinogen and serum albumin, were predominantly measured. After more prolonged incubation, this protein adsorption pattern changed towards intracellular proteins e.g., histones and actin.

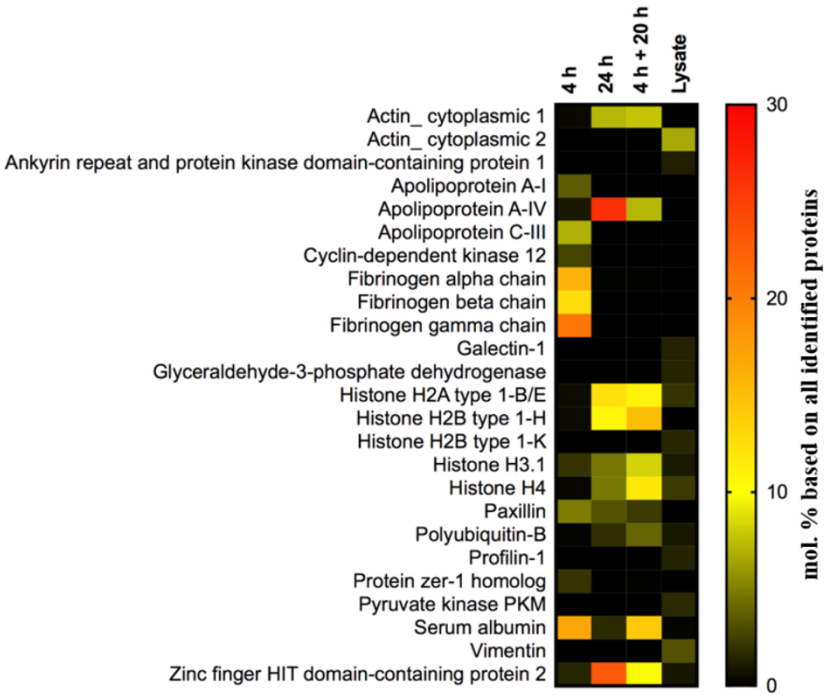

Figure 6.3: Proteomic analysis of the protein corona on the surface of GNPs after uptake in PLX-PAD cells. The heatmap is displaying the combined TOP 10 proteins of each condition (25 proteins in total) identified by LC-MS. The values are reported as the mol% based on all identified proteins in the protein corona.

Next, we analyzed to which intracellular compartments the proteins in the protein corona belong. Therefore, the enrichment factor of the proteins in the protein corona compared with cell lysate was calculated. Only proteins with a 1.5-fold enrichment were considered for annotation to an intracellular compartment. First, we used DAVID to assign the number of the enriched proteins of each condition to the different cellular compartments (Fig. 6.4A). We observed that most of the enriched proteins of all conditions are associated with extracellular vesicles. The highest protein count for extracellular vesicle proteins can be seen in the 4 + 20 h condition and the least protein count in the 4 h condition. For the categories - cell surface, secretory vesicles, early endosomes, cytoplasmic region, and endocytic vesicles - no difference between the different conditions was observed. The higher protein count for the 4 + 20 h condition comes from the fact that, in total, more proteins were enriched in the corona for this condition, indicating that these particles traversed longer through the cells and encountered a more complex protein milieu.

In order to determine whether the protein corona indicates if a particle is exocytosed or not, we analyzed the proteins annotated to the extracellular pathway (Fig. 6.4B). Here, again, the proteins found in the protein corona after 4 h of incubation clearly differ from the proteins in the corona after 24 h and 4 + 20 h. Many proteins that were already found under the TOP 20 list were observed here again, but some proteins that are not that highly represented could also be annotated to this group. After 4 h of incubation time, more apolipoproteins and vitronectin could be seen in the protein corona. However, after further incubation (i.e., 24 h and 20 + 4 h), the protein composition changed and the amount of intracellular proteins increased. Moreover, only one representative of the proteins involved in the exocytosis, namely Rab-13, could be detected in a small amount in the protein corona after 24 h. However, Rab-13 is involved in the formation of intracellular vesicles and involved in both endocytotic and exocytotic processes, and cannot be unequivocally assigned as an exocytosis marker [286-287]. The fast exocytosis of the GNPs observed for the low loading protocols is probably due to the protein corona, which was mainly formed by extracellular proteins. The obtained results suggest that prolonged nanoparticle incubation protocols allow intracellular protein corona changes and lead to a deeper and longer internalization in the cells.

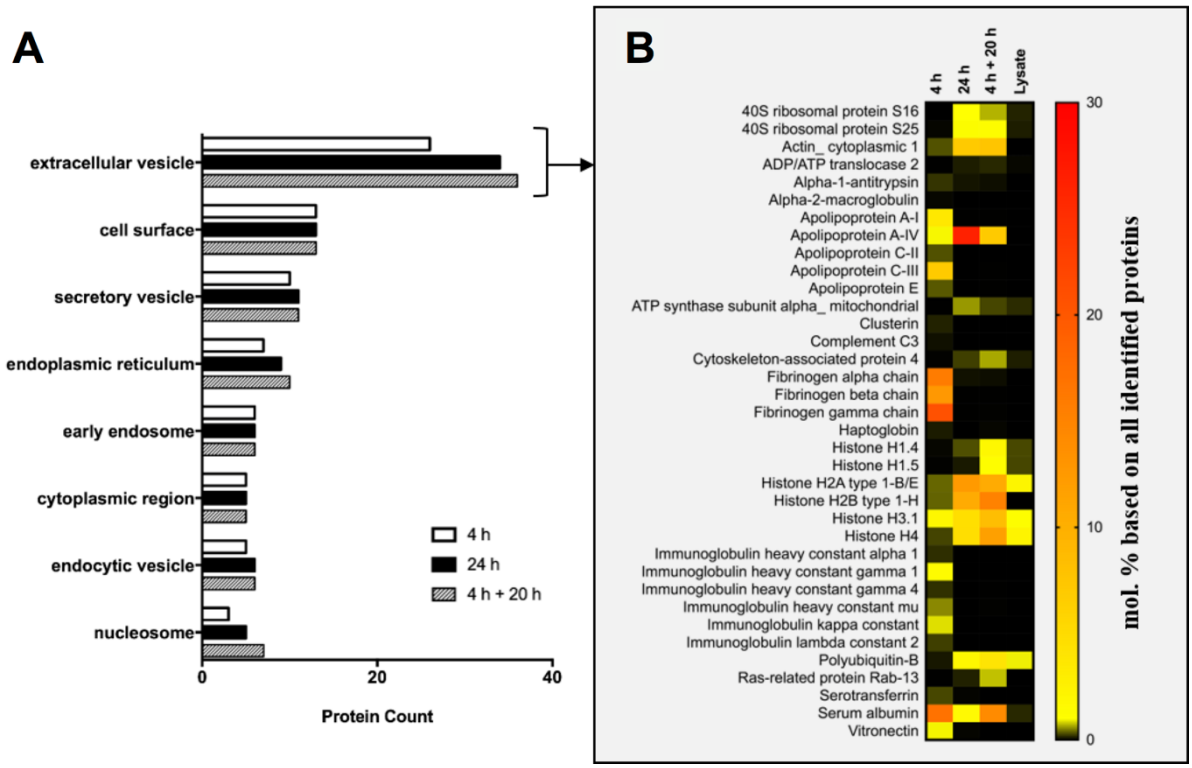

Figure 6.4: Protein annotation and proteins of the "extracellular vesicle" GOTERM. (A) Annotation of the proteins bound on the particles to intracellular compartments. Proteins were desorbed from GNPs after incubation and lysis of the PLX-PAD cells. The protein corona was analyzed by LC-MS and proteins assigned to selected intracellular compartments using DAVID-based functional annotation clustering by GOTERM_CC_FAT. A detailed list of all annotated proteins to the intracellular GOTERMs can be found in Table S6.1-S6.10. **(B)** Heatmap of all proteins assigned to the extracellular vesicle GOTERM. Different incubation time points are displayed in comparison with cell lysate of PLX PAD cells.

6.5 Conclusion

Here, we demonstrated that a longer incubation protocol allows for higher loading of gold nanoparticles in PLX-PAD cells and leads to reduced exocytosis of these nanoparticles from the cells. Moreover, with the analysis of the protein corona, we showed that, with a prolonged incubation time, the serum proteins in the protein corona are exchanged to intracellular proteins, which probably leads to the reduced exocytosis. A low exocytosis rate of gold nanoparticles is absolutely necessary for long-term tracking of stem cells in vivo as background signals from other cells are reduced and the signal intensity of the stem cells remains stable over time. These findings could help to better understand the in vivo fate of stem cells and intracellular biokinetics of glucose-PEG-coated gold nanoparticles. It can also support on the design of nanoparticles' uptake protocols for the labelling and tracking of cells used as therapeutic agents.

6.6 Supplementary information

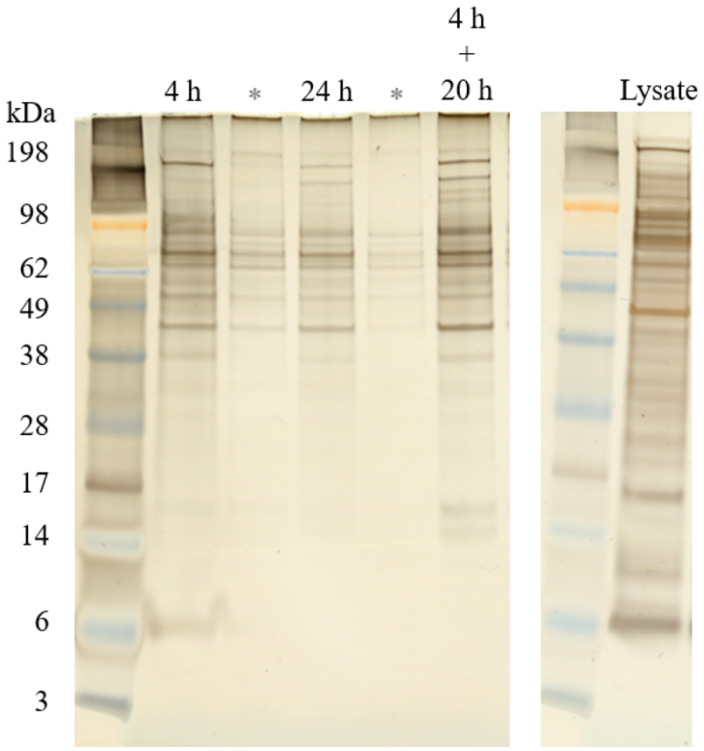

Figure S6.1: Hard corona proteins separated by SDS-PAGE and stained by a silver staining. The lanes are labelled according to the incubation time and Lysate corresponds to the cell lysate of PLX PAD cells. Lanes labelled with * are not relevant here.

Table S6.1: List of enriched proteins in the protein corona identified by LC-MS. Displayed are the 1.5-fold enriched proteins compared to the proteins of the lysate.

Uniprot Accession	Protein Name
P62249	40S ribosomal protein S16
P62851	40S ribosomal protein S25
P60709	Actin_ cytoplasmic 1
P12235	ADP/ATP translocase 1
P05141	ADP/ATP translocase 2
P01009	Alpha-1-antitrypsin
P01023	Alpha-2-macroglobulin
P02647	Apolipoprotein A-I
P06727	Apolipoprotein A-IV
P02655	Apolipoprotein C-II
P02656	Apolipoprotein C-III
P02649	Apolipoprotein E
O43150	Arf-GAP with SH3 domain_ ANK repeat and PH domain-containing protein 2
P25705	ATP synthase subunit alpha_mitochondrial
P25098	Beta-adrenergic receptor kinase 1
P10909	Clusterin
P01024	Complement C3
Q9NYV4	Cyclin-dependent kinase 12
Q07065	Cytoskeleton-associated protein 4
P04843	Dolichyl-diphosphooligosaccharide–protein glycosyltransferase subunit 1
P02671	Fibrinogen alpha chain
P02675	Fibrinogen beta chain
P02679	Fibrinogen gamma chain
P00738	Haptoglobin
Q8WYB5	Histone acetyltransferase KAT6B
P10412	Histone H1.4
P16401	Histone H1.5
P04908	Histone H2A type 1-B/E
Q93079	Histone H2B type 1-H
P68431	Histone H3.1
P62805	Histone H4
Q14520	Hyaluronan-binding protein 2
P01876	Immunoglobulin heavy constant alpha 1
P01857	Immunoglobulin heavy constant gamma 1
P01861	Immunoglobulin heavy constant gamma 4
P01871	Immunoglobulin heavy constant mu
P01834	Immunoglobulin kappa constant
P0DOY2	Immunoglobulin lambda constant 2
Q5T7N2	LINE-1 type transposase domain-containing protein 1
P49023	Paxillin
P0CG47	Polyubiquitin-B
Q13045	Protein flightless-1 homolog
P61619	Protein transport protein Sec61 subunit alpha isoform 1
Q7Z7L7	Protein zer-1 homolog
P51153	Ras-related protein Rab-13
P02787	Serotransferrin
P02768	Serum albumin
P0DPH7	Tubulin alpha-3C chain
P04004	Vitronectin
Q9UHR6	Zinc finger HIT domain-containing protein 2
P21506	Zinc finger protein 10

Table S6.2: List of proteins annotated to the GOTERM "extracellular vesicle" by DAVID. Proteins were identified via LC-MS proteomics workflow and annotated to the corresponding intracellular compartment with DAVID. Displayed are the Uniprot Accession number and the protein name of each protein.

Extracellular Vesicle	
Uniprot Accession	**Protein Name**
P62249	40S ribosomal protein S16
P62851	40S ribosomal protein S25
P60709	Actin_ cytoplasmic 1
P05141	ADP/ATP translocase 2
P01009	Alpha-1-antitrypsin
P01023	Alpha-2-macroglobulin
P02647	Apolipoprotein A-I
P06727	Apolipoprotein A-IV
P02655	Apolipoprotein C-II
P02656	Apolipoprotein C-III
P02649	Apolipoprotein E
P25705	ATP synthase subunit alpha_mitochondrial
P10909	Clusterin
P01024	Complement C3
Q07065	Cytoskeleton-associated protein 4
P02671	Fibrinogen alpha chain
P02675	Fibrinogen beta chain
P02679	Fibrinogen gamma chain
P00738	Haptoglobin
P10412	Histone H1.4
P16401	Histone H1.5
P04908	Histone H2A type 1-B/E
Q93079	Histone H2B type 1-H
P68431	Histone H3.1
P62805	Histone H4
P01876	Immunoglobulin heavy constant alpha 1
P01857	Immunoglobulin heavy constant gamma 1
P01861	Immunoglobulin heavy constant gamma 4
P01871	Immunoglobulin heavy constant mu
P01834	Immunoglobulin kappa constant
P0DOY2	Immunoglobulin lambda constant 2
P0CG47	Polyubiquitin-B
P51153	Ras-related protein Rab-13
P02787	Serotransferrin
P02768	Serum albumin
P04004	Vitronectin

Table S6.3: List of proteins annotated to the GOTERM "cell surface" by DAVID. Proteins were identified via LC-MS and annotated to the corresponding intracellular compartment with DAVID. Displayed are the Uniprot Accession number and the protein name of each protein.

Cell Surface	
Uniprot Accession	**Protein Name**
P02647	Apolipoprotein A-I
P06727	Apolipoprotein A-IV
P10909	Clusterin
P02671	Fibrinogen alpha chain
P02675	Fibrinogen beta chain
P02679	Fibrinogen gamma chain
P01876	Immunoglobulin heavy constant alpha 1
P01857	Immunoglobulin heavy constant gamma 1
P01861	Immunoglobulin heavy constant gamma 4
P01871	Immunoglobulin heavy constant mu
P01834	Immunoglobulin kappa constant
P0DOY2	Immunoglobulin lambda constant 2
P02787	Serotransferrin

Table S6.4: List of proteins annotated to the secretory vesicle pathway by DAVID. Proteins were identified via LC-MS and annotated to the corresponding intracellular compartment with DAVID. Displayed are the Uniprot Accession number and the protein name of each protein.

Secretory Vesicle	
Uniprot Accession	**Protein Name**
P01009	Alpha-1-antitrypsin
P01023	Alpha-2-macroglobulin
P02647	Apolipoprotein A-I
P10909	Clusterin
Q07065	Cytoskeleton-associated protein 4
P02671	Fibrinogen alpha chain
P02675	Fibrinogen beta chain
P02679	Fibrinogen gamma chain
P51153	Ras-related protein Rab-13
P02787	Serotransferrin
P02768	Serum albumin

Table S6.5: List of proteins annotated to the endoplasmic reticulum by DAVID. Proteins were identified via LC-MS and annotated to the corresponding intracellular compartment with DAVID. Displayed are the Uniprot Accession number and the protein name of each protein.

Endoplasmatic Reticulum	
Uniprot Accession	**Protein Name**
P01009	Alpha-1-antitrypsin
P02647	Apolipoprotein A-I
P06727	Apolipoprotein A-IV
P02649	Apolipoprotein E
P10909	Clusterin
Q07065	Cytoskeleton-associated protein 4
P04843	Dolichyl-diphosphooligosaccharide–protein glycosyltransferase subunit 1
P61619	Protein transport protein Sec61 subunit alpha isoform 1
P02768	Serum albumin
P04004	Vitronectin

Table S6.6: List of proteins annotated to the early endosome pathway by DAVID. Proteins were identified via LC-MS and annotated to the corresponding intracellular compartment with DAVID. Displayed are the Uniprot Accession number and the protein name of each protein.

Early Endosome	
Uniprot Accession	**Protein Name**
P02647	Apolipoprotein A-I
P06727	Apolipoprotein A-IV
P02655	Apolipoprotein C-II
P02656	Apolipoprotein C-III
P02649	Apolipoprotein E
P02787	Serotransferrin

Table S6.7: List of proteins annotated to the cytoplasmatic region by DAVID. Proteins were identified via LC-MS and annotated to the corresponding intracellular compartment with DAVID. Displayed are the Uniprot Accession number and the protein name of each protein.

Cytoplasmatic Region	
Uniprot Accession	**Protein Name**
P60709	Actin_ cytoplasmic 1
P02671	Fibrinogen alpha chain
P02675	Fibrinogen beta chain
P02679	Fibrinogen gamma chain
P49023	Paxillin

Table S6.8: List of proteins annotated to the endocytotic vesicle pathway by DAVID. Proteins were identified via LC-MS and annotated to the corresponding intracellular compartment with DAVID. Displayed are the Uniprot Accession number and the protein name of each protein.

Endocytotic Vesicle	
Uniprot Accession	**Protein Name**
P02647	Apolipoprotein A-I
P02649	Apolipoprotein E
P00738	Haptoglobin
P0CG47	Polyubiquitin-B
P51153	Ras-related protein Rab-13
P02787	Serotransferrin

Table S6.9: List of proteins annotated to the nucleosome by DAVID. Proteins were identified via LC-MS and annotated to the corresponding intracellular compartment with DAVID. Displayed are the Uniprot Accession number and the protein name of each protein.

Nucleosome	
Uniprot Accession	**Protein Name**
Q8WYB5	Histone acetyltransferase KAT6B
P10412	Histone H1.4
P16401	Histone H1.5
P04908	Histone H2A type 1-B/E
Q93079	Histone H2B type 1-H
P68431	Histone H3.1
P62805	Histone H4

Table S6.10: List of proteins in negative control identified by LC-MS. The negative control cells and tubes were treated in the same way as the samples to ensure that only corona proteins are analyzed and to exclude cell contamination.

Negative Control		
Uniprot Accession	**Protein Name**	**Mol %**
P62736	Actin_ aortic smooth muscle	4.54
P60709	Actin_ cytoplasmic 1	6.94
P05141	ADP/ATP translocase 2	0.36
P12236	ADP/ATP translocase 3	0.41
P25705	ATP synthase subunit alpha_ mitochondrial	0.48
P06576	ATP synthase subunit beta_ mitochondrial	0.29
P00403	Cytochrome c oxidase subunit 2	0.30
Q07065	Cytoskeleton-associated protein 4	0.16
P10412	Histone H1.4	1.55
P16401	Histone H1.5	0.92
P04908	Histone H2A type 1-B/E	13.43
P0C0S5	Histone H2A.Z	0.41
O60814	Histone H2B type 1-K	10.10
P68431	Histone H3.1	5.87
P62805	Histone H4	14.02
P60660	Myosin light polypeptide 6	0.31
O14950	Myosin regulatory light chain 12B	0.22
P35579	Myosin-9	1.35
Q00325	Phosphate carrier protein_ mitochondrial	0.61
Q96DU9	Polyadenylate-binding protein 5	1.45
P0CG47	Polyubiquitin-B	1.76
P02545	Prelamin-A/C	0.33
P35232	Prohibitin	0.17
Q6UXU0	Putative uncharacterized protein	0.26
P06753	Tropomyosin alpha-3 chain	0.57
Q8NEP4	Uncharacterized protein C17orf47	23.96
O95399	Urotensin-2	0.06
P08670	Vimentin	0.30
Q5T200	Zinc finger CCCH domain-containing protein 13	1.35
Q9UHR6	Zinc finger HIT domain-containing protein 2	7.54

Chapter C - Protein adsorption on biomaterial surfaces

Chapter C contains two subchapters. Subchapter 7 introduces the reader to biomaterials for bone substitution, specifically CaP. Next, mechanisms of bone regeneration, such as angiogenesis, are discussed. Last, the process and the consequences of protein adsorption for bulk biomaterials are detailed. Then subchapter 8 presents publication **[5]** that investigated protein adsorption from hemoderivatives on CaP surfaces and analyzed the pro-angiogenic effect on endothelial cells. Publication **[5]** was previously published in a peer-reviewed journal and is presented as a verbatim reproduction with slight adaptions.

[5] **da Costa Marques, R.***, ___, ___, ___, ___, ___. Proteomics reveals differential adsorption of angiogenic platelet lysate proteins on calcium phosphate bone substitute materials. *Regenerative Biomaterials*, **2022**, *9*, rbac044. (* shared first)

7. Theoretical Background

7.1 Biomaterials for bone substitution

The two previous chapters focused on the extracellularly and intracellularly formed protein corona. The protein corona is a phenomenon strongly associated with nanoscale particular materials, so far referred to as NPs. Yet, biomaterials outside the conventional nanoscale range might also be subjected to protein adsorption, specifically if these biomaterials exhibit a nanostructured surface and if these biomaterials form contacts with biological matter, such as tissues or biological fluids [3-4].

According to one definition, biomaterials are substances, other than drugs, of synthetic or natural origin that augment or replace tissue, organ, or body functions for quality-of-life improvements [288]. Thus, biomaterials share common utilization in medical devices or implants [17-18]. However, a strict definition remains elusive [288], and particularly the rise of nanotechnology has contributed to the complexity of defining and discriminating the term “biomaterials” [289]. Nevertheless, the coming sections will focus on calcium phosphate (CaP) biomaterials with nanostructured surfaces and a material size outside the nano range.

A well-known field of biomaterial applications is bone substitution [4, 288]. Here specifically, biomaterials are utilized in bone grafting. Bone grafting encompasses all surgical procedures for bone augmentation, such as replacing damaged bone or filling bone cavities [19, 290]. Bone was described as the second most transplanted tissue after blood [291], and the future demand for bone grafts will most likely rise in aging populations [19, 292]. Here, the current gold standard regarding successful bone regeneration remains autografts, bone grafts harvested from patients themselves [293]. Typical autografts are collected from non-essential bones, typically from the iliac crest or the fibula [293]. Yet, autografts impose high morbidity caused by the harvesting process and might not be suitable for geriatric patients or patients with conflicting predispositions [293-294]. On the other hand, allografts - banked bone grafts from other individuals - might lead to immunological reactions and harbor infection risks [293, 295]. To counteract the limits of auto- and allografts in bone grafting, synthetic biomaterials for bone substitution provide a promising solution [19]. Different materials were introduced as suitable bone substitute materials, such as calcium sulfates, calcium phosphates, bioactive glass, and poly(methyl methacrylate) bone cement [19]. Among these, CaPs are widely used candidates for bone grafting procedures [19]. CaPs are produced as synthetic mineral salt by high-temperature sintering, excluding water vapor, and molding the CaPs by high-pressure compaction [296]. By this, CaPs can be produced with different shapes and porosities, making them a versatile material [19, 293]. CaPs can be further distinguished: Hydroxyapatite (HA) and tricalcium

phosphate (TCP) are commonly used CaPs for bone substitution and appear as biphasic calcium phosphate if combined [19]. HA with the formula $Ca_{10}(PO_4)_6(OH)_2$, has a similar molecular structure to bone mineral, showing brittle properties under tension but mechanical resistance to compressive loads [19, 297]. TCP with the formula $Ca_3(PO_4)_2$ is predominantly manufactured in its rhombohedral β-TCP form. Because of the lower Ca/P ratio, β-TCP shows a faster absorption rate [297-299]. However, β-TCP has weaker mechanical properties than HA [300]. By combining HA and TCP to biphasic calcium phosphate, the absorptive and mechanical properties can be controlled and adjusted by the ratio [19].

Despite the promising capabilities of CaPs in bone substitution, their regenerative potential falls behind autografts. Therefore, it is necessary to understand the role of CaPs within the bone regeneration process and identify chances for refinement. Only by further refining the regenerative capabilities of CaPs, synthetic bone substitutes will become an advantageous option for bone grafting.

7.2 Bone regeneration and angiogenesis

Bone is a metabolically-active connective tissue that provides structural support, movement (in combination with muscle tissue), protection of vital structures, and a storage for minerals and growth factors [301]. By volume, bone consists of 10% cellular material and 90% bone matrix [301-302]. The cellular component can be divided into bone matrix-producing osteoblasts, bone-resorbing osteoclasts, and bone hemostasis-maintaining osteocytes [303]. Bone matrix has four different components. The inorganic bone matrix is mainly composed of natural HA [303]. Natural HA resembles a substituted form of the above-described synthetic HA, replacing, for example, phosphates and hydroxyl groups with carbonates and silicates [293, 303]. The inorganic bone matrix provides the tissues' mechanical stability and a storage depot for calcium, phosphorous, magnesium, and sodium [302]. The organic bone matrix contains predominantly type 1 collagen and additionally proteoglycans, glycoproteins, and growth factors [301]. These organic components induce flexible properties and, therefore, resistance to mechanical stress. Furthermore, growth factors are involved in bone modeling and remodeling [304]. The two remaining components of the bone matrix, lipids and water, constitute up to 15% [301].

Bone maintenance and healing are driven by the processes of bone modeling and remodeling [19, 305]. Bone modeling represents bone formation during growth, involving only little resorption [305]. Conversely, bone remodeling involves bone resorption and replacement by newly formed bone tissue. These complementary processes ensure a lifelong system for

skeletal growth and adaption to external factors [305]. Particularly spontaneous and extreme loads or persistent and gradual mechanical stress can cause bone fractures, requiring bone healing mechanisms [19, 305]. Here, the fracture size plays a decisive role in the exact healing mechanism [306]. Small and stabilized fractures can be joined through primary healing, also intramembranous ossification [307]. After initial hematoma formation, this process is completed through an inflammatory process and ossification, without cartilage formation. However, larger fractions with disconnected bone ends require secondary bone healing [307]. During secondary bone healing, also endochondral ossification, hematoma formation and inflammation are followed by cartilage formation due to low oxygen conditions within the large gap [307-308]. The cartilage is then gradually replaced by bone remodeling until acquiring an established and stable union of bone tissue [307-308]. Nevertheless, very large fracture gaps due to high-energy trauma, concomitant diseases, or developmental defects can hamper bone healing and lead to a non-union, requiring further treatment [19, 306].

Necessary factors which drive bone regeneration are the recruitment of progenitor cells, growth factors, an established extracellular matrix for structural support, and, most importantly, angiogenesis [307]. Angiogenesis describes the process of blood vessel sprouting from preexisting blood vessels as a consequence of tissue requirements [309-310]. Accordingly, efficient angiogenesis improves the vascularization in wound sites, serving as a crucial factor in bone healing [311]. Indeed, efficient vascularization serves as an infrastructure for oxygen and nutrient transport, waste egress, and the recruitment of inflammatory and bone progenitor cells [311]. Therefore, angiogenesis was identified as a target for improved bone regeneration in bone grafting procedures [19]. Endothelial cells (ECs) are the central cell type involved in angiogenesis. Being connected by adherence and tight junctions, ECs form blood vessel tubes. Angiogenesis occurs through different mechanisms. Yet, the mechanism of sprouting angiogenesis remains the best studied so far [309]. Here, early pro-angiogenic growth factors, such as vascular endothelial growth factor (VEGF) or fibroblast growth factors (FGFs), initiate the branching [309-310]. These growth factors are sequestered by hypoxic, tumor, or inflammatory cells. Upon binding EC-receptors, such as VEGF receptor-2 or FGF receptors, ECs become activated and mediate the detachment of neighboring pericytes through the metalloproteinase-driven degradation of the intertwined extracellular matrix [309]. Through a rising VEGF gradient, a selected EC matures to a tip cell, while neighboring ECs downregulate VEGF receptor-2 and become stalk cells [309]. Stalk elongation is then driven by the tip cell's sensing of molecular environmental guidance signals through filopodia [309]. The stalk itself is elongated by stalk cell division until fusion with another vessel branch occurs [309]. Finally, late-stage angiogenic factors, such as platelet-derived growth factor B (PDGF-B) and transforming growth factor-β (TGF-β), recruit pericytes to cover and stabilize the newly formed vessel [309-310].

To summarize, bone healing and angiogenesis are highly dependent on the supply of selected growth factors. Therefore, supplying these growth factors alongside CaPs has become a promising option [312]. Here, surface modification through protein adsorption of these proteins is a desired concept to promote bone regeneration.

7.3 Protein adsorption on biomaterial surfaces

Protein adsorption occurs on biomaterials that form contact with tissues or biological fluids [3]. Similar to the protein corona formation on NPs, protein adsorption on biomaterials occurs spontaneously, changing the physicochemical properties of the biomaterials' surface [3, 313]. For biomaterials with tissue contact (e. g. in bone grafting applications), the proteins adsorb before the biomaterial-cell contact is established [313]. Therefore, the changed surface properties directly affect cell adhesion [314], cell signaling [315], and implant integration [312-313]. Here, the underlying principles of protein adsorption are comparable to the protein adsorption on NPs, including the Vroman effect [59, 313]. Similarly, the properties of the protein environment play a large role, as already discussed in subchapter 1.3. However, unlike NPs, bulk biomaterials represent an extensive surface with different categories of physicochemical properties that influence protein adsorption [4, 313]. These influential physicochemical properties of biomaterials are depicted in Figure 7.1.

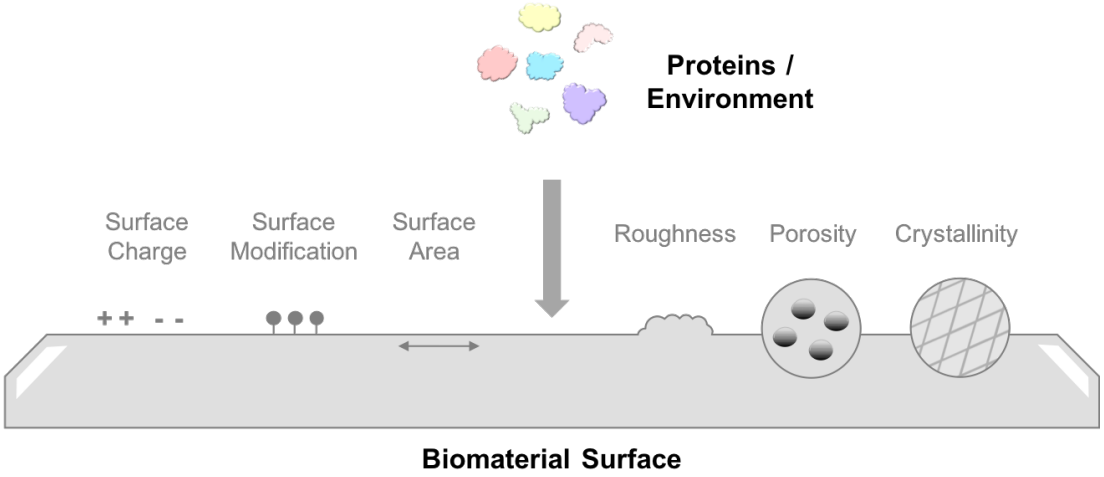

Figure 7.1: Protein adsorption on biomaterial surfaces. The scheme visualizes the process of protein adsorption on biomaterials. The biomaterial properties that impact protein adsorption are depicted.

Previous studies mentioned that charge and electrostatic interactions primarily cause the adsorption of proteins, specifically for ceramic-based biomaterials, such as the above-described CaPs [316-317]. For example, previous works immobilized amino acids or carboxylic acid to enhance electrostatic interactions between proteins and CaP surfaces to increase protein adsorption [4, 318-319]. Surface modifications by physical or chemical immobilization are, thus, also influencing protein adsorption on biomaterial surfaces [4]. Another impacting factor is the surface area. It is commonly accepted that a larger surface area increases the amount of adsorbed proteins [317, 320]. Notably, the surface area of CaPs increases with a smaller granule size, a higher surface roughness (on the nanometer scale), and a higher microporosity, making these factors influential for protein adsorption [4, 321-322]. However, the pore size must be large enough for proteins to enter the material. Last, the biomaterials' crystallinity impacts protein adsorption [323]. For instance, biomaterials with a lower crystallinity show a higher solubility [4]. Consequently, the solubility increases the ionic strength in the protein environment, potentially altering the confirmation of the proteins in solution and indirectly affecting the adsorption behavior [4, 323].

Unique to biomaterial surfaces, nanoscale topography is influential for protein adsorption. In the case of bone substitution with synthetic CaPs, protein adsorption through blood or tissue contact, or coating approaches, determine the success of implant integration.

8. Proteomics reveals differential adsorption of angiogenic platelet lysate proteins on calcium phosphate bone substitute materials

Aim:

CaPs represent an efficient biomaterial platform for bone substitution. To further improve bone regeneration, CaPs are often combined with hemoderivatives, e. g. blood plasma or platelet lysates. Here, proteins adsorb to the CaP surface, and the adsorption of proteins with regenerative effects is highly desired. However, the protein adsorption in this setting remains uninvestigated. Therefore, this study aimed to reveal the adsorbed protein composition for three different hemoderivatives and six types of CaPs by LC-MS proteomics. Additionally, the regenerative effects were studied by employing tube formation assays with endothelial cells.

Copyright:

[5] **da Costa Marques, R.***, ___, ___, ___, ___, ___. Proteomics reveals differential adsorption of angiogenic platelet lysate proteins on calcium phosphate bone substitute materials. *Regenerative Biomaterials*, **2022**, *9*, rbac044. (* shared first)

Contributions:

I prepared both types of platelet lysates. I performed the protein adsorption experiments and characterized the protein samples by quantification, SDS-PAGE, and ELISA. I performed the LC-MS sample preparation and LC-MS data evaluation. I conducted the cell culture methods and the tube formation assays. I created and edited the figures and wrote the manuscript. ___ performed the LC-MS measurements. ___ and ___ provided the TCP/HA materials and the characterization data. ___ imaged the SEM pictures. ___ supervised and supported the preparation of the washed platelet lysates. The project was supervised by ___, ___, and ___.

8.1 Abstract

Protein adsorption on biomaterials for bone substitution, such as calcium phosphates (CaP), evokes biological responses and shapes the interactions of biomaterials with the surrounding biological environment. Proteins adsorb when CaP materials are combined with growth factor-rich hemoderivatives prior to implantation to achieve enhanced angiogenesis and stimulate new bone formation. However, the identification of the adsorbed proteins and their angiogenic effect on bone homeostasis remain incompletely investigated. In this study, we analyzed the adsorbed complex protein composition on CaP surfaces when using the hemoderivatives plasma, platelet lysate in plasma (PL), and washed platelet lysate proteins (wPL). We detected highly abundant, non-regenerative proteins and anti-angiogenic proteins adsorbed on CaP surfaces after incubation with PL and wPL by liquid chromatography and mass spectrometry (LC–MS) proteomics. Additionally, we measured a decreased amount of adsorbed pro-angiogenic growth factors. Tube formation assays with human umbilical endothelial cells demonstrated that the CaP surfaces only stimulate an angiogenic response when kept in the hemoderivative medium but not after washing with PBS. Our results highlight the necessity to correlate biomaterial surfaces with complex adsorbed protein compositions to tailor the biomaterial surface toward an enrichment of pro-angiogenic factors.

8.2 Introduction

Differences in adsorption characteristics of proteins on biomaterial surfaces must be considered for the engineering of biomaterials to enhance their regenerative potential [3, 317, 324]. For bone substitution, biomaterial engineering has put forth a variety of synthetic bone substitute materials [20, 325]. Among these, calcium phosphates (CaP) and other synthetic bone substitute materials are more frequently used for smaller bone defects [19, 325-326]. CaPs represent an absorbable and bioactive biomaterial platform with versatile and promising functionalization approaches to improve regenerative effects after application [327-330]. However, the application of CaPs in larger bone defects has been limited because of their inherent lack of growth factors [19, 21]. This lack of growth factors results in the inefficiency of CaPs to stimulate the formation of new bone [21]. To improve the formation of new bones, a crucial process is an efficient angiogenesis, the sprouting of new blood vessels [21, 311].

Previous studies have suggested the use of hemoderivative materials as growth factor-rich sources. Here, plasma, serum, platelet-rich plasma (PRP), or platelet lysates (PL) are currently combined with synthetic bone substitute materials [22-23]. These hemoderivative materials are cheap and easily obtainable sources of growth factors compared with single and isolated growth factors [19]. However, combining the promising hemoderivative growth factor sources with bone substitute materials remains a disputable method with controversial results [19, 22-23].

To understand these controversial results, we critically considered the complexity of proteins in hemoderivatives and the surface-adsorbed proteins that can induce but also inhibit angiogenesis. Activated platelets are well-known modulators of angiogenesis by the differential release of pro- and anti-angiogenic factors from platelet α-granules in an agonist-dependent manner [331-333]. Therefore, resting platelets are an excellent source of a variety of enriched angiogenic factors [334]. Highly abundant and potent pro-angiogenic growth factors stored in platelet α-granules include vascular endothelial growth factor (VEGF), fibroblast growth factor 2 (FGF-2) and platelet derived growth factor AB (PDGF-AB), which are essentially involved in proliferation and migration of endothelial cells in early and late stages of vessel branching, respectively [309]. The chemokine platelet factor 4 (PF4, CXCL4), the matricellular response to injury protein thrombospondin-1 (TSP-1) and endostatin, a C-terminal fragment of collagen type XVIII, represent prominent platelet-derived anti-angiogenic factors, which commonly inhibit the ligation of distinct growth factors, e.g. VEGF, FGF-2, to endothelial cells [335-337]. Presently, the protein adsorption on ‘modified’ bone substitute materials and the biological effect remain poorly studied for combining hemoderivatives with bone substitute materials. Therefore, we revealed the protein adsorption and its impact on angiogenesis in the case of CaP surfaces combined with hemoderivatives.

Here, we present for the first time a label-free liquid chromatography-mass spectrometry (LC -MS) proteomics approach to analyze the complex composition of the adsorbed proteins on CaP surfaces when incubated in the commonly used hemoderivatives citrate plasma (cP), platelet lysate with plasma (PL), and washed PL without plasma components (wPL). Additionally, we determined the concentrations of selected growth factors on the CaP surfaces by enzyme-linked immuno- sorbent assay (ELISA). Finally, we analyzed the angiogenic potential of preincubated CaP surfaces in tube-formation assays with human umbilical endothelial cells (HUVECs). We report our findings of highly abundant, non-regenerative proteins and single anti-angiogenic proteins on CaP surfaces when utilizing PL and wPL as a hemoderivative source. The adsorbed proteins only led to a non-angiogenic response when the CaP granules were washed before application. Further, we demonstrate that the CaP were only able to stimulate an angiogenic response when kept in the hemoderivative medium.

8.3 Materials and methods

Human citrate plasma. Human citrate plasma (cP) was provided by the Department of Transfusion Medicine Mainz from healthy donors in accordance with the Declaration of Helsinki. Citrate plasma was generated by plasmapheresis. A plasma pool from ten healthy donors was created, aliquoted and stored at -80 °C.

Freeze–thaw preparation for generating human PL. PL was obtained from human apheresis platelet concentrate by performing a previously published, standardized freeze-thaw lysis method [338]. The human platelet apheresis from ten healthy donors was obtained from the Transfusion Center of the University Medical Center Mainz in accordance with the Declaration of Helsinki. The platelet apheresis from all donors was pooled and aliquoted. The lysis was performed in five freeze-thaw cycles by freezing for 10-40 min at 80 °C and thawing for 7.5 min at 37 °C. To remove cellular debris, PL was centrifuged at 1 410*g* for 40 min at 22 °C (5702R, Eppendorf, Germany). The supernatant was collected, aliquoted and stored at -80 °C.

Platelet preparation for generating human washed PL. Human whole blood was obtained from healthy volunteers in accordance with the Declaration of Helsinki. The study was approved by the Ethics Committee of the University Medical Center Mainz (Study No. 837.302.12; 2018-13290_1). The volunteers did not take any medication for at least 10 days. All donors gave their informed consent before participating in the study. Venous blood was collected and anticoagulated with 10.6 mM trisodium citrate. Platelet isolation and washing were performed as previously published [339]. To bind remaining free calcium, a 0.5 M EGTA solution was added for a final concentration of 2 mM. The blood samples were centrifuged at 200*g*, for 10 min at room temperature (RT; Allegra X-30R, Beckman Coulter, USA). The supernatant, containing PRP was diluted with the same volume of CGS buffer (120 mM NaCl, 12.9 mM Tri-Na–citrate, 30 mM glucose, pH 6.5). Diluted PRP was centrifuged at 69*g* for 10 min at RT to pellet leukocytes. The supernatant was collected and centrifuged at 400*g* for 10 min at RT to pellet the platelets. The supernatant was discarded and the platelet pellet was resuspended in 3 ml CGS buffer. Following an incubation of 5-10 min at RT, samples were centrifuged at 400 g for 10 min at RT and the supernatant was discarded. The platelet pellet was resuspended in HEPES buffer (145 mM NaCl, 5 mM KCl, 1 mM $MgCl_2$, 10 mM glucose, 10 mM HEPES, pH 7.4) and the platelet concentration was adjusted to $2*10^9$ platelets ml $^{-1}$. Platelets were incubated at 37 °C in the water bath for 15 min. Platelet samples were frozen in liquid nitrogen for shock freeze lysis to obtain wPL and stored at -80 °C.

Bone substitute granules. We included six different CaPs in the experiments. Four kinds of granular, biphasic CaP (TCP/HA), with an intimate molecular mixture of 20% hydroxyapatite (HA) and 80% tricalcium phosphate (TCP), were kindly provided by Dr. Guy Daculsi (Biomatlante, France). The TCP/HA materials were synthesized and characterized according to the methods previously described in literature [340-341]. The sample TCP/HA-1 was the conventional MBCP+ from Biomatlante (Biomatlante AMS group, CEmark and US FDA). The sample TCP/HA-2 was produced according to the same protocol with a higher sintering temperature to increase the crystal size and reduce microporosity [342]. The TCP/HA-3 sample was a smaller, rounded granule type with the same chemical composition and sintering as TCP/HA-1. The TCP/HA-4 sample had the same smaller size and rounded morphology as TCP/HA-3, but was produced with a higher sintering temperature as TCP/HA-2 [342]. Two kinds of granular β-TCP were purchased as chronOS Granules from DePuy Synthes, USA. No further modification was applied for the experiments. The characterization data for the β-TCP samples were retrieved from a previous study from Duan et al. [343], in which the values are linked to the sample 'chronos'.

Brunauer, Emmett and Teller measurement. The specific surface area (SSA) of the TCP/HA samples was determined by the Brunauer, Emmett and Teller (BET) method, which was already described in previous works [340, 342, 344]. The measurements were performed by nitrogen gas adsorption on Micromeritics 3-FLEX equipment. About 100 mg per sample was weighed and degassed in vacuum conditions with 10^{-3} mbar at 150 °C for 24 h. Next, the weight of the samples was precisely measured. The SSA was calculated from the range of relative pressure of adsorption–desorption isotherms by 0.05-0.2. The unit of the SSA, determined by BET is in $m^2\ g^{-1}$.

Scanning electron microscopy. The morphology of the CaP materials was characterized by performing scanning electron microscopy (SEM) with a LEO 1530 GEMINI (Zeiss, Germany). The CaP surfaces were imaged in their native state at 3 kV and 121 V, without utilizing precious metal sputter coating.

Protein adsorption preparation. Protein adsorption preparation was performed with modifications as previously described [62]. After thawing, human cP, PL, and wPL were centrifuged at 20 000*g* for 30 min at 4 °C (5804R, Eppendorf, Germany) to remove protein aggregates and cellular debris. To ensure reproducibility, 10 mg of CaPs were used and

incubated in either 1 ml cP or PL, or in 100 µl wPL. The samples were incubated for 1 h at 37 °C. To deplete loosely bound or free protein, the CaPs were washed three times with PBS with centrifugation steps of 20 000*g* for 10 min at 4 °C, discarding the supernatant and adding 1 ml PBS to the granules. The washed and adsorbed proteins were desorbed by adding 50-100 µl of desorption buffer (2% (w/v) SDS, 62.5 mM Tris-HCl) to the CaPs, incubating the samples at 95 °C for 5 min and centrifuging at 20 000*g* for 10 min at 4 °C. This protein desorption approach was performed and described in previous studies with different materials [52, 62, 345]. The supernatant was collected and analyzed further by protein quantification, sodium dodecyl sulfate-polyacrylamide gel electrophoresis (SDS-PAGE), ELISA, and LC-MS. To utilize CaPs with washed and adsorbed proteins in tube formation assays, 10 mg CaP was added to 5 ml Medium 200 after the abovementioned protein adsorption preparation for a concentration of 2 mg ml^{-1}. For the experiments with unwashed CaPs, CaPs were added directly to the supplemented medium for a concentration of 2 mg ml^{-1}. Medium 200 was supplemented with 100 U ml^{-1} penicillin, 100 mg ml^{-1} streptomycin and with or without simple concentrated (1X) large vessel endothelial supplement (LVES; all Gibco, Germany) after washing steps.

Protein quantification. Protein concentration of cP, PL, wPL, and adsorbed protein samples was quantified with Pierce™ 660 nm Protein Assay Reagent (Thermo Scientific, Germany) according to the manufacturer's instructions. For samples containing SDS, such as the desorbed proteins, Ionic Detergent Compatibility Reagent (Thermo Scientific, Germany) was added to the assay reagent, before employing the measurement. Bovine serum albumin (Sigma- Aldrich, Germany) was used as a standard. Absorption was measured by an Infinite M1000 plate reader (Tecan, Switzerland) at 660 nm.

Sodium dodecyl sulfate-polyacrylamide gel electrophoresis. For cP, PL, wPL, and adsorbed protein samples, 2 mg of protein was adjusted with deionized water to a total volume of 26 µl. To the diluted samples, 4 µl of NuPAGE™ Sample Reducing Agent and 10 µl of NuPAGE™ LDS Sample Buffer (both Invitrogen, Germany) were added and incubated at 70 °C for 10 min to denature the proteins. The samples were loaded on a Bolt™ 10% Bis-Tris Plus gel using NuPAGE™ MES SDS Running Buffer (both Invitrogen, Germany) and run for 1 h at 200 V. SeeBlue™ Plus2 Pre-Stained Standard (Invitrogen, Germany) was used as a molecular weight marker. The gels were stained with SilverQuest™ Silver Staining Kit (Invitrogen, Germany) according to the manufacturer's instructions and documented with the Scanning system View Pix 1100 (Biostep, Germany).

Enzyme-linked immunosorbent assay. The concentration of human VEGF, human FGF-2 and human platelet-derived growth factor (PDGF-AB) was measured for cP, PL, wPL, and wPL-adsorbed proteins samples by ELISA. Samples and reagents were prepared and processed according to the manufacturer's instructions of the utilized Human VEGF Quantikine ELISA Kit, Human FGF2 Quantikine ELISA Kit and Human PDGF-AB Quantikine ELISA Kit (all R&D Systems, Germany). The absorption was measured by an Infinite M1000 plate reader at 450 nm with a wavelength correction at 570 nm.

In solution digestion. Adsorbed protein samples were processed with Pierce™ Detergent Removal Spin Columns (Thermo Scientific, Germany) to remove SDS. The procedure was performed according to the manufacturer's instructions before digestion. Subsequent protein digestion was carried out according to published protocols [52, 183]. For cP, PL, wPL, and adsorbed protein samples, 25 µg was precipitated with ProteoExtract Protein Precipitation Kit (CalBioChem, Germany), following the manufacturer's instructions. Afterwards, Proteins were isolated by centrifugation at 10 000*g* for 10 min at RT and washed twice with ProteoExtract Protein Precipitation Washing Solution. The supernatant was discarded and the pellet left to dry for 5-10 min. Subsequently, the pellets were resuspended in 0.1% RapiGest SF surfactant (Waters Corporation, Germany), dissolved in 50 mM ammonium carbonate buffer. Samples were incubated at 80 °C for 15 min to solubilize protein. Protein disulfide bonds were reduced by adding dithiothreitol (Sigma, Germany) solution in a final concentration of 5 mM. The reaction was performed at 56 °C for 45 min. Next, proteins were alkylated by adding 500 mM iodoacetamide (Sigma, Germany) solution for a final concentration of 15 mM. The reaction was carried out in the dark for 1 h. Protein digestion was performed with a ratio of 50:1 of protein:trypsin (Promega, Germany) for 16 h at 37 °C. The digestion was stopped by adding 2 µl of hydrochloric acid (Sigma, Germany) and incubating for 45 min at 37 °C. Lastly, samples were centrifuged at 13 000*g* for 15 min to remove degradation products and the supernatant was transferred into new tubes.

Liquid chromatography coupled to mass spectrometry analysis. The LC-MS measurements were performed with modifications from previously described methods [62]. Samples were diluted with LC-MS grade water (Merck, Germany) containing 0.1% formic acid (Sigma, Germany). Samples were spiked with 50 fmol μl^{-1} HI3 E.coli Standard (Waters Corporation, Germany) for absolute protein quantification [185]. The digested peptides were applied to a nanoACQUITY UPLC system, equipped with a C18 nanoACQUITY trap column (5 µm, 180 µm, 20 mm) and a C18 analytical reversed-phase column (1.7 µm, 75 µm, 150 mm; all Waters Corporation, Germany). The two mobile phases consisted of (A) 0.1% (v/v)

formic acid in water and 0.1% (v/v) formic acid in acetonitrile (Biosolve, Germany) and a gradient of 2-37% of mobile phase B over 70 min were used for separation. The samples were infused with a flow rate of 0.3 µl min^{-1} and the referent components Glu-Fibrinopeptide and LE (both Sigma, Germany) were set to a flow rate of 0.5 µl min^{-1}. The nanoACQUITY UPLC system was coupled with a Synapt G2-Si mass spectrometer(Waters Corporation, Germany). Electrospray ionization (ESI) was performed with a NanoLockSpray source was in positive mode. The measurements were conducted in resolution mode and experiments were carried out with data-independent acquisition (MS^E). Each measurement was performed in technical triplicates. A mass to charge range of 50-2 000 Da, scan time of 1 s, ramped trap collision energy from 20 to 40 V was set and data were acquired over 90 min. For data acquisition and processing, the software MassLynx 4.1 (Waters Corporation) was utilized.

Protein identification. Peptides and proteins were identified with the software Progenesis QI 2.0 (Nonlinear Dynamics) [62]. Noise reduction threshold for low energy, elevated energy and peptide intensity were set to 120, 25, and 750 counts, respectively. A human data base with reviewed proteins was downloaded from uniport (SWISS PROT) and modified with the sequence information of Hi3 E.coli standard for absolute quantification. Following parameters were selected: one missed cleavage, maximum protein mass 600 kDa, fixed carbamidomethyl modification for cysteine and variable oxidation for methionine. Protein identification requirements were restricted to at least two assigned peptides and five assigned fragments. Peptide identification requirements were based on three assigned fragments. Identified peptides with a score parameter below 4 were excluded. Protein amount in fmol was calculated by TOP3/Hi3 approach [104].

Human umbilical vein endothelial cell culture. Human umbilical vein endothelial cells (HUVECs) (Gibco, Germany) were cultured with Medium 200, which was supplemented with simple concentrated (1X) LVES, 100 U ml^{-1} penicillin and 100 mg ml^{-1} streptomycin. The cells were kept in an incubator at 37 °C, 5% CO_2 and 95% relative humidity (CO_2 Incubator C200, Labotect, Germany) for cultivation. For cell subculture and harvesting for experiments, cells were briefly washed with PBS, followed by cell detachment with 0.25% Trypsin-EDTA (Gibco, Germany) for 5 min at 37 °C, 5% CO_2 and 95% relative humidity. The cell suspension was transferred with LVES-supplemented medium and centrifuged at 130*g* for 5 min at RT (5810R, Eppendorf, Germany). The supernatant was discarded and the cell pellet resuspended in LVES- supplemented medium. Cell viability and cell count were determined by equally mixing 20 ml of cell suspension and trypan blue and measuring by an automated cell counter (TC10, Bio- Rad, Germany).

Tube formation assay. Geltrex™ LDEV-Free Reduced Growth Factor Basement Membrane Matrix (Gibco, Germany) was thawed on ice at 4 °C overnight. The wells of a µ-Slide Angiogenesis (Ibidi, Germany) were covered with 10 µl of basement membrane matrix and incubated at 37 °C, 5% CO_2 and 95% relative humidity for 1 h to solidify. HUVECs with a passage number between 2 and 6 were harvested and centrifuged as described above. The pellet was resuspended in Medium 200 without LVES to avoid undesired stimulation. The cell concentration was adjusted to 400 000 cell ml^{-1} and mixed with the same volume of supplemented medium for each test condition, respectively. A cell number of 10 000 cells per well was seeded. The cells were incubated at 37 °C, 5% CO_2 and 95% relative humidity and examined for tube formation after 18 h under a CKX41 inverted microscope (Olympus, Germany). One picture was taken per well by utilizing the software analySIS getIT (Olympus Soft Imaging Solutions GmbH). Pictures were evaluated with ImageJ (National Institutes of Health, USA) and the plugin Angiogenesis Analyzer (Gilles Carpentier) [346], measuring the total segment length.

Data representation. Data were presented as means ± standard deviation (SD) of the values. Statistical analysis was performed with GraphPad Prism 7 (GraphPad Software, USA). For a comparison of two data sets, the unpaired t-test was utilized. For statistical analysis, involving multiple data sets, one-way analysis of variance (ANOVA) with Tukey's multiple comparison test or Dunnett's multiple comparison test were performed. All tests were carried out choosing a P values of <0.05 to be statistically significant.

8.4 Results and discussion

We investigated lysates of platelet with plasma (PL) and from washed platelets (wPL) in a divided workflow with two steps (Fig. 8.1). Additionally, we included human citrate plasma (cP) to compare the PL preparations with plasma and without. These three hemoderivative protein sources (cP, PL, and wPL) were used to study protein adsorption on CaP surfaces. The hemoderivative protein sources and adsorbed protein samples were analyzed qualitatively by SDS-PAGE and by LC-MS for quantitative proteomic data. In addition, the samples were analyzed for selected pro-angiogenic growth factors by ELISA. Finally, the pro-angiogenic potential of the samples was evaluated by employing tube formation assays.

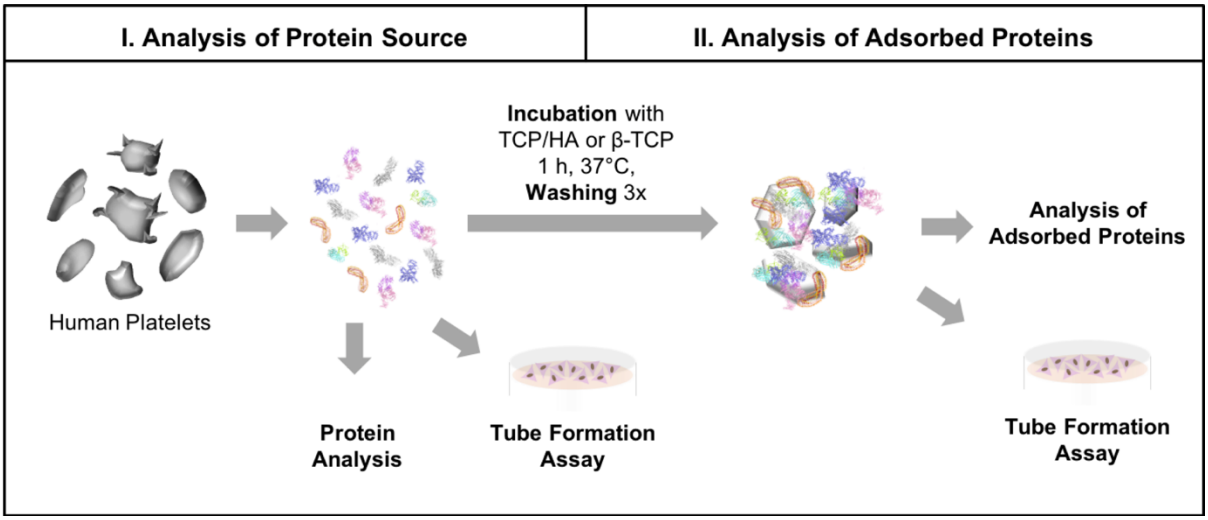

Figure 8.1: Principal workflow of protein source and adsorbed protein analysis. Platelet lysates were generated from human platelets in plasma and from washed platelets, respectively. Different bone substitutes were incubated with hemoderivative protein sources for protein adsorption. Incubated bone substitutes were washed three times with PBS, pH 7.4 to remove loosely bound and free proteins. Afterward, adsorbed proteins were recovered by a protein desorption step. Protein sources and adsorbed protein samples were analyzed by protein quantification, SDS-PAGE, silver staining, and LC-MS. Tube formation assays were employed to study pro-angiogenic effects of hemoderivative protein sources and bone substitutes with adsorbed proteins. Protein crystal structures were taken from RCSB Protein Data Bank. Images are not drawn to scale.

Hemoderivative protein sources

The three hemoderivative protein sources used in this study were distinct in composition and source material (Fig. 8.2A). Human cP was obtained from the blood bank. The first type of human PL was generated from human platelet apheresis concentrates by a freeze–thaw preparation of five cycles. The human wPL was generated from whole blood of single healthy

human donors. Here, the platelets were washed to remove plasma components before lysis. Both lysates were generated with a similar platelet concentration. However, wPL showed a lower protein concentration when compared with PL, indicating the depletion of plasma proteins.

The plasma protein depletion was also demonstrated by SDS-PAGE, observing a distinct band pattern for wPL compared with the other two sources (Fig. 8.2B). To further detail the differences of the complex protein composition between the hemoderivatives we performed quantitative LC-MS measurements. LC-MS-identified proteins of the three sources were assigned to nine different protein function classes (Fig. 8.2C). Here, cytoskeletal and coagulation-related proteins were more pronounced in wPL when compared with PL and cP and tissue leakage proteins were more pronounced in wPL when compared with cP. Conversely, a lower amount of immunoglobulins and serum albumin was detected in wPL. Minor differences were uncovered for PL in contrast to cP like a higher percentage amount of tissue leakage proteins, indicating lysed platelets. PL proteins, such as platelet factor 4 and platelet basic protein were also found within the ten most abundantly detected proteins for wPL, whereas plasma proteins, such as serum albumin and immunoglobulins were among the most abundant in cP and PL (Tab. S8.1).

To provide data for pro-angiogenic growth factors, the concentration of VEGF, fibrinogen growth factor 2 (FGF-2) and platelet derived growth factor (PDGF-AB) were measured by ELISA (Fig. 8.2D-F). Here, both, PL and wPL showed a statistically significant higher concentration of all three growth factors when compared with cP. Comparing PL and wPL, the highest concentration for all three pro-angiogenic growth factors was found in wPL. However, as wPL was generated from single-donor blood, the concentration of all three growth factors showed donor-dependent differences (Fig. S8.1).

A

	Citrate Plasma (cP)	Platelet Lysate (PL)	Washed Platelet Lysate (wPL)
Composition	Citrate plasma	Citrate plasma and platelet lysate	Platelet lysate
Source	Plasma from blood bank	Platelet apheresis concentrate	Whole blood
Method	Separated by centrifugation	Freeze thaw preparation (5 cycles)	Flash freezing
Total protein [mg mL^{-1}]	64.22 ± 6.69	65.64 ± 5.62	2.48 ± 0.63
Platelets [PLT mL^{-1}]	N/A	0.8-2 x 10^9	2 x 10^9

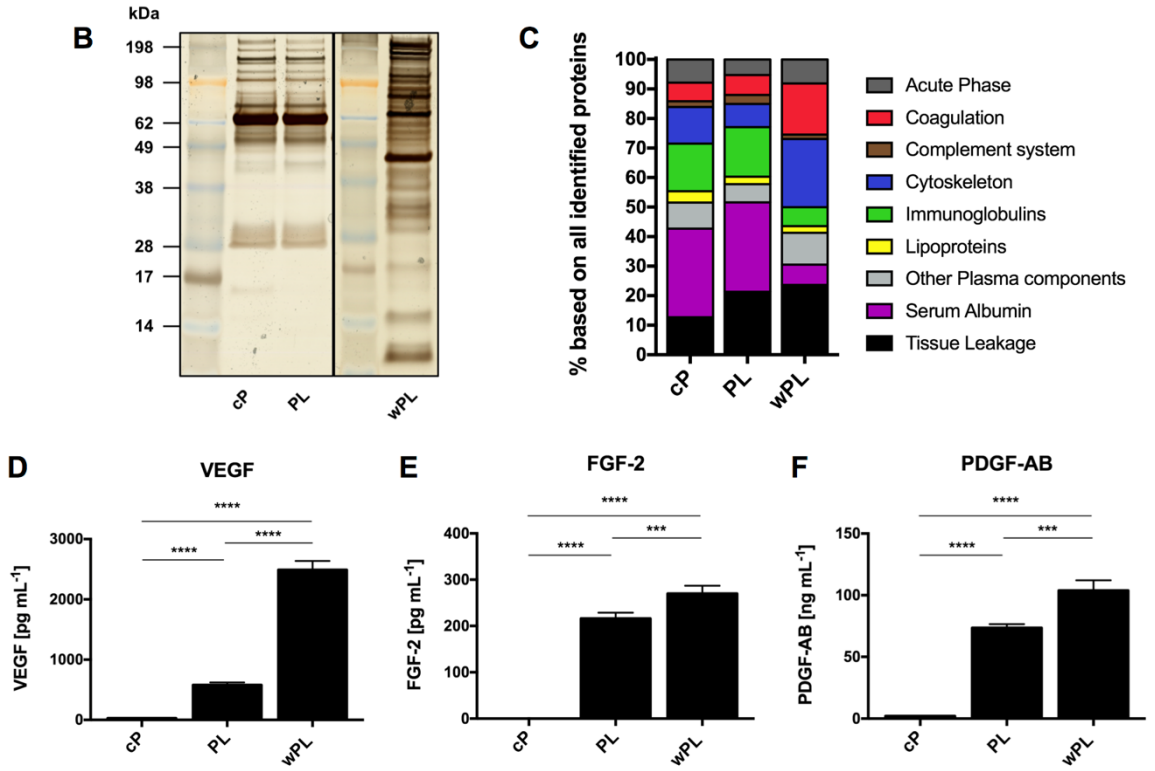

Figure 8.2: Human washed PL differs from plasma and PL in protein composition and growth factor concentration. (A) Characteristics of utilized hemoderivative protein sources. The main composition, source of material, preparation method, protein concentration (mg ml^{-1} ± SD, n = 4-8) and platelet (PLT) count are listed. Protein sources were analyzed by **(B)** SDS-PAGE with silver staining and **(C)** quantitative LC–MS proteomics. The bars indicate the percentage based on all identified proteins with protein annotation in nine different functional classes. **(D-F)** Protein sources were evaluated for pro-angiogenic growth factors. The concentration of VEGF, FGF-2 and PDGF-AB was measured by ELISA (data are shown as mean ± SD, n (PDGF-AB, cP) = 2, n (others) = 4). The statistical significance was calculated by ANOVA with Tukey's multiple comparison test (***P < 0.001,****P < 0.0001); N/a, data not available.

In addition, we performed tube formation assays to study the pro-angiogenic potential and complement the protein data. Alongside the tested samples, we included non-supplemented cell medium as negative control (-) and LVES supplemented medium as positive, tube stimulating, control (+). Generally, increasing the concentration of all three hemoderivatives, respectively, increased the tube formation with statistical significance (Fig. 8.3A-C). Yet, a

peak in total tube length was observed for cP at 5%, achieving slightly better results than 10% (Fig. 8.3A). Comparing the three hemoderivative sources at the same protein concentration of 1.1 mg ml^{-1} revealed wPL to be the most potent inducer of tube formation (Fig. 8.3D/E). The enhanced tube formation by wPL could be observed microscopically and evaluated by the Angiogenesis Analyzer Plug-In of ImageJ, resulting in a statistically significant result. Comparable to the donor-dependent differences in growth factor concentration, the effect of the tube formation assays differed among the various donor samples (Fig. S8.2).

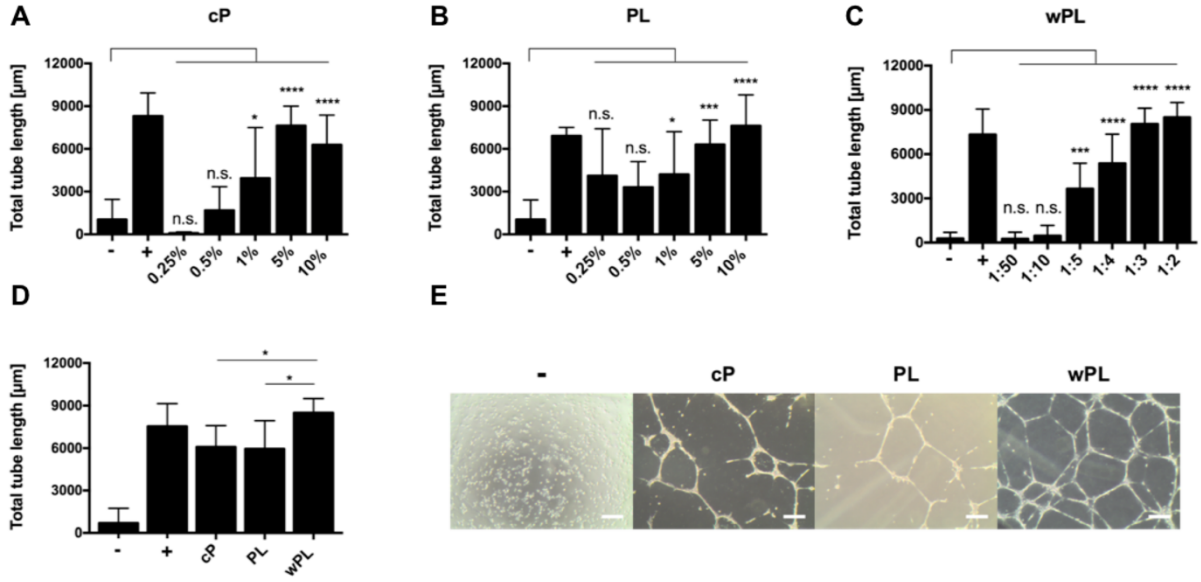

Figure 8.3: Human wPL induces stronger angiogenic response in tube formation assays. (A-C) The pro-angiogenic effect of hemoderivative protein sources was analyzed by employing tube formation assays with HUVECs. HUVECs were incubated with different concentrations of citrate plasma (cP), platelet lysate in plasma (PL) and lysate of washed platelets (wPL) on Geltrex™ LDEV-Free reduced growth factor basement membrane matrix for 18 h. For cP and PL different percentual dilutions (0.25-10%) in the cell culture medium were tested. For wPL different ratios of wPL in total volume (1:50-1:2) with cell culture medium were tested. Total tube length was evaluated with ImageJ and the plugin angiogenesis analyzer (-, negative control: medium without LVES; +, positive control: medium with LVES; data are shown as mean 6 SD, n = 3-8). **(D)** Tube formation was analyzed with a comparable protein concentration of 1.1 mg ml^{-1} for all three protein sources (data are shown as mean ± SD, n = 6-17). The statistical significance was calculated by ANOVA with Dunnett's multiple comparison test (*P < 0.05, **P < 0.01, ***P < 0.001, ****P < 0.0001), performing the comparison with the negative control (A–C) or with wPL (D). **(E)** HUVECs on Geltrex™ after 18 h incubation with different hemoderivative protein sources at the same concentration, as seen in (D). The scale bars represent 200 µm.

Protein adsorption

Protein adsorption influences the interplay between biomaterial surfaces and their biological environment. In this part, we investigated the protein adsorption of the three abovementioned and characterized protein sources on different CaP surfaces. Additionally, we measured the concentration of the same growth factors and linked the protein results to the results of the tube formation assays.

Four different CaP surfaces consisting of 80% TCP and 20% HA (HA/TCP) with two different granule sizes were selected. Additionally, we included two different CaP surfaces consisting of β-TCP with two different sizes, which were commercially purchased as chronOS (DePuy Synthes). The physicochemical characterization revealed differences between the materials (Fig. 8.4A/B, Fig. S8.3). The HA/TCP samples showed an increasing crystal size with a raising sample number. The β-TCP samples showed the highest crystal size with HA/TCP-4. Conversely, the SSA decreased within HA/TCP a raising sample number, and the β-TCP samples showed the smallest SSA with HA/TCP-4. The microporosity decreased within HA/TCP sample number. The microporosity of β-TCP was comparable to the higher microporosity of HA/TCP-1 (Fig. 8.4A).

To investigate the protein adsorption, we incubated the CaP materials with the hemoderivatives for 1 h at 37 °C and subsequently washed them three times before a desorption step. This protein desorption approach was performed and described in previous studies with different materials [52, 62, 345]. Proteins were detected for all material variations incubated in all three hemoderivative sources. We did not perform and analyze protein adsorption of wPL on β-TCP-2 due to limited quantities of wPL and great similarities between β-TCP-1 and β-TCP-2 in the case of adsorption with cP and PL. Interestingly, the highest concentration of adsorbed proteins was consistently measured for all materials after being incubated in wPL when compared with the other sources (Fig. 8.4C/D). For cP, we observed similar amounts of protein regardless of the used CaP surface. On the other hand, we noticed a decreasing trend of protein amount in the case of PL, which was following the decreasing SSA for the materials, reversibly the increasing crystal size. This same trend was observed for wPL in the case of the TCP/HA samples.

A

Sample	Composition	Granule Size [mm]	Crystal Size [µm]	SSA Specific Surface Area [m²/g]	Microporosity (<10 µm)
TCP/HA-1	80 % Tricalcium phosphate, 20% Hydroxyapatite	0.5 - 1.0	< 0.5	> 6	> 25%
TCP/HA-2		0.5 - 1.0	1 - 2	1 - 3	< 20%
TCP/HA-3		0.08 - 0.2	0.5 - 2	1 - 3	< 20%
TCP/HA-4		0.08 - 0.2	5 - 7	0.5 - 1	< 10%
β-TCP-1	β-Tricalcium phosphate	0.5 - 0.7	5.03 ± 1.90 *	0.51 *	31.52 *
β-TCP-2		0.7 - 1.4			

B

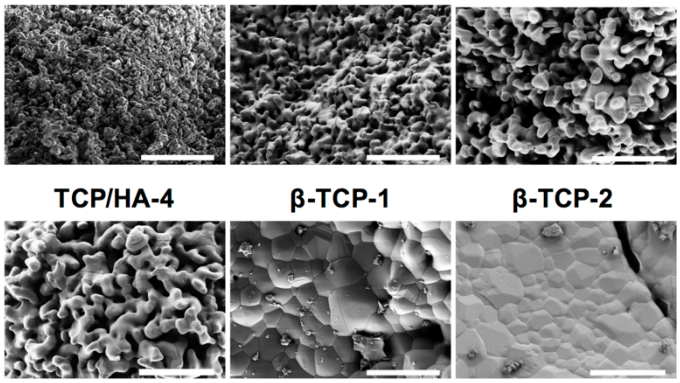

C

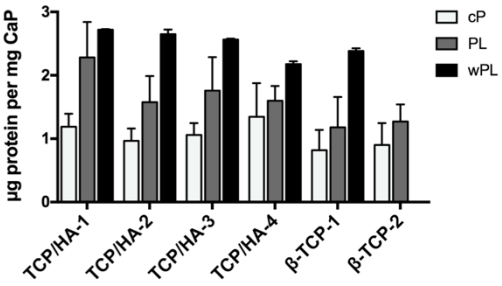

D

µg protein per mg CaP	cP	PL	wPL
TCP/HA-1	1.19 ± 0.20	2.28 ± 0.56	2.72 ± 0.01
TCP/HA-2	0.97 ± 0.20	1.58 ± 0.41	2.65 ± 0.07
TCP/HA-3	1.06 ± 0.19	1.76 ± 0.53	2.56 ± 0.01
TCP/HA-4	1.35 ± 0.53	1.60 ± 0.23	2.18 ± 0.04
β-TCP-1	0.82 ± 0.32	1.18 ± 0.48	2.38 ± 0.04
β-TCP-2	0.90 ± 0.35	1.27 ± 0.27	-

Figure 8.4: CaP Material characterization, SEM images and protein adsorption. (A) The physicochemical characterization of utilized CaP materials. The composition, size of the granules, crystal size, SSA, microporosity, and the manufacturing processes are listed. Crystal size, SSA and microporosity for β-TCP materials (marked with *) were retrieved from previously published measurements [343]. **(B)** SEM images of granular CaP surfaces. The scale bars represent 10 µm. **(C)** Quantification of adsorbed proteins on CaPs, shown as a bar diagram. CaPs were incubated for 1 h in cP, PL and wPL, respectively. Protein adsorption of wPL on β-TCP 2 was not performed and analyzed due to limited quantities of wPL and strong similarities between β-TCP 1 and β-TCP 2 for cP and PL. Subsequently, three wash steps were performed and proteins were desorbed with 2% SDS. Proteins were quantified by Pierce 660 nm Assay (data are shown as mean ± SD, n = 2-7). **(D)** Quantification of adsorbed proteins on CaPs, shown as a table, as seen in (C) (data are shown as mean ± SD, n = 2-7).

The band pattern of the adsorbed proteins, as seen on SDS-PAGE, differed slightly from their original hemoderivative protein sources' pattern. The protein pattern complexity was slightly reduced for wPL-related protein adsorption compared with cP and PL, respectively (Fig. 8.5A/B, Fig. S8.4A). Differences were more pronounced when the adsorbed proteins from wPL were compared with the absorbed proteins from cP and PL. Both cP and PL showed their strongest band at ~66 kDa, suggesting the rough molecular weight of serum albumin [239]. The strongest band for wPL was defined at ~42 kDa, suggesting β-actin [239, 347]. Interestingly, the band pattern was similar across the different materials when incubated in the same hemoderivative source. Only slight differences were observed on the gel between TCP/HA materials and β-TCP.

We employed LC-MS measurements to further characterize the complex adsorbed protein composition. Using the same protein functional classes as shown for the hemoderivatives, large differences in adsorbed proteins were revealed depending on the utilized hemoderivative. After the incubation in cP, the most abundant protein was serum albumin, followed by immunoglobulins (Fig. S8.4B). Likewise, serum albumin remained the highest protein in PL, although decreased. The other protein functional classes in PL, such as coagulation, complement, cytoskeleton and immunoglobulins were distributed more evenly (Fig. 8.5C). The protein functional class distribution of wPL was quite distinct compared with cP and PL. Here, cytoskeleton proteins were found to be the most abundant group with more than 60% on every CaP surface used, followed by tissue-leakage proteins and coagulation (Fig. 8.5D). Generally, the protein composition by protein functional classes did not differ much between the different CaP materials within the same adsorbed protein source.

Next, we quantified the three previously described pro- angiogenic growth factors by ELISA in the adsorbed protein samples and compared them with the original hemoderivative. The ELISA experiment was exclusively performed for TCP/HA-4, incubated in wPL. We chose to investigate TCP/HA-4 principally because of the small size of the granules (Fig. 8.4A) and therefore its suitability for the tube formation assays. We chose wPL as the hemoderivative for its best performance in the tube formation assays (Fig. 8.3D/E). Despite the promisingly high concentration of VEGF, FGF-2 and PDGF-AB in wPL, a great decrease was measured after protein adsorption (Fig. 8.5E-G). The value for VEGF was measured below the detection limit. FGF-2 was depleted ~10-fold and PDGF-AB ~700-fold.

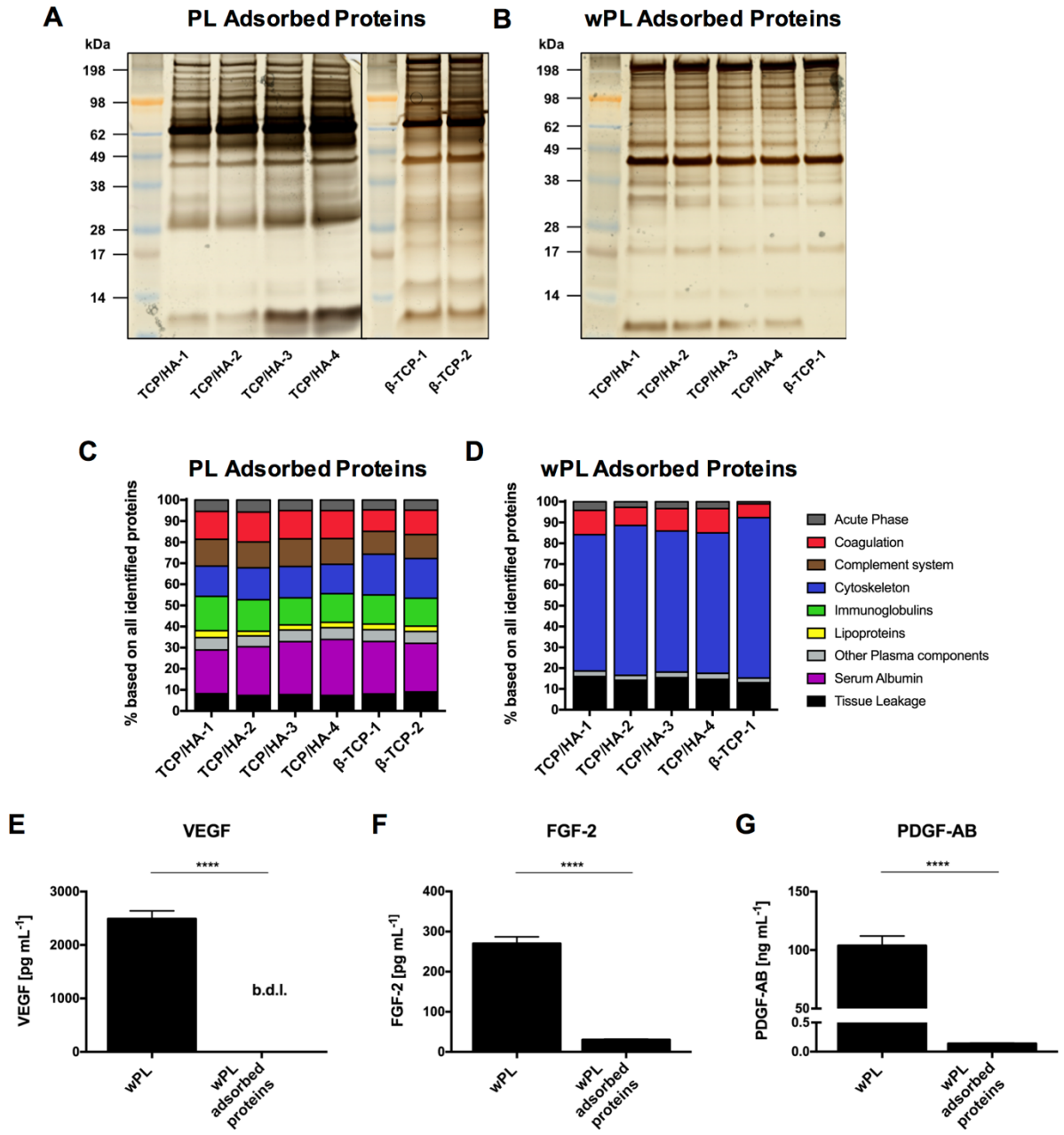

Figure 8.5: Cytoskeletal proteins from human washed PL are enriched on CaP surfaces while pro-angiogenic growth factors are depleted. CaP surfaces were incubated for 1 h in the hemoderivative protein source. After three subsequent washing steps, proteins were desorbed with 2% SDS. **(A, B)** SDS-PAGE and silver staining were performed for adsorbed proteins on different CaP surfaces incubated in PL and wPL, respectively. Protein adsorption of wPL on β-TCP 2 was not performed and analyzed due to limited quantities of wPL and strong similarities between β-TCP 1 and β-TCP 2 for cP and PL. **(C, D)** Adsorbed proteins on CaP surfaces from PL and wPL, respectively, were analyzed by quantitative LC-MS proteomics and identified proteins were classified into nine different protein functional classes. The bars indicate the percentage based on all identified proteins. **(F-G)** Adsorbed proteins on the CaP surface of TCP/HA-4, incubated in wPL, were evaluated for angiogenesis-involved growth factors and compared with wPL. The concentration of VEGF, FGF-2, and

PDGF-AB was measured by ELISA (b.d.l. = below detection limit; data are shown as mean ± SD, n = 4). The statistical significance was calculated by an unpaired t test (****P < 0.0001).

Additionally, single non-angiogenic and anti-angiogenic proteins were found among the 20 most abundant proteins in both PL and wPL-adsorbed protein samples. In case of the adsorbed proteins from PL, TSP-1 was found to be present among the top20 proteins. An anti-angiogenic potential of TSP-1 has been previously reported [348]. The other proteins detected were mainly non-angiogenic plasma proteins, such as albumin, immunoglobulin chains, and complement factors (Fig. 8.6A). For the adsorption of wPL proteins, the highest abundant proteins were found to be cytoskeleton proteins or cytoskeleton-associated proteins. Among these proteins were cytoplasmatic actin, myosin-family proteins, tubulin and gelosin, an actin-binding protein. Platelet prominent proteins detected were platelet basic protein, a precursor of the pro-angiogenic chemokines connective tissue-activating peptide III (CTAP-3) and neutrophil-activating peptide-2 (NAP-2), TSP-1, and PF4, a chemokine involved in anti-angiogenic signaling (Fig. 8.6B) [349-350]. In comparison, the most abundantly adsorbed proteins after incubation in cP were serum albumin and several immunoglobulin chains, apolipoproteins and other prominent plasma proteins (Fig. S8.4C). Here, the composition of the abundant proteins was found to be highly influenced by the presence of plasma proteins. In summary, non-angiogenic cytoskeleton proteins and anti-angiogenic platelet proteins adsorbed on the CaP surfaces and the inclusion of plasma drastically changes the adsorbed proteins.

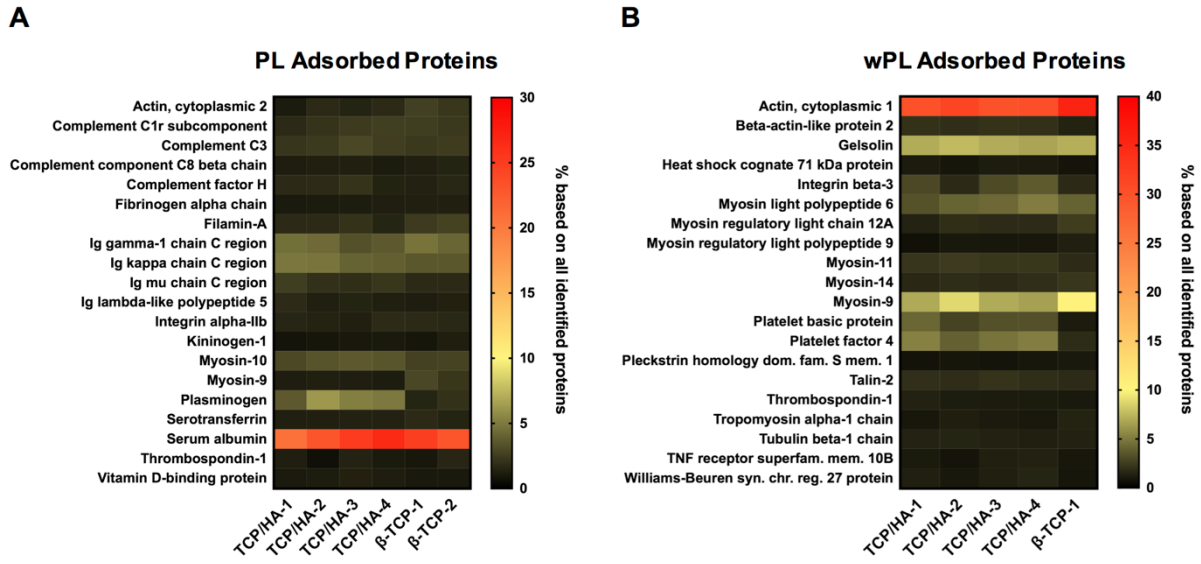

Figure 8.6: Non-regenerative and anti-angiogenic proteins are detected among the most abundant proteins on PL incubated CaP. (A, B) The heat maps show the 20 most abundant proteins for TCP/HA-4 compared with the other CaP surfaces. The values represent the percentage based on all identified proteins.

Subsequently, the selected CaP material, TCP/HA-4 was tested without and with preincubation in wPL in tube formation assays to investigate the effects on the angiogenic performance of HUVECs. While wPL potently induced tube formation, no angiogenic effect was observed when preincubated with TCP/HA and then washed with PBS. In this case, we obtained the same negative result for non-treated CaP materials and wPL preincubated CaP materials (Fig. 8.7).

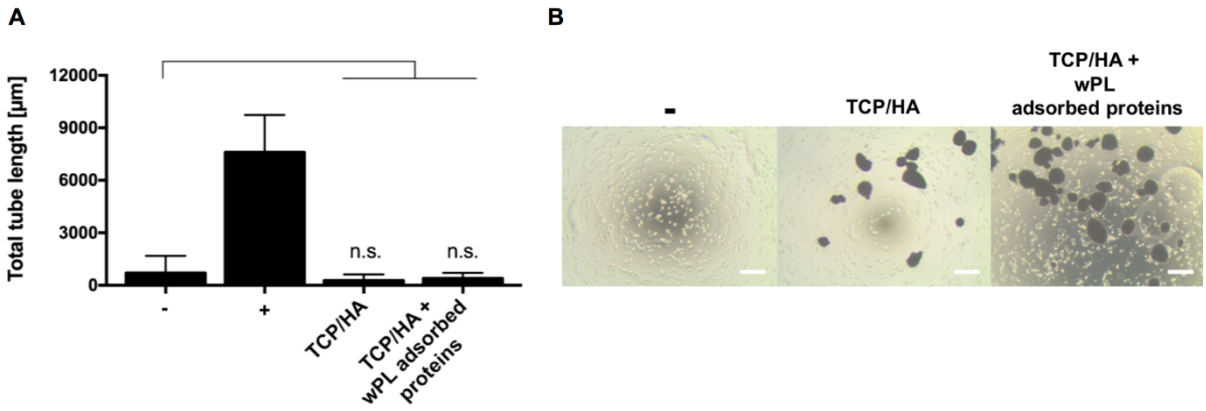

Figure 8.7: Washed CaP surfaces incubated in human washed PL show no pro-angiogenic effect. **(A)** The pro-angiogenic effect was analyzed by employing tube formation assays with HUVECs. HUVECs were incubated with untreated CaP surfaces and CaP surfaces, incubated in wPL and washed three times (all TCP/HA-4). HUVECs were then seeded on Geltrex™ LDEV-Free reduced growth factor basement membrane matrix for 18 h. Total tube length was evaluated with ImageJ and the plugin angiogenesis analyzer (-, negative control: medium without LVES; +, positive control: medium with LVES; data are shown as mean ± SD, n = 4-9). The statistical significance was calculated by ANOVA with Dunnett's multiple comparison test (*P < 0.05), performing the comparison with the negative control. **(B)** HUVECs on Geltrex™ after 18 h incubation with untreated CaP surfaces and CaP surfaces (seen as dark spots in the images), incubated in wPL and washed three times, as seen in (A). The scale bars represent 200 µm.

Additional tube formation assays were performed with TCP/HA-4 in the presence of the three respective hemoderivatives, but without removing the hemoderivatives and washing with PBS after adding TCP/HA-4 to the hemoderivatives. For the three hemoderivatives, concentration-dependent effects on the tube formation were observed, similar to the experiments without CaP surfaces. However, CaP surfaces incubated in both, CP and wPL seemed to induce less tube formation when incubated in the lowest dilution, 10% and 1:2, respectively (Fig. 8.8A-C). Also, similar protein concentrations of the hemoderivative were tested. Unlike the results for hemoderivative sources without CaP surfaces, all three hemoderivatives induced tube

formation, but without statistical difference between the hemoderivative groups (Fig. 8.8D). However, the tube formation efficiency tended to be visually stronger for the conditions with PL and wPL compared with cP. Here, the HUVECs attached to the CaP surfaces and formed tubes with the CaP surfaces as central nodes (Fig. 8.8E).

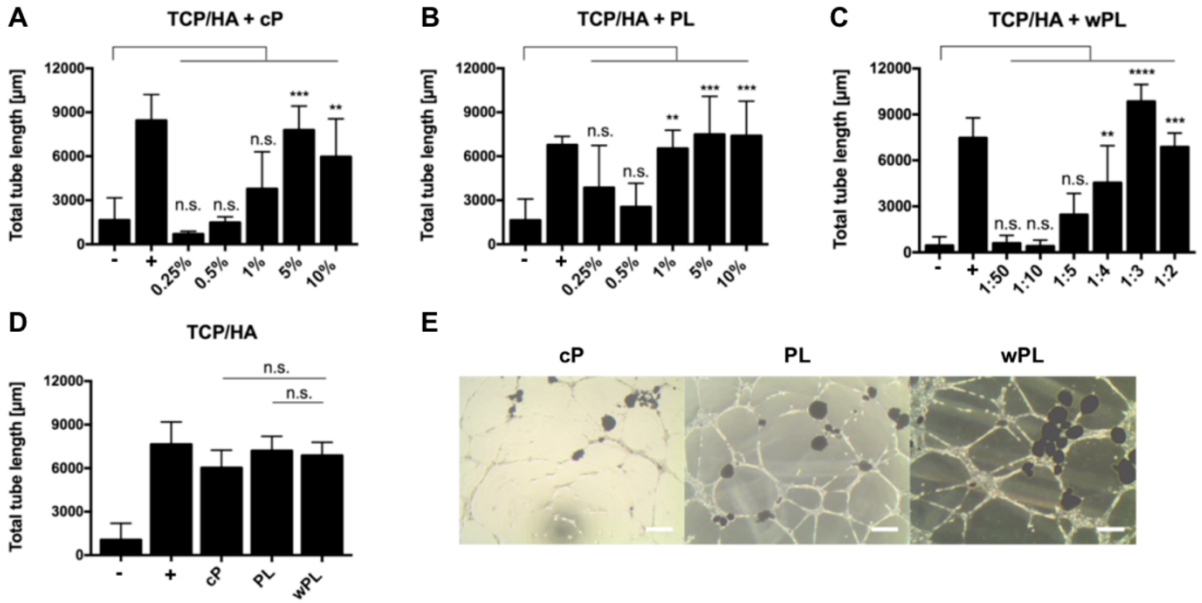

Figure 8.8: CaP Surfaces kept in different hemoderivative protein source show a similar pro-angiogenic stimulation. (A-C) The pro-angiogenic effect of CaP surfaces in hemoderivative protein sources was analyzed by employing tube formation assays with HUVECs. HUVECs were incubated with different concentrations of cP, PL, and wPL, containing CaP on Geltrex™ LDEV-Free reduced growth factor basement membrane matrix for 18 h (all TCP/HA-4). for cP and PL different percentual dilutions (0.25–10%) in the cell culture medium were tested. For wPL different ratios of wPL in total volume (1:50–1:2) with cell culture medium were tested. Total tube length was evaluated with ImageJ and the plugin angiogenesis analyzer (-, negative control: medium without LVES; +, positive control: medium with LVES; data are shown as mean ± SD, n = 3–6). **(D)** Tube formation was analyzed with the same protein concentration of 1.1 mg ml^{-1} for all three protein sources, containing CaP without additional washing with PBS (all TCP/HA-4, data are shown as mean ± SD, n = 6–17). The statistical significance was calculated by ANOVA with Dunnett's multiple comparison test (*P < 0.05, **P < 0.01, ***P < 0.001, ****P < 0.0001), performing the comparison with the negative control (A–C) or with wPL (D). **(E)** HUVECs on Geltrex™ after 18 h incubation with different hemoderivative protein sources at the same concentration, containing CaP (seen as dark spots in the images), as shown in (D). The scale bars represent 200 µm.

In this study, we investigated comparatively cP (citrate plasma), PL (lysate of platelets in plasma), and wPL (lysates of washed platelets without plasma) and their effect as sources of pro-angiogenic factors adsorbed on CaP surfaces. Despite the difference in composition of the

three hemoderivative sources, all of these promoted tube formation of HUVECs, which is in accordance with other reports [351-353]. However, the concentration of the prominent growth factors VEGF, FGF-2, and PDGF-AB was higher in the platelet-derived sources, PL and wPL than in plasma alone. Depleting plasma components from isolated platelets by washing resulted in both, an elevated concentration of growth factors and improved tube formation, indicating the effectiveness of lysates, such as wPL for regenerative effects. Nevertheless, it has to be considered that non-pooled wPL show inter-individual differences in the experiments, which might have an impact on the use of autologous donor materials to promote regenerative effects. Using the same workflow, including mass spectrometry-based proteomic analysis, we investigated the complex protein composition of the hemoderivatives adsorbed on different CaP materials, which revealed significant differences. Despite differences in the physicochemical properties of the CaP surfaces, we quantified comparable amounts of protein per amount of CaP in the case of cP and wPL but observed a decrease in protein amount with a decrease of the material's SSA for adsorbed PL and wPL. For the latter protein source, the trend was observed for the TCP/ HA samples. The impact of the SSA on protein adsorption was described in the literature [343, 354]. In any case, the protein adsorption on biomaterials represents a highly complex process that is driven by multiple factors and, therefore, challenging to predict. As described through experimental observations, adsorption on CaPs is influenced on one hand by the material's physicochemical properties such as the surface area, the chemical composition, hydrophobicity and the topography. On the other hand, the proteins' properties, such as size, charge, and structure add a secondary dimension of influence [4, 317]. Complex protein mixtures as the herein described hemoderivative protein sources can therefore bring a variation to the adsorption result. Despite having a lower SSA, β-TCP-1 adsorbed more protein from wPL than the TCP/HA samples with a higher SSA. Seemingly, the higher microporosity and the chemical composition influence this result. For the cP-related adsorption, it is necessary to point out that plasma proteins are vastly different from lysate-derived proteins. While both lysates contain a significant amount of cellular components, such as membrane proteins, lipids and metabolites, plasma is comprised mainly of secreted and globular proteins. This difference in composition results in similar protein amounts adsorbed throughout all CaP samples despite their physicochemical features. Similar observations were made in a study when incubating various CaP in serum [355]. Accordingly, the biomaterial's physicochemical properties must be considered together with the composition of the protein source to evaluate the performance of protein adsorption.

Increased adsorption of cytoskeleton proteins was observed when PLs, especially from wPL, were incubated with the CaP materials. Among the 20 most abundant platelet proteins, non-regenerative proteins, such as cytoskeleton proteins, and anti-angiogenic proteins, such as PF4 and TSP-1 were identified. These proteins are abundantly expressed in human platelets

with estimated copy numbers of 563 000 and 101 000 per platelet, respectively [356]. PF4 and TSP-1 inhibit the proliferation and migration of endothelial cells and induce apoptosis via multiple mechanisms [357-358]. One major anti-angiogenic effect of PF4 on endothelial cells is its ligation of the important growth factors VEGF and FGF-2, thereby preventing their endothelial interaction, especially through its competitive binding to heparin and heparin sulfate of proteoglycan receptors [359-360]. Similar to PF4, TSP-1 also interferes with endothelial cell binding of VEGF. In addition, TSP-1 signals via CD47, which is coupled to the VEGF receptor R2 to reduce VEGF-mediated activation and which counteracts nitric oxide signaling in endothelial cells [361-362]. However, there are also studies reporting pro-angiogenic effects of TSP-1 via indirect signaling through myofibroblasts [348, 363]. Furthermore, a recent study demonstrated a pro-angiogenic potential of TSP-1 for biomaterial surface modification [364]. Future studies must clarify the role of TSP-1 as a stimulant for pro-angiogenic biomaterial modification. CXCL7 is the most abundant platelet chemokine stored in the α-granules. Platelet basic protein represents a pre-cursor CXCL7 variant of the pro-angiogenic active forms CTAP-III and NAP-2 [350] with an estimated copy number of 479 000 per platelet [356]. It has been shown that the proteolytic cleavage product of platelet basic protein, CTAP-III mediates chemotaxis of endothelial cells in vitro [365]. However, NAP-2 showed the most chemotactically regulatory activity on neutrophils [350]. Platelet basic protein exerts antimicrobial activity, but its effect on endothelial cells is unknown so far [366].

The observed lacking pro-angiogenic response of HUVECs after incubation with CaP materials adsorbed with proteins from PLs might be due to a decreased binding affinity of the growth factors VEGF, FGF-2, PDGF-AB and increased binding affinity of the anti-angiogenic protein platelet factor 4 for the CaP materials, which were washed with PBS. Potentially, this washing procedure in the absence of divalent cations, e.g. Ca^{2+} and Mg^{2+} ions, may affect the types and amount of adsorbed proteins as non-washed CaP surfaces kept in hemoderivative protein source, still induced angiogenesis of cultured HUVECs. However, here all three tested plasma and platelet protein sources showed similar pro-angiogenic effects compared with the positive control (LVES-supplemented medium). Additionally, we observed an inclusion of the CaPs in the HUVEC's tubular structures, demonstrating an interaction between the cells and the CaPs. This adhesion of HUVECs on CaPs was already described in the literature [367]. It can be assumed that integrins on HUVECs establish contact with several adsorbed proteins with integrin-binding domains on the CaPs, such as fibronectin or vitronectin. This formation of a focal contact between CaPs and cells through protein contacts was experimentally explained for marrow stromal cells, osteosarcoma cells, and bone-marrow-derived mesenchymal stem cells [368-369]. Upon establishing this cell-CaP contact through integrins, a rearrangement of intracellular actin can occur, enabling signaling cascades involving mitogen-activated protein kinase (MAPK) signaling [370]. MAPK signaling is involved through Jagged/Notch gene activity

in the release of common angiogenic growth factors in HUVECs, as well as the expression of their associated receptors [371]. Furthermore, the growth factors in the surrounding hemoderivative contribute strongly to tube formation as seen for the addition of the sole hemoderivatives.

Conversely to our work, a previous study has demonstrated pro-angiogenic effects after rinsing PL-preincubated CaP scaffolds, resulting in the secretion of pro-angiogenic growth factors by mesenchymal stromal cells [312]. However, the CaP materials used in this study were washed once in HBSS. Therefore, it is likely that different coating and washing procedures may influence the binding properties of platelet-derived proteins to CaP materials which have to be optimized in future studies. Thus, a comprehensive analysis of protein adsorption on hemoderivative-preincubated CaP materials in combination with their pro-angiogenic potential is crucial for biomaterial surface engineering using PLs as hemoderivative source.

8.5 Conclusion

We state that all three hemoderivatives, as generated for this work, induced an angiogenic stimulus to HUVECs, with wPL showing the greatest effect. However, after adsorption on the CaP surfaces, the most abundant proteins identified by LC-MS were non-angiogenic or anti-angiogenic. In fact, we observed a reduction of pro-angiogenic VEGF, FGF-2, and PDGF-AB as measured by ELISA. The adsorbed proteins on the CaPs alone did not induce tube formation in HUVECs. Instead, tube formation was induced by keeping the hemoderivatives in the experiment. Consequently, biomaterial surfaces must be engineered to tightly adsorb pro-angiogenic growth factors and prevent dissipation out of wound cavities after implantation. We conclude that it is essential to analyze the protein adsorption on surfaces of synthetic bone substitute materials regarding pro-angiogenic responses. This correlation between material surface and the complex composition of adsorbed proteins must be considered to modify bone substitute materials with efficient regenerative capabilities. Overcoming the lack of angiogenesis or regenerative capabilities will lead to a reliable improvement of bone substitute materials to treat larger bone defects with higher success. Until then, the pro-angiogenic PL or wPL should not be washed away during the preparation of bone substitutes with these complex mixtures of proteins.

8.6 Supplementary Information

Table S8.1: The ten most abundant proteins identified by LC-MS in the hemoderivative protein sources. (A-C) The 10 most abundant proteins in citrate Plasma (cP), platelet lysate in plasma (PL), and lysate of washed platelets (wPL) are listed. The values represent the percentage of total proteins identified.

cP		PL		wPL	
Identified Proteins	**% of total protein**	**Identified Proteins**	**% of total protein**	**Identified Proteins**	**% of total protein**
Serum albumin	30,06	Serum albumin	30,33	Serum albumin	6,83
Ig gamma-1 chain C region	6,53	Ig kappa chain C region	5,53	Platelet factor 4	5,26
Clathrin heavy chain 1	4,32	Zinc finger protein 354C	4,72	Platelet basic protein	4,67
Ig kappa chain C region	4,26	Ig gamma-1 chain C region	3,91	Thrombospondin-1	3,23
Myosin-14	2,38	Gamma-enolase	3,10	Fermitin family homolog 3	2,99
Serotransferrin	2,35	Fibrinogen beta chain	2,66	Glyceraldehyde-3-phosphate dehydrogenase	2,68
Myosin-9	2,02	Myosin-10	2,64	Fibrinogen gamma chain	2,59
Ceruloplasmin	1,83	Ig lambda-2 chain C regions	2,59	Filamin-A	2,51
Talin-1	1,70	C1GALT1-specific chaperone 1	2,59	Vinculin	2,27
Ig alpha-1 chain C region	1,70	Serotransferrin	1,87	Profilin-1	2,22
Top 10 Total	**57.16**	**Top 10 Total**	**59.92**	**Top 10 Total**	**35.52**

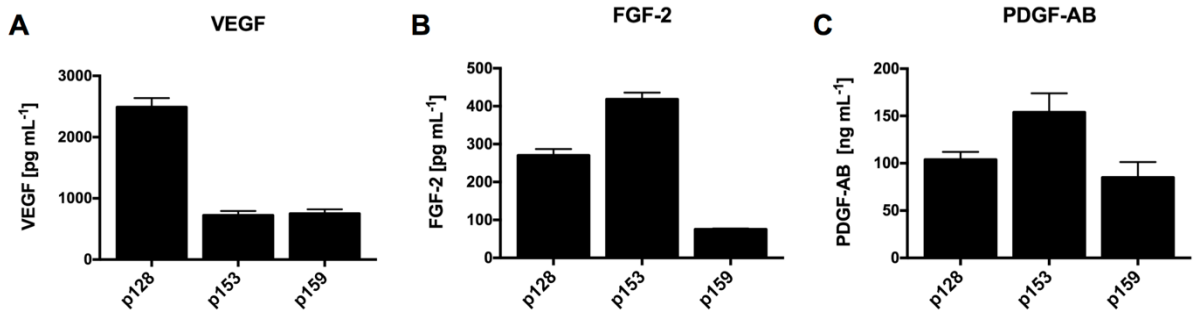

Figure S8.1: Concentration of pro-angiogenic growth factors is donor-dependent in human washed platelet lysates. (A-C) Washed platelet lysates from three different donors were evaluated for angiogenesis-involved growth factors. The concentration of VEGF, FGF-2, and PDGF-AB was measured by ELISA (data are shown as mean ± SD, n = 4).

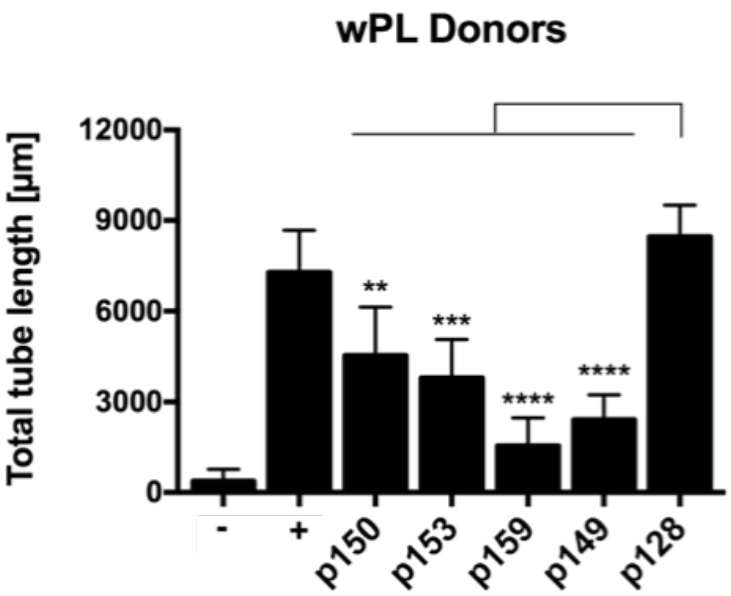

Figure S8.2: Pro-angiogenic response in tube formation assays is donor-dependent for human washed platelet lysates. The proangiogenic effect of washed platelet lysates from five different donors was analyzed by tube formation assays with HUVECs. HUVECs were incubated with the same concentration of wPL from five different donors on Geltrex™ LDEV-Free Reduced Growth Factor Basement Membrane Matrix for 18 h. Total tube length was evaluated with ImageJ and the plugin Angiogenesis Analyzer (-, negative control: medium without LVES, +, positive control: medium with LVES; data are shown as mean ± SD, n = 3-9).

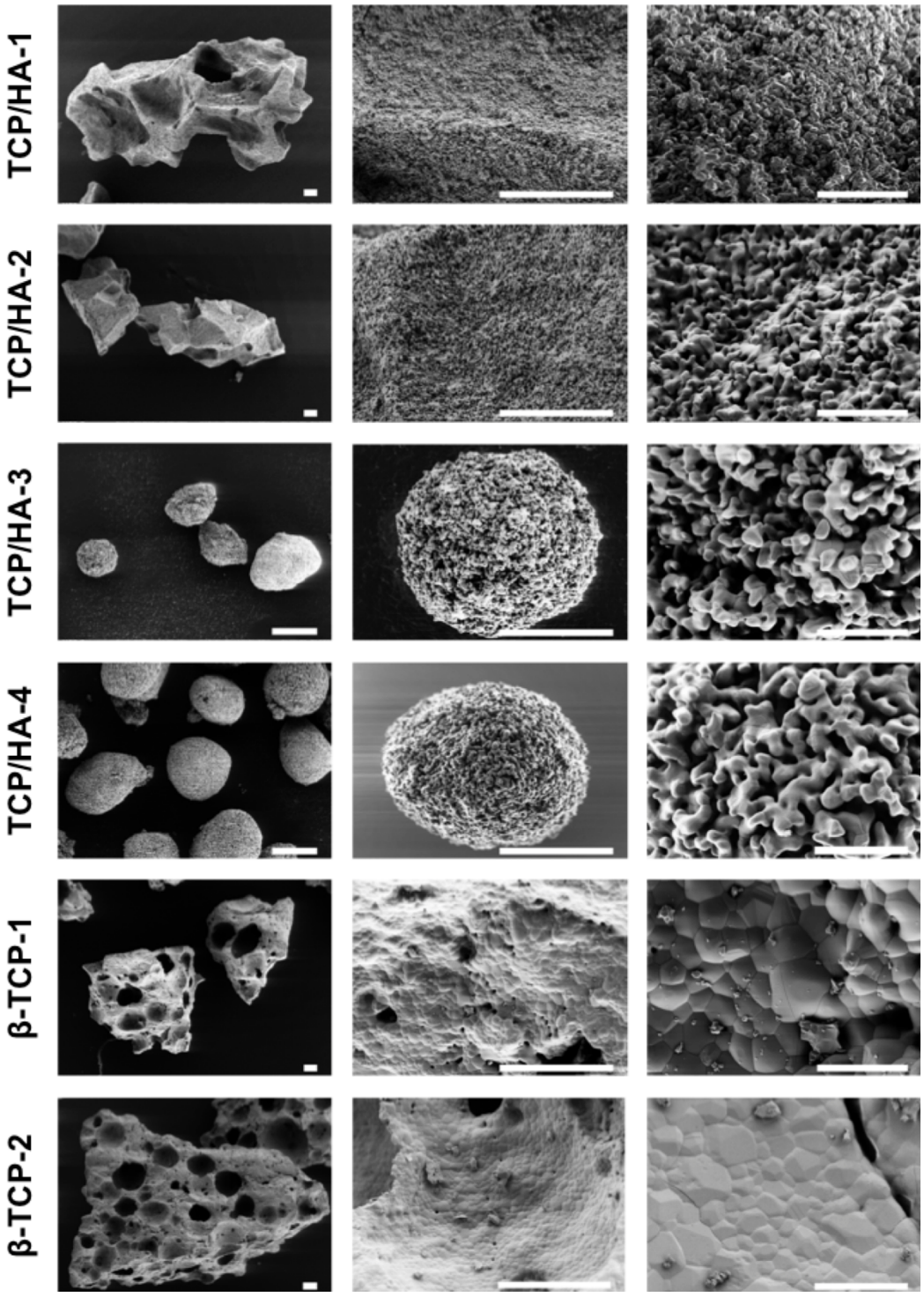

Figure S8.3: SEM images of CaP materials. Surface characterization in three magnifications. The left row scale bars represent 100 µm, the middle row scale bars represent 50 µm, and the right row scale bars represent 10 µm.

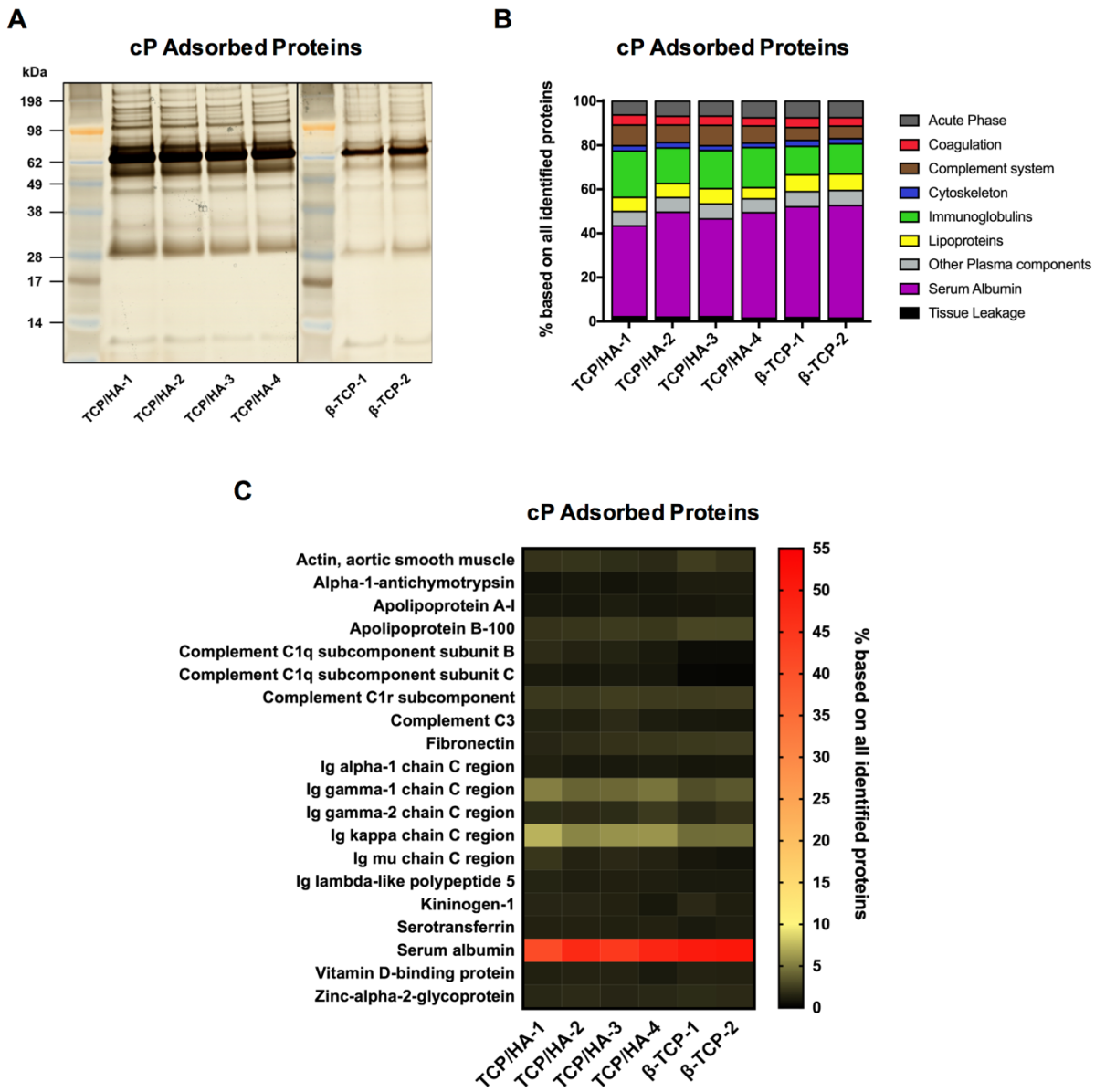

Figure S8.4: Analysis of adsorbed proteins from human plasma on CaP surfaces. CaP materials were incubated for 1 h in cP. After three subsequent washing steps, proteins were desorbed with 2% SDS. **(A)** SDS-PAGE and silver staining were performed for adsorbed proteins on different CaP surfaces incubated in cP. **(B)** Adsorbed proteins on CaP surfaces from cP were analyzed by quantitative LC-MS proteomics and identified proteins were classified into nine different protein groups. The bars indicate the percentage based on all identified proteins. **(C)** The heat map show the 20 most abundant proteins for TCP/HA-4 compared to the other CaP surfaces. The values represent the percentage based on all identified proteins.

Conclusion

Nano- and biomaterial design remains challenged by the adsorption of biomolecules, specifically the adsorption of proteins. Protein adsorption changes the surface properties of these materials tremendously, limiting their success in clinical translation. The studies presented within this thesis aimed to address questions within the challenging field of nanomedicine and nanomaterial design.

Protein adsorption is a complex process, influenced by the protein-containing environment, but also by the NPs' physicochemical properties. Despite the many efforts to study protein adsorption - also named the protein corona - for different NP systems, the overall comparability between these studies remains limited. The limitations of lacking comparability were addressed in **chapter A** by systematically analyzing the influence of temperature, concentration, and surface modification on the protein corona composition. While past studies focused on the formation of the protein corona in extracellular environments, the intracellular trafficking and evolution of the protein corona remain poorly investigated. The studies of **chapter B** were dedicated to investigating the intracellular fate of the protein corona and its importance of unraveling the intracellular trafficking and exocytosis process of NPs. Last, protein adsorption also affects the performances of bulk biomaterials with nanostructured surfaces. Here, the study of **chapter C** analyzed the composition of adsorbed proteins from hemoderivatives on CaP surfaces for bone substitution. Specifically, the pro-angiogenic effect of the adsorbed hemoderivative proteins was intensively investigated. The following paragraphs give a concise overview of the findings:

The study in **subchapter 2 in chapter A** determined temperature and concentration of the protein environment but also NP surface modification as impacting factors for the protein corona composition and, eventually, for the cellular uptake. Here, we observed a decreased uptake in endothelial cells when increasing the protein concentration and increasing the temperature during the protein corona formation, respectively. The results suggest that the conditions for in-vitro protein corona experiments must be carefully chosen when mimicking in-vivo conditions. If non-mimicking conditions are intentionally selected, as for temperature-responsive materials, suitable controls should be considered to exclude differing outcomes by the conditions alone.

The study presented in **subchapter 4 in chapter B** provided a reconstruction of the intracellular separation of a pre-formed, fluorescently-labeled protein corona and associated NPs. This separation occurred over several hours. The eventual endosomal sorting, which led the protein corona into MVBs and NPs into REs, was visualized for the first time by high-

resolution CLEM and was supported by flow cytometry data. The results provide a further understanding of the cellular processing of intentionally formed artificial protein coronas, such as for (intra-)cellular targeting.

Next, the study in **subchapter 5 in chapter B** analyzed the uptake pathway and intracellular trafficking of biocompatible NPs, implementing a proteomic workflow to investigate the intracellular protein corona composition. By using conventional methods, such as flow cytometry and microcopy for different time points, the evolution of the protein corona was correlated to cellular uptake kinetics. Specifically, HES-NPs with a slower uptake were linked to a gradually evolving intracellular protein corona, whereas HSA-NCs with a fast uptake demonstrated a stable intracellular protein corona. Furthermore, the composition of the intracellular protein corona revealed a molecular insight into the NPs' intracellular trafficking. The data demonstrates the advantages of evaluating the protein corona for intracellular studies, particularly for NPs with cellular targeting.

The proteomic workflow to analyze intracellular protein coronas was applied in the study in **subchapter 6 in chapter B.** Here, the exocytosis of gold NPs in stem cell-like stromal cells was investigated with two loading protocols. The results demonstrate that a longer incubation results in a reduced exocytosis rate. The composition of the intracellular protein corona indicates that a longer incubation time results in an enrichment of adsorbed intracellular proteins, possibly favoring a higher exocytosis rate. Reducing exocytosis rates remains necessary for NP-based cell labeling. Therefore, these results will improve NP design for imaging applications.

Finally, the study presented in **subchapter 8 in chapter C** analyzed the protein adsorption of potential pro-angiogenic hemoderivatives, such as plasma and platelet lysates on CaP biomaterial surfaces. The proteomic findings were correlated with results by ELISA and tube formation assays utilizing endothelial cells to co-evaluate the pro-angiogenic potential. The results demonstrate an abundance of adsorbed non-angiogenic and anti-angiogenic proteins, while pro-angiogenic growth factors were decreased. Washing the materials after incubation in the hemoderivatives, resulted in a decreased angiogenic effect, suggesting that the adsorbed proteins alone do not evoke the desired regenerative effect. Instead, CaP surfaces should be utilized in bone regeneration without washing procedures when coated in hemoderivatives.

In conclusion, the studies emphasize the value of protein adsorption analysis for nano- and biomaterials with medical applications. Ultimately, the progression of our understanding of nano-bio interactions will truly result in precisely tailored nano- and biomaterials with a successful clinical translation.

References

1. Monopoli, M. P.; Aberg, C.; Salvati, A.; Dawson, K. A., Biomolecular coronas provide the biological identity of nanosized materials. *Nat Nanotechnol* **2012,** *7* (12), 779-86.

2. Docter, D.; Westmeier, D.; Markiewicz, M.; Stolte, S.; Knauer, S.; Stauber, R., The nanoparticle biomolecule corona: lessons learned–challenge accepted? *Chemical Society Reviews* **2015,** *44* (17), 6094-6121.

3. Horbett, T. A., Protein Adsorption on Biomaterials. In *Biomaterials, interfacial phenomena and applications*, Cooper, S. L.; Peppas, N. A.; Hoffman, A. S.; Ratner, B. D., Eds. American Chemical Society: Washington, D.C., 1982; pp 233-244.

4. Lee, W.-H.; Loo, C.-Y.; Rohanizadeh, R., A review of chemical surface modification of bioceramics: effects on protein adsorption and cellular response. *Colloids and Surfaces B: Biointerfaces* **2014,** *122*, 823-834.

5. Pelaz, B.; Alexiou, C.; Alvarez-Puebla, R. A.; Alves, F.; Andrews, A. M.; Ashraf, S.; Balogh, L. P.; Ballerini, L.; Bestetti, A.; Brendel, C.; Bosi, S.; Carril, M.; Chan, W. C.; Chen, C.; Chen, X.; Chen, X.; Cheng, Z.; Cui, D.; Du, J.; Dullin, C.; Escudero, A.; Feliu, N.; Gao, M.; George, M.; Gogotsi, Y.; Grunweller, A.; Gu, Z.; Halas, N. J.; Hampp, N.; Hartmann, R. K.; Hersam, M. C.; Hunziker, P.; Jian, J.; Jiang, X.; Jungebluth, P.; Kadhiresan, P.; Kataoka, K.; Khademhosseini, A.; Kopecek, J.; Kotov, N. A.; Krug, H. F.; Lee, D. S.; Lehr, C. M.; Leong, K. W.; Liang, X. J.; Ling Lim, M.; Liz-Marzan, L. M.; Ma, X.; Macchiarini, P.; Meng, H.; Mohwald, H.; Mulvaney, P.; Nel, A. E.; Nie, S.; Nordlander, P.; Okano, T.; Oliveira, J.; Park, T. H.; Penner, R. M.; Prato, M.; Puntes, V.; Rotello, V. M.; Samarakoon, A.; Schaak, R. E.; Shen, Y.; Sjoqvist, S.; Skirtach, A. G.; Soliman, M. G.; Stevens, M. M.; Sung, H. W.; Tang, B. Z.; Tietze, R.; Udugama, B. N.; VanEpps, J. S.; Weil, T.; Weiss, P. S.; Willner, I.; Wu, Y.; Yang, L.; Yue, Z.; Zhang, Q.; Zhang, Q.; Zhang, X. E.; Zhao, Y.; Zhou, X.; Parak, W. J., Diverse Applications of Nanomedicine. *ACS Nano* **2017,** *11* (3), 2313-2381.

6. Abdel-Mageed, H. M.; AbuelEzz, N. Z.; Radwan, R. A.; Mohamed, S. A., Nanoparticles in nanomedicine: a comprehensive updated review on current status, challenges and emerging opportunities. *J Microencapsul* **2021,** *38* (6), 414-436.

7. Barenholz, Y., Doxil(R)--the first FDA-approved nano-drug: lessons learned. *J Control Release* **2012,** *160* (2), 117-34.

8. Polack, F. P.; Thomas, S. J.; Kitchin, N.; Absalon, J.; Gurtman, A.; Lockhart, S.; Perez, J. L.; Perez Marc, G.; Moreira, E. D.; Zerbini, C.; Bailey, R.; Swanson, K. A.; Roychoudhury, S.; Koury, K.; Li, P.; Kalina, W. V.; Cooper, D.; Frenck, R. W., Jr.; Hammitt, L. L.; Tureci, O.; Nell, H.; Schaefer, A.; Unal, S.; Tresnan, D. B.; Mather, S.; Dormitzer, P. R.; Sahin, U.; Jansen, K. U.; Gruber, W. C.; Group, C. C. T., Safety and Efficacy of the BNT162b2 mRNA Covid-19 Vaccine. *N Engl J Med* **2020,** *383* (27), 2603-2615.

9. Walsh, E. E.; Frenck, R. W., Jr.; Falsey, A. R.; Kitchin, N.; Absalon, J.; Gurtman, A.; Lockhart, S.; Neuzil, K.; Mulligan, M. J.; Bailey, R.; Swanson, K. A.; Li, P.; Koury, K.; Kalina, W.; Cooper, D.; Fontes-Garfias, C.; Shi, P. Y.; Tureci, O.; Tompkins, K. R.; Lyke, K. E.; Raabe, V.; Dormitzer, P. R.; Jansen, K. U.; Sahin, U.; Gruber, W. C., Safety and Immunogenicity of Two RNA-Based Covid-19 Vaccine Candidates. *N Engl J Med* **2020,** *383* (25), 2439-2450.

10. Ke, P. C.; Lin, S.; Parak, W. J.; Davis, T. P.; Caruso, F., A decade of the protein corona. *ACS nano* **2017,** *11* (12), 11773-11776.

11. Cedervall, T.; Lynch, I.; Lindman, S.; Berggard, T.; Thulin, E.; Nilsson, H.; Dawson, K. A.; Linse, S., Understanding the nanoparticle-protein corona using methods to quantify exchange rates and affinities of proteins for nanoparticles. *Proc Natl Acad Sci U S A* **2007,** *104* (7), 2050-5.

12. Walczyk, D.; Bombelli, F. B.; Monopoli, M. P.; Lynch, I.; Dawson, K. A., What the cell “sees” in bionanoscience. *Journal of the American Chemical Society* **2010,** *132* (16), 5761-5768.

13. Corbo, C.; Molinaro, R.; Parodi, A.; Toledano Furman, N. E.; Salvatore, F.; Tasciotti, E., The impact of nanoparticle protein corona on cytotoxicity, immunotoxicity and target drug delivery. *Nanomedicine (Lond)* **2016,** *11* (1), 81-100.

14. Berrecoso, G.; Crecente-Campo, J.; Alonso, M. J., Unveiling the pitfalls of the protein corona of polymeric drug nanocarriers. *Drug Deliv Transl Res* **2020,** *10* (3), 730-750.

15. Martel, J.; Young, D.; Young, A.; Wu, C. Y.; Chen, C. D.; Yu, J. S.; Young, J. D., Comprehensive proteomic analysis of mineral nanoparticles derived from human body fluids and analyzed by liquid chromatography-tandem mass spectrometry. *Anal Biochem* **2011,** *418* (1), 111-25.

16. Simon, J.; Kuhn, G.; Fichter, M.; Gehring, S.; Landfester, K.; Mailänder, V., Unraveling the In Vivo Protein Corona. *Cells* **2021,** *10* (1), 132.

17. Huebsch, N.; Mooney, D. J., Inspiration and application in the evolution of biomaterials. *Nature* **2009,** *462* (7272), 426-32.

18. Williams, D. F., On the nature of biomaterials. *Biomaterials* **2009,** *30* (30), 5897-909.

19. Wang, W. Y., K.W.K., Bone grafts and biomaterials substitutes for bone defect repair: A review. *Bioactive Materials* **2017,** *2*, 224 - 247.

20. Bauer, T. W.; Muschler, G. F., Bone graft materials. An overview of the basic science. *Clin Orthop Relat Res* **2000,** (371), 10-27.

21. Malhotra, A.; Habibovic, P., Calcium Phosphates and Angiogenesis: Implications and Advances for Bone Regeneration. *Trends Biotechnol* **2016,** *34* (12), 983-992.

22. Altaie, A.; Owston, H.; Jones, E., Use of platelet lysate for bone regeneration - are we ready for clinical translation? *World J Stem Cells* **2016,** *8* (2), 47-55.

23. Nair, M. B.; Varma, H. K.; Menon, K. V.; Shenoy, S. J.; John, A., Reconstruction of goat femur segmental defects using triphasic ceramic-coated hydroxyapatite in combination with autologous cells and platelet-rich plasma. *Acta Biomater* **2009,** *5* (5), 1742-55.

24. Krukemeyer, M.; Krenn, V.; Huebner, F.; Wagner, W.; Resch, R., History and possible uses of nanomedicine based on nanoparticles and nanotechnological progress. *J. Nanomed. Nanotechnol* **2015,** *6* (6), 336.

25. Satalkar, P.; Elger, B. S.; Shaw, D. M., Defining nano, nanotechnology and nanomedicine: why should it matter? *Science and engineering ethics* **2016,** *22* (5), 1255-1276.

26. Merriam-Webster. Medicine. 2011. In Merriam-Webster.com. https://www.merriam-webster.com/dictionary/medicine. Accessed 25 September 2022.

27. Drexler, K.; Peterson, C.; Pergamit, G., *Unbounding the Future: The nanotechnology revolution*. Morrow, New York., 1991.

28. Freitas, R. A., *Nanomedicine, volume I: basic capabilities*. Landes Bioscience Georgetown, TX: 1999; Vol. 1.

29. Halwani, A. A., Development of Pharmaceutical Nanomedicines: From the Bench to the Market. *Pharmaceutics* **2022,** *14* (1), 106.

30. Leuvering, J.; Thal, P.; Schuurs, A., Sol particle agglutination immunoassay for human chorionic gonadotrophin. *Fresenius' Zeitschrift für analytische Chemie* **1980,** *301* (2), 132-132.

31. Saito, N.; Haniu, H.; Usui, Y.; Aoki, K.; Hara, K.; Takanashi, S.; Shimizu, M.; Narita, N.; Okamoto, M.; Kobayashi, S.; Nomura, H.; Kato, H.; Nishimura, N.; Taruta, S.; Endo, M., Safe clinical use of carbon nanotubes as innovative biomaterials. *Chem Rev* **2014,** *114* (11), 6040-79.

32. Paulo, C. S.; Vidal, M.; Ferreira, L. S., Antifungal nanoparticles and surfaces. *Biomacromolecules* **2010,** *11* (10), 2810-7.

33. Batty, C. J.; Bachelder, E. M.; Ainslie, K. M., Historical perspective of clinical nano and microparticle formulations for delivery of therapeutics. *Trends in molecular medicine* **2021,** *27* (6), 516-519.

34. Sun, Q.; Radosz, M.; Shen, Y., Challenges in design of translational nanocarriers. *J Control Release* **2012,** *164* (2), 156-69.

35. Mitchell, M. J.; Billingsley, M. M.; Haley, R. M.; Wechsler, M. E.; Peppas, N. A.; Langer, R., Engineering precision nanoparticles for drug delivery. *Nat Rev Drug Discov* **2021,** *20* (2), 101-124.

36. Meena, J.; Gupta, A.; Ahuja, R.; Singh, M.; Bhaskar, S.; Panda, A. K., Inorganic nanoparticles for natural product delivery: A review. *Environmental Chemistry Letters* **2020,** *18* (6), 2107-2118.

37. Yang, W.; Liang, H.; Ma, S.; Wang, D.; Huang, J., Gold nanoparticle based photothermal therapy: Development and application for effective cancer treatment. *Sustainable Materials and Technologies* **2019,** *22*, e00109.

38. Dykman, L.; Khlebtsov, N., Gold nanoparticles in biology and medicine: recent advances and prospects. *Acta Naturae* **2011,** *3* (2 (9)), 34-55.

39. Arias, L. S.; Pessan, J. P.; Vieira, A. P. M.; Lima, T. M. T. d.; Delbem, A. C. B.; Monteiro, D. R., Iron oxide nanoparticles for biomedical applications: A perspective on synthesis, drugs, antimicrobial activity, and toxicity. *Antibiotics* **2018,** *7* (2), 46.

40. Banik, B. L.; Fattahi, P.; Brown, J. L., Polymeric nanoparticles: the future of nanomedicine. *Wiley Interdiscip Rev Nanomed Nanobiotechnol* **2016,** *8* (2), 271-99.

41. Abd Ellah, N. H.; Abouelmagd, S. A., Surface functionalization of polymeric nanoparticles for tumor drug delivery: approaches and challenges. *Expert Opin Drug Deliv* **2017,** *14* (2), 201-214.

42. Cai, K.; He, X.; Song, Z.; Yin, Q.; Zhang, Y.; Uckun, F. M.; Jiang, C.; Cheng, J., Dimeric drug polymeric nanoparticles with exceptionally high drug loading and quantitative loading efficiency. *J Am Chem Soc* **2015,** *137* (10), 3458-61.

43. Liu, X.; Li, C.; Lv, J.; Huang, F.; An, Y.; Shi, L.; Ma, R., Glucose and H2O2 dual-responsive polymeric micelles for the self-regulated release of insulin. *ACS Applied Bio Materials* **2020,** *3* (3), 1598-1606.

44. Sercombe, L.; Veerati, T.; Moheimani, F.; Wu, S. Y.; Sood, A. K.; Hua, S., Advances and challenges of liposome assisted drug delivery. *Frontiers in pharmacology* **2015,** *6*, 286.

45. Senior, J. H., Fate and behavior of liposomes in vivo: a review of controlling factors. *Critical reviews in therapeutic drug carrier systems* **1987,** *3* (2), 123-193.

46. Gabizon, A.; Goren, D.; Horowitz, A. T.; Tzemach, D.; Lossos, A.; Siegal, T., Long-circulating liposomes for drug delivery in cancer therapy: a review of biodistribution studies in tumor-bearing animals. *Advanced Drug Delivery Reviews* **1997,** *24* (2-3), 337-344.

47. Piradashvili, K.; Fichter, M.; Mohr, K.; Gehring, S.; Wurm, F. R.; Landfester, K., Biodegradable protein nanocontainers. *Biomacromolecules* **2015,** *16* (3), 815-21.

48. Kang, B.; Opatz, T.; Landfester, K.; Wurm, F. R., Carbohydrate nanocarriers in biomedical applications: functionalization and construction. *Chemical Society Reviews* **2015,** *44* (22), 8301-8325.

49. Frey, M. L.; Han, S.; Halim, H.; Kaltbeitzel, A.; Riedinger, A.; Landfester, K.; Lieberwirth, I., Nanocarriers Made of Proteins: Intracellular Visualization of a Smart Biodegradable Drug Delivery System. *Small* **2022,** *18* (15), 2106094.

50. Hüppe, N.; Schunke, J.; Fichter, M.; Mailänder, V.; Wurm, F. R.; Landfester, K., Multicomponent Encapsulation into Fully Degradable Protein Nanocarriers via Interfacial Azide-Alkyne Click Reaction Allows the Co-Delivery of Immunotherapeutics. *Nanoscale Horizons* **2022**.

51. Nel, A. E.; Madler, L.; Velegol, D.; Xia, T.; Hoek, E. M.; Somasundaran, P.; Klaessig, F.; Castranova, V.; Thompson, M., Understanding biophysicochemical interactions at the nano-bio interface. *Nat Mater* **2009,** *8* (7), 543-57.

52. Tenzer, S.; Docter, D.; Rosfa, S.; Wlodarski, A.; Kuharev, J.; Rekik, A.; Knauer, S. K.; Bantz, C.; Nawroth, T.; Bier, C.; Sirirattanapan, J.; Mann, W.; Treuel, L.; Zellner, R.; Maskos, M.; Schild, H.; Stauber, R. H., Nanoparticle size is a critical physicochemical determinant of the human blood plasma corona: a comprehensive quantitative proteomic analysis. *ACS Nano* **2011,** *5* (9), 7155-67.

53. Hellstrand, E.; Lynch, I.; Andersson, A.; Drakenberg, T.; Dahlbäck, B.; Dawson, K. A.; Linse, S.; Cedervall, T., Complete high‐density lipoproteins in nanoparticle corona. *The FEBS journal* **2009,** *276* (12), 3372-3381.

54. Müller, J.; Prozeller, D.; Ghazaryan, A.; Kokkinopoulou, M.; Mailänder, V.; Morsbach, S.; Landfester, K., Beyond the protein corona–lipids matter for biological response of nanocarriers. *Acta biomaterialia* **2018,** *71*, 420-431.

55. Zeng, Z.; Patel, J.; Lee, S.-H.; McCallum, M.; Tyagi, A.; Yan, M.; Shea, K. J., Synthetic polymer nanoparticle–polysaccharide interactions: A systematic study. *Journal of the American Chemical Society* **2012,** *134* (5), 2681-2690.

56. Vroman, L., Effect of adsorbed proteins on the wettability of hydrophilic and hydrophobic solids. *Nature* **1962,** *196* (4853), 476-477.

57. Tenzer, S.; Docter, D.; Kuharev, J.; Musyanovych, A.; Fetz, V.; Hecht, R.; Schlenk, F.; Fischer, D.; Kiouptsi, K.; Reinhardt, C., Rapid formation of plasma protein corona critically affects nanoparticle pathophysiology. In *Nano-Enabled Medical Applications*, Jenny Stanford Publishing: 2020; pp 251-278.

58. Casals, E.; Pfaller, T.; Duschl, A.; Oostingh, G. J.; Puntes, V., Time evolution of the nanoparticle protein corona. *ACS nano* **2010,** *4* (7), 3623-3632.

59. Vroman, L.; Adams, A.; Fischer, G.; Munoz, P., Interaction of high molecular weight kininogen, factor XII, and fibrinogen in plasma at interfaces. **1980**.

60. Vilanova, O.; Mittag, J. J.; Kelly, P. M.; Milani, S.; Dawson, K. A.; Radler, J. O.; Franzese, G., Understanding the Kinetics of Protein-Nanoparticle Corona Formation. *ACS Nano* **2016,** *10* (12), 10842-10850.

61. Lundqvist, M.; Stigler, J.; Cedervall, T.; Berggard, T.; Flanagan, M. B.; Lynch, I.; Elia, G.; Dawson, K., The evolution of the protein corona around nanoparticles: a test study. *ACS Nano* **2011,** *5* (9), 7503-9.

62. Kokkinopoulou, M.; Simon, J.; Landfester, K.; Mailander, V.; Lieberwirth, I., Visualization of the protein corona: towards a biomolecular understanding of nanoparticle-cell-interactions. *Nanoscale* **2017,** *9* (25), 8858-8870.

63. Milani, S.; Baldelli Bombelli, F.; Pitek, A. S.; Dawson, K. A.; Radler, J., Reversible versus irreversible binding of transferrin to polystyrene nanoparticles: soft and hard corona. *ACS nano* **2012,** *6* (3), 2532-2541.

64. Van Hong Nguyen, B.-J. L., Protein corona: a new approach for nanomedicine design. *International journal of nanomedicine* **2017,** *12*, 3137.

65. Walkey, C. D.; Olsen, J. B.; Guo, H.; Emili, A.; Chan, W. C., Nanoparticle size and surface chemistry determine serum protein adsorption and macrophage uptake. *Journal of the American Chemical Society* **2012,** *134* (4), 2139-2147.

66. Hühn, D.; Kantner, K.; Geidel, C.; Brandholt, S.; De Cock, I.; Soenen, S. J.; Rivera_Gil, P.; Montenegro, J.-M.; Braeckmans, K.; Mullen, K., Polymer-coated nanoparticles interacting with proteins and cells: focusing on the sign of the net charge. *ACS nano* **2013,** *7* (4), 3253-3263.

67. Gagner, J. E.; Lopez, M. D.; Dordick, J. S.; Siegel, R. W., Effect of gold nanoparticle morphology on adsorbed protein structure and function. *Biomaterials* **2011,** *32* (29), 7241-7252.

68. Maiorano, G.; Sabella, S.; Sorce, B.; Brunetti, V.; Malvindi, M. A.; Cingolani, R.; Pompa, P. P., Effects of cell culture media on the dynamic formation of protein− nanoparticle complexes and influence on the cellular response. *ACS nano* **2010,** *4* (12), 7481-7491.

69. Gräfe, C.; Weidner, A.; vd Lühe, M.; Bergemann, C.; Schacher, F. H.; Clement, J. H.; Dutz, S., Intentional formation of a protein corona on nanoparticles: Serum concentration affects protein corona mass, surface charge, and nanoparticle–cell interaction. *The international journal of biochemistry & cell biology* **2016,** *75*, 196-202.

70. Gessner, A.; Lieske, A.; Paulke, B. R.; Müller, R. H., Functional groups on polystyrene model nanoparticles: influence on protein adsorption. *Journal of Biomedical Materials Research Part A: An Official Journal of The Society for Biomaterials, The Japanese Society for Biomaterials, and The Australian Society for Biomaterials and the Korean Society for Biomaterials* **2003,** *65* (3), 319-326.

71. Mahmoudi, M.; Abdelmonem, A. M.; Behzadi, S.; Clement, J. H.; Dutz, S.; Ejtehadi, M. R.; Hartmann, R.; Kantner, K.; Linne, U.; Maffre, P.; Metzler, S.; Moghadam, M. K.; Pfeiffer, C.; Rezaei, M.; Ruiz-Lozano, P.; Serpooshan, V.; Shokrgozar, M. A.; Nienhaus, G. U.; Parak, W. J., Temperature: the "ignored" factor at the NanoBio interface. *ACS Nano* **2013,** *7* (8), 6555-62.

72. Mahmoudi, M.; Shokrgozar, M. A.; Behzadi, S., Slight temperature changes affect protein affinity and cellular uptake/toxicity of nanoparticles. *Nanoscale* **2013,** *5* (8), 3240-3244.

73. O'Brien, J.; Shea, K. J., Tuning the protein corona of hydrogel nanoparticles: the synthesis of abiotic protein and peptide affinity reagents. *Accounts of chemical research* **2016,** *49* (6), 1200-1210.

74. Gheshlaghi, Z. N.; Riazi, G. H.; Ahmadian, S.; Ghafari, M.; Mahinpour, R., Toxicity and interaction of titanium dioxide nanoparticles with microtubule protein. *Acta biochimica et biophysica Sinica* **2008,** *40* (9), 777-782.

75. Wangoo, N.; Suri, C. R.; Shekhawat, G., Interaction of gold nanoparticles with protein: a spectroscopic study to monitor protein conformational changes. *Applied Physics Letters* **2008,** *92* (13), 133104.

76. Garvas, M.; Testen, A.; Umek, P.; Gloter, A.; Koklic, T.; Strancar, J., Protein Corona Prevents TiO2 Phototoxicity. *PLoS One* **2015,** *10* (6), e0129577.

77. Yin, H.; Chen, R.; Casey, P. S.; Ke, P. C.; Davis, T. P.; Chen, C., Reducing the cytotoxicity of ZnO nanoparticles by a pre-formed protein corona in a supplemented cell culture medium. *RSC advances* **2015,** *5* (90), 73963-73973.

78. Schottler, S.; Becker, G.; Winzen, S.; Steinbach, T.; Mohr, K.; Landfester, K.; Mailander, V.; Wurm, F. R., Protein adsorption is required for stealth effect of poly(ethylene glycol)- and poly(phosphoester)-coated nanocarriers. *Nat Nanotechnol* **2016,** *11* (4), 372-7.

79. Gref, R.; Lück, M.; Quellec, P.; Marchand, M.; Dellacherie, E.; Harnisch, S.; Blunk, T.; Müller, R., 'Stealth'corona-core nanoparticles surface modified by polyethylene glycol (PEG): influences of the corona (PEG chain length and surface density) and of the core composition on phagocytic uptake and plasma protein adsorption. *Colloids and Surfaces B: Biointerfaces* **2000,** *18* (3-4), 301-313.

80. Simon, J.; Müller, L. K.; Kokkinopoulou, M.; Lieberwirth, I.; Morsbach, S.; Landfester, K.; Mailänder, V., Exploiting the biomolecular corona: Pre-coating of nanoparticles enables controlled cellular interactions. *Nanoscale* **2018,** *10* (22), 10731-10739.

81. Astarita, C.; Palchetti, S.; Massaro-Giordano, M.; Di Domenico, M.; Petrillo, F.; Boffo, S.; Caracciolo, G.; Giordano, A., Artificial Protein Coronas Enable Controlled Interaction with Corneal Epithelial Cells: New Opportunities for Ocular Drug Delivery. *Pharmaceutics* **2021,** *13* (6).

82. Dal Magro, R.; Albertini, B.; Beretta, S.; Rigolio, R.; Donzelli, E.; Chiorazzi, A.; Ricci, M.; Blasi, P.; Sancini, G., Artificial apolipoprotein corona enables nanoparticle brain targeting. *Nanomedicine* **2018,** *14* (2), 429-438.

83. Cao, H.; Zou, L.; He, B.; Zeng, L.; Huang, Y.; Yu, H.; Zhang, P.; Yin, Q.; Zhang, Z.; Li, Y., Albumin biomimetic nanocorona improves tumor targeting and penetration for synergistic therapy of metastatic breast cancer. *Advanced Functional Materials* **2017,** *27* (11), 1605679.

84. Winzen, S.; Schoettler, S.; Baier, G.; Rosenauer, C.; Mailaender, V.; Landfester, K.; Mohr, K., Complementary analysis of the hard and soft protein corona: sample preparation critically effects corona composition. *Nanoscale* **2015,** *7* (7), 2992-3001.

85. Carrillo-Carrion, C.; Carril, M.; Parak, W. J., Techniques for the experimental investigation of the protein corona. *Current Opinion in Biotechnology* **2017,** *46*, 106-113.

86. Baimanov, D.; Cai, R.; Chen, C., Understanding the chemical nature of nanoparticle–protein interactions. *Bioconjugate Chemistry* **2019,** *30* (7), 1923-1937.

87. García-Álvarez, R.; Vallet-Regí, M., Hard and soft protein corona of nanomaterials: Analysis and relevance. *Nanomaterials* **2021,** *11* (4), 888.

88. Dominguez-Medina, S.; Chen, S.; Blankenburg, J.; Swanglap, P.; Landes, C. F.; Link, S., Measuring the hydrodynamic size of nanoparticles using fluctuation correlation spectroscopy. *Annual review of physical chemistry* **2016,** *67*, 489-514.

89. Dobrovolskaia, M. A.; Patri, A. K.; Zheng, J.; Clogston, J. D.; Ayub, N.; Aggarwal, P.; Neun, B. W.; Hall, J. B.; McNeil, S. E., Interaction of colloidal gold nanoparticles with human blood: effects on particle size and analysis of plasma protein binding profiles. *Nanomedicine: Nanotechnology, Biology and Medicine* **2009,** *5* (2), 106-117.

90. Mirshafiee, V.; Kim, R.; Park, S.; Mahmoudi, M.; Kraft, M. L., Impact of protein pre-coating on the protein corona composition and nanoparticle cellular uptake. *Biomaterials* **2016,** *75*, 295-304.

91. Gebauer, J. S.; Malissek, M.; Simon, S.; Knauer, S. K.; Maskos, M.; Stauber, R. H.; Peukert, W.; Treuel, L., Impact of the nanoparticle–protein corona on colloidal stability and protein structure. *Langmuir* **2012,** *28* (25), 9673-9679.

92. Weber, C.; Morsbach, S.; Landfester, K., Possibilities and limitations of different separation techniques for the analysis of the protein corona. *Angewandte Chemie International Edition* **2019,** *58* (37), 12787-12794.

93. Kruszewska, J.; Zajda, J.; Matczuk, M., How to effectively prepare a sample for bottom-up proteomic analysis of nanoparticle protein corona? A critical review. *Talanta* **2021,** *226*, 122153.

94. Brewer, S. H.; Glomm, W. R.; Johnson, M. C.; Knag, M. K.; Franzen, S., Probing BSA binding to citrate-coated gold nanoparticles and surfaces. *Langmuir* **2005,** *21* (20), 9303-9307.

95. Syrový, I.; Hodný, Z., Staining and quantification of proteins separated by polyacrylamide gel electrophoresis. *Journal of Chromatography B: Biomedical Sciences and Applications* **1991,** *569* (1-2), 175-196.

96. Lundqvist, M.; Stigler, J.; Elia, G.; Lynch, I.; Cedervall, T.; Dawson, K. A., Nanoparticle size and surface properties determine the protein corona with possible implications for biological impacts. *Proceedings of the National Academy of Sciences* **2008,** *105* (38), 14265-14270.

97. Chetwynd, A. J.; Wheeler, K. E.; Lynch, I., Best practice in reporting corona studies: Minimum information about Nanomaterial Biocorona Experiments (MINBE). *Nano Today* **2019,** *28*, 100758.

98. Lai, Z. W.; Yan, Y.; Caruso, F.; Nice, E. C., Emerging techniques in proteomics for probing nano–bio interactions. *ACS nano* **2012,** *6* (12), 10438-10448.

99. Distler, U.; Kuharev, J.; Tenzer, S., Biomedical applications of ion mobility-enhanced data-independent acquisition-based label-free quantitative proteomics. *Expert review of proteomics* **2014,** *11* (6), 675-684.

100. Silva, J. C.; Denny, R.; Dorschel, C. A.; Gorenstein, M.; Kass, I. J.; Li, G.-Z.; McKenna, T.; Nold, M. J.; Richardson, K.; Young, P., Quantitative proteomic analysis by accurate mass retention time pairs. *Analytical chemistry* **2005,** *77* (7), 2187-2200.

101. Geromanos, S. J.; Vissers, J. P.; Silva, J. C.; Dorschel, C. A.; Li, G. Z.; Gorenstein, M. V.; Bateman, R. H.; Langridge, J. I., The detection, correlation, and comparison of peptide precursor and product ions from data independent LC‐MS with data dependant LC‐MS/MS. *Proteomics* **2009,** *9* (6), 1683-1695.

102. Valentine, S. J.; Liu, X.; Plasencia, M. D.; Hilderbrand, A. E.; Kurulugama, R. T.; Koeniger, S. L.; Clemmer, D. E., Developing liquid chromatography ion mobility mass spectometry techniques. *Expert Review of Proteomics* **2005,** *2* (4), 553-565.

103. Shliaha, P. V.; Bond, N. J.; Gatto, L.; Lilley, K. S., Effects of traveling wave ion mobility separation on data independent acquisition in proteomics studies. *Journal of proteome research* **2013,** *12* (6), 2323-2339.

104. Silva, J. C.; Gorenstein, M. V.; Li, G. Z.; Vissers, J. P.; Geromanos, S. J., Absolute quantification of proteins by LCMSE: a virtue of parallel MS acquisition. *Mol. Cell. Proteomics* **2006,** *5* (1), 144-56.

105. Manzari, M. T.; Shamay, Y.; Kiguchi, H.; Rosen, N.; Scaltriti, M.; Heller, D. A., Targeted drug delivery strategies for precision medicines. *Nature Reviews Materials* **2021,** *6* (4), 351-370.

106. Farjadian, F.; Ghasemi, A.; Gohari, O.; Roointan, A.; Karimi, M.; Hamblin, M. R., Nanopharmaceuticals and nanomedicines currently on the market: challenges and opportunities. *Nanomedicine* **2019,** *14* (1), 93-126.

107. Tonigold, M.; Simon, J.; Estupinan, D.; Kokkinopoulou, M.; Reinholz, J.; Kintzel, U.; Kaltbeitzel, A.; Renz, P.; Domogalla, M. P.; Steinbrink, K.; Lieberwirth, I.; Crespy, D.; Landfester, K.; Mailander, V., Pre-adsorption of antibodies enables targeting of nanocarriers despite a biomolecular corona. *Nat Nanotechnol* **2018,** *13* (9), 862-869.

108. Yu, L.; Xu, M.; Xu, W.; Xiao, W.; Jiang, X.-h.; Wang, L.; Gao, H., Enhanced cancer-targeted drug delivery using precoated nanoparticles. *Nano Letters* **2020,** *20* (12), 8903-8911.

109. Monopoli, M. P.; Walczyk, D.; Campbell, A.; Elia, G.; Lynch, I.; Baldelli Bombelli, F.; Dawson, K. A., Physical− chemical aspects of protein corona: relevance to in vitro and in vivo biological impacts of nanoparticles. *Journal of the American Chemical Society* **2011,** *133* (8), 2525-2534.

110. Lara, S.; Alnasser, F.; Polo, E.; Garry, D.; Lo Giudice, M. C.; Hristov, D. R.; Rocks, L.; Salvati, A.; Yan, Y.; Dawson, K. A., Identification of receptor binding to the biomolecular corona of nanoparticles. *ACS nano* **2017,** *11* (2), 1884-1893.

111. Francia, V.; Yang, K.; Deville, S.; Reker-Smit, C.; Nelissen, I.; Salvati, A., Corona composition can affect the mechanisms cells use to internalize nanoparticles. *ACS nano* **2019,** *13* (10), 11107-11121.

112. Schottler, S.; Landfester, K.; Mailander, V., Controlling the Stealth Effect of Nanocarriers through Understanding the Protein Corona. *Angew. Chem. Int. Ed. Engl.* **2016,** *55* (31), 8806-15.

113. Xue, C.; Yonet-Tanyeri, N.; Brouette, N.; Sferrazza, M.; Braun, P. V.; Leckband, D. E., Protein adsorption on poly(N-isopropylacrylamide) brushes: dependence on grafting density and chain collapse. *Langmuir* **2011,** *27* (14), 8810-8.

114. Cedervall, T.; Lynch, I.; Foy, M.; Berggard, T.; Donnelly, S. C.; Cagney, G.; Linse, S.; Dawson, K. A., Detailed identification of plasma proteins adsorbed on copolymer nanoparticles. *Angew Chem Int Ed Engl* **2007,** *46* (30), 5754-6.

115. Yoshimatsu, K.; Lesel, B. K.; Yonamine, Y.; Beierle, J. M.; Hoshino, Y.; Shea, K. J., Temperature-responsive "catch and release" of proteins by using multifunctional polymer-based nanoparticles. *Angew Chem Int Ed Engl* **2012,** *51* (10), 2405-8.

116. Lesniak, A.; Campbell, A.; Monopoli, M. P.; Lynch, I.; Salvati, A.; Dawson, K. A., Serum heat inactivation affects protein corona composition and nanoparticle uptake. *Biomaterials* **2010,** *31* (36), 9511-8.

117. Simon, J.; Muller, J.; Ghazaryan, A.; Morsbach, S.; Mailander, V.; Landfester, K., Protein denaturation caused by heat inactivation detrimentally affects biomolecular corona formation and cellular uptake. *Nanoscale* **2018,** *10* (45), 21096-21105.

118. Aoyama, M.; Hata, K.; Higashisaka, K.; Nagano, K.; Yoshioka, Y.; Tsutsumi, Y., Clusterin in the protein corona plays a key role in the stealth effect of nanoparticles against phagocytes. *Biochemical and biophysical research communications* **2016,** *480* (4), 690-695.

119. Simon, J.; Wolf, T.; Klein, K.; Landfester, K.; Wurm, F. R.; Mailander, V., Hydrophilicity Regulates the Stealth Properties of Polyphosphoester-Coated Nanocarriers. *Angew Chem Int Ed Engl* **2018,** *57* (19), 5548-5553.

120. Jiang, S.; Prozeller, D.; Pereira, J.; Simon, J.; Han, S.; Wirsching, S.; Fichter, M.; Mottola, M.; Lieberwirth, I.; Morsbach, S.; Mailander, V.; Gehring, S.; Crespy, D.; Landfester, K., Controlling protein interactions in blood for effective liver immunosuppressive therapy by silica nanocapsules. *Nanoscale* **2020,** *12* (4), 2626-2637.

121. Schwartz, R. S. a. C., C. L. Blood. https: //www.britannica.com/science/blood-biochemistry. Accessed 16 November 2021.

122. Firkowska-Boden, I.; Zhang, X.; Jandt, K. D., Controlling Protein Adsorption through Nanostructured Polymeric Surfaces. *Adv Healthc Mater* **2018,** *7* (1).

123. Weber, C.; Simon, J.; Mailänder, V.; Morsbach, S.; Landfester, K., Preservation of the soft protein corona in distinct flow allows identification of weakly bound proteins. *Acta biomaterialia* **2018,** *76*, 217-224.

124. Donahue, N. D.; Acar, H.; Wilhelm, S., Concepts of nanoparticle cellular uptake, intracellular trafficking, and kinetics in nanomedicine. *Adv Drug Deliv Rev* **2019,** *143*, 68-96.

125. Clift, M. J.; Brandenberger, C.; Rothen-Rutishauser, B.; Brown, D. M.; Stone, V., The uptake and intracellular fate of a series of different surface coated quantum dots in vitro. *Toxicology* **2011,** *286* (1-3), 58-68.

126. Chen, J.; Yu, Z.; Chen, H.; Gao, J.; Liang, W., Transfection efficiency and intracellular fate of polycation liposomes combined with protamine. *Biomaterials* **2011,** *32* (5), 1412-1418.

127. Panariti, A.; Miserocchi, G.; Rivolta, I., The effect of nanoparticle uptake on cellular behavior: disrupting or enabling functions? *Nanotechnology, science and applications* **2012,** *5*, 87.

128. Mosquera, J.; García, I.; Liz-Marzán, L. M., Cellular uptake of nanoparticles versus small molecules: a matter of size. *Accounts of chemical research* **2018,** *51* (9), 2305-2313.

129. Foroozandeh, P.; Aziz, A. A., Insight into cellular uptake and intracellular trafficking of nanoparticles. *Nanoscale research letters* **2018,** *13* (1), 1-12.

130. Hillaireau, H.; Couvreur, P., Nanocarriers' entry into the cell: relevance to drug delivery. *Cellular and molecular life sciences* **2009,** *66* (17), 2873-2896.

131. Rennick, J. J.; Johnston, A. P.; Parton, R. G., Key principles and methods for studying the endocytosis of biological and nanoparticle therapeutics. *Nature nanotechnology* **2021,** *16* (3), 266-276.

132. Elkin, S. R.; Lakoduk, A. M.; Schmid, S. L., Endocytic pathways and endosomal trafficking: a primer. *Wiener Medizinische Wochenschrift* **2016,** *166* (7), 196-204.

133. Neutra, M. R.; Ciechanover, A.; Owen, L. S.; Lodish, H. F., Intracellular transport of transferrin- and asialoorosomucoid-colloidal gold conjugates to lysosomes after receptor-mediated endocytosis. *J Histochem Cytochem* **1985,** *33* (11), 1134-44.

134. Carpentier, J. L.; Gorden, P.; Anderson, R. G.; Goldstein, J. L.; Brown, M. S.; Cohen, S.; Orci, L., Co-localization of 125I-epidermal growth factor and ferritin-low density lipoprotein in coated pits: a quantitative electron microscopic study in normal and mutant human fibroblasts. *J Cell Biol* **1982,** *95* (1), 73-7.

135. Keen, J. H., Clathrin assembly proteins: affinity purification and a model for coat assembly. *J Cell Biol* **1987,** *105* (5), 1989-98.

136. Robinson, M. S., Forty Years of Clathrin-coated Vesicles. *Traffic* **2015,** *16* (12), 1210-38.

137. Ungewickell, E.; Branton, D., Assembly units of clathrin coats. *Nature* **1981,** *289* (5796), 420-422.

138. Roth, T. F.; Porter, K. R., Yolk Protein Uptake in the Oocyte of the Mosquito Aedes Aegypti. L. *J Cell Biol* **1964,** *20*, 313-32.

139. Harush-Frenkel, O.; Rozentur, E.; Benita, S.; Altschuler, Y., Surface charge of nanoparticles determines their endocytic and transcytotic pathway in polarized MDCK cells. *Biomacromolecules* **2008,** *9* (2), 435-43.

140. Panyam, J.; Labhasetwar, V., Dynamics of endocytosis and exocytosis of poly(D,L-lactide-co-glycolide) nanoparticles in vascular smooth muscle cells. *Pharm Res* **2003,** *20* (2), 212-20.

141. Bareford, L. M.; Swaan, P. W., Endocytic mechanisms for targeted drug delivery. *Adv Drug Deliv Rev* **2007,** *59* (8), 748-58.

142. Pelkmans, L.; Helenius, A., Endocytosis via caveolae. *Traffic* **2002,** *3* (5), 311-320.

143. Pelkmans, L.; Kartenbeck, J.; Helenius, A., Caveolar endocytosis of simian virus 40 reveals a new two-step vesicular-transport pathway to the ER. *Nature cell biology* **2001,** *3* (5), 473-483.

144. Huotari, J.; Helenius, A., Endosome maturation. *The EMBO journal* **2011,** *30* (17), 3481-3500.

145. Oh, P.; Borgström, P.; Witkiewicz, H.; Li, Y.; Borgström, B. J.; Chrastina, A.; Iwata, K.; Zinn, K. R.; Baldwin, R.; Testa, J. E., Live dynamic imaging of caveolae pumping targeted antibody rapidly and specifically across endothelium in the lung. *Nature biotechnology* **2007,** *25* (3), 327-337.

146. Dauty, E.; Remy, J. S.; Zuber, G.; Behr, J. P., Intracellular delivery of nanometric DNA particles via the folate receptor. *Bioconjug Chem* **2002,** *13* (4), 831-9.

147. Gradishar, W. J., Albumin-bound paclitaxel: a next-generation taxane. *Expert Opin Pharmacother* **2006,** *7* (8), 1041-53.

148. Buckley, C. M.; King, J. S., Drinking problems: mechanisms of macropinosome formation and maturation. *The FEBS journal* **2017,** *284* (22), 3778-3790.

149. Lin, X. P.; Mintern, J. D.; Gleeson, P. A., Macropinocytosis in different cell types: similarities and differences. *Membranes* **2020,** *10* (8), 177.

150. Racoosin, E. L.; Swanson, J. A., M-CSF-induced macropinocytosis increases solute endocytosis but not receptor-mediated endocytosis in mouse macrophages. *Journal of cell science* **1992,** *102* (4), 867-880.

151. Lee, H.-J.; Woo, Y.; Hahn, T.-W.; Jung, Y. M.; Jung, Y.-J., Formation and maturation of the phagosome: a key mechanism in innate immunity against intracellular bacterial infection. *Microorganisms* **2020,** *8* (9), 1298.

152. Grislain, L.; Couvreur, P.; Lenaerts, V.; Roland, M.; Deprez-Decampeneere, D.; Speiser, P., Pharmacokinetics and distribution of a biodegradable drug-carrier. *International journal of pharmaceutics* **1983,** *15* (3), 335-345.

153. Wang, T.; Bai, J.; Jiang, X.; Nienhaus, G. U., Cellular uptake of nanoparticles by membrane penetration: a study combining confocal microscopy with FTIR spectroelectrochemistry. *ACS nano* **2012,** *6* (2), 1251-1259.

154. Jiang, Y.; Huo, S.; Mizuhara, T.; Das, R.; Lee, Y.-W.; Hou, S.; Moyano, D. F.; Duncan, B.; Liang, X.-J.; Rotello, V. M., The interplay of size and surface functionality on the cellular uptake of sub-10 nm gold nanoparticles. *ACS nano* **2015,** *9* (10), 9986-9993.

155. Kube, S.; Hersch, N.; Naumovska, E.; Gensch, T.; Hendriks, J.; Franzen, A.; Landvogt, L.; Siebrasse, J.-P.; Kubitscheck, U.; Hoffmann, B., Fusogenic liposomes as nanocarriers for the delivery of intracellular proteins. *Langmuir* **2017,** *33* (4), 1051-1059.

156. Langston Suen, W. L.; Chau, Y., Size-dependent internalisation of folate-decorated nanoparticles via the pathways of clathrin and caveolae-mediated endocytosis in ARPE-19 cells. *J Pharm Pharmacol* **2014,** *66* (4), 564-73.

157. Cheng, X.; Tian, X.; Wu, A.; Li, J.; Tian, J.; Chong, Y.; Chai, Z.; Zhao, Y.; Chen, C.; Ge, C., Protein Corona Influences Cellular Uptake of Gold Nanoparticles by Phagocytic and Nonphagocytic Cells in a Size-Dependent Manner. *ACS Appl Mater Interfaces* **2015,** *7* (37), 20568-75.

158. Maxfield, F. R.; McGraw, T. E., Endocytic recycling. *Nat Rev Mol Cell Biol* **2004,** *5* (2), 121-32.

159. Cullen, P. J., Endosomal sorting and signalling: an emerging role for sorting nexins. *Nat Rev Mol Cell Biol* **2008,** *9* (7), 574-82.

160. Maxfield, F. R.; Yamashiro, D. J., Endosome acidification and the pathways of receptor-mediated endocytosis. *Immunobiology of proteins and peptides IV* **1987**, 189-198.

161. Hu, Y. B.; Dammer, E. B.; Ren, R. J.; Wang, G., The endosomal-lysosomal system: from acidification and cargo sorting to neurodegeneration. *Transl Neurodegener* **2015,** *4*, 18.

162. Mellman, I.; Fuchs, R.; Helenius, A., Acidification of the endocytic and exocytic pathways. *Annu Rev Biochem* **1986,** *55*, 663-700.

163. Martinez, O.; Goud, B., Rab proteins. *Biochimica et Biophysica Acta (BBA)-Molecular Cell Research* **1998,** *1404* (1-2), 101-112.

164. Rink, J.; Ghigo, E.; Kalaidzidis, Y.; Zerial, M., Rab conversion as a mechanism of progression from early to late endosomes. *Cell* **2005,** *122* (5), 735-49.

165. Muthukottiappan, P.; Winter, D., A proteomic view on lysosomes. *Mol Omics* **2021,** *17* (6), 842-859.

166. Trivedi, P. C.; Bartlett, J. J.; Pulinilkunnil, T., Lysosomal Biology and Function: Modern View of Cellular Debris Bin. *Cells* **2020,** *9* (5).

167. Luzio, J. P.; Pryor, P. R.; Bright, N. A., Lysosomes: fusion and function. *Nat Rev Mol Cell Biol* **2007,** *8* (8), 622-32.

168. Serda, R. E.; Mack, A.; van de Ven, A. L.; Ferrati, S.; Dunner, K., Jr.; Godin, B.; Chiappini, C.; Landry, M.; Brousseau, L.; Liu, X.; Bean, A. J.; Ferrari, M., Logic-embedded vectors for intracellular partitioning, endosomal escape, and exocytosis of nanoparticles. *Small* **2010,** *6* (23), 2691-700.

169. Melamed, J. R.; Ioele, S. A.; Hannum, A. J.; Ullman, V. M.; Day, E. S., Polyethylenimine-Spherical Nucleic Acid Nanoparticles against Gli1 Reduce the Chemoresistance and Stemness of Glioblastoma Cells. *Mol Pharm* **2018,** *15* (11), 5135-5145.

170. Xu, X.; Wu, J.; Liu, Y.; Yu, M.; Zhao, L.; Zhu, X.; Bhasin, S.; Li, Q.; Ha, E.; Shi, J.; Farokhzad, O. C., Ultra-pH-Responsive and Tumor-Penetrating Nanoplatform for Targeted siRNA Delivery with Robust Anti-Cancer Efficacy. *Angew Chem Int Ed Engl* **2016,** *55* (25), 7091-7094.

171. Prasetyanto, E. A.; Bertucci, A.; Septiadi, D.; Corradini, R.; Castro-Hartmann, P.; De Cola, L., Breakable Hybrid Organosilica Nanocapsules for Protein Delivery. *Angew Chem Int Ed Engl* **2016,** *55* (10), 3323-7.

172. Oh, N.; Park, J. H., Endocytosis and exocytosis of nanoparticles in mammalian cells. *Int J Nanomedicine* **2014,** *9 Suppl 1*, 51-63.

173. Sakhtianchi, R.; Minchin, R. F.; Lee, K.-B.; Alkilany, A. M.; Serpooshan, V.; Mahmoudi, M., Exocytosis of nanoparticles from cells: role in cellular retention and toxicity. *Advances in colloid and interface science* **2013,** *201*, 18-29.

174. Almers, W., Exocytosis. *Annual Review of Physiology* **1990,** *52* (1), 607-624.

175. Kim, C.; Tonga, G. Y.; Yan, B.; Kim, C. S.; Kim, S. T.; Park, M. H.; Zhu, Z.; Duncan, B.; Creran, B.; Rotello, V. M., Regulating exocytosis of nanoparticles via host-guest chemistry. *Org Biomol Chem* **2015,** *13* (8), 2474-2479.

176. Qin, J.; Xu, Q., Functions and application of exosomes. *Acta Pol Pharm* **2014,** *71* (4), 537-543.

177. Rodríguez, A.; Webster, P.; Ortego, J.; Andrews, N. W., Lysosomes behave as Ca2+-regulated exocytic vesicles in fibroblasts and epithelial cells. *The Journal of cell biology* **1997,** *137* (1), 93-104.

178. Chu, Z.; Huang, Y.; Tao, Q.; Li, Q., Cellular uptake, evolution, and excretion of silica nanoparticles in human cells. *Nanoscale* **2011,** *3* (8), 3291-3299.

179. Chithrani, B. D.; Chan, W. C., Elucidating the mechanism of cellular uptake and removal of protein-coated gold nanoparticles of different sizes and shapes. *Nano letters* **2007,** *7* (6), 1542-1550.

180. Abbina, S.; Takeuchi, L. E.; Anilkumar, P.; Yu, K.; Rogalski, J. C.; Shenoi, R. A.; Constantinescu, I.; Kizhakkedathu, J. N., Blood circulation of soft nanomaterials is governed by dynamic remodeling of protein opsonins at nano-biointerface. *Nat Commun* **2020,** *11* (1), 3048.

181. Behzadi, S.; Serpooshan, V.; Sakhtianchi, R.; Muller, B.; Landfester, K.; Crespy, D.; Mahmoudi, M., Protein corona change the drug release profile of nanocarriers: the "overlooked" factor at the nanobio interface. *Colloids Surf B Biointerfaces* **2014,** *123*, 143-9.

182. Obst, K.; Yealland, G.; Balzus, B.; Miceli, E.; Dimde, M.; Weise, C.; Eravci, M.; Bodmeier, R.; Haag, R.; Calderon, M.; Charbaji, N.; Hedtrich, S., Protein Corona Formation on Colloidal Polymeric Nanoparticles and Polymeric Nanogels: Impact on Cellular Uptake, Toxicity, Immunogenicity, and Drug Release Properties. *Biomacromolecules* **2017,** *18* (6), 1762-1771.

183. Hofmann, D.; Tenzer, S.; Bannwarth, M. B.; Messerschmidt, C.; Glaser, S. F.; Schild, H.; Landfester, K.; Mailander, V., Mass spectrometry and imaging analysis of nanoparticle-containing vesicles provide a mechanistic insight into cellular trafficking. *ACS Nano* **2014,** *8* (10), 10077-88.

184. Bertoli, F.; Garry, D.; Monopoli, M. P.; Salvati, A.; Dawson, K. A., The Intracellular Destiny of the Protein Corona: A Study on its Cellular Internalization and Evolution. *ACS Nano* **2016,** *10* (11), 10471-10479.

185. Bradshaw, R. A.; Burlingame, A. L.; Carr, S.; Aebersold, R., Reporting protein identification data: the next generation of guidelines. *Molecular & Cellular Proteomics* **2006,** *5* (5), 787-788.

186. Schwille, P.; Meyer-Almes, F.-J.; Rigler, R., Dual-color fluorescence cross-correlation spectroscopy for multicomponent diffusional analysis in solution. *Biophysical journal* **1997,** *72* (4), 1878-1886.

187. Rigler, R.; Elson, E. S., *Fluorescence Correlation Spectroscopy: Theory and Applications*. 1 ed.; Springer Berlin, Heidelberg: Germany, 2001; p 487.

188. Han, S.; Raabe, M.; Hodgson, L.; Mantell, J.; Verkade, P.; Lasser, T.; Landfester, K.; Weil, T.; Lieberwirth, I., High-Contrast Imaging of Nanodiamonds in Cells by Energy Filtered and Correlative Light-Electron Microscopy: Toward a Quantitative Nanoparticle-Cell Analysis. *Nano Lett* **2019,** *19* (3), 2178-2185.

189. Kim, J. A.; Aberg, C.; Salvati, A.; Dawson, K. A., Role of cell cycle on the cellular uptake and dilution of nanoparticles in a cell population. *Nat Nanotechnol* **2011,** *7* (1), 62-8.

190. Ekkapongpisit, M.; Giovia, A.; Nicotra, G.; Ozzano, M.; Caputo, G.; Isidoro, C., Labeling and exocytosis of secretory compartments in RBL mastocytes by polystyrene and mesoporous silica nanoparticles. *International Journal of Nanomedicine* **2012,** *7*, 1829-1840.

191. Fiorentino, I.; Gualtieri, R.; Barbato, V.; Mollo, V.; Braun, S.; Angrisani, A.; Turano, M.; Furia, M.; Netti, P. A.; Guarnieri, D.; Fusco, S.; Talevi, R., Energy independent uptake and release of polystyrene nanoparticles in primary mammalian cell cultures. *Exp Cell Res* **2015,** *330* (2), 240-247.

192. Grant, B. D.; Donaldson, J. G., Pathways and mechanisms of endocytic recycling. *Nat Rev Mol Cell Biol* **2009,** *10* (9), 597-608.

193. Tooze, J.; Hollinshead, M., In Att20 and Hela-Cells Brefeldin-a Induces the Fusion of Tubular Endosomes and Changes Their Distribution and Some of Their Endocytic Properties. *Journal of Cell Biology* **1992,** *118* (4), 813-830.

194. Gruenberg, J.; Stenmark, H., The biogenesis of multivesicular endosomes. *Nat Rev Mol Cell Bio* **2004,** *5* (4), 317-323.

195. Fader, C. M.; Colombo, M. I., Autophagy and multivesicular bodies: two closely related partners. *Cell Death Differ* **2009,** *16* (1), 70-78.

196. Thery, C.; Zitvogel, L.; Amigorena, S., Exosomes: composition, biogenesis and function. *Nat Rev Immunol* **2002,** *2* (8), 569-79.

197. Raoufi, M.; Hajipour, M. J.; Kamali Shahri, S. M.; Schoen, I.; Linn, U.; Mahmoudi, M., Probing fibronectin conformation on a protein corona layer around nanoparticles. *Nanoscale* **2018,** *10* (3), 1228-1233.

198. Kihara, S.; van der Heijden, N. J.; Seal, C. K.; Mata, J. P.; Whitten, A. E.; Koper, I.; McGillivray, D. J., Soft and Hard Interactions between Polystyrene Nanoplastics and Human Serum Albumin Protein Corona. *Bioconjugate Chemistry* **2019,** *30* (4), 1067-1076.

199. Hadjidemetriou, M.; Kostarelos, K., NANOMEDICINE Evolution of the nanoparticle corona. *Nature Nanotechnology* **2017,** *12* (4), 288-290.

200. Mohammad-Beigi, H.; Hayashi, Y.; Zeuthen, C. M.; Eskandari, H.; Scavenius, C.; Juul-Madsen, K.; Vorup-Jensen, T.; Enghild, J. J.; Sutherland, D. S., Mapping and identification of soft corona proteins at nanoparticles and their impact on cellular association. *Nature Communications* **2020,** *11* (1).

201. Vila-Vicosa, D.; Campos, S. R.; Baptista, A. M.; Machuqueiro, M., Reversibility of prion misfolding: insights from constant-pH molecular dynamics simulations. *J Phys Chem B* **2012,** *116* (30), 8812-21.

202. Strojan, K.; Leonardi, A.; Bregar, V. B.; Križaj, I.; Svete, J.; Pavlin, M., Dispersion of nanoparticles in different media importantly determines the composition of their protein corona. *PLoS one* **2017,** *12* (1), e0169552.

203. Wang, C.; Chen, B.; He, M.; Hu, B., Composition of Intracellular Protein Corona around Nanoparticles during Internalization. *ACS nano* **2021,** *15* (2), 3108-3122.

204. Cai, R.; Ren, J.; Guo, M.; Wei, T.; Liu, Y.; Xie, C.; Zhang, P.; Guo, Z.; Chetwynd, A. J.; Ke, P. C., Dynamic intracellular exchange of nanomaterials' protein corona perturbs proteostasis and remodels cell metabolism. *Proceedings of the National Academy of Sciences* **2022,** *119* (23), e2200363119.

205. Rosenblum, D.; Joshi, N.; Tao, W.; Karp, J. M.; Peer, D., Progress and challenges towards targeted delivery of cancer therapeutics. *Nat Commun* **2018,** *9* (1), 1410.

206. Bertoli, F.; Davies, G. L.; Monopoli, M. P.; Moloney, M.; Gun'ko, Y. K.; Salvati, A.; Dawson, K. A., Magnetic nanoparticles to recover cellular organelles and study the time resolved nanoparticle-cell interactome throughout uptake. *Small* **2014,** *10* (16), 3307-15.

207. Qin, M.; Zhang, J.; Li, M.; Yang, D.; Liu, D.; Song, S.; Fu, J.; Zhang, H.; Dai, W.; Wang, X.; Wang, Y.; He, B.; Zhang, Q., Proteomic analysis of intracellular protein corona of nanoparticles elucidates nano-trafficking network and nano-bio interactions. *Theranostics* **2020,** *10* (3), 1213-1229.

208. Noga, M.; Edinger, D.; Kläger, R.; Wegner, S. V.; Spatz, J. P.; Wagner, E.; Winter, G.; Besheer, A., The effect of molar mass and degree of hydroxyethylation on the controlled shielding and deshielding of hydroxyethyl starch-coated polyplexes. *Biomaterials* **2013,** *34* (10), 2530-2538.

209. Sabado, R. L.; Balan, S.; Bhardwaj, N., Dendritic cell-based immunotherapy. *Cell Res* **2017,** *27* (1), 74-95.

210. Bannwarth, M. B.; Kazer, S. W.; Ulrich, S.; Glasser, G.; Crespy, D.; Landfester, K., Well-defined nanofibers with tunable morphology from spherical colloidal building blocks. *Angew Chem Int Ed Engl* **2013,** *52* (38), 10107-11.

211. Schindelin, J.; Arganda-Carreras, I.; Frise, E.; Kaynig, V.; Longair, M.; Pietzsch, T.; Preibisch, S.; Rueden, C.; Saalfeld, S.; Schmid, B., Fiji: an open-source platform for biological-image analysis. *Nature methods* **2012,** *9* (7), 676-682.

212. Oliveros, J. C. Venny. An interactive tool for comparing lists with Venn's diagrams. https://bioinfogp.cnb.csic.es/tools/venny/index.html.

213. Sherman, B. T.; Hao, M.; Qiu, J.; Jiao, X.; Baseler, M. W.; Lane, H. C.; Imamichi, T.; Chang, W., DAVID: a web server for functional enrichment analysis and functional annotation of gene lists (2021 update). *Nucleic Acids Res* **2022**.

214. Huang, D. W.; Sherman, B. T.; Lempicki, R. A., Systematic and integrative analysis of large gene lists using DAVID bioinformatics resources. *Nature protocols* **2009,** *4* (1), 44-57.

215. Zhu, X.; Meng, G.; Dickinson, B. L.; Li, X.; Mizoguchi, E.; Miao, L.; Wang, Y.; Robert, C.; Wu, B.; Smith, P. D.; Lencer, W. I.; Blumberg, R. S., MHC class I-related neonatal Fc receptor for IgG is functionally expressed in monocytes, intestinal macrophages, and dendritic cells. *J Immunol* **2001,** *166* (5), 3266-76.

216. Wu, L.; Chen, M.; Mao, H.; Wang, N.; Zhang, B.; Zhao, X.; Qian, J.; Xing, C., Albumin-based nanoparticles as methylprednisolone carriers for targeted delivery towards the neonatal Fc receptor in glomerular podocytes. *Int J Mol Med* **2017,** *39* (4), 851-860.

217. Macia, E.; Ehrlich, M.; Massol, R.; Boucrot, E.; Brunner, C.; Kirchhausen, T., Dynasore, a cell-permeable inhibitor of dynamin. *Dev Cell* **2006,** *10* (6), 839-50.

218. Park, R. J.; Shen, H.; Liu, L.; Liu, X.; Ferguson, S. M.; De Camilli, P., Dynamin triple knockout cells reveal off target effects of commonly used dynamin inhibitors. *J Cell Sci* **2013,** *126* (Pt 22), 5305-12.

219. Yamada, H.; Abe, T.; Li, S.-A.; Masuoka, Y.; Isoda, M.; Watanabe, M.; Nasu, Y.; Kumon, H.; Asai, A.; Takei, K., Dynasore, a dynamin inhibitor, suppresses lamellipodia formation and cancer cell invasion by destabilizing actin filaments. *Biochemical and biophysical research communications* **2009,** *390* (4), 1142-1148.

220. Kitajima, Y.; Sekiya, T.; Nozawa, Y., Freeze-fracture ultrastructural alterations induced by filipin, pimaricin, nystatin and amphotericin B in the plasma membranes of Epidermophyton, Saccharomyces and red blood cells. A proposal of models for polyene· ergosterol complex-induced membrane lesions. *Biochimica et Biophysica Acta (BBA)-Biomembranes* **1976,** *455* (2), 452-465.

221. Ros-Baro, A.; Lopez-Iglesias, C.; Peiro, S.; Bellido, D.; Palacin, M.; Zorzano, A.; Camps, M., Lipid rafts are required for GLUT4 internalization in adipose cells. *Proc Natl Acad Sci U S A* **2001,** *98* (21), 12050-5.

222. Jess, T. J.; Belham, C. M.; Thomson, F. J.; Scott, P. H.; Plevin, R. J.; Gould, G. W., Phosphatidylinositol 3'-kinase, but not p70 ribosomal S6 kinase, is involved in membrane protein recycling: wortmannin inhibits glucose transport and downregulates cell-surface transferrin receptor numbers independently of any effect on fluid-phase endocytosis in fibroblasts. *Cell Signal* **1996,** *8* (4), 297-304.

223. Gladhaug, I. P.; Christoffersen, T., Amiloride inhibits constitutive internalization and increases the surface number of epidermal growth factor receptors in intact rat hepatocytes. *J Cell Physiol* **1990,** *143* (1), 188-95.

224. Brenner, S. L.; Korn, E. D., Substoichiometric concentrations of cytochalasin D inhibit actin polymerization. Additional evidence for an F-actin treadmill. *J Biol Chem* **1979,** *254* (20), 9982-5.

225. Davies, P. J.; Davies, D. R.; Levitzki, A.; Maxfield, F. R.; Milhaud, P.; Willingham, M. C.; Pastan, I. H., Transglutaminase is essential in receptor-mediated endocytosis of alpha 2-macroglobulin and polypeptide hormones. *Nature* **1980,** *283* (5743), 162-7.

226. Wang, L. H.; Rothberg, K. G.; Anderson, R. G., Mis-assembly of clathrin lattices on endosomes reveals a regulatory switch for coated pit formation. *J Cell Biol* **1993,** *123* (5), 1107-17.

227. Kilsdonk, E. P.; Yancey, P. G.; Stoudt, G. W.; Bangerter, F. W.; Johnson, W. J.; Phillips, M. C.; Rothblat, G. H., Cellular cholesterol efflux mediated by cyclodextrins. *J Biol Chem* **1995,** *270* (29), 17250-6.

228. Parton, R. G.; Joggerst, B.; Simons, K., Regulated internalization of caveolae. *J Cell Biol* **1994,** *127* (5), 1199-215.

229. Le, P. U.; Nabi, I. R., Distinct caveolae-mediated endocytic pathways target the Golgi apparatus and the endoplasmic reticulum. *J Cell Sci* **2003,** *116* (Pt 6), 1059-71.

230. Deacon, S. W.; Beeser, A.; Fukui, J. A.; Rennefahrt, U. E.; Myers, C.; Chernoff, J.; Peterson, J. R., An isoform-selective, small-molecule inhibitor targets the autoregulatory mechanism of p21-activated kinase. *Chem Biol* **2008,** *15* (4), 322-31.

231. Vlahos, C. J.; Matter, W. F.; Hui, K. Y.; Brown, R. F., A specific inhibitor of phosphatidylinositol 3-kinase, 2-(4-morpholinyl)-8-phenyl-4H-1-benzopyran-4-one (LY294002). *J Biol Chem* **1994,** *269* (7), 5241-8.

232. Araki, N.; Johnson, M. T.; Swanson, J. A., A role for phosphoinositide 3-kinase in the completion of macropinocytosis and phagocytosis by macrophages. *J Cell Biol* **1996,** *135* (5), 1249-60.

233. Hoebeke, J.; Van Nijen, G.; De Brabander, M., Interaction of oncodazole (R 17934), a new antitumoral drug, with rat brain tubulin. *Biochem Biophys Res Commun* **1976,** *69* (2), 319-24.

234. Conner, S. D.; Schmid, S. L., Regulated portals of entry into the cell. *Nature* **2003,** *422* (6927), 37-44.

235. Freeman, S. A.; Grinstein, S., Resolution of macropinosomes, phagosomes and autolysosomes: Osmotically driven shrinkage enables tubulation and vesiculation. *Traffic* **2018,** *19* (12), 965-974.

236. Piper, R. C.; Katzmann, D. J., Biogenesis and function of multivesicular bodies. *Annu Rev Cell Dev Biol* **2007,** *23*, 519-47.

237. Yanes, R. E.; Tarn, D.; Hwang, A. A.; Ferris, D. P.; Sherman, S. P.; Thomas, C. R.; Lu, J.; Pyle, A. D.; Zink, J. I.; Tamanoi, F., Involvement of lysosomal exocytosis in the excretion of mesoporous silica nanoparticles and enhancement of the drug delivery effect by exocytosis inhibition. *Small* **2013,** *9* (5), 697-704.

238. Ganley, I. G.; Carroll, K.; Bittova, L.; Pfeffer, S., Rab9 GTPase regulates late endosome size and requires effector interaction for its stability. *Mol Biol Cell* **2004,** *15* (12), 5420-30.

239. Anderson, L.; Anderson, N. G., High resolution two-dimensional electrophoresis of human plasma proteins. *Proc Natl Acad Sci U S A* **1977,** *74* (12), 5421-5.

240. Fujii, M.; Kawai, K.; Egami, Y.; Araki, N., Dissecting the roles of Rac1 activation and deactivation in macropinocytosis using microscopic photo-manipulation. *Sci Rep* **2013,** *3*, 2385.

241. Tanna, C. E.; Goss, L. B.; Ludwig, C. G.; Chen, P. W., Arf GAPs as Regulators of the Actin Cytoskeleton-An Update. *Int J Mol Sci* **2019,** *20* (2).

242. Williamson, C. D.; Donaldson, J. G., Arf6, JIP3, and dynein shape and mediate macropinocytosis. *Mol Biol Cell* **2019,** *30* (12), 1477-1489.

243. Hansen, C. G.; Bright, N. A.; Howard, G.; Nichols, B. J., SDPR induces membrane curvature and functions in the formation of caveolae. *Nat Cell Biol* **2009,** *11* (7), 807-14.

244. Jeon, D.; Yang, Y. M.; Jeong, M. J.; Philipson, K. D.; Rhim, H.; Shin, H. S., Enhanced learning and memory in mice lacking Na+/Ca2+ exchanger 2. *Neuron* **2003,** *38* (6), 965-76.

245. Pasternak, S. H.; Bagshaw, R. D.; Guiral, M.; Zhang, S.; Ackerley, C. A.; Pak, B. J.; Callahan, J. W.; Mahuran, D. J., Presenilin-1, nicastrin, amyloid precursor protein, and gamma-secretase activity are co-localized in the lysosomal membrane. *J Biol Chem* **2003,** *278* (29), 26687-94.

246. Pizon, V.; Desjardins, M.; Bucci, C.; Parton, R. G.; Zerial, M., Association of Rap1a and Rap1b proteins with late endocytic/phagocytic compartments and Rap2a with the Golgi complex. *J Cell Sci* **1994,** *107 (Pt 6)*, 1661-70.

247. Nishi, T.; Kawasaki-Nishi, S.; Forgac, M., Expression and function of the mouse V-ATPase d subunit isoforms. *J Biol Chem* **2003,** *278* (47), 46396-402.

248. Hofmann, I.; Munro, S., An N-terminally acetylated Arf-like GTPase is localised to lysosomes and affects their motility. *Journal of cell science* **2006,** *119* (8), 1494-1503.

249. Chistiakov, D. A.; Killingsworth, M. C.; Myasoedova, V. A.; Orekhov, A. N.; Bobryshev, Y. V., CD68/macrosialin: not just a histochemical marker. *Lab Invest* **2017,** *97* (1), 4-13.

250. Stoka, V.; Turk, V.; Turk, B., Lysosomal cathepsins and their regulation in aging and neurodegeneration. *Ageing Res Rev* **2016,** *32*, 22-37.

251. Bandyopadhyay, U.; Kaushik, S.; Varticovski, L.; Cuervo, A. M., The chaperone-mediated autophagy receptor organizes in dynamic protein complexes at the lysosomal membrane. *Mol Cell Biol* **2008,** *28* (18), 5747-63.

252. Leng, C.; Overeem, A. W.; Carton-Garcia, F.; Li, Q.; Klappe, K.; Kuipers, J.; Cui, Y.; Zuhorn, I. S.; Arango, D.; van, I. S. C. D., Loss of MYO5B expression deregulates late endosome size which hinders mitotic spindle orientation. *PLoS Biol* **2019,** *17* (11), e3000531.

253. Schafer, J. C.; Baetz, N. W.; Lapierre, L. A.; McRae, R. E.; Roland, J. T.; Goldenring, J. R., Rab11-FIP2 interaction with MYO5B regulates movement of Rab11a-containing recycling vesicles. *Traffic* **2014,** *15* (3), 292-308.

254. Ko, D. C.; Binkley, J.; Sidow, A.; Scott, M. P., The integrity of a cholesterol-binding pocket in Niemann-Pick C2 protein is necessary to control lysosome cholesterol levels. *Proc Natl Acad Sci U S A* **2003,** *100* (5), 2518-25.

255. Han, Y.; Li, X.; Zhang, Y.; Han, Y.; Chang, F.; Ding, J., Mesenchymal stem cells for regenerative medicine. *Cells* **2019,** *8* (8), 886.

256. Motiei, M.; Dreifuss, T.; Sadan, T.; Omer, N.; Blumenfeld-Katzir, T.; Fragogeorgi, E.; Loudos, G.; Popovtzer, R.; Ben-Eliezer, N., Trimodal Nanoparticle Contrast Agent for CT, MRI and SPECT Imaging: Synthesis and Characterization of Radiolabeled Core/Shell Iron Oxide@Gold Nanoparticles. *Chemistry Letters* **2019,** *48* (3), 291-294.

257. Chemla, Y.; Betzer, O.; Markus, A.; Farah, N.; Motiei, M.; Popovtzer, R.; Mandel, Y., Gold nanoparticles for multimodal high-resolution imaging of transplanted cells for retinal replacement therapy. *Nanomedicine* **2019,** *14* (14), 1857-1871.

258. Hahn, M. A.; Singh, A. K.; Sharma, P.; Brown, S. C.; Moudgil, B. M., Nanoparticles as contrast agents for in-vivo bioimaging: current status and future perspectives. *Analytical and bioanalytical chemistry* **2011,** *399* (1), 3-27.

259. Barthélémy, I.; Thibaud, J.-L.; de Fornel, P.; Cassano, M.; Punzón, I.; Mauduit, D.; Vilquin, J.-T.; Devauchelle, P.; Sampaolesi, M.; Blot, S., In vivo stem cell tracking using scintigraphy in a canine model of DMD. *Scientific reports* **2020,** *10* (1), 1-13.

260. Glover, J. C.; Aswendt, M.; Boulland, J.-L.; Lojk, J.; Stamenković, S.; Andjus, P.; Fiori, F.; Hoehn, M.; Mitrecic, D.; Pavlin, M., In vivo cell tracking using non-invasive imaging of iron oxide-based particles with particular relevance for stem cell-based treatments of neurological and cardiac disease. *Molecular Imaging and Biology* **2020,** *22* (6), 1469-1488.

261. Kim, J.; Chhour, P.; Hsu, J.; Litt, H. I.; Ferrari, V. A.; Popovtzer, R.; Cormode, D. P., Use of nanoparticle contrast agents for cell tracking with computed tomography. *Bioconjugate chemistry* **2017,** *28* (6), 1581-1597.

262. Chithrani, B. D.; Ghazani, A. A.; Chan, W. C., Determining the size and shape dependence of gold nanoparticle uptake into mammalian cells. *Nano letters* **2006,** *6* (4), 662-668.

263. Senut, M. C.; Zhang, Y.; Liu, F.; Sen, A.; Ruden, D. M.; Mao, G., Size‐dependent toxicity of gold nanoparticles on human embryonic stem cells and their neural derivatives. *Small* **2016,** *12* (5), 631-646.

264. Meir, R.; Shamalov, K.; Betzer, O.; Motiei, M.; Horovitz-Fried, M.; Yehuda, R.; Popovtzer, A.; Popovtzer, R.; Cohen, C. J., Nanomedicine for cancer immunotherapy: tracking cancer-specific T-cells in vivo with gold nanoparticles and CT imaging. *ACS nano* **2015,** *9* (6), 6363-6372.

265. Yu, C.; Bao, H.; Chen, Z.; Li, X.; Liu, X.; Wang, W.; Huang, J.; Zhang, Z., Enhanced and long-term CT imaging tracking of transplanted stem cells labeled with temperature-responsive gold nanoparticles. *Journal of Materials Chemistry B* **2021,** *9* (12), 2854-2865.

266. Bao, H.; Xia, Y.; Yu, C.; Ning, X.; Liu, X.; Fu, H.; Chen, Z.; Huang, J.; Zhang, Z., CT/Bioluminescence Dual‐Modal Imaging Tracking of Mesenchymal Stem Cells in Pulmonary Fibrosis. *Small* **2019,** *15* (46), 1904314.

267. Ning, X.; Bao, H.; Liu, X.; Fu, H.; Wang, W.; Huang, J.; Zhang, Z., Long-term in vivo CT tracking of mesenchymal stem cells labeled with Au@ BSA@ PLL nanotracers. *Nanoscale* **2019,** *11* (43), 20932-20941.

268. Ramot, Y.; Meiron, M.; Toren, A.; Steiner, M.; Nyska, A., Safety and biodistribution profile of placental-derived mesenchymal stromal cells (PLX-PAD) following intramuscular delivery. *Toxicologic pathology* **2009,** *37* (5), 606-616.

269. Zahavi-Goldstein, E.; Blumenfeld, M.; Fuchs-Telem, D.; Pinzur, L.; Rubin, S.; Aberman, Z.; Sher, N.; Ofir, R., Placenta-derived PLX-PAD mesenchymal-like stromal cells are efficacious in rescuing blood flow in hind limb ischemia mouse model by a dose-and site-dependent mechanism of action. *Cytotherapy* **2017,** *19* (12), 1438-1446.

270. Norgren, L.; Weiss, N.; Nikol, S.; Hinchliffe, R. J.; Lantis, J. C.; Patel, M. R.; Reinecke, H.; Ofir, R.; Rosen, Y.; Peres, D., PLX-PAD cell treatment of critical limb ischaemia: rationale and design of the PACE trial. *European Journal of Vascular and Endovascular Surgery* **2019,** *57* (4), 538-545.

271. Chatterjee, P.; Chiasson, V. L.; Pinzur, L.; Raveh, S.; Abraham, E.; Jones, K. A.; Bounds, K. R.; Ofir, R.; Flaishon, L.; Chajut, A., Human placenta-derived stromal cells decrease inflammation, placental injury and blood pressure in hypertensive pregnant mice. *Clinical Science* **2016,** *130* (7), 513-523.

272. Rubinstein, L.; Paul, A. M.; Houseman, C.; Abegaz, M.; Tabares Ruiz, S.; O'Neil, N.; Kunis, G.; Ofir, R.; Cohen, J.; Ronca, A. E., Placenta-expanded stromal cell therapy in a rodent model of simulated weightlessness. *Cells* **2021,** *10* (4), 940.

273. Prather, W. R.; Toren, A.; Meiron, M.; Ofir, R.; Tschope, C.; Horwitz, E. M., The role of placental-derived adherent stromal cell (PLX-PAD) in the treatment of critical limb ischemia. *Cytotherapy* **2009,** *11* (4), 427-434.

274. Barkama, R.; Mayo, A.; Paz, A.; Solopov, A.; Mann, T.; Vadasz, Z.; Appel, T.; Ofir, R.; Shani, L.; Sheleg, M., Placenta-derived cell therapy to treat patients with respiratory failure due to coronavirus disease 2019. *Critical care explorations* **2020,** *2* (9).

275. Winkler, T.; Perka, C.; von Roth, P.; Agres, A. N.; Plage, H.; Preininger, B.; Pumberger, M.; Geissler, S.; Hagai, E. L.; Ofir, R.; Pinzur, L.; Eyal, E.; Stoltenburg-Didinger, G.; Meisel, C.; Consentius, C.; Streitz, M.; Reinke, P.; Duda, G. N.; Volk, H. D., Immunomodulatory placental-expanded, mesenchymal stromal cells improve muscle function following hip arthroplasty. *J Cachexia Sarcopenia Muscle* **2018,** *9* (5), 880-897.

276. Maleitzke, T.; Reinke, P.; Agres, A. N.; Alves, S. A.; Akyüz, L.; Fleckenstein, F. N.; Bichmann, A.; Ofir, R.; Perka, C.; Duda, G. N., Intramuscular and intratendinous placenta‐derived mesenchymal stromal‐like cell treatment of a chronic quadriceps tendon rupture. *Journal of Cachexia, Sarcopenia and Muscle* **2022**.

277. Papait, A.; Vertua, E.; Magatti, M.; Ceccariglia, S.; De Munari, S.; Silini, A. R.; Sheleg, M.; Ofir, R.; Parolini, O., Mesenchymal stromal cells from fetal and maternal placenta possess key similarities and differences: potential implications for their applications in regenerative medicine. *Cells* **2020,** *9* (1), 127.

278. Consentius, C.; Akyüz, L.; Schmidt‐Lucke, J.; Tschöpe, C.; Pinzur, L.; Ofir, R.; Reinke, P.; Volk, H. D.; Juelke, K., Mesenchymal stromal cells prevent allostimulation in vivo and control checkpoints of Th1 priming: migration of human DC to lymph nodes and NK cell activation. *Stem cells* **2015,** *33* (10), 3087-3099.

279. Lahiani, A.; Zahavi, E.; Netzer, N.; Ofir, R.; Pinzur, L.; Raveh, S.; Arien-Zakay, H.; Yavin, E.; Lazarovici, P., Human placental eXpanded (PLX) mesenchymal-like adherent stromal cells confer neuroprotection to nerve growth factor (NGF)-differentiated PC12 cells exposed to ischemia by secretion of IL-6 and VEGF. *Biochimica et Biophysica Acta (BBA)-Molecular Cell Research* **2015,** *1853* (2), 422-430.

280. Ding, L.; Yao, C.; Yin, X.; Li, C.; Huang, Y.; Wu, M.; Wang, B.; Guo, X.; Wang, Y.; Wu, M., Size, shape, and protein corona determine cellular uptake and removal mechanisms of gold nanoparticles. *Small* **2018,** *14* (42), 1801451.

281. Wang, Y.; Wu, Q.; Sui, K.; Chen, X.-X.; Fang, J.; Hu, X.; Wu, M.; Liu, Y., A quantitative study of exocytosis of titanium dioxide nanoparticles from neural stem cells. *Nanoscale* **2013,** *5* (11), 4737-4743.

282. Renz, P.; Kokkinopoulou, M.; Landfester, K.; Lieberwirth, I., Imaging of polymeric nanoparticles: hard challenge for soft objects. *Macromolecular Chemistry and Physics* **2016,** *217* (17), 1879-1885.

283. Huang, D. W.; Sherman, B. T.; Lempicki, R. A., Bioinformatics enrichment tools: paths toward the comprehensive functional analysis of large gene lists. *Nucleic acids research* **2009,** *37* (1), 1-13.

284. Nölte, J., *ICP Emissionsspektrometrie für Praktiker: Grundlagen, Methodenentwicklung, Anwendungsbeispiele*. John Wiley & Sons: 2020.

285. Karpievitch, Y. V.; Polpitiya, A. D.; Anderson, G. A.; Smith, R. D.; Dabney, A. R., Liquid chromatography mass spectrometry-based proteomics: biological and technological aspects. *The annals of applied statistics* **2010,** *4* (4), 1797.

286. Nokes, R. L.; Fields, I. C.; Collins, R. N.; Fölsch, H., Rab13 regulates membrane trafficking between TGN and recycling endosomes in polarized epithelial cells. *The Journal of cell biology* **2008,** *182* (5), 845-853.

287. Morimoto, S.; Nishimura, N.; Terai, T.; Manabe, S.; Yamamoto, Y.; Shinahara, W.; Miyake, H.; Tashiro, S.; Shimada, M.; Sasaki, T., Rab13 mediates the continuous endocytic recycling of occludin to the cell surface. *Journal of Biological Chemistry* **2005,** *280* (3), 2220-2228.

288. Marin, E.; Boschetto, F.; Pezzotti, G., Biomaterials and biocompatibility: An historical overview. *Journal of Biomedical Materials Research Part A* **2020,** *108* (8), 1617-1633.

289. Williams, D., The relationship between biomaterials and nanotechnology. *Biomaterials* **2008,** *29* (12), 1737-1738.

290. Dimitriou, R.; Jones, E.; McGonagle, D.; Giannoudis, P. V., Bone regeneration: current concepts and future directions. *BMC medicine* **2011,** *9* (1), 1-10.

291. Van Heest, A.; Swiontkowski, M., Bone-graft substitutes. *The Lancet* **1999,** *353*, S28-S29.

292. Greenwald, A. S.; Boden, S. D.; Goldberg, V. M.; Khan, Y.; Laurencin, C. T.; Rosier, R. N., Bone-graft substitutes: facts, fictions, and applications. *Jbjs* **2001,** *83* (2), S98-103.

293. Campana, V.; Milano, G.; Pagano, E.; Barba, M.; Cicione, C.; Salonna, G.; Lattanzi, W.; Logroscino, G., Bone substitutes in orthopaedic surgery: from basic science to clinical practice. *Journal of Materials Science: Materials in Medicine* **2014,** *25* (10), 2445-2461.

294. Baumhauer, J.; Pinzur, M. S.; Donahue, R.; Beasley, W.; DiGiovanni, C., Site selection and pain outcome after autologous bone graft harvest. *Foot & ankle international* **2014,** *35* (2), 104-107.

295. Mroz, T. E.; Joyce, M. J.; Steinmetz, M. P.; Lieberman, I. H.; Wang, J. C., Musculoskeletal allograft risks and recalls in the United States. *JAAOS-Journal of the American Academy of Orthopaedic Surgeons* **2008,** *16* (10), 559-565.

296. Carson, J. S.; Bostrom, M. P., Synthetic bone scaffolds and fracture repair. *Injury* **2007,** *38* (1), S33-S37.

297. Zwingenberger, S.; Nich, C.; Valladares, R. D.; Yao, Z.; Stiehler, M.; Goodman, S. B., Recommendations and considerations for the use of biologics in orthopedic surgery. *BioDrugs* **2012,** *26* (4), 245-256.

298. Yamada, S.; Heymann, D.; Bouler, J.-M.; Daculsi, G., Osteoclastic resorption of calcium phosphate ceramics with different hydroxyapatite/β-tricalcium phosphate ratios. *Biomaterials* **1997,** *18* (15), 1037-1041.

299. Le Huec, J. C.; Clement, D.; Brouillaud, B.; Barthe, N.; Dupuy, B.; Foliguet, B.; Basse-Cathalinat, B., Evolution of the local calcium content around irradiated beta-tricalcium phosphate ceramic implants: in vivo study in the rabbit. *Biomaterials* **1998,** *19* (7-9), 733-8.

300. Bhatt, R. A.; Rozental, T. D., Bone graft substitutes. *Hand Clin* **2012,** *28* (4), 457-68.

301. Buck, D. W.; Dumanian, G. A., Bone biology and physiology: Part I. The fundamentals. *Plastic and reconstructive surgery* **2012,** *129* (6), 1314-1320.

302. Buckwalter, J.; Glimcher, M.; Cooper, R.; Recker, R., Bone biology. *J Bone Joint Surg Am* **1995,** *77* (8), 1256-75.

303. Clarke, B., Normal bone anatomy and physiology. *Clinical journal of the American Society of Nephrology* **2008,** *3* (Supplement 3), S131-S139.

304. Gundberg, C. M., Matrix proteins. *Osteoporos Int* **2003,** *14 Suppl 5*, S37-40; discussion S40-2.

305. Lieberman, J. R.; Friedlaender, G. E., *Bone regeneration and repair: biology and clinical applications*. Springer: 2005.

306. Claes, L.; Eckert-Hübner, K.; Augat, P., The fracture gap size influences the local vascularization and tissue differentiation in callus healing. *Langenbeck's archives of surgery* **2003,** *388* (5), 316-322.

307. Sathyendra, V.; Darowish, M., Basic science of bone healing. *Hand clinics* **2013,** *29* (4), 473-481.

308. McKibbin, B., The biology of fracture healing in long bones. *The Journal of bone and joint surgery. British volume* **1978,** *60* (2), 150-162.

309. Carmeliet, P.; Jain, R. K., Molecular mechanisms and clinical applications of angiogenesis. *Nature* **2011,** *473* (7347), 298-307.

310. Risau, W., Mechanisms of angiogenesis. *Nature* **1997,** *386* (6626), 671-674.

311. Hankenson, K. D.; Dishowitz, M.; Gray, C.; Schenker, M., Angiogenesis in bone regeneration. *Injury* **2011,** *42* (6), 556-61.

312. Leotot, J.; Coquelin, L.; Bodivit, G.; Bierling, P.; Hernigou, P.; Rouard, H.; Chevallier, N., Platelet lysate coating on scaffolds directly and indirectly enhances cell migration, improving bone and blood vessel formation. *Acta Biomater* **2013,** *9* (5), 6630-40.

313. Roach, P.; Eglin, D.; Rohde, K.; Perry, C. C., Modern biomaterials: a review—bulk properties and implications of surface modifications. *Journal of Materials Science: Materials in Medicine* **2007,** *18* (7), 1263-1277.

314. Webster, T. J.; Ergun, C.; Doremus, R. H.; Siegel, R. W.; Bizios, R., Specific proteins mediate enhanced osteoblast adhesion on nanophase ceramics. *Journal of Biomedical Materials Research: An Official Journal of The Society for Biomaterials, The Japanese Society for Biomaterials, and The Australian Society for Biomaterials and the Korean Society for Biomaterials* **2000,** *51* (3), 475-483.

315. Wang, J.; Chen, X.; Guo, B.; Yang, X.; Zhou, Y.; Zhu, X.; Zhang, K.; Fan, Y.; Tu, C.; Zhang, X., A serum protein adsorption profile on BCP ceramics and influence of the elevated adsorption of adhesive proteins on the behaviour of MSCs. *Journal of Materials Chemistry B* **2018,** *6* (45), 7383-7395.

316. Pasche, S.; Vörös, J.; Griesser, H. J.; Spencer, N. D.; Textor, M., Effects of ionic strength and surface charge on protein adsorption at PEGylated surfaces. *The Journal of Physical Chemistry B* **2005,** *109* (37), 17545-17552.

317. Wang, K.; Zhou, C.; Hong, Y.; Zhang, X., A review of protein adsorption on bioceramics. *Interface focus* **2012,** *2* (3), 259-277.

318. Lee, W. H.; Loo, C. Y.; Zavgorodniy, A. V.; Rohanizadeh, R., High protein adsorptive capacity of amino acid‐functionalized hydroxyapatite. *Journal of Biomedical Materials Research Part A* **2013,** *101* (3), 873-883.

319. Lee, W.-H.; Loo, C.-Y.; Zavgorodniy, A. V.; Ghadiri, M.; Rohanizadeh, R., A novel approach to enhance protein adsorption and cell proliferation on hydroxyapatite: citric acid treatment. *RSC advances* **2013,** *3* (12), 4040-4051.

320. Duan, R.; Barbieri, D.; de Groot, F.; de Bruijn, J. D.; Yuan, H., Modulating Bone Regeneration in Rabbit Condyle Defects with Three Surface-Structured Tricalcium Phosphate Ceramics. *ACS Biomater Sci Eng* **2018,** *4* (9), 3347-3355.

321. Rechendorff, K.; Hovgaard, M. B.; Foss, M.; Zhdanov, V.; Besenbacher, F., Enhancement of protein adsorption induced by surface roughness. *Langmuir* **2006,** *22* (26), 10885-10888.

322. Zhang, K.; Fan, Y.; Dunne, N.; Li, X., Effect of microporosity on scaffolds for bone tissue engineering. *Regenerative biomaterials* **2018,** *5* (2), 115-124.

323. Lee, W. H.; Zavgorodniy, A. V.; Loo, C. Y.; Rohanizadeh, R., Synthesis and characterization of hydroxyapatite with different crystallinity: effects on protein adsorption and release. *Journal of Biomedical Materials Research Part A* **2012,** *100* (6), 1539-1549.

324. Horbett, T. A., The role of adsorbed proteins in tissue response to biomaterials. In *Biomaterials science : an introduction to materials in medicine*, 2nd ed.; Ratner, B. D., Ed. Elsevier Academic Press: Amsterdam ; Boston, 2004; pp 237-2346.

325. Kurien, T.; Pearson, R. G.; Scammell, B. E., Bone graft substitutes currently available in orthopaedic practice: the evidence for their use. *Bone Joint J* **2013,** *95-B* (5), 583-97.

326. Fernandez de Grado, G.; Keller, L.; Idoux-Gillet, Y.; Wagner, Q.; Musset, A. M.; Benkirane-Jessel, N.; Bornert, F.; Offner, D., Bone substitutes: a review of their characteristics, clinical use, and perspectives for large bone defects management. *J Tissue Eng* **2018,** *9*, 2041731418776819.

327. Zhou, K.; Ren, X.; Zhao, M.; Mei, X.; Zhang, P.; Chen, Z.; Zhu, X., Promoting proliferation and differentiation of BMSCs by green tea polyphenols functionalized porous calcium phosphate. *Regenerative Biomaterials* **2017,** *5* (1), 35-41.

328. Wang, D.; Zhang, P.; Mei, X.; Chen, Z., Repair calvarial defect of osteoporotic rats by berberine functionalized porous calcium phosphate scaffold. *Regenerative Biomaterials* **2021,** *8* (3).

329. Meng, D.; Dong, L.; Yuan, Y.; Jiang, Q., In vitro and in vivo analysis of the biocompatibility of two novel and injectable calcium phosphate cements. *Regenerative Biomaterials* **2018,** *6* (1), 13-19.

330. Kjalarsdóttir, L.; Dýrfjörd, A.; Dagbjartsson, A.; Laxdal, E. H.; Örlygsson, G.; Gíslason, J.; Einarsson, J. M.; Ng, C.-H.; Jónsson, H., Jr, Bone remodeling effect of a chitosan and calcium phosphate-based composite. *Regenerative Biomaterials* **2019,** *6* (4), 241-247.

331. Italiano, J. E., Jr.; Richardson, J. L.; Patel-Hett, S.; Battinelli, E.; Zaslavsky, A.; Short, S.; Ryeom, S.; Folkman, J.; Klement, G. L., Angiogenesis is regulated by a novel mechanism: pro- and antiangiogenic proteins are organized into separate platelet alpha granules and differentially released. *Blood* **2008,** *111* (3), 1227-33.

332. Battinelli, E. M.; Markens, B. A.; Italiano, J. E., Jr., Release of angiogenesis regulatory proteins from platelet alpha granules: modulation of physiologic and pathologic angiogenesis. *Blood* **2011,** *118* (5), 1359-69.

333. Chatterjee, M.; Huang, Z.; Zhang, W.; Jiang, L.; Hultenby, K.; Zhu, L.; Hu, H.; Nilsson, G. P.; Li, N., Distinct platelet packaging, release, and surface expression of proangiogenic and antiangiogenic factors on different platelet stimuli. *Blood* **2011,** *117* (14), 3907-11.

334. Peterson, J. E.; Zurakowski, D.; Italiano, J. E., Jr.; Michel, L. V.; Fox, L.; Klement, G. L.; Folkman, J., Normal ranges of angiogenesis regulatory proteins in human platelets. *Am J Hematol* **2010,** *85* (7), 487-93.

335. Zaslavsky, A.; Baek, K. H.; Lynch, R. C.; Short, S.; Grillo, J.; Folkman, J.; Italiano, J. E., Jr.; Ryeom, S., Platelet-derived thrombospondin-1 is a critical negative regulator and potential biomarker of angiogenesis. *Blood* **2010,** *115* (22), 4605-13.

336. Kim, Y. M.; Hwang, S.; Kim, Y. M.; Pyun, B. J.; Kim, T. Y.; Lee, S. T.; Gho, Y. S.; Kwon, Y. G., Endostatin blocks vascular endothelial growth factor-mediated signaling via direct interaction with KDR/Flk-1. *J Biol Chem* **2002,** *277* (31), 27872-9.

337. Brill, A.; Elinav, H.; Varon, D., Differential role of platelet granular mediators in angiogenesis. *Cardiovasc Res* **2004,** *63* (2), 226-35.

338. Strandberg, G.; Sellberg, F.; Sommar, P.; Ronaghi, M.; Lubenow, N.; Knutson, F.; Berglund, D., Standardizing the freeze-thaw preparation of growth factors from platelet lysate. *Transfusion* **2017,** *57* (4), 1058-1065.

339. Kumm, E. J.; Pagel, O.; Gambaryan, S.; Walter, U.; Zahedi, R. P.; Smolenski, A.; Jurk, K., The Cell Cycle Checkpoint System MAST(L)-ENSA/ARPP19-PP2A is Targeted by cAMP/PKA and cGMP/PKG in Anucleate Human Platelets. *Cells* **2020,** *9* (2).

340. Daculsi, G.; Jegoux, F.; Layrolle, P., The micro macroporous biphasic calcium phosphate concept for bone reconstruction and tissue engineering. Wiley-American Ceramic Society: Hoboken, NJ, USA: 2009; p 768.

341. d'Arros, C.; Borget, P.; Miramond, T.; Daculsi, G., Calcium Phosphate Bioceramics in Biomaterials Development and Applications. In *Encyclopedia of Biophysics*, Roberts, G.; Watts, A., Eds. Springer Berlin Heidelberg: Berlin, Heidelberg, 2020; pp 1-10.

342. Daculsi, G.; LeGeros, R. Z.; Grimandi, G.; Soueidan, A.; Aguado, E.; Goyenvalle, E.; LeGeros, J. P. In *Effect of sintering process of HA/TCP bioceramics on microstructure, dissolution, cell*

proliferation and bone ingrowth, Key Engineering Materials, Trans Tech Publ: 2008; pp 1139-1142.

343. Duan, R.; Barbieri, D.; Luo, X.; Weng, J.; Bao, C.; de Bruijn, J. D.; Yuan, H., Variation of the bone forming ability with the physicochemical properties of calcium phosphate bone substitutes. *Biomater Sci* **2017,** *6* (1), 136-145.

344. d'Arros, C.; Rouillon, T.; Veziers, J.; Malard, O.; Borget, P.; Daculsi, G., Bioactivity of Biphasic Calcium Phosphate Granules, the Control of a Needle-Like Apatite Layer Formation for Further Medical Device Developments. *Front Bioeng Biotechnol* **2019,** *7*, 462.

345. Docter, D.; Distler, U.; Storck, W.; Kuharev, J.; Wunsch, D.; Hahlbrock, A.; Knauer, S. K.; Tenzer, S.; Stauber, R. H., Quantitative profiling of the protein coronas that form around nanoparticles. *Nat Protoc* **2014,** *9* (9), 2030-44.

346. Carpentier, G.; Berndt, S.; Ferratge, S.; Rasband, W.; Cuendet, M.; Uzan, G.; Albanese, P., Angiogenesis Analyzer for ImageJ - A comparative morphometric analysis of "Endothelial Tube Formation Assay" and "Fibrin Bead Assay". *Sci Rep* **2020,** *10* (1), 11568.

347. Coppinger, J. A.; Cagney, G.; Toomey, S.; Kislinger, T.; Belton, O.; McRedmond, J. P.; Cahill, D. J.; Emili, A.; Fitzgerald, D. J.; Maguire, P. B., Characterization of the proteins released from activated platelets leads to localization of novel platelet proteins in human atherosclerotic lesions. *Blood* **2004,** *103* (6), 2096-104.

348. Lawler, J., Thrombospondin-1 as an endogenous inhibitor of angiogenesis and tumor growth. *J Cell Mol Med* **2002,** *6* (1), 1-12.

349. Bikfalvi, A.; Gimenez-Gallego, G., The control of angiogenesis and tumor invasion by platelet factor-4 and platelet factor-4-derived molecules. *Semin Thromb Hemost* **2004,** *30* (1), 137-44.

350. Gleissner, C. A.; von Hundelshausen, P.; Ley, K., Platelet chemokines in vascular disease. *Arterioscler Thromb Vasc Biol* **2008,** *28* (11), 1920-7.

351. van der Bijl, I.; Vlig, M.; Middelkoop, E.; de Korte, D., Allogeneic platelet-rich plasma (PRP) is superior to platelets or plasma alone in stimulating fibroblast proliferation and migration, angiogenesis, and chemotaxis as relevant processes for wound healing. *Transfusion* **2019,** *59* (11), 3492-3500.

352. Berndt, S.; Carpentier, G.; Turzi, A.; Borlat, F.; Cuendet, M.; Modarressi, A., Angiogenesis Is Differentially Modulated by Platelet-Derived Products. *Biomedicines* **2021,** *9* (3), 251.

353. Barsotti, M. C.; Losi, P.; Briganti, E.; Sanguinetti, E.; Magera, A.; Al Kayal, T.; Feriani, R.; Di Stefano, R.; Soldani, G., Effect of platelet lysate on human cells involved in different phases of wound healing. *PLoS One* **2013,** *8* (12), e84753.

354. Yuan, H.; Fernandes, H.; Habibovic, P.; de Boer, J.; Barradas, A. M.; de Ruiter, A.; Walsh, W. R.; van Blitterswijk, C. A.; de Bruijn, J. D., Osteoinductive ceramics as a synthetic alternative to autologous bone grafting. *Proc Natl Acad Sci U S A* **2010,** *107* (31), 13614-9.

355. Wang, J.; Chen, Y.; Zhu, X.; Yuan, T.; Tan, Y.; Fan, Y.; Zhang, X., Effect of phase composition on protein adsorption and osteoinduction of porous calcium phosphate ceramics in mice. *Journal of biomedical materials research Part A* **2014,** *102* (12), 4234-4243.

356. Burkhart, J. M.; Vaudel, M.; Gambaryan, S.; Radau, S.; Walter, U.; Martens, L.; Geiger, J.; Sickmann, A.; Zahedi, R. P., The first comprehensive and quantitative analysis of human platelet protein composition allows the comparative analysis of structural and functional pathways. *Blood* **2012,** *120* (15), e73-82.

357. Pilatova, K.; Greplova, K.; Demlova, R.; Bencsikova, B.; Klement, G. L.; Zdrazilova-Dubska, L., Role of platelet chemokines, PF-4 and CTAP-III, in cancer biology. *Journal of Hematology & Oncology* **2013,** *6* (1), 42.

358. Lawler, P. R.; Lawler, J., Molecular basis for the regulation of angiogenesis by thrombospondin-1 and -2. *Cold Spring Harb Perspect Med* **2012,** *2* (5), a006627.

359. Perollet, C.; Han, Z. C.; Savona, C.; Caen, J. P.; Bikfalvi, A., Platelet factor 4 modulates fibroblast growth factor 2 (FGF-2) activity and inhibits FGF-2 dimerization. *Blood* **1998,** *91* (9), 3289-99.

360. Fricke, I.; Mitchell, D.; Petersen, F.; Bohle, A.; Bulfone-Paus, S.; Brandau, S., Platelet factor 4 in conjunction with IL-4 directs differentiation of human monocytes into specialized antigen-presenting cells. *FASEB J* **2004,** *18* (13), 1588-90.

361. Kaur, S.; Roberts, D. D., CD47 applies the brakes to angiogenesis via vascular endothelial growth factor receptor-2. *Cell Cycle* **2011,** *10* (1), 10-2.

362. Isenberg, J. S.; Ridnour, L. A.; Dimitry, J.; Frazier, W. A.; Wink, D. A.; Roberts, D. D., CD47 is necessary for inhibition of nitric oxide-stimulated vascular cell responses by thrombospondin-1. *J Biol Chem* **2006,** *281* (36), 26069-80.

363. Nicosia, R. F.; Tuszynski, G. P., Matrix-bound thrombospondin promotes angiogenesis in vitro. *J Cell Biol* **1994,** *124* (1-2), 183-93.

364. Eckrich, J. M., A.; Jurk, K.; Strieth, S.; Kumm, E.; Brieger, J., The role of thrombospondin-1 in biomaterial integration of porous polyethylene. *Laryngo-Rhino-Otologie* **2019,** *98* (S02), 199 - 200.

365. Strieter, R. M.; Polverini, P. J.; Kunkel, S. L.; Arenberg, D. A.; Burdick, M. D.; Kasper, J.; Dzuiba, J.; Van Damme, J.; Walz, A.; Marriott, D.; et al., The functional role of the ELR motif in CXC chemokine-mediated angiogenesis. *J Biol Chem* **1995,** *270* (45), 27348-57.

366. Tang, Y. Q.; Yeaman, M. R.; Selsted, M. E., Antimicrobial peptides from human platelets. *Infect Immun* **2002,** *70* (12), 6524-33.

367. Chen, Y.; Wang, J.; Zhu, X.; Tang, Z.; Yang, X.; Tan, Y.; Fan, Y.; Zhang, X., Enhanced effect of β-tricalcium phosphate phase on neovascularization of porous calcium phosphate ceramics: in vitro and in vivo evidence. *Acta biomaterialia* **2015,** *11*, 435-448.

368. Kilpadi, K. L.; Sawyer, A. A.; Prince, C. W.; Chang, P. L.; Bellis, S. L., Primary human marrow stromal cells and Saos‐2 osteosarcoma cells use different mechanisms to adhere to hydroxylapatite. *Journal of Biomedical Materials Research Part A: An Official Journal of The Society for Biomaterials, The Japanese Society for Biomaterials, and The Australian Society for Biomaterials and the Korean Society for Biomaterials* **2004,** *68* (2), 273-285.

369. Sawyer, A.; Hennessy, K.; Bellis, S., Regulation of mesenchymal stem cell attachment and spreading on hydroxyapatite by RGD peptides and adsorbed serum proteins. *Biomaterials* **2005,** *26* (13), 1467-1475.

370. Chen, X.; Wang, J.; Chen, Y.; Cai, H.; Yang, X.; Zhu, X.; Fan, Y.; Zhang, X., Roles of calcium phosphate-mediated integrin expression and MAPK signaling pathways in the osteoblastic differentiation of mesenchymal stem cells. *Journal of Materials Chemistry B* **2016,** *4* (13), 2280-2289.

371. Kiec-Wilk, B.; Grzybowska-Galuszka, J.; Polus, A.; Pryjma, J.; Knapp, A.; Kristiansen, K., The MAPK-dependent regulation of the Jagged/Notch gene expression by VEGF, bFGF or PPARγ mediated angiogenesis in HUVEC. *Journal of Physiology and Pharmacology* **2010,** *61* (2), 217.

Curriculum Vitae

Gelöscht für die elektronische Version.

Acknowledgements

Gelöscht für die elektronische Version.